ATLAS BASED IMAGE RECONSTRUCTION FOR DIFFUSE OPTICAL IMAGING OF THE HUMAN BRAIN

By

XUE WU

A thesis submitted to the
University of Birmingham
For the degree of
DOCTOR OF PHILOSOPHY

School of Computer Science
College of Engineering and Physical Sciences
University of Birmingham
September 2015

Abstract

Diffuse Optical Tomography (DOT) is a near infrared (NIR) light based imaging modality which measures light propagation through the subject, recovers small changes in optical properties based on the measured data and reconstructs brain activations based on the recovered changes. Compared to other imaging modalities, DOT is a non-ionizing and non-invasive imaging approach with portable and low-cost imaging systems that can be applied to hospitalised patients and infants. The recovery approach of DOT is divided into two steps: generation of a forward model which simulates light propagation in the subject and an inverse processing of the forward model for parameter-recovery. The forward model is normally generated based on subject-specific structural information obtained from other imaging modalities such as Magnetic resonance imaging (MRI). Registered-atlas based subject models are acceptable alternatives when subject-specific models are not available. Accuracy of atlas-based forward models are directly affected by the accuracy of the registration.

In this work, a number of landmark-based rigid registration methods are quantitatively evaluated and compared based on multiple subjects in geometrical accuracy of the registration result, accuracy of light propagation approximation and recovery accuracy of the brain activations. Since geometrical accuracy of the same subject with the same registration varies in different brain regions, accuracy of the forward model is not distributed uniformly. In this work, landmark-based rigid registration methods are also quantitatively evaluated and compared based on the whole head and localized head regions of the subjects. The most suitable registration methods are selected for the whole head and some specific head regions based on accuracy and efficiency. Registration method based on 19 landmarks from the EEG 10/20 system and non-iterative Point to Point algorithms (EEG 19 nP2P registration) is the

most suitable registration method for recovery of whole cortex activation, and the registration method based on the four external anatomical landmarks (Basic-4 landmark registration) is the most suitable registration method for recovery of focal activations in the visual cortex. A selection criteria for the most suitable registration methods based on the functional brain regions involved is also defined. Besides the recovery accuracy, efficiency of the recovery process is another popular research areas in DOT brain imaging. For a typical head mesh with ~235000 nodes and ~3500 source and detector pairs, generation of light propagation model takes ~3 hours. In previous studies, efficiency of the recovery process was improved by modification of the inverse process. In this work, a modified generation approach of the light propagation approximation is designed based on a reduced sensitivity matrix and parallelisation process. The modified generation approach is evaluated based on a number of subject meshes with different nodes intensity. Compared to conventional approach, it improves the storage efficiency by >1000% and time efficiency by ~400%. The modified generation approach contributes to the real-time DOT brain imaging. Based on this approach, the brain activation recovery of DOT can be processed on a computer without large memory requirements such as a normal laptop which is more suitable for a portable system.

Acknowledgments

I would like to express my sincere gratitude to my supervisor, Dr Hamid Dehghani, for always finding the time to talk with me about my research and patiently sharing his abundance of knowledge. Without him, much of this work would have been impossible to complete. I am also grateful to my Thesis Group members, Prof Ela Claridge, Dr Iain Styles and Prof Ales Leonardis, and to our collaborators, Dr Silvina Ferradal, Dr Adam Eggebrecht and Prof Joseph Culver, in Washington University for their support throughout my Ph.D research. Many thanks are due to my Research Students Administrator, Patrycja Adams, and my Research Students Tutors, Peter Hancox and Dave Parker, who have been extremely helpful throughout my studies. I should also express my gratitude to my colleagues, Hector Basevi, Michael Clancy, Jenny Cutter, and Shelley Taylor, for their help and encouragement. Finally I would like to thank my parents among other lovely members of my family for for their extensive support.

This work has been in part funded by the National Institutes of Health (NIH) Grant R01EB009233-2, RO1-CA132750 and Autism Speaks Meixner Translational Postdoctoral Fellowship 7962.

Contents:

List of Figures:

List of Tables:

List of Notations:

$\Delta\mu$:	The recovered change in optical properties
Δy:	The change in boundary data
α:	The Tikhonov regularisation parameter
A:	The relative refractive index mismatch between tissue and air
$Atlas_i$:	The landmark from atlas model
$Atlas_i^k$:	The landmark from subject surface from iteration k
c:	The speed of light
CC:	The similarity measurement based on the correlation coefficient
$d_H(A,B)$:	The Hausdorff distance between curve A and curve B
E:	The surface error parameter
$f(\hat{s}',\hat{s},r)$:	The scattering phase function characterizing the intensity of a wave incident in direction $\hat{s}'$ scattered into direction $\hat{s}$
$G(r,r')$:	The diffusion Green's function
g:	The mean cosine of the scattering phase function
$I(r,\hat{s},t)$:	The radiance I at time t position r into direction $\hat{s}$
I:	The identity matrix
I:	The log amplitude of boundary data
$I_r(x)$:	The image intensity at location x
$I_s(t(x))$:	The corresponding image intensity of the transformed source image based on transformation t
J:	The sensitivity matrix
$J_{(total,n)}$:	The total sensitivity value at node n for all measurements
J_{err}:	The error of the sensitivity matrix
J_{ref}:	The reference sensitivity matrix
J_{subj}:	The sensitivity matrix of the subject mesh
N:	The number of voxels in the ROI
n:	The number of surface nodes pair.
n:	The number of pairs in the landmark system
NM:	The number of measurements
NN:	The number of nodes
$nodes$:	The number of nodes in activation region
P_i:	The probability of intensity I occurring in source or reference subject
$q(r,\hat{s},t)$:	The source term
q_0:	The source term
Ref_{ci}:	The closest nodes from the reference surface

Ref_i:	The corresponding nodes from the reference surface
SSD:	The similarity measurement based on SSD
Sub_i	The corresponding landmark of atlas from subject i
Sub_i:	The surface node of the registered subject model
T:	The affine transformation matrix
u:	A set of D-dimensional vectors basis functions
u_k:	The associated finite element basis (shape) function
v_{ov}:	The relative percentage overlay of the recovered region
$v_{overlay}$:	The volume of overlay between simulated activation and recovered activation
v_{per}:	Relative recovered volume of the region
v_r:	The volume of the recovered activation
v_s:	The volume of the target simulated activation
$x_{ni}\, y_{ni}\, z_{ni}$:	The coordinate of node i in the region
$x_r\, y_r\, z_r$:	The coordinate of the centre of mass of the recovered activation
$x_s\, y_s\, z_s$:	The coordinate of centre of target simulated activation
β:	The spatial regularisation factor
κ:	The diffusion property
λ:	The regularization parameter
μ_a:	The absorption coefficient
μ_{ani}:	The recovered change of optical parameter of node i
μ_r:	The average contrast in the recovered activation
μ_s:	The scatter coefficient
μ_{sim}:	The simulated change of optical parameter
μ'_s:	The reduced scatter coefficient
μ_0:	An estimate of the parameters
$\Phi(r,t)$:	The radiance of NIR light at position r time t
$\Phi(r,\omega)$:	The fluence of NIR light at position r frequency ω
Φ:	The radiance of NIR light
Φ^j:	The fluence due to source i at nodes k of an element τ associated with a mesh node r
$\Phi_{Adj}{}^{\wedge j}$:	The corresponding Adjoint fluence due to detector j with
Φ_{Calc}:	The simulated data based on the reconstruction
Φ_{Meas}:	The measured data.

List of Abbreviations:

DOT:	Diffuse Optical Tomography
ADHD:	Attention Deficit And Hyperactivity Disorder
AIR:	Automatic Image Registration
APD:	Avalanche Photo Diode
ART:	Automatic Registration Toolbox
BCI:	Brain–Computer Interfacing
BOLD:	Blood Oxygenation Level-Dependent
CC:	Correlation Coefficient
CNR:	Contrast-To-Noise Ratio
CPU:	Central Processing Units
CSF:	Cerebrospinal Fluid
CT:	Computerized Tomography
CW:	Continuous Wave
DA:	Diffusion Approximation
DOI:	Diffuse Optical Imaging
DSM:	Downhill Simplex Method
ECL:	Extra-Cerebral Layers
EEG:	Electroencephalography
F-18 FDG:	Fluorine-18 Fluorodeoxyglucose
FEM:	Finite Element Model
fMRI:	Functional Magnetic Resonance Imaging
Gas:	Genetic Algorithms
GPU:	Graphics Processor Unit
HD:	High-Density
IBSR:	Internet Brain Segmentation Repository
ICBM:	International Consortium For Brain Mapping
ICG:	Indocyanine Green
ICP:	Iterative Closest Point
LED:	Light-Emitting Diode
MC:	Monte Carlo
MEG:	Magnetoencephalography
MI:	Mutual Information
MNI:	Montreal Neurological Institute And Hospital
MRI:	Magnetic Resonance Imaging
MS:	Multiple Sclerosis

NIH:	National Institutes Of Health
NIR:	Near Infra-Red
NIRS:	Near-Infrared Spectroscopy
NMR:	Nuclear Magnetic Resonance
NP2P:	Non-Iterative Point To Point
P2P:	Iterative Point To Point
PET:	Positron Emission Tomography
PMTs:	Photomultiplier Tubes
RF coils:	Radiofrequency Coils
ROI:	Region Of Interest
RTE:	Radiative Transfer Equation
SPM:	Statistical Parametric Mapping
SSD:	Sum Of The Squared Differences
TD:	Talairach Daemon
US:	Ultrasound
X-rays:	X-Radiation

List of publications:

Journal Publications

- **Xue Wu**, Adam T. Eggebrecht, Silvina L. Ferradal, Joseph P. Culver, and Hamid Dehghani, *Fast and efficient image reconstruction for high density diffuse optical imaging of the human brain*, Biomedical Optics Express, Vol 6(11) , pp 4567-4584 doi:10.1364/BOE.6.004567 (2015)
- **Xue Wu**, Adam T Eggebrecht, Silvina L Ferradal, Joseph P Culver, Hamid Dehghani, *Evaluation of rigid registration methods for whole head imaging in diffuse optical tomography,* Neurophotonics 2 (3), 035002-035002,(2015)
- **Xue Wu**, Adam T. Eggebrecht, Silvina L. Ferradal, Joseph P. Culver, and Hamid Dehghani, *Quantitative evaluation of atlas-based high-density diffuse optical tomography for imaging of the human visual cortex*, Biomedical optics express, Vol 5(11), pp 3882-3900, doi: 10.1364/BOE.5.003882 (2014)

Compiled volumes and refereed Conference proceedings

- **Xue Wu**, Adam T Eggebrecht, Silvina L Ferradal, Joseph P Culver, H Dehghani, *Efficient method for near real-time diffuse optical tomography of the human brain,* European Conferences on Biomedical Optics, 953804-953804-5 ,(2015)
- **Xue Wu**, Adam T Eggebrecht, Silvina L Ferradal, Joseph P Culver, Hamid Dehghani, *Atlas-based high-density diffuse optical tomography for imaging the whole human cortex,* SPIE BiOS, 931907-931907-6, (2015)
- **Xue Wu**, Adam T Eggebrecht, Silvina Ferradal, Joseph P Culver, Hamid Dehghani, *Evaluation of Atlas-Based Diffuse Optical Tomography Using Different Registration Methods for Image Recovery,* Biomedical Optics Topical Meeting on CD-ROM (The Optical Society of America, Washington, DC), April 26-30, (2014)
- **Xue Wu**, Adam Eggebrecht, Joseph Culver, Yuxuan Zhan, Hector Basevi, and Hamid Dehghani, *Quantitative evaluation of registration methods for atlas-based diffuse optical tomography,* Proceedings of SPIE Vol. 8799, (2013)
- Kazuki Kurihara, **Xue Wu**, Eiji Okada, and Hamid Dehghani, *A hybrid MC-FEM model for analysis of light propagation in highly scattering medium,* Proceedings of SPIE Vol. 8799, (2013)

CHAPTER 1: INTRODUCTION

Diffuse Optical Tomography (DOT) is a near infra-red (NIR) light based imaging technique which recovers optical properties by monitoring light transmission through the subject. When exposed to NIR light (wavelengths between ~650nm and ~900nm), physiologically interesting molecules such as oxygenated haemoglobin and deoxygenated haemoglobin have characteristic absorption and scattering spectra. Therefore, near infra-red (NIR) light based imaging technique also known as diffuse optical imaging can be used to monitor tissue chromophores such as oxygenated haemoglobin and deoxygenated haemoglobin in different tissue regions. Near-infrared spectroscopy (NIRS) measures the hemodynamics and oxidative metabolism in different tissue regions such as muscles and brain cortex to monitor the activation in these tissue areas. Diffuse optical topography (2D) and diffuse optical tomography (3D) images reconstruct spatial maps of the tissue chromophores based on NIR light. Beside recovery of absolute value, small change in the tissue chromophores can also be recovered based on NIR light. Functional NIRS (fNIRS) monitors activations in human brain by measuring changes in the tissue hemodynamics and oxidative metabolism in the cortex area. Functional DOT also recovers small changes in tissue chromophores by monitoring changes in the measured NIR data during brain activation. DOT is a non-ionizing and non-invasive 3D imaging approach with portable and low cost imaging systems that can be applied to hospitalised patients [1, 2] and infants [3]. DOT brain imaging has been applied to recovery of functional brain activations in the subject [4, 5] during stimulation or resting state [6, 7].

The recovery process of DOT is divided into two steps: generation of a forward model, and inverse processing of the measured data [8]. The forward model simulates propagation of

near-infrared light through the subject based on the distribution of optical properties within the subject. A subject-specific forward model is generated based on anatomical structures of different tissue regions in the subject and their optical properties such as absorption coefficient and scatter coefficient [9, 10]. The anatomical structure of the subject is normally obtained based on other imaging modalities such as MRI. When the subject-specific information is not available, a registered atlas-based subject model has been used as an alternative [9, 11]. Accuracy of the atlas based forward model and its effect on accuracy of recovery is one of the main research areas in the study of atlas-based DOT.

Functional brain activation of a simple stimulation normally appears in the related cortex regions. For example, brain activations during visual stimulations are mainly located in the visual cortex. However, it has been proved that complex tasks such as the hierarchical language tasks affect multiple brain regions [12, 13]. Functional connectivity brain imaging is focused on the correlation between diverse brain regions and mapping of the functional networks [14-16]. Therefore, recovery accuracy of specific regions and the whole cortex are both investigated in neuroimaging studies. For atlas-based DOT recovery, accuracy distribution of the forward model for the whole cortex is worth investigating.

Another main issue in DOT brain recovery is the processing efficiency. Recovery of brain activation in DOT imaging can be extremely time-consuming. The recovery process of brain activation of an adult human takes several hours. Designing an efficient recovery process that recovers the whole cortex activation within 45 minutes is one of the popular research areas in the study of DOT recovery.

1.1. Motivation

Generation of the forward model which simulates the light propagation is one of the main processes in DOT recovery. Several different models have been applied to the generation process, and numerical models such as the finite element model are one of the most commonly used forward models for complex subject such as human brain. The numerical model divides the subject volume into small elements with linearly varying optical properties in each element, and propagation of NIR light is simulated based on each element. The optical properties vary for different tissue types in the human brain; for example, the reduced scattering coefficient for the gray matter is between 20 and 30 per cm and for the white matter is between 70 and 120 per cm [17]. To ensure the accuracy of the approximation in areas with fine structure such as the cortex surface, layered masks from different tissue regions such as skull, gray matter and white matter are used in the generation of the forward model. The layered masks are generated from tissue classification of the subject. The accuracy of the tissue classification has a direct influence on accuracy of the layered masks. Normally, subject specific tissue classification is generated based on imaging data of the same subject from other imaging modalities such as head MRI. However, this approach requires additional brain imaging modalities which increase the cost of DOT brain imaging and are not always available. An alternative approach is generating the tissue classification based on a general atlas [18, 19] which is a series of maps containing structural information from the general population. The atlas-based subject model is created based on registration between the atlas and the subject. Accuracy of the registered atlas-based forward model affects recovery accuracy, and is hence worth investigating.

Different registration methods have been designed for the registration between the atlas head model and subject head model based on different similarity measurement or

transformation model. Based on similarity measurement, the registration methods are divided into feature-based registration and image intensity-based registration. Based on the transformation model, the registration methods are divided into rigid registration and non-rigid registration. For all of the registration methods, the geometrical accuracy of the registered model is not necessarily distributed uniformly in the whole head. For example, the accuracy distribution of the landmark-based registration is affected by the position and density of the landmarks. Accuracies of the forward model in different brain regions as well as the whole head are worth investigating.

Alongside the recovery accuracy, the efficiency of the recovery process is another popular research area in DOT brain imaging [20, 21]. To achieve a satisfactory resolution for recovery of brain activations, high-density DOT is used in brain imaging. Moreover, the human head, especially the adult head, is a relatively large volume with complex fine internal structure. Therefore, the conventional recovery process of brain activation based on DOT is extremely time-consuming and the recovery of whole cortex activation can take ~3 hours to generate. Designing an efficient calculation approach for either the generation of the forward model or its inverse process can improve efficiency of the DOT recovery of brain activations.

1.2. Goals and Contributions

Three problems are addressed in this work: 1) finding the most suitable registration method for atlas based DOT of a specific cortex region; 2) determining whether the most suitable registration method varies based on region of interest (ROI); and 3) designing an efficient recovery approach for DOT recovery. Solving the first problem requires quantitative evaluation and comparison of different registration methods based on registration accuracy, process efficiency and recovery accuracy for atlas-based DOT recovery in a specific brain

region and selection of the most suitable registration method. Solving the second problem requires determination of a single most suitable registration method for all brain regions, or proving the most suitable registration variations for different brain regions and designing a region of interest (ROI) based registration method selection approach. Solving the third problem requires design of an efficient DOT recovery approach which can recover the brain activation of the whole cortex within 45 minutes.

Previous studies about the registration methods for atlas-based DOT recovery have focused on evaluation of a single registration method, the comparison between different non-rigid registration method [22] or comparisons between non-rigid registration methods and a rigid registration method [10]. The evaluations in these studies are only based on the geometrical accuracy of the registration result and accuracy of the recovery results. In this work, multiple rigid registration methods with different landmark systems and different optimization approaches are designed, evaluated and compared. Geometrical accuracy of the registration result, accuracy of light propagation approximation and the recovery accuracy are analysed for each registration method. The result of this work demonstrates the relationship between these three quantities and the most suitable registration method for a specific cortex region is selected for further use.

Previous studies have investigated atlas-based DOT recovery of localized brain activities in different cortex regions [3, 23, 24]. However, evaluation and comparison of multiple registration methods in different brain regions across the whole brain is novel in this work. Results of this work determine whether location of the ROI should be taken into consideration when selecting a registration method for atlas-based DOT recovery. It also provides the most suitable rigid registration method for the recovery of whole cortex activation and a selection approach for the most suitable registration methods based on ROI.

Previous studies on improving the efficiency of the DOT recovery process are focused on modification of the inverse process [20, 21]. Modification of the generation process of light propagation approximation based on a modified sensitivity matrix has not yet been investigated. Since approximation of the light propagation in the subject only relies on structural information of the subject and the position of the sources and detectors, the same light propagation approximation can be applied to multiple functional activation recovery of the same subject. In this work, a modified generation approach of the light propagation approximation is designed to improve time and storage efficiency. It contributes to real-time functional brain imaging. Additionally, based on the modified approach, the recovery of DOT brain imaging can be processed using a computer without specific memory requirements such as a normal laptop which is more suitable for a portable system.

1.3. Outline of the thesis

In this work, the most suitable registration method for atlas based DOT of a certain cortex region are studied and selected based on detailed quantitative evaluation. For the focal activations in the visual cortex and temporal cortex, the basic-4 landmark based registration method among different registration methods is shown to be the most efficient registration method. It is shown that the most suitable registration method varies based on region of interest (ROI) and the EEG19 landmark with non-iterative point to point (nP2P) registration method is the suitable efficient method for the whole cortex activation studies. Moreover, the geometrical accuracy of the registration based on the ROI can be used to select the most suitable registration method for DOT recovery. Finally, an efficient recovery approach for DOT is designed that reduces storage memory by >1000% and the processing time by ~400% in the generation of the sensitivity matrix. A fast and user friendly approach to generate a layered mesh based on subject MRI data with ~15 minutes process time is also designed.

This thesis consists of 9 chapters.

Chapter 1 (this chapter) is the introduction of the work undertaken.

Chapter 2 is a review of different neuroimaging modalities and a brief introduction of DOT brain imaging and the recovery approach used in this work.

Chapter 3 is the introduction and comparison of commonly used human brain atlases and the atlas used in atlas-based DOT recovery in this work.

Chapter 4 is the introduction and comparison of commonly used segmentation methods for human brain imaging data, and the introduction of a near automatic generation approach for layered FEM mesh-based subject MRI.

Chapter 5 is the introduction and comparison of commonly used registration methods for the human head and the registration methods used in this work for atlas-subject registration.

Chapter 6 is the evaluation of registration methods for atlas-based DOT recovery of visual cortex.

Chapter 7 is the evaluation of registration methods for atlas-based DOT recovery based on the whole cortex and multiple brain regions across the whole head.

Chapter 8 presents an efficient generation process of the light propagation approximation based on a reduced sparse sensitivity matrix and parallelisation process.

Chapter 9 is the summary and conclusion.

CHAPTER 2: REVIEW OF NEUROIMAGING MODALITIES AND INTRODUCTION OF DOT IMAGING

The brain is one of the major components of the central nervous system. The average human brain contains ~85 billion neurons and the average adult brain weighs ~1400 grams [25]. Blood flows in brain regions are regulated to match the metabolic demands over a wide range of arterial blood pressure. When a specific area of the brain becomes active, each of the neuronal cells in this area creates an electrical membrane potential known as the action potential which is then transmitted along the axons in the form of electrical impulses and dendrites to the adjacent cell membranes. Each of these action potential signals causes an increase in oxygen consumption by the neuronal cells, and generates a proportional increase in local blood flows. Therefore, neuronal activation is accompanied by increased regional cerebral blood flows, which is also known as the 'neurovascular coupling effect'. The increase in regional cerebral blood flow and oxygen consumption can be the consequence of regional brain activation. Functional brain imaging modalities rely on measures of electrical neural responses or vascular responses of the neuronal activation.

Neuroimaging obtains anatomical structure of the human brain and monitors brain activations during stimulations or resting-state. Various imaging modalities have been developed for brain imaging. Electrical neural responses of neuronal activities are collected by image modalities such as electroencephalography (EEG) and magnetoencephalography (MEG) [15, 26]. Vascular responses of brain activations have been recovered by imaging modalities such as magnetic resonance imaging (MRI) and diffuse optical imaging (DOI) [27, 28]. Electrical response based imaging modalities measure the neuronal activities directly with millisecond imaging temporal resolution [29], whereas vascular response based imaging

modalities measure vascular signals developed a few seconds after the neuronal signal with millimetre spatial resolution [30]. With development of the imaging techniques, acquisition time and resolution of the images has improved significantly. However, compared to vascular responses based imaging modalities, electrical responses based imaging modalities such as EEG and MEG still suffer from low spatial resolution [31, 32]. In general, brain imaging is classified into two categories: structural imaging and functional imaging [33, 34]. Structural imaging obtains absolute value from the images data to recover the anatomical structure of the brain. Functional imaging measures small changes in the image data and recovers the brain activities during stimulations or resting-state. A brief review of brain imaging modalities and introduction of DOT brain imaging recovery are presented in this chapter.

2.1. Brain imaging modalities

2.1.1 X-ray imaging and Computerized Tomography

X-ray imaging [35, 36] is one of the earliest medical imaging modalities which use X-radiation (X-rays) to image a subject. X-ray is an electromagnetic radiation wave with wavelength between 0.01nm and10 nm. High-density tissues such as bone tissue absorb more X-rays than tissue with lower density such as the soft tissue, therefore the structure of the human skeleton can be obtained from X-ray images. Although X-ray imaging is usually applied in the study of bone structure, it also has some application in soft tissue study such as the identification of some lung diseases. Since different soft tissues are normally difficult to distinguish in X-ray images, it only provides limited structural information in human organs such as the brain.

Computerized Tomography (CT) [35, 37] is the combination of a series of X-ray images acquired from different angles. An example of a typical CT system is shown in Figure 2.1. CT

imaging process is divided into two steps: first, a series of X-ray images are acquired from various angles. Second, these images are combined to reconstruct the 3D structures of the subject. Since CT imaging is the combination of X-ray images, it provides limited anatomical in the soft tissue region as the X-ray images.

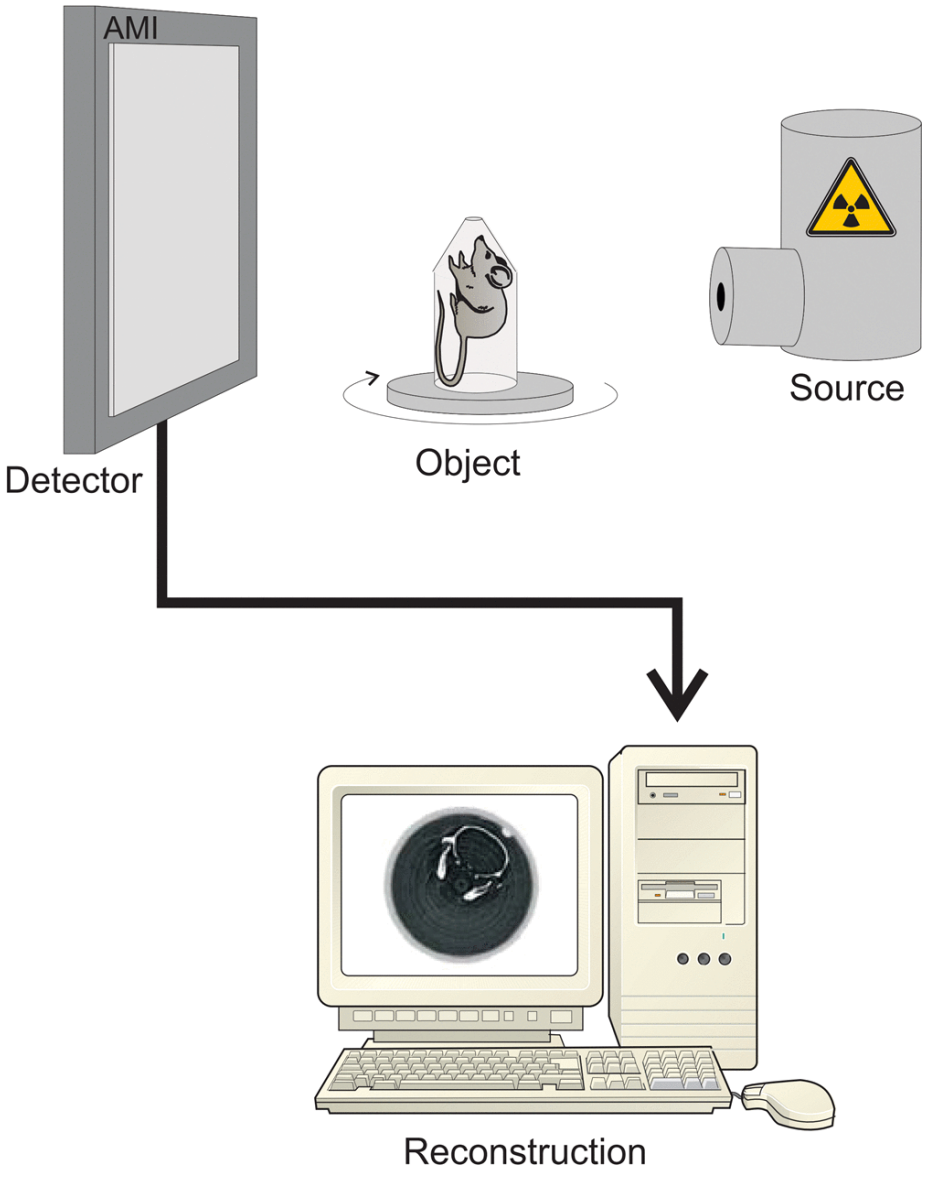

Figure 2.1. A typical micro-CT system with an x-ray source tube, a plain silicon diode detector and a rotational stage [38].

CT imaging has been applied to clinical situations such as identification of brain injuries [39] and guidance of stereotactic brain surgery [40]. An example of a CT image of an adult

brain is shown in Figure 2.2. CT imaging of the human brain which provides detailed spatial structure of the skull is an ionising process. However, since it has low resolution in soft tissue such as the gray matter and white matter, it fails to provide anatomical details in some brain regions such as the cortex surface. Additionally, X-ray is an ionizing radiation which is harmful to living tissue [41]. It limits application of CT imaging such as repeated imaging.

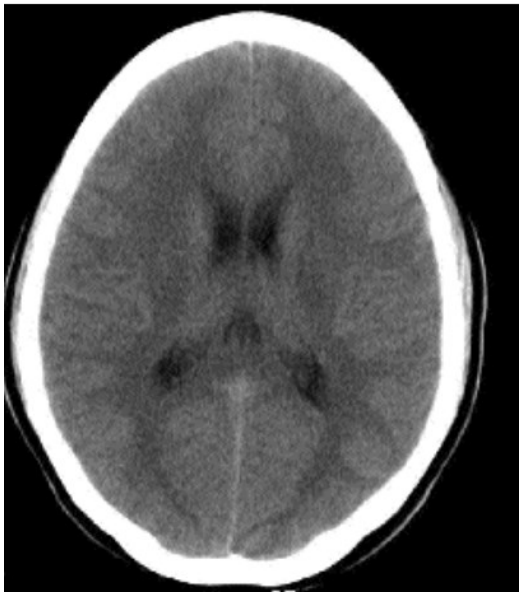

Figure 2.2.A CT image of an adult human brain (Axial scan) [42].

2.1.2 Positron Emission Tomography

Positron Emission Tomography (PET) [43, 44] is a functional imaging modality which detects metabolic responses during stimulation by tracking biologically active compounds and their traces in brain regions. In PET image process, a 'tracer', which is a biologically active molecule containing a radioisotope, is injected into the subject. The radioisotope emits a positron during positron emission decay and produces a pair of photons during the annihilation with an electron. These gamma photons are then detected by photomultiplier tubes (PMTs) used as PET detectors. Different tracers have been used in PET imaging. For example, fluorine-18 (F-18) fluorodeoxyglucose (FDG) [43, 45] is a widely used PET tracer

for monitoring glucose uptake of tissue regions during brain activation. An example of PET brain images are shown in Figure 2.3.

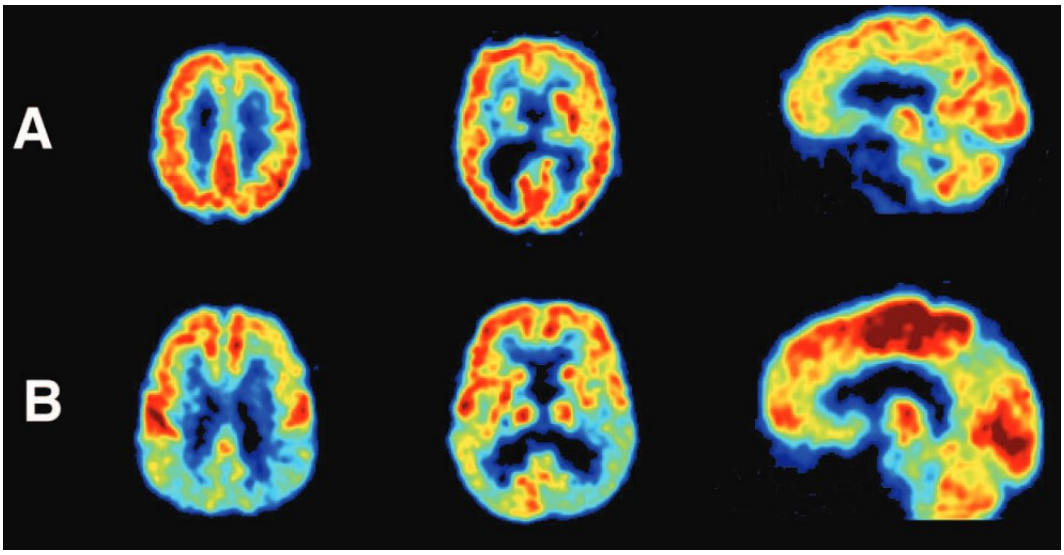

Figure 2.3. PET scans of two human brains. A is a set of PET scans of a health subject and B is a set of PET scans of a subject with Alzheimer's disease [46].

PET imaging is a high resolution functional imaging modality, and it has been used to evaluate and monitor progression of brain diseases such as brain tumours [47]. Resolution of PET images relies on its tracking of tracer, it have high-sensitivity in recovering functional changes but lacks resolving morphology. PET imaging is normally used by combining with structural imaging modalities which provide accurate anatomical information for locating the functional changes. Combined imaging systems for PET-CT and PET-MRI scanners [48, 49] have been designed and an example of a PET-MRI system is shown in Figure 2.4. With the development of inter-modality registration, the registered PET-CT images and PET-MRI images can be generated without the combined imaging systems. PET images and images from structural imaging modalities such as CT and MRI can be acquired sequentially and registered afterwards. Moreover, PET imaging exposes the subject to ionizing radiation, although the tracer has a relatively short half-life. Compared to other imaging modalities such as CT and MRI, PET scans are more expensive.

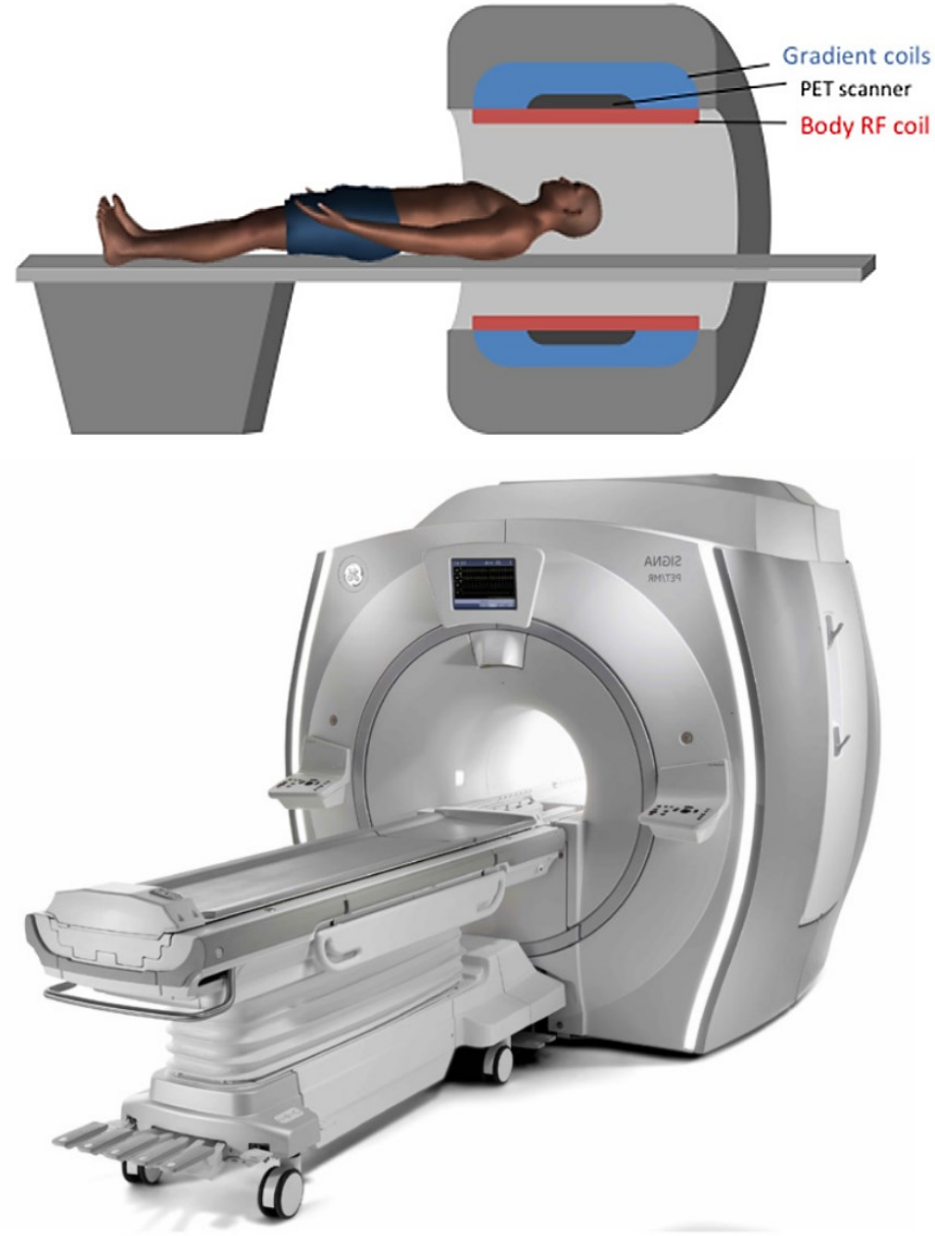

Figure 2.4. A simultaneous PET-MRI system. Upper figure is a schematic diagram of a PET-MRI system. The main magnet, Gradient coils and Radiofrequency coils (RF coils) for sending and receiving the signal are the key components of the MRI scanner, and a PET scanner is placed inside the MRI scanner. Lower figure is the GE PET-MRI system [50].

2.1.3 Ultrasound

Ultrasound (US) imaging [51, 52], also known as sonogram, recovers the internal structure of a subject based on analysis of ultrasonic echoes backscattered by internal tissue regions. In the US imaging process, ultrasound waves are projected into the region of interest,

and US images are reconstructed based on the response times and amplitudes of the ultrasonic echoes. Since reflection of ultrasound varies in different tissues, ultrasound imaging can recover the internal anatomical structure of the subject. An example of a neonatal cranial ultrasound image is shown in Figure 2.5.

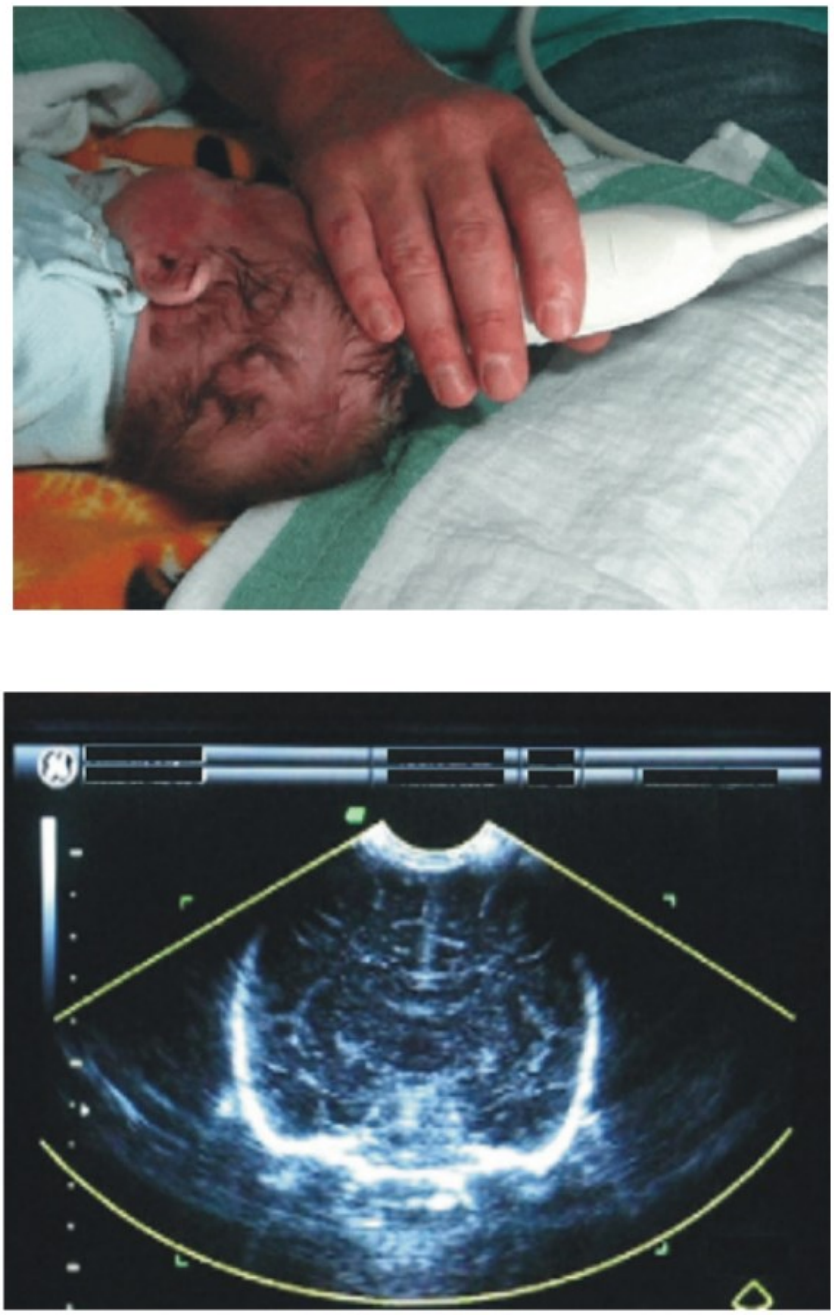

Figure 2.5. A neonatal cranial ultrasound imaging. Upper figure is a neonatal cranial ultrasound imaging system, and lower figure is an ultrasound image of the neonatal brain[53].

Ultrasound imaging is a real-time, portable and low cost imaging modality, and it does not involve ionizing radiation. It has been widely used in diagnosis and monitoring procedures in obstetric examinations and cranial studies of neonates [54]. However, ultrasound images have low spatial resolution especially in deep tissue regions [55, 56] and it is difficult to reconstruct structures behind bone and air [56], therefore application of US in imaging of the adult brain is limited.

2.1.4 Magnetic Resonance Imaging

Magnetic Resonance Imaging (MRI) [57, 58] recovers the internal structure of the subject based on the nuclear magnetic resonance (NMR) phenomenon. In a strong magnetic field, a nucleus that possesses spin absorbs and re-emits radio frequency energy. The radio frequency signal generated in the process is then detected and used to recover the MRI images. The hydrogen atoms are the selected nucleus in the MRI, because they are highly sensitive to the magnetic field and most biological tissues primarily consist of hydrogen-rich component such as water and fat. Since soft tissue such as muscles and brain contains more water than other tissues such as bones, soft tissue has a higher contrast in MRI images. MRI has been applied in the study of the human brain. An example of MRI imaging system is shown in Figure 2.6.

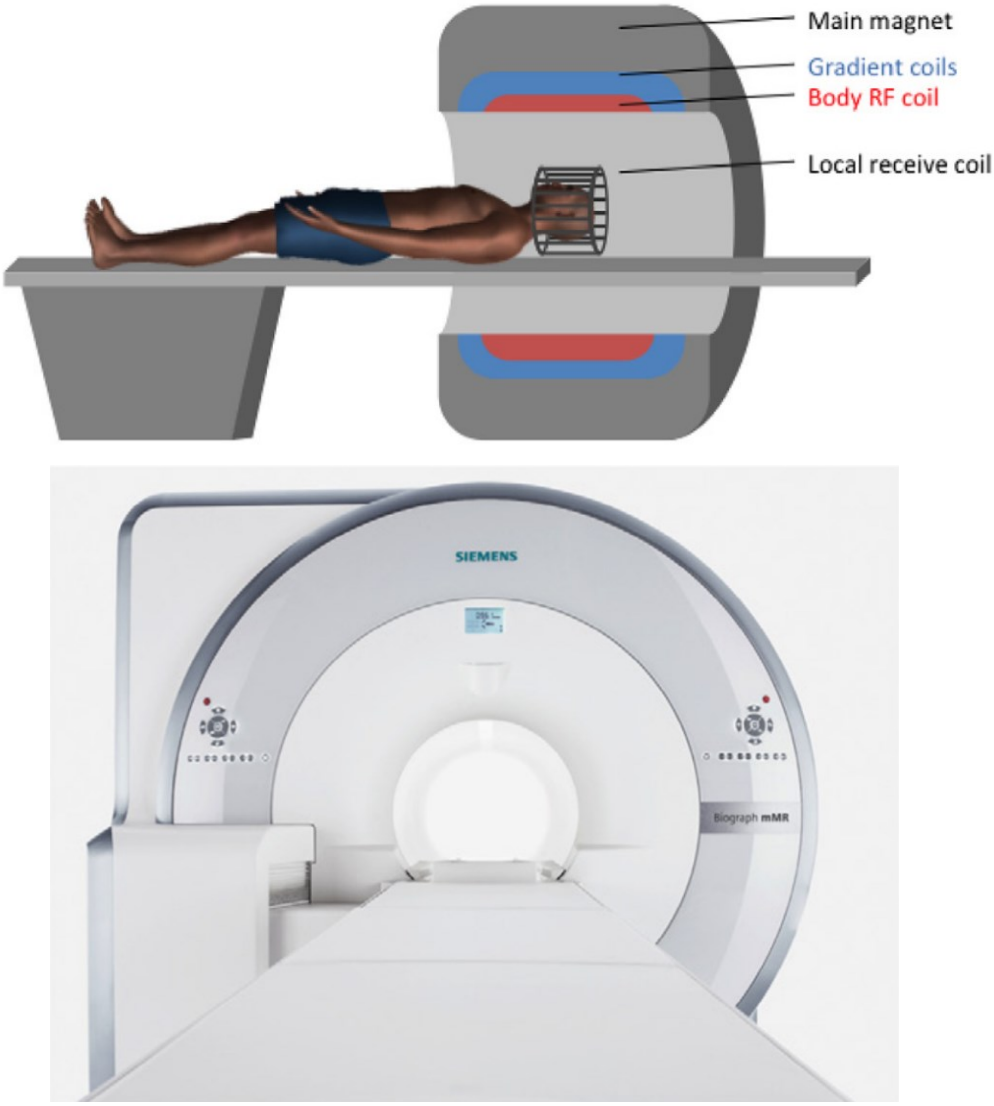

Figure 2.6. An example of MRI systems. Upper figure is a schematic diagram of a MRI system. The main magnet, Gradient coils and Radiofrequency coils (RF coils) for sending and receiving the signal are the key components of the MRI scanner, and the local receiving coil is used to increase the SNR. Lower figure is the Siemens MRI system [50].

MRI of the human brain is divided into two categories: structural MRI and functional MRI (fMRI) [59, 60]. Structural MRI reconstructs the tissues distributions and anatomical structures of the human brain by recovery of absolute image intensity. Functional MRI monitors brain activations during stimulation or resting-state by recovery of changes in image intensity. fMRI measures brain activity based on a blood oxygenation level-dependent (BOLD) contrast [61, 62],which reflects localized changes in brain blood flow and blood

oxygenation. Since BOLD signals are coupled to underlying neuronal activity by the neurovascular coupling effect, MRI can be used to monitor brain activations. fMRI is the most commonly used imaging modality for recovery of brain activations and is often used as a reference in the evaluation of other functional imaging modalities [63].

MRI is a non-invasive and non-ionising imaging modality and it provides millimetre spatial resolution in the whole brain region. Since MRI relies on a strong magnetic field, it cannot be applied to subjects with metallic implants such as pacemakers. Additionally, the MRI imaging system produces a loud noise during image acquisition, so it may not be suitable for experiments based on sedation of the subjects.

2.1.5 Summary

Four neuroimaging modalities are introduced in this part, and their advantages and disadvantages are listed in table 2.1.

Table 2.1. Comparison of the four neuroimaging modalities.

Imaging modalities	Spatial resolution	Temporal resolution	Invasive & ionising	Cost of scan
CT	millimetre	hundreds of millisecond	Yes	$1200~ $3200
PET	millimetre	second	Yes	$3,000~$6,000
US	A few millimetres	dozens of millisecond	No	$100~$1000
MRI	millimetre	second	No	$1,200~$4,000

There are some limitations in the application of each imaging modality. Because CT and US imaging have low resolution in some or all of the brain tissues, they are not suitable for quantitative recovery of brain activations for adult subjects. PET imaging is a high cost

imaging technique and it requires structural information from other imaging modalities. It is limited for brain analysis involving repeated imaging and long-term monitoring. MRI cannot be applied to subjects with metallic implants such as pacemakers. Because of the system setting for CT, PET and MRI, they are not portable and are difficult to apply to some patients such as those with claustrophobia or extreme obesity problems. Therefore, the development of high resolution low cost and portable neuroimaging modalities is necessary.

2.2. Diffuse optical tomography brain imaging recovery

2.2.1 Introduction of diffuse optical imaging

Physiologically interesting molecules such as oxygenated haemoglobin and deoxygenated haemoglobin have characteristic absorption and scattering spectra when exposed to light and near-infrared light. As shown in figure 2.7, NIR light (wavelengths between ~650nm and ~900nm) has lower absorption and is therefore suitable for in vivo imaging. DOT uses NIR light to recover absolute values or changes in optical properties such as absorption and scattering coefficients and to monitor the location and quantities of tissue chromophores such as oxygenated haemoglobin, deoxygenated haemoglobin, water, and lipids in the subject [64, 65]. In diffuse optical imaging , NIR light is injected into the volume of interest from light sources such as light-emitting diodes (LEDs) and the fluence of light is measured by detectors such as avalanche photo diode (APD) detectors [6, 66]. Light sources and detectors are placed on the volume surface within a few centimetres distance. The measured data, also known as ‘boundary data’, is then analysed based on the inversion of a model of light propagation to recover internal information of the subject [7, 13, 67]. Since the NIR spectra contains light with wavelengths between 650nm and 900nm, DOT can be processed based on multiple wavelengths [5, 68]. The absorption coefficient and scattering coefficient of the subject are

recovered in each wavelength, and distributions of tissue chromophores are calculated based on the recovered optical properties.

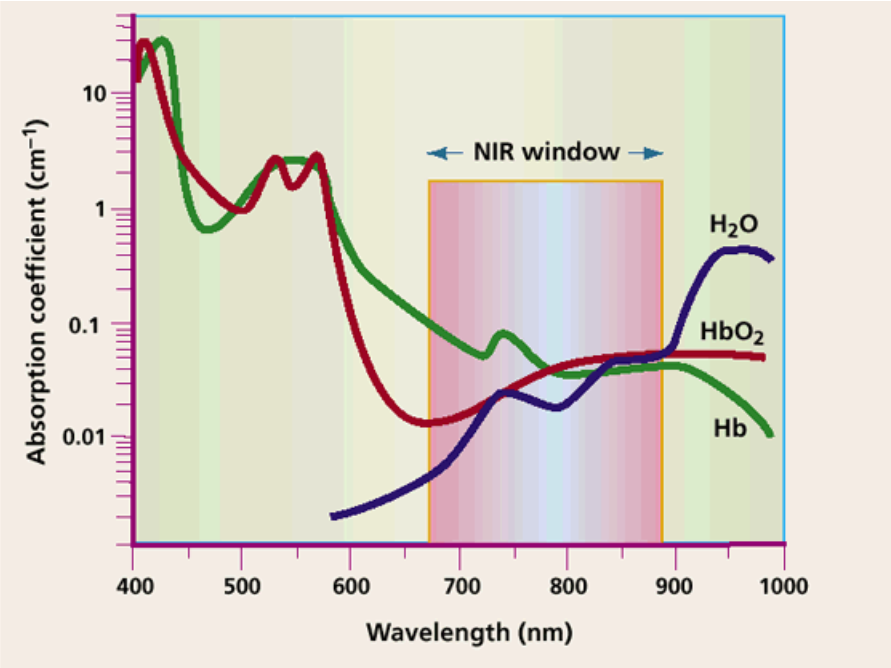

Figure 2.7. absorption coefficient for oxygenated haemoglobin (HbO2), deoxygenated haemoglobin(Hb) and water (H2O) [69].

Near-infrared spectroscopy (NIRS) measures the hemodynamics and oxidative metabolism in different tissue regions such as muscles and brain cortex to monitor the activation in these tissue areas. An example of a NIRS system is shown in figure 2.8. However, NIRS generally does not record spatial information, which is a clear limitation in locating the activation. Diffuse optical imaging also recovers tissue chromophores based on NIR light. It is divided into two categories: diffuse optical topography which produces two-dimensional (2D) images and diffuse optical tomography which produces three-dimensional (3D) images. Diffuse optical topography of the human brain measures NIR light propagation based on a source and detector pad placed on the surface of the subject and recovers images in a plane parallel to the source and detector pad. An example of a diffuse optical topography system is shown in figure 2.9. Although diffuse optical topography reconstructs some spatial

information about the recovered activations, it provides limited depth information. Therefore, the use of diffuse optical imaging is necessary to recover activation in 3D.

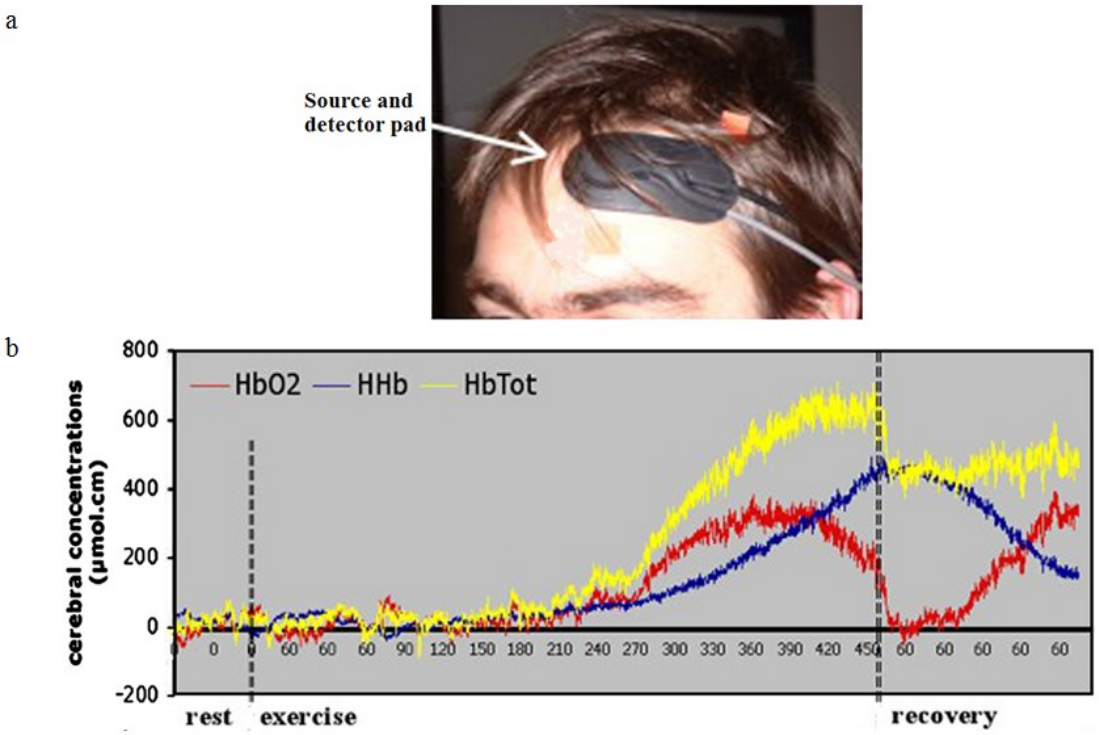

Figure 2.8. An example of a NIRS setup. a. Source and detector pad for NIRS of human brain. b. Changes in oxy-haemoglobin ([HbO2]), deoxy-haemoglobin ([HHb]) and total haemoglobin ([HbTot]) in brain tissue during a cycling exercise [70].

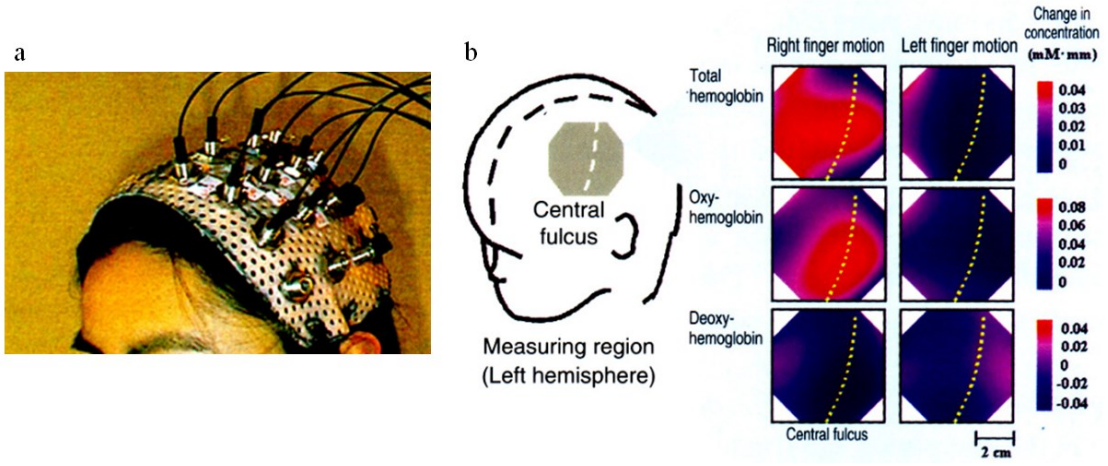

Figure 2.9 . an example of diffuse optical topography setup. a. Source and detector pad for diffuse optical topography. b. Recovered diffuse optical topography images in a finger motion experiment [71].

2.2.2 Introduction of DOT

Diffuse Optical Tomography (DOT) is a three-dimensional NIR-based imaging modality. Since DOT is a non-ionizing technique, it can be applied to human subjects continuously over several hours and regularly over the course of weeks and months without causing tissue damage. Comparing to other imaging modalities such as PET and MRI, DOT can be implement as a low cost and portable system constructed using LED light source and photodiode detector placed on surface of the subject and their connected optical fibres [13]. It can be used in bedside monitoring. Density of the source and detector can affect the imaging resolution of DOT [72]. Examples of DOT systems with different source and detector pads are shown in Figure 2.10. The source and detector pad is designed based on the region of interest in DOT experiments. For example, source and detector pads have been designed to monitor brain activations in different cortex regions simultaneously (Figure 2.11). Source and detector pads for both single region (chapter 6) and multiple regions (chapter 7) are applied in this work.

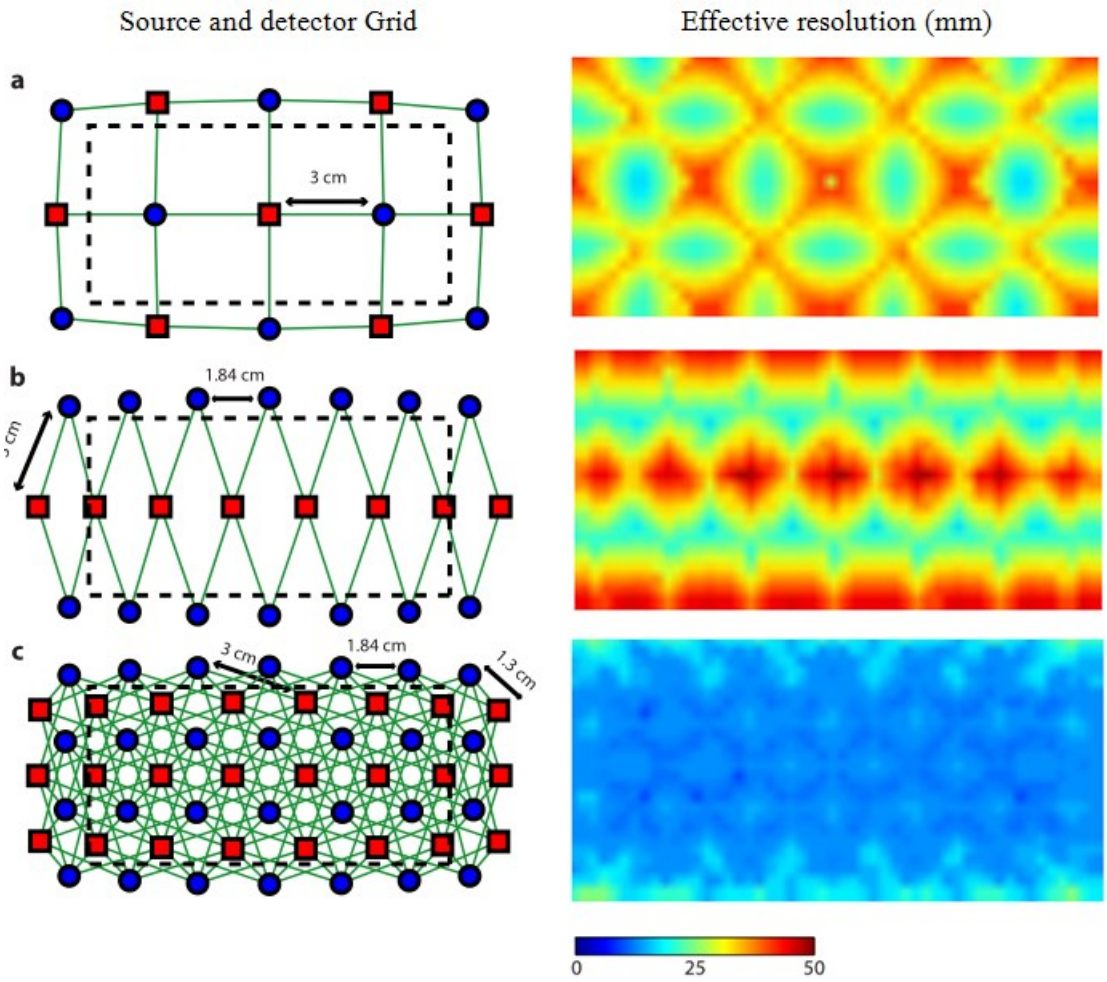

Figure 2.10. DOT systems with different source and detector pads. a. Square Sparse Grid. b. Triangular Sparse Grid. c. High-Density Grid. Sources are red squares, detectors are blue circles, and measurements are green lines. The effective resolution was defined as the diameter of the circle centred at each target position needed to enclose the response [72].

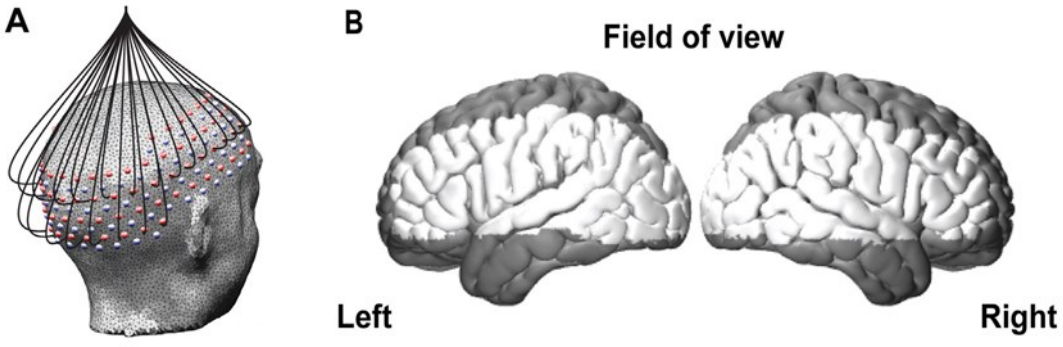

Figure 2.11. An example of a DOT system for multiple brain regions. a. A high-density source and detector pad. Sources are red circles and detectors are blue circles. b. Field of view on the cortex surface [73].

DOT imaging has been applied to various subjects such as small animals including rats and mice [74] and human organs including breast and brain [7, 67]. It has been used to locate tissue anomalies such as a tumour [75, 76] and to recover functional activities such as brain activations [7]. Different imaging systems are created for different subjects such as small animal imaging [74] and adult brain imaging [13]. The fluorescence and bioluminescence image has been introduced to DOT of small animals to increase the imaging sensitivity and accuracy [77-79]. Because of the complex anatomical structure and varying optical properties in human tissue, DOT reconstruction is challenging for human subjects. However, DOT imaging has been applied to recovery of the anatomical structure and functional activities in the different human organs, and auxiliary diagnosis tumour or other anomalies in some human organs such as in the female breast [67, 80], peripheral muscle [81, 82] and infant brain [3, 83]. Compared to other imaging modalities such as CT and MRI, DOT can be applied to some subjects such as infants and hospitalized patients for long-term monitoring. It therefore demonstrates potential for wider clinical applications.

DOT imaging can recover both absolute optical properties and relative changes in optical properties. However, measurement data are affected by noise and error from the imaging system and environment. The small changes are recovered based on comparison of two measurements, and systematic errors in the model are largely cancelled out in the process. Since the absolute values are recovered based on a single measurement, it is more difficult to reduce the noise than the relative changes in measurement data. A number of factors have a major influence on absolute measurements such as coupling between optical fibres and tissue surface, positional uncertainties of sources and detectors, and the complex condition of the subject surface such as hair or variation in skin colour. Several studies have been focused on absolute image recovery of DOT breast imaging [84, 85]. Based on these studies, recovery

errors of the absolute values (~1%) are larger than the errors of relative changes (~0.01%) [86]. Current DOT studies of the adult brain are focused on recovery of relative changes. In this work, DOT imaging of the human brain is used to recover relative changes to analyse brain activations.

One of the first applications of DOT in brain imaging was recovery of the changes in the total haemoglobin concentration and oxygenation of the whole brain after a stimulus [87, 88]. Since then, DOT imaging has been applied in recovery of human brain activations for infants and adults, and this work is focused on DOT imaging recovery for the adult brain. Despite the limitations of the NIR imaging technique and the complexity of the human brain, areas of brain injury and activated region have been observed. Previous studies of DOT brain imaging have investigated identification of brain injuries [89-91] and diagnosis of diseases such as hypoxic-ischemic injury [92] and intraventricular haemorrhage [83]. Spontaneous brain activation and stimulus based functional activations [14, 93] have also been investigated (details in chapter 7).

2.2.3 Recovery process of DOT

DOT brain imaging measures propagation of NIR light in the brain and recovers small changes in optical properties of different brain regions. The propagation of NIR light in the brain is considered as nearly isotropic based on the previous study [94], and the scatter coefficient in brain tissue is generally larger than the absorption coefficient. For recovery of the absorption coefficient which contains physiological information of the brain activation, a reduced scatter coefficient is defined as $\mu'_s = (1 - g)\mu_s$ where μ_s is the scatter coefficient and g is the mean cosine of the scattering phase function and μ'_s is the reduced scatter coefficient. DOT recoveres the optical properties based on the measured data and a light

propagation approximation model of the subject. The recovery process of DOT is divided into two steps: generation of a forward model which simulates the light propagation and inverse processing of the forward model.

2.2.3.1 Forward model in DOT recovery

The forward model simulates propagation of near-infrared light through the subject based on the distribution of optical properties within the subject. Photon transmission in the subject obeys the radiative transfer equation (RTE) [95]:

$$\frac{1}{c}\frac{\partial I}{\partial t} + \hat{s}\cdot\nabla I(\boldsymbol{r},t,\hat{s}) + (\mu_a+\mu_s)I(\boldsymbol{r},t,\hat{s}) = \mu_s\int p(\hat{s}',\hat{s})I(\boldsymbol{r},t,\hat{s}')d^2\hat{s}' + q(\boldsymbol{r},t,\hat{s}) \quad \boldsymbol{r}\in\Omega \tag{2.1}$$

Where intensity $I(r,t,\hat{s})$ is the intensity at the position r in the direction $\hat{s}$ at time t. μ_a and μ_s are the absorption and scattering coefficients, $q(r,t,\hat{s})$ is the light source and p is the phase function.

Data acquisition in DOT can be accomplished with time-domain, frequency-domain, and continuous wave (CW) (figure 2.12) [96]. Time-domain systems inject picosecond laser pulses sequentially into the subject and measure the temporal distribution of the exit photons. Comparing to the injected light pulses, the measured light is delayed, broadened and attenuated. This imaging system relies on measurement of the temporal point spread function to recover the optical parameters of the ROI. The Shimadzu OMM 2001 is a typical time-domain system for diffuse optical imaging [76]. Since the flight time of the exit photon is proportional to the travelled distance, time-domain system with additional temporal information has better resolution and depth localization as compared to CW system [97]. However, time-domain systems are usually more expensive and have a slower acquisition rate

than frequency domain and CW systems. Frequency-domain system projects high-frequency light with continuous intensity into the subject and measures the reduction in modulation amplitude and phase shift of the detected data. Since the attenuation in amplitude is caused by tissue absorption and shift in phase is dependent on the photon pathlength, optical properties in the tissue region can be recovered using a frequency domain system. The ISS OxiplexTS is a typical frequency-domain system for diffuse optical imaging [76]. Frequency-domain systems are less expensive than time-domain systems and still capable of provide some temporal information by measuring differential pathlength. Since each measurement in a frequency-domain contains information from a single frequency whereas each measurement in a time-domain system contains information from all frequencies, frequency-domain systems normally require multiple measurements at several frequencies. Continuous wave (CW) systems can be considered as a frequency-domain system using light with constant amplitude (or modulated at low-frequency) and only measures intensity of the propagated light. In CW systems, the scattering remains constant throughout the measurement and the changes in light intensity relies on changes of absorption in tissue. The Hitachi ETG-100 system is a typical CW system for diffuse optical imaging [76]. Although CW systems do not record temporal information and cannot recover scattering properties of the tissue, it is the least expensive and most compact system among the three systems. A CW system is used in all DOT experiments in chapter 6-8.

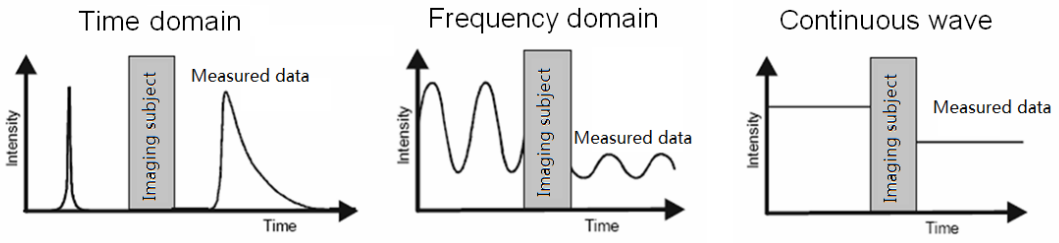

Figure 2.12. Schematic of the three main types of data acquisition in DOT

The diffusion approximation (DA) to the RTE is used in DOT imaging, and time-dependent diffusion equation [equation 2.2] and frequency-domain diffusion equation [equation 2.3] are used depending on the nature of the imaging system. The DA of CW is defined as the frequency-domain differential equations with zero frequency [98].

$$\frac{\delta\Phi(r,t)}{c\delta t} - \nabla\cdot\Phi(r)\nabla\kappa(r,t) + \mu_a(\mathrm{r})\Phi(r,t) = q_0(r,t) \tag{2.2}$$

$$-\nabla\kappa(r)\nabla\Phi(r,\omega) + \left(\mu_a(\mathrm{r}) + \frac{i\omega}{c}\right)\Phi(r,\omega) = q_0(r,w) \tag{2.3}$$

where q_0 is the source term, $\Phi(r,\omega)$ is the fluence of NIR light at position r frequency ω , $\Phi(r,t)$ is the radiance of NIR light at position r time t, μ_a is the absorption property, κ is the diffusion property, $\kappa = \frac{1}{3}(\mu_a + \mu_s')$, μ_s' is the reduced scattering property.

Since the optical properties change dramatically on the air-tissue boundary and the fluence exits the subject without return, the Robin (type 3) boundary condition [99] is used to simulate the photon transfer on the edge for the DA. The Robin boundary condition is defined as:

$$\Phi(r,\omega) = 2An\kappa(r)\nabla\Phi(r,\omega) \tag{2.4}$$

where $\Phi(r,\omega)$ is the fluence of NIR light, $\kappa(r)$ is the diffusion property, A is the relative refractive index mismatch between tissue and air.

A variety of forward models have been employed in brain DOT and they can be classified into three categories: analytical models, stochastic models and numerical models [96, 98]. The analytical models are based on analytical solutions to the diffusion equation. Since Green's function can be applied to solve the diffusion equation [100], a Green's function based analytical model can be generated. Stochastic models simulate individual photon trajectories

through the subject to compute fluence at each position. The Monte Carlo model [101] is a typical stochastic model. Finite element model (FEM) [8] is a typical numerical model. It divides the subject into finite non-overlapping cells and solves the transport model locally in each element. A brief introduction of each category based on an example model is presented in this chapter.

2.2.3.1.1 Analytical models: Green's function based forward model

An analytical solution to the diffusion equation [equation 2.5] can be derived by the application of the Green's function technique [102] in cases where the geometry of the subject has a geometrically simple boundary.

$$\Phi(r,t) = \int d^3r' G(r,r') q_0(r') \tag{2.5}$$

Where q_0 is the source term, Φ is the radiance of NIR light, *G(r,r')* is the diffusion Green's function:

$$[-\nabla \mathrm{r} \cdot \kappa(\mathrm{r}) + \mu_a(r) - i\omega] G(r,r') = \delta(r - r') \tag{2.5.1}$$

where *G(r,r')* is the diffusion Green's function, μ_a is the absorption property, $\kappa = \frac{1}{3}(\mu_a + \mu_s')$, μ_s' is the reduced scattering property.

Forward models for various homogeneous geometries, such as slabs, cylinders, and spheres have been generated based on Green's functions and can be applied to reconstruction directly [100]. However, since the analytical solutions heterogeneous and irregularly shaped geometries remain scarce, a complex object such as the human brain cannot be neatly expressed in an analytical form. Therefore, the analytical model is not suitable for complex object such as the human brain.

2.2.3.1.2 Stochastic models: Monte Carlo based forward model

The stochastic model also known as statistical model is one of the most commonly used forward models for DOT recovery. It generates the fluence at each position in the spatial distribution of photon trajectories in the subject. The Monte Carlo (MC) statistical model simulates individual photon trajectories according to the posterior probability distribution, representing the randomness of each scattering event based on a pseudorandom model. A trajectory of individual photons is recorded until the required counting statistics are obtained [103, 104]. The MC model is a robust forward model and the accuracy of this model can be improved by involving prior information. However, the process of the Monte Carlo model is relatively complex and time consuming. It may not be the best forward model generation process for brain DOT studies with a large number of subjects.

2.2.3.1.3 Numerical models: Finite element forward model

Numerical models approximate the light propagation within tissue based on finite non-overlapping cells in the subject. It has the potential to model complex geometries as well as complex internal heterogeneities. The finite element model (FEM) [8, 105] is the most commonly used numerical model for brain imaging. It divides the subject volume into finite non-overlapping uniformed elements and the optical properties in each element are consistent. The solution of the DA is simulated as:

$$\Phi(\mathrm{r},\mathrm{t}) = \sum_{i=1}^{D}(\Phi_i(t)u_i(\mathrm{r})) \tag{2.6}$$

Where q is the source term, Φ is the fluence of NIR light, u is a set of D-dimensional vectors basis functions. The frequency domain DA is approximated as:

$$\left(\kappa(\kappa) + \mathrm{C}(\mu) + \frac{A^2}{2} + i\omega B\right)\Phi = q_0 \tag{2.7}$$

$$\text{Where } \kappa_{ij} = \int \kappa(r)\nabla u_i(r) d^n r \tag{2.7.1}$$

$$C_{ij} = \int \mu_a(r) u_i(r) u_j(r) d^n r \tag{2.7.2}$$

$$B_{ij} = \frac{1}{c}\int u_i(r) u_j(r) d^n r \tag{2.7.3}$$

The FEM approach consists of two steps: dividing the subject into finite elements and simulation of light propagation in each element. It is suitable for highly inhomogeneous objects and objects with complex structures such as the human brain. The FEM of the human brain is generated based on tissue classification of the subject brain.

Other numerical models including the finite difference method (FDM), finite volume methods (FVM) and boundary element methods (BEM) [96] are also used in DOT studies. FDM can be considered as the FEM with uniform elements. In the FDM, the subject is divided into finite non-overlapping uniform elements joined at surface or internal nodes. The light propagation is simulated in each element. Compared to FEM, DOT reconstruction based FDM can be less time-consuming because of uniformity of the elements. However, it can be difficult to divide a complex subject such as the human brain into uniform elements without losing some fine structural detail. FVM and BEM describe the optical flux field through its integral on the surface of each element. In FVM, the subject is divided into finite non-overlapping elements joined at vertex nodes. The optical flux at the surfaces of each element is calculated by the surface integrals. Although the FVM can applied to irregular subjects using unstructured grids, the calculation for surface integrals can be over complex. In BEM, the subject is divided by a layered grid and optical flux at the boundary of each layer is calculated by the surface integrals. The boundary element method is normally applied to subjects with large regions of homogeneous media.

2.2.3.2 Inverse method in DOT recovery

The inverse process in DOT recovery calculates the solution of the DA based on inverse processing of the forward model. Various reconstruction methods have been applied in DOT recovery such as back-projection methods, perturbation methods and nonlinear optimization methods.

The back projection method [95, 96] projects each of photon detected on the boundary through all possible transfer routes back to the light source and creates a probability map for the volume. Since this method is highly dependent on a reliable inverse transformation of the photon transfer equation, it is challenging especially for subjects with complex structure such as the human brain.

The perturbation methods [95, 96] is the linear optimization approach, which solves the DA based on its approximate such as the Taylor series. It requires an initial estimate close to the ideal solution. Therefore, it is only used for recovery of small changes of optical properties in the subject. The linear optimization method can also be processed based on a FEM. Minimization function for the FEM based linear inverse method is defined as:

$$\chi^2 = \sum_{i=1}^{NM}(\Phi_{Calci} - \Phi_{Measi})^2 \tag{2.8}$$

where *NM* is the number of measurements, Φ_{Calci} is simulation data and Φ_{Measi} is the measured data for measurement *i.* The changes in the optical properties are recovered as:

$$\Delta\mu = J^T[JJ^T]^{-1}\Delta\Phi \tag{2.9}$$

where $\Delta\mu = \mu - \mu_0$, $\mu = (\mu_a, \kappa)$,$\kappa = \frac{1}{3}(\mu_a + \mu_s')$, μ_a is the absorption property , μ_s' is the reduced scattering property.μ_0 is an estimate of the parameters. $\Delta\Phi = \Phi_{Calc} - \Phi_{Meas}$. Φ_{Calc}

is simulated data based on the reconstruction and Φ_{Meas} is the measured data. *J* is the sensitivity matrix:

$$J = \begin{bmatrix} \frac{\partial lnI_1}{\partial \kappa_1} & \frac{\partial lnI_1}{\partial \kappa_2} & \cdots & \frac{\partial lnI_1}{\partial \kappa_{NN}}; & \frac{\partial lnI_1}{\partial \mu_{a_1}} & \frac{\partial lnI_1}{\partial \mu_{a_2}} & \cdots & \frac{\partial lnI_1}{\partial \mu_{a_{NN}}}; \\ \frac{\partial \theta_1}{\partial \kappa_1} & \frac{\partial \theta_1}{\partial \kappa_2} & & \frac{\partial \theta_1}{\partial \kappa_{NN}}; & \frac{\partial \theta_1}{\partial \mu_{a_1}} & \frac{\partial \theta_1}{\partial \mu_{a_2}} & & \frac{\partial \theta_1}{\partial \mu_{a_{NN}}}; \\ \frac{\partial lnI_2}{\partial \kappa_1} & \frac{\partial lnI_2}{\partial \kappa_2} & & \frac{\partial lnI_2}{\partial \kappa_{NN}}; & \frac{\partial lnI_2}{\partial \mu_{a_1}} & \frac{\partial lnI_2}{\partial \mu_{a_2}} & & \frac{\partial lnI_2}{\partial \mu_{a_{NN}}}; \\ \frac{\partial \theta_2}{\partial \kappa_1} & \frac{\partial \theta_2}{\partial \kappa_2} & & \frac{\partial \theta_2}{\partial \kappa_{NN}}; & \frac{\partial \theta_2}{\partial \mu_{a_1}} & \frac{\partial \theta_2}{\partial \mu_{a_2}} & & \frac{\partial \theta_2}{\partial \mu_{a_{NN}}}; \\ \vdots & & \ddots & \vdots & \vdots & & \ddots & \vdots \\ \frac{\partial lnI_{NM}}{\partial \kappa_1} & \frac{\partial lnI_{NM}}{\partial \kappa_2} & \cdots & \frac{\partial lnI_{NM}}{\partial \kappa_{NN}} & \frac{\partial lnI_{NM}}{\partial \mu_{a_1}} & \frac{\partial lnI_{NM}}{\partial \mu_{a_2}} & \cdots & \frac{\partial lnI_{NM}}{\partial \mu_{a_{NN}}} \\ \frac{\partial \theta_{NM}}{\partial \kappa_1} & \frac{\partial \theta_{NM}}{\partial \kappa_2} & & \frac{\partial \theta_{NM}}{\partial \kappa_{NN}}: & \frac{\partial \theta_{NM}}{\partial \mu_{a_1}} & \frac{\partial \theta_{NM}}{\partial \mu_{a_2}} & & \frac{\partial \theta_{NM}}{\partial \mu_{a_{NN}}}: \end{bmatrix} \quad (2.9.1)$$

Where $\frac{\partial lnI_i}{\partial \kappa_j}$ and $\frac{\partial lnI_i}{\partial \mu_{a_j}}$ are the matrix elements that define as the change in log of amplitude I_i of the *i* th measurement arising from a small change in κ and μ_a at the *j* th reconstructed node. $\frac{\partial \theta_i}{\partial \kappa_j}$ and $\frac{\partial \theta_i}{\partial \mu_{a_j}}$ are the matrix elements that define as the change in phase θ_i of the *i* th measurement arising from a small change in κ and μ_a at the *j* th reconstructed node. *NM* is the number of measurements. *NN* is the number of nodes.

Since the inverse process of FEM is under-determined and ill-posed, some artefacts may be introduced by the inverse process. Regularization methods such as Tikhonov regularization have been applied to the inverse process to reduce errors. Tikhonov regularization [106], also known as the Tikhonov–Miller method, is one of the most commonly used regularization methods in FEM-based DOT recovery. An initial estimate of the solution is used as the additional information in this regularization. For the linear inverse methods for FEM with Tikhonov regularization, the minimization function becomes:

$$\chi^2 = \sum_{i=1}^{NM}(\Phi_{Calci} - \Phi_{Measi})^2 + \lambda \sum_{j=1}^{NN} I(\mu_j - \mu_0)^2 \quad (2.10)$$

where μ_0 is the additional information which is the initial estimate in this regularization. λ is the regularization parameter, and I the identity matrix. The changes in the optical properties are recovered as:

$$\Delta\mu = J^T[JJ^T + \lambda I]^{-1}\Delta\Phi \tag{2.11}$$

The recovery approach based on FEM with Tikhonov regularization has been applied to DOT imaging of the human brain in this work.

The nonlinear optimization method is an iterative process in which each iteration is a perturbation inverse process [68, 98]. Compared to direct inverse methods such as the perturbation method which only recovers small changes in optical properties, the iterative optimization methods can be applied to the recovery of the absolute optical properties. This optimization method also requires an initial estimation of the solution. Since the DA is ill-posed, there may be more than one solution that fits the measured data. Therefore, the initial estimation should be close to the ideal solution [68, 96, 107]. In each iteration process, firstly, simulation data is generated based on the initial estimation or an updated estimation of the solution. Secondly, the simulation data are compared to the measured data and updates of the solution are generated based on the difference between the measured data and the simulation data. Thirdly, the solution is updated and then used as the new estimation in the next iteration. This approach is processed iteratively until it reaches a pre-set number of iterations or the difference between the measured data and the simulation data reaches an acceptable minimum. The FEM based nonlinear inverse method has been successfully applied in brain imaging [108]. However, as this is more computationally consuming than the other two methods, it is not the most suitable for recovery of small changes in optical properties during brain activations.

2.2.3.3 Software for DOT recovery

Several software packages have been developed for DOT reconstruction, including Nirfast [68, 109] and TOAST [110].

TOAST++ (Time-resolved Optical Absorption and Scattering Tomography) [110] is a software package for image reconstruction in DOT. It is being developed by Martin Schweiger and Simon Arridge at University College London. In Toast++, the image reconstruction of DOT is based on a finite element forward model and a nonlinear inverse problem solution. CW, time- and frequency-domain data acquisition systems in DOT can all be modelled by Toast++. This software package is implemented in C++ and bindings for Matlab and Python is also contained in the software package. Toast++ can be used to simulate light propagation in highly scattering media with complex boundaries and inhomogeneous internal distribution, such as the human brain.

NIRFAST (Near Infrared Florescence and Spectral Tomography)[68, 109] is another software package for image reconstruction in DOT. It is being developed by the Optics in Medicine group at Dartmouth College. Nirfast can also be used for the reconstruction of multimodal NIR imaging, fluorescence and bioluminescence imaging. For DOT, the reconstruction process in Nirfast is based on a finite element forward model and a nonlinear inverse problem solution. Nirfast is a Matlab-based open source software package and the input and output data of Nirfast are stored as the standard Matlab matrix. This software package contains a meshing module which can be applied directly to segmentation results from Nirview software package which is a segmentation and visualization toolbox for medical images. A segmentation-meshing approach is discussed in chapter 4. Nirfast can be used to simulate light propagation in inhomogeneous subjects with complex internal structure,

therefore it is suitable for analysing brain activation based on DOT. The DOT reconstructions in this project are recovered by the Nirfast software and modification of the reconstruction process in Nirfast.

2.2.4 Summary

DOT is a NIR light based imaging modality which recovers optical properties by measuring light propagation through the subject. It is a non-ionizing and non-invasive approach with a portable and low cost imaging system which can be applied to hospitalised patients and infants. DOT recovery has been applied to various objects such as small animals and human organs. DOT imaging can recover absolute value and changes in some tissues regions, however DOT brain imaging is focused on recovering changes during brain activation. The recovery process of DOT is divided into two steps: generation of forward model and inverse processing of the forward model. Three different forward models: Green's function based model, the MC model and the FEM model are introduced in this chapter and FEM is the most efficient forward model for the human brain. Three different inverse methods: back-projection methods, linear methods and nonlinear optimization methods are also introduced. The linear method with Tikhonov regularization based on FEM is used for DOT recovery in this work. Since FEM is generated based on tissue classification of the subject and atlas-based structural information is a common alternative when subject specific information is not available, the review of human head atlases is presented in the following chapter.

CHAPTER 3: HUMAN BRAIN ATLAS BASED ON MRI DATA

3.1. Introduction of brain atlases

A brain Atlas is a series of maps that contain the anatomical structure of the subject head. It is normally generated based on the average of head images of a group of subjects. Different imaging modalities such as CT, MRI, and ultrasound imaging are used in generation of brain atlases [111-113]. Structural information from the post-mortem examination is also used in some of the generations [114, 115]. For example, MRI-based brain atlas is a series of images similar to MRI scans which are generated based on intensity average of co-registered MRI scans from a group of subjects [116, 117]. Some brain atlases also contain other distribution maps besides the average of MRI scans [112, 118]. Tissue classification maps represent segmentation of different tissue regions such as gray matter and white matter in the head volumes. Tissue probability maps are similar to tissue classification maps but represent the probability distribution of each tissue instead of the absolute tissue classification. Structural region maps [119] and functional region maps [120] represent the distribution of structural brain regions such as the sub-thalamic nucleus and functional brain regions such as visual cortex respectively. They are also included in some brain atlases [121].

The animal brain atlases have been developed in the past decades. Brain atlases of difference species such as rats, mice, rabbits and monkeys have been generated from different subject groups [122-125]. For human subjects, age and race-specific atlases and disease-specific brain atlases have also been generated based on different groups of subjects in the previous studies [126, 127] . For example, brain atlases for patients with cerebrovascular diseases such as stroke and subdural hematoma, neoplastic diseases such as glioma and meningioma, degenerative diseases such as Alzheimer's disease and Huntington's disease, and

infectious diseases such as Lyme encephalopathy and herpes encephalitis have already been generated [128-130]. Atlases of the general healthy population have also been generated in the previous study based on averages of subjects with a wide age and racial range [112, 131, 132].

The brain atlases of the general healthy population have been used to guide the segmentation of MRI scans for individual subject. Comparison between a healthy brain atlas and an atlas for a specific neurobiological disease has improved understanding of the healthy brain and the cause of the disease. It also contributes to diagnosis and monitoring of the neurobiological disease [129, 133, 134]. Human brain atlases with region distribution maps have been applied in the investigation of functional brain activation and connection between related functional regions [119, 135]. Age and race specific atlases provide structural information of healthy subjects with specific limitations. They are used in the studies of the growth and aging process in the human brain and racial difference in brain structure [127, 136, 137]. The general human brain atlas provides a standard space where results from different subjects are compared and correlated. The standard head space also provides the opportunity to share results and findings in different research areas across imaging modalities which contributes to the multidisciplinary research [138].

This chapter is a brief introduction of MRI based human brain atlases. Two single subject based atlases and two multi-subjects based atlases are investigated in part 2. Examples of age-specific atlases and distribution maps such as the tissue probability maps are presented in part 3. The most suitable atlas for atlas-based DOT recovery in this work is also selected.

3.2. Single subject based atlas

A single subject based brain atlas is generated based on the anatomical information from brain images of a single subject. Early brain atlases were derived from an individual post-mortem specimen and the brain images are obtained by photographic images of the cryosectioned brain [139]. However, there exist some differences in brain structure between a live subject and a frozen specimen, and the post-mortem examination also jeopardises some of the fine structure in the cortex. Non-invasive imaging techniques provide the opportunity to create brain atlases from living subjects. After the generation of brain image-based maps, distribution maps of tissue types or brain regions are created by manual segmentation of the image-based maps. Single subject based atlases are also generated based on the same subject using multiple imaging modalities to reduce noise and error introduced in imaging process [140, 141]. Only MRI based atlases such as the Talairach Atlas [120, 142] and Colin 27 atlas [143] are investigated in this chapter.

3.2.1 Talairach Atlas

Talairach Atlas is one of the earliest human brain atlases with accurate structure details [142]. It is generated from head MRI scans of a 60-year old right-handed European female and structural information from the single post-mortem dissection is also involved in the generation process. The talairach Atlas is a symmetrical atlas with identical left and right hemispheres of the brain, though the majority of normal human brains exhibit some left-right asymmetry. This atlas exhibits good accuracy in some regions of the brain but lacks anatomical details in some fine structure such as the cortical surface. The talairach Atlas contains a set of structural brain region maps [Figure 3.1] in which tissue labels are assigned

according to the Brodmann areas[144]. Structural landmarks including the original point (AC-PC line) of the Brodmann areas are extracted manually from this atlas.

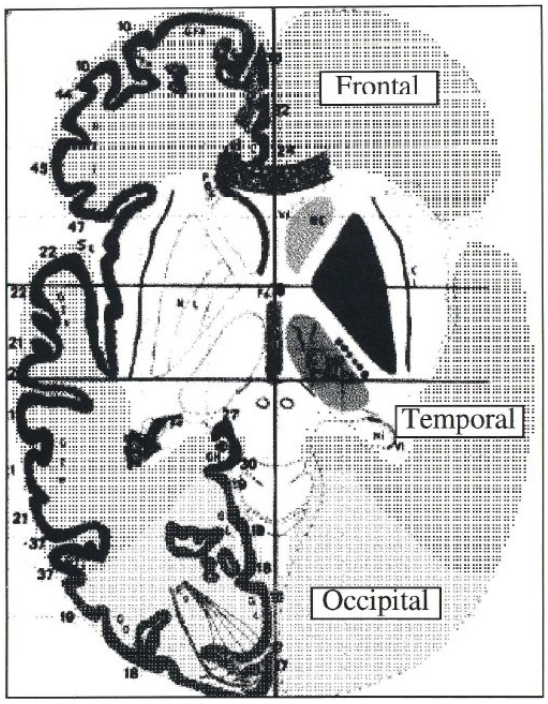

Figure 3.1. A brain region distribution map in the Talairach Atlas[145]. Brodmann areas is present in the left hemisphere and four lobes (Frontal lobe, Temporal lobe, Parietal lobe and Occipital lobe)based segmentation is presented in the right hemisphere.

The talairach atlas has been used as a typical reference of human brain structure. Talairach space, also known as Talairach coordinates, is developed based on the Talairach Atlas. For analysis of imaging data from multiple subjects and generation of other brain atlases, brain images from other subjects and atlases have been registered to the Talairach space with registration processes such as line fitting registration based on the AC-PC line [146]. The talairach Daemon (TD) system [145, 147], which is an open access database for location based querying and retrieving of human brain structure, is also developed based on this atlas. The BrainMap project [148, 149] developed a database similar to the Talairach Daemon (TD) system based on the Talairach space where functional and structural neuroimaging can be

published. Most general brain atlases such as the MNI305 atlas [150, 151]and the ICBM152 atlas [112, 117] are generated in the Talairach space or a modified Talairach space.

3.2.2 Colin27 atlas

With the development of MRI technique, atlases with higher definition than the Talairach atlas have become possible. The Colin27 atlas [Figure 3.2] is a high definition atlas generated based on a single subject [143, 152]. Firstly, 27 3D MRI scans from the same subject are acquired over a period of three months. Secondly, these scans are aligned together and intensity-averaged images are generated based on the registered MRI scans. Thirdly, the intensity- average image is non-rigid registered to the MNI space (discussed in part 3.1) to create the Colin27 atlas. Compared with the Talairach Atlas, the Colin27 atlas has a higher SNR and structural definition.

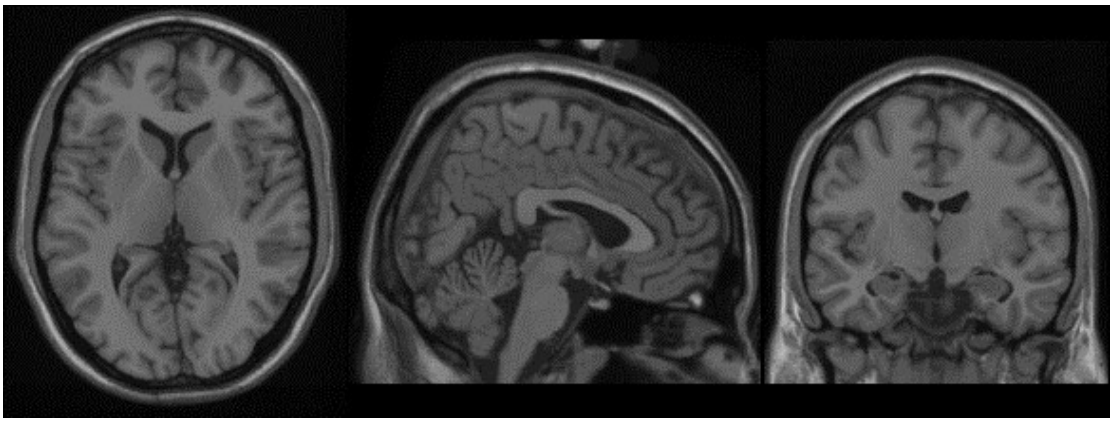

Figure 3.2. intensity-averaged MRI scans of the Colin27 atlas [153].

As a single subject atlas, the Colin27 atlas contains artefacts from similar idiosyncrasies to the Talairach atlas. However, since this atlas contains fine structural details of the human brain and is mapped to a common space (MNI space), it has been adopted as a stereotactic template in many projects such as SPM [131, 154] and Fieldtrip [155, 156].

3.3. Multi-subject based atlas

The multi-subject based atlas is a series of brain maps that contains the common brain structural information of a subject group. Based on the selection criteria of the group, multi-subject based atlases represent common brain structures of subjects with specific disease [130], within specific age range [136] or the general human population [112]. Multi-subject based atlases do not suffer from idiosyncratic artefacts, and hence are more suitable for studies of brain structure of general subjects and changes in brain structure caused by disease or aging [157].

Intensity-averaged MRI images in multi-subject based atlases are generated by a registration-averaging process [146, 151]. Firstly, each subject in the subject group is registered respectively to a common space based on an existing atlas such as the Talairach Atlas or a selected subject from the group. Secondly, average intensities of the MRI images are calculated voxel-by-voxel based on the registered MRIs of all subjects for the intensity-averaged MRI images of the atlas. A few improvements of the generation process have been developed to increase the anatomical accuracy of the atlas. For improvement of the registration, the size and orientation of each subject brain is normalized based on the common space before registration. Since non-brain tissues often have larger variances than brain tissue, subject MRI scans are segmented into brain tissue and non-brain tissue, and the registration is then processed based on the brain tissue and non-brain tissue separately [158]. To improve the averaging process, outliers are excluded by a standard deviation-based exclusion process on the voxel intensity to reduce the influence of imaging noise, registration error and idiosyncratic artefacts. The accuracy of the multi-subject based atlases can also be improved by using MRI scans with higher resolution.

Multi-subject based atlases have been used in studies of structural and functional information of the human brain and development of the human brain [136]. They are also applied to segmentation of individual subject and comparison analysis across subjects [127, 132]. Two of the most commonly used multi-subjects based atlases are the MNI305 atlas and ICBM152 atlas.

3.3.1 MNI305 atlas

The MNI305 atlas [Figure 3.3] [150], also known as the MNI Average Brain, is a multi-subject based atlas averaged from 305 young healthy subjects (239 males, 66 females; age: 23.4 +/- 4.1 year.). It is developed by the Montreal Neurological Institute and Hospital (MNI) group for the purpose of overcoming the idiosyncrasies of single subject based atlases. The MNI305 atlas is generated based on the MNI average250 atlas which is one of the earliest multi-subject based atlases generated by the same research group. The generation process of the MNI average250 atlas is divided into two steps. Firstly, anatomical landmarks are extracted manually from 250 subjects based on the fiducial marks in the Talairach atlas. A simulated AC-PC line is also created for each subject by least squares linear regression of the extracted landmarks. The 250 subjects are realigned based on the AC-PC line. Secondly, the 250 MRI scans are mapped to a common space based on a whole-brain 9-parameter linear image registration, and intensity-averaged MRI images are generated based on the registered MRI scans to create the MNI average250 atlas. The MNI305 atlas is created based on the same generation approach as the average250 atlas with a further 55 subjects. The intensity-averaged images from the results are 172x220x156 with 1mm slices. Since the MNI305 atlas is created based on the Talairach atlas, MNI-space based on this atlas is an approximation of the original Talairach space with ~3.5 mm difference in the Z-coordinate. MNI-space has

become one of the most commonly used spaces for comparison and correlation of results from different subjects [159].

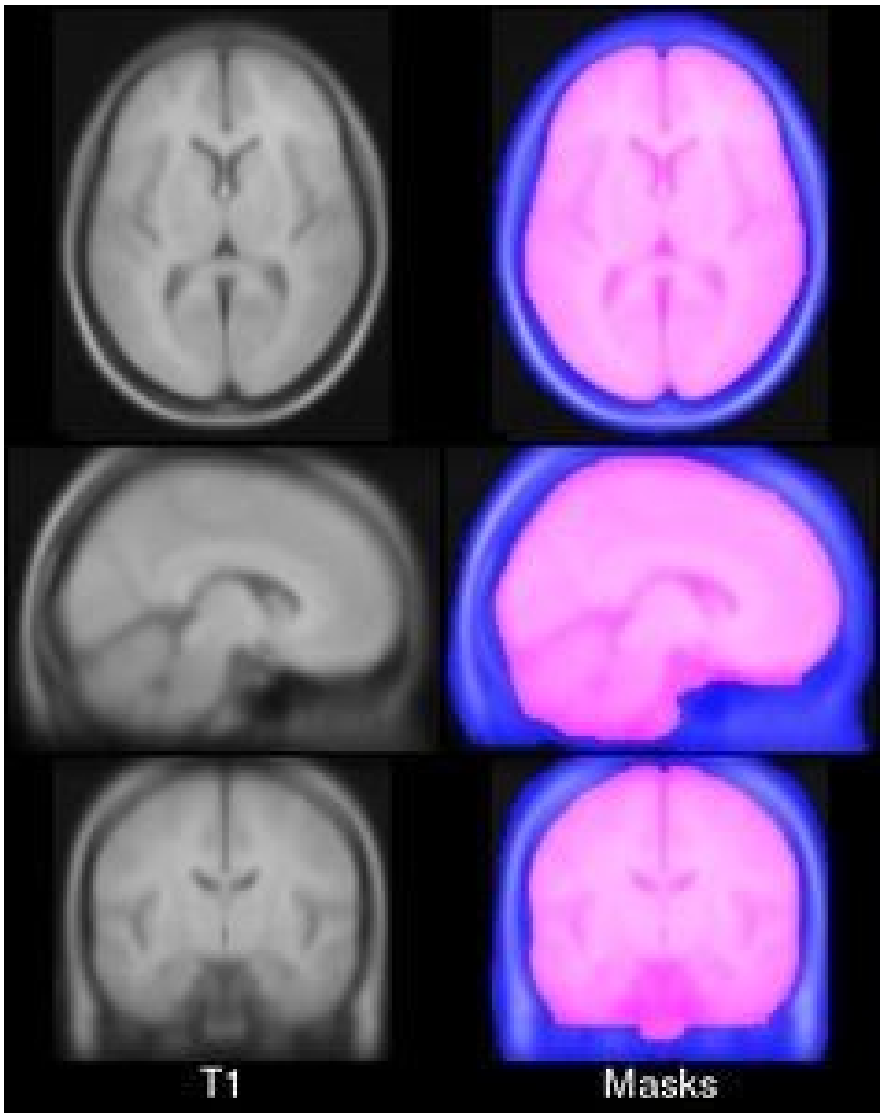

Figure 3.3. The MNI305 atlas [160]. Left figures are the intensity-averaged MRI scans and right figures are the masks based on segmentation of brain tissue and non-brain tissue.

3.3.2 ICBM152 atlas

The ICBM atlases [112] are a group of atlases developed in the International Consortium for Brain Mapping (ICBM) projects with a wide ethnic and racial distribution and age range. The ICBM atlases contain general population atlases as well as age-specific atlases. Each atlas contains intensity-averaged MRI scans and tissue probability maps based on the tissue

classification of the subjects. Distribution maps of functional regions and attributes such as blood flow are also included in some of the atlases.

The ICBM152 atlas [Figure 3.4] is one of the ICBM atlases designed for the healthy young adult population. It is generated based on an average of T1-weighted MRI scans from 152 health subjects aged 18.5–43.5 years. The generation process of ICBM152 is similar to generation process of the MNI305 atlas. Each subject is linearly registered and mapped to MNI space, and then intensity-averaged images are generated based on the registered image data. The T2 and PD based atlases are also generated based on T2 and PD weighted MRI scans and the registration of T1 scans.

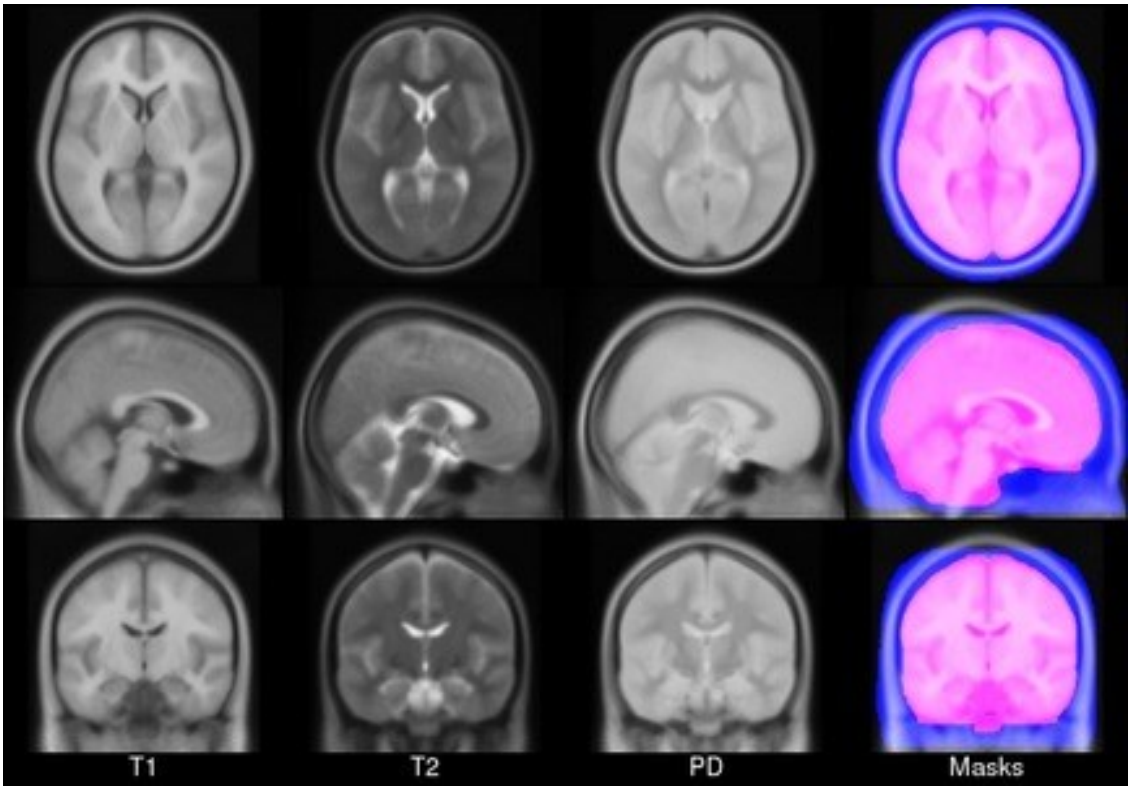

Figure 3.4. ICBM152 atlas[161]. From left to right, T1-based intensity-averaged MRI scans, T2-based intensity-averaged MRI scans, PD-based intensity-averaged MRI scans and the masks based on segmentation of brain tissue and non-brain tissue are shown in this figure.

Compared with the MNI305 atlas, the ICBM152 atlas is generated from MRI images at a higher resolution [162] which leads to a better contrast for the atlas. The ICBM152 atlas also

includes subjects with a wider age range which leads to a better definition of some structure such as the bottom of the cerebellum. Since the ICBM atlases group contains age-specific atlases which are co-registered to the same space using the same registration method, the can be used for analysis of brain growth for children.

3.3.3 Examples of other atlases and brain maps

Beside brain atlases of the general population, age-specific atlases and disease-specific atlases are also developed based on a similar generation approach. The NIHPD Objective atlases [136] are a group of age-specific atlases generated based on MRI data from the NIH paediatric database. These atlases are generated based on a similar approach to the ICBM152 atlas. 108 children aged from birth to 4.5 years old and 324 children aged from 4.5 to 18.5 years old are involved in this study. Part of the NIHPD Objective atlases is shown in Figure 3.5.

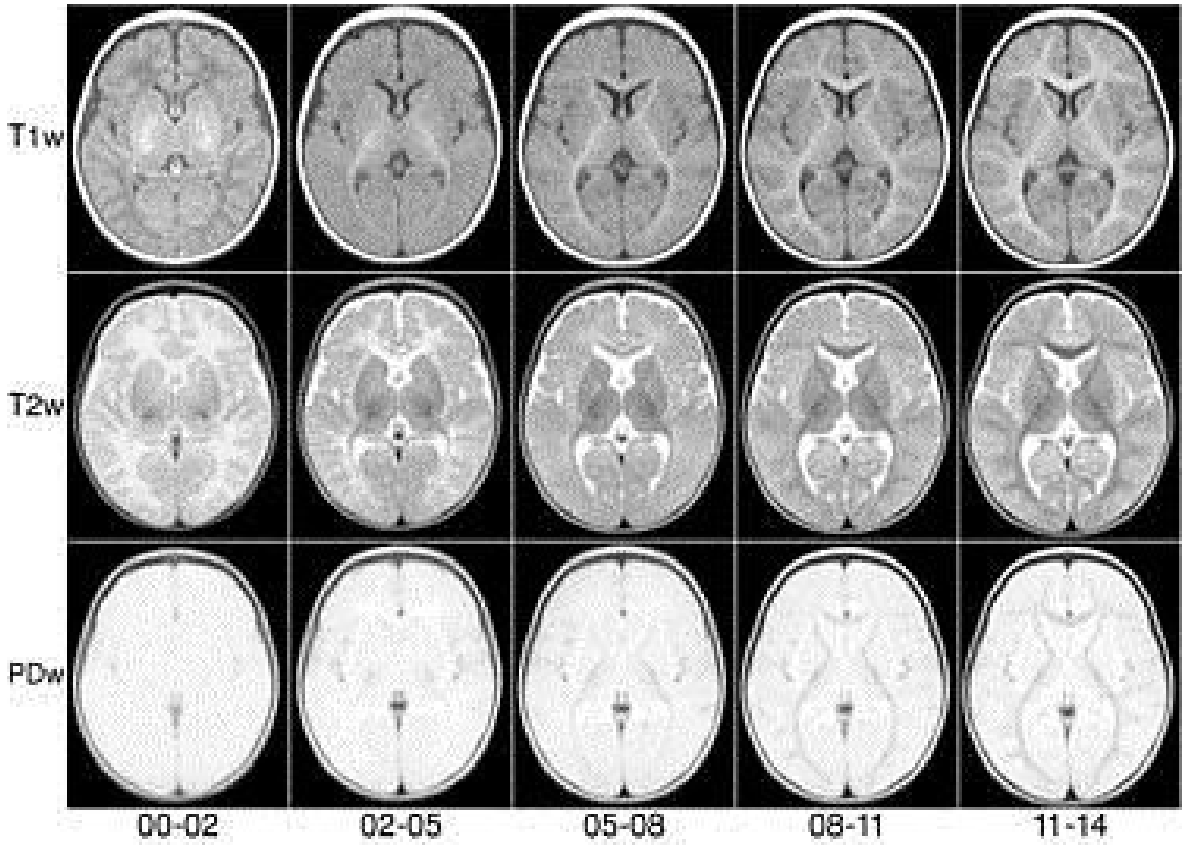

Figure 3.5. Examples of NIHPD Objective atlases [163]. Upper figures are T1-based intensity-averaged MRI scans, middle figures are T2-based intensity-averaged MRI scans, and lower figures are PD-based intensity-averaged MRI scans. From left to right, atlas for 0-2 years old subjects, 2-5 years old subjects, 5-8 years old subjects, 8-11 years old subjects, and 11-14 years old subjects are shown in this figure.

A 4D neonatal head model [Figure 3.6 and 3.7] was generated based on average of MRI scans from 324 infants (160 female) between the ages of 27 and 47 weeks (post-menstrual age) [164]. The atlas contains 1) a tissue classification map with six tissue types: extra-cerebral layers (ECL), cerebrospinal fluid (CSF), gray matter, white matter, cerebellum and brainstem; 2) a high-density layered head mesh based on the tissue classification; 3) three surface masks of head surface, cortex surface and white matter surface and 4) external landmarks based on EEG 10-5 locations (details in chapter 5 section 5,2.1.1). This atlas is used to investigate rapid growth and maturation of the infant brain and to optimize image reconstruction in DOT of the infant brain.

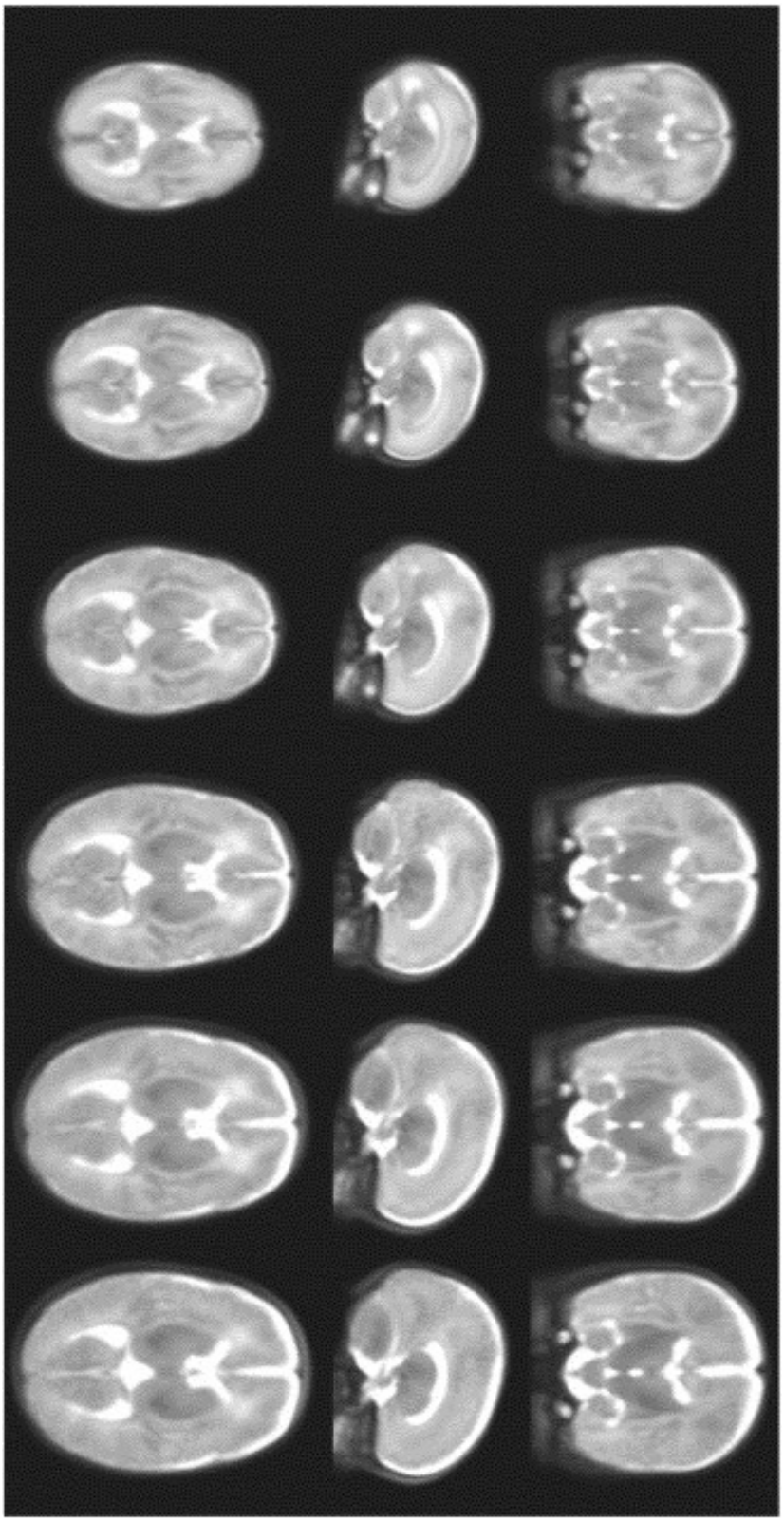

Figure 3.6. Intensity-averaged MRI intensity image 4D neonatal head models [164]. From left to right: atlas of 29, 32, 35, 38, 41 and 44 weeks old infants are shown in this figure.

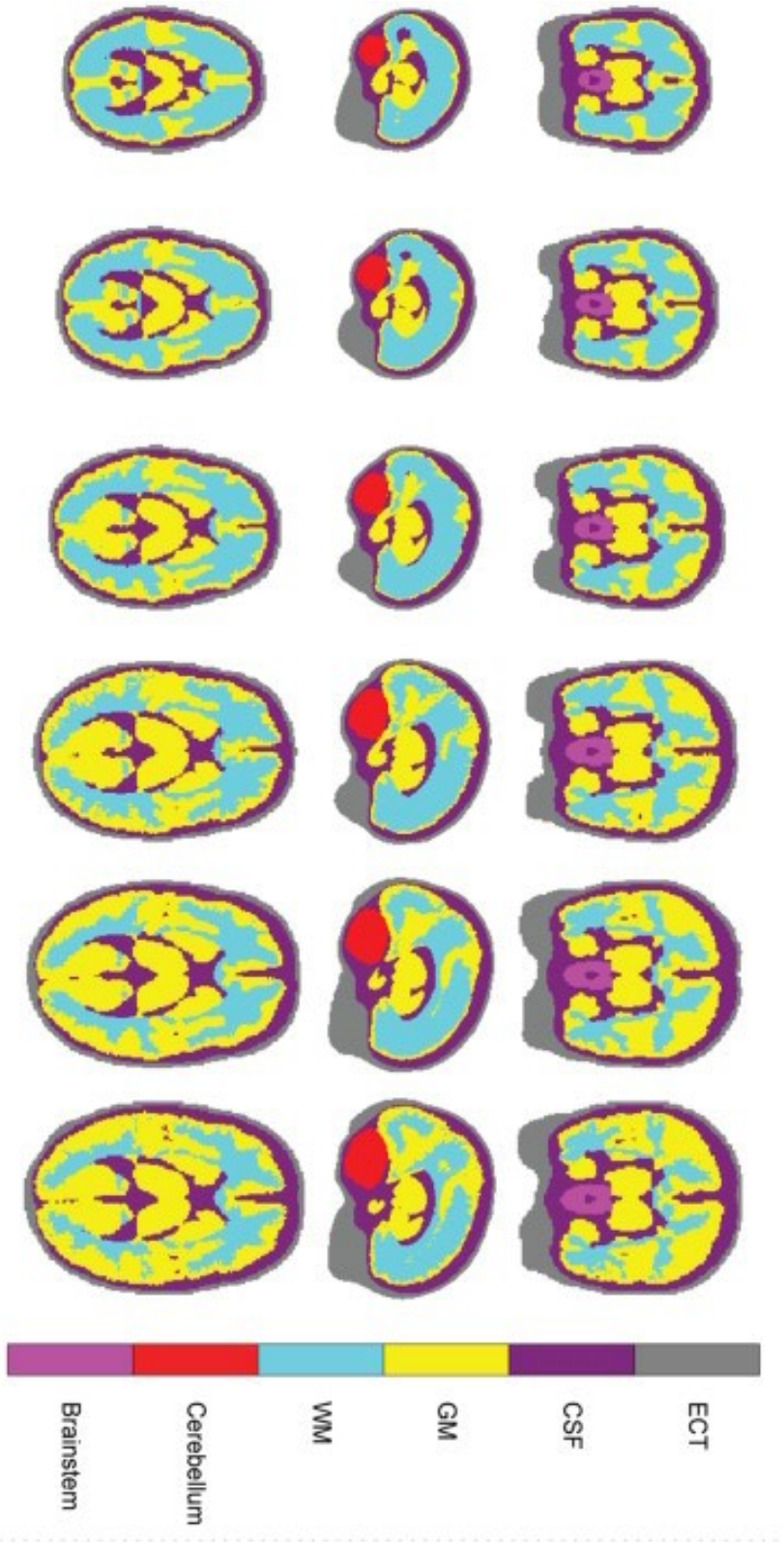

Figure 3.7. Tissue classification maps of 4D neonatal head models [164] with six tissue types: extra-cerebral layers (ECL), cerebrospinal fluid(CSF), gray matter, white matter, cerebellum and brainstem. From left to right: atlas of 29, 32, 35, 38, 41 and 44 weeks old infants are shown in this figure.

Since brain atlases are generated based on image data from the subjects, the types of images in the atlas depend on the types of images provided for each subject. Region distribution maps are generated based on structural or functional region segmentation of subjects. Tissue classification maps and tissue probability maps are generated based on tissue region segmentation of subject images. The ICBM152 2009c Nonlinear Symmetric atlas [Figure 3.8] contains intensity-averaged MRI images for T1 T2 and PD weighted MRI scans, tissue probability maps for brain matter such as gray matter, white matter and CSF, and structural regional distribution maps [165].

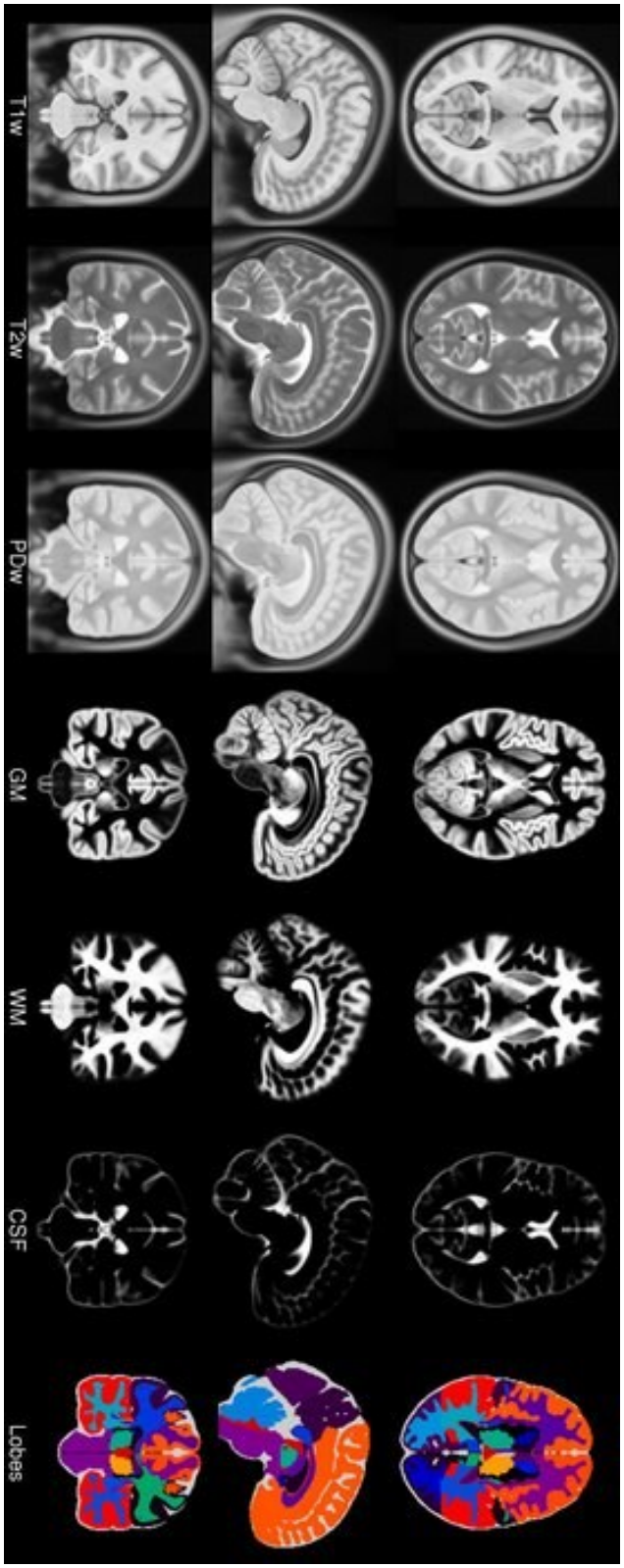

Figure 3.8. ICBM152 2009c Nonlinear Symmetric atlas[131]. From left to right, average-intensity MRI images for T1 T2 and PD weighted MRI scans, tissue probability maps for gray matter, white matter and CSF, and region distribution maps are shown in this figure.

3.4. Summary

The human brain atlas is a series of maps generated from brain images of single or multiple subjects. It contains the common anatomical brain information of the subject group. Where the corresponding segmentation is available for the subjects, the brain atlases can contain information on tissue classification and brain region distribution. The commonly used atlases are categorized as follow.

Table 3.1: Summary of different atlases

Atlases	Category	Generation base	Example of applications	Examples of the atlases
Single-subject based		Single subject	• Common space (such as the MNI space) • Stereotaxic template	• Talairach atlas [142] • Colin27 atlas [143, 152]
Multi-subject based	General population	Multiple subjects from the general population	• Studies of the structural and functional information of the average human brain • Segmentation of individual subjects	• MNI305 atlas [150] • ICBM152 atlas [112]
	Specific subject group	Multiple subjects from a specific subject group	• Studies of the structural and functional information of the specific subject group • Studies of the development of a brain related disease	• The NIHPD Objective atlases [136] • The 4D neonatal head model [164]

The multi-subjects based atlas is generated based on a registration-averaging approach. Image data from all the subjects are registered to a common space such as the MNI space, and then intensity-averaged images are generated based on the average of registered images.

Segmentation of each subject, if available, is also transformed to the common space based on the registration result. Tissue classification maps and brain region distribution maps are generated based on the registered segmentation images. Multi-subjects based atlases have a clear advantage over single-subject based atlases as they reduce the error from idiosyncrasies of the single subject and some noise introduced in the imaging process. In the two most commonly use atlases for general population, the ICBM 152 atlas has higher image resolution and wider age variations. It is used as the human head atlas in this work of atlas based brain DOT recovery.

Customised atlases can be easily generated based on multiple subjects. A modified approach based on the generation process of the multi-subject based atlases is used for this generation. Firstly, subject images are segmented into brain tissue and non-brain tissue, and size and orientation of each subject brain is normalized based on an existing atlas such as the MNI305 atlas. Secondly, all subjects are registered to the selected atlas space based on the brain tissue and non-brain tissue respectively. Thirdly, the average intensity of each image pixel is calculated based on the registered images with an outlier exclusion process. Intensity-averaged images of the customised atlas are created based on the subjects group. If segmented images of the subjects are available, region distribution maps can also be generated based on realigning the segmentation images by the registration result from the second step.

In DOT brain recovery, the human brain atlas is used as an alternative to MRI scans to provide internal structural information for the generation of the forward model. ICBM152 is a brain atlas for the general population based on high-resolution MRIs, and it is used as the brain atlas for generation of the forward model in this work. For a generation forward model based on both MRI scans and the atlas, tissue region segmentation is the main process to

extract internal structural information. Different registration methods for human heads are discussed in the following chapter.

CHAPTER 4: SEGMENTATION METHODS FOR HUMAN BRAIN IMAGING

4.1. Introduction

Functional activations in the human brain can be recovered based on DOT imaging. The recovery process of DOT is divided into two steps: generation of the forward model and inverse processing of the forward data. A homogenous head model has been used as the forward model to recover changes in tissue chromophores in the whole brain hemisphere [166-171]. Since then, forward models based on subject-specific anatomical structure have been developed and proved to give higher recovery accuracy than the recovery based on a homogenous model [172-176]. With the advent of non-invasive neuroimaging, anatomical structural information can be extracted from neuroimaging data such as head MRIs. In brain DOT recovery, subject-specific information is usually obtained based on the segmentation of brain images [4, 11, 75, 177]. Segmentation of brain images such as MRI scans is one of the main processes involved in the generation of subject-specific forward models.

In head MRI scans, most tissues are distinguishable based on image intensity and spatial distribution. There are clear intensity differences between some tissue types such as the skull region and skin region, whereas other brain tissues such as the skull region and CSF do not have a clear difference in image intensity, which makes them difficult to distinguish [178, 179]. Anatomical structures of human brain tissue contain some spatial distribution patterns. Therefore, tissue classification in human head images can be generated based on image intensity and anatomical structures. General anatomical models such as brain atlases are created based on pre-segmented subjects to guide the segmentation [18, 180, 181].

Segmentation methods for human head images are divided into three categories: segmentation methods based on the image intensity, segmentation methods based on anatomical model, and a combination of the first and second methods [182, 183].

In this chapter, eight segmentation methods from the three categories above are discussed and compared. The most suitable segmentation methods from MRI scans are selected for this work. A near automatic layered subject mesh generation approach is also designed in this work.

4.2. Methods

4.2. 1 Intensity based segmentation

For brain MRIs, different types of tissue can be distinguished based on the image intensity and spatial distribution. Intensity based segmentation is a segmentation method based only on MRI data of the subject. Basic anatomical structure patterns and MRI tissue-intensity correlation is used in this segmentation. Commonly used anatomical structure patterns include that white matter is a single connected component located in the centre of the head and gray matter is a layer of connected component surrounding the white matter, while the CSF is a layer of component surrounding the gray matter. Commonly used intensity patterns include that white matter has a higher intensity than gray matter and the CSF region has the lowest image intensity in the brain and non-brain tissue in T1 imaging [184-186]. An example of a set of 3D MRI head images and its intensity histogram are shown in Figure 4.1 and Figure 4.2.

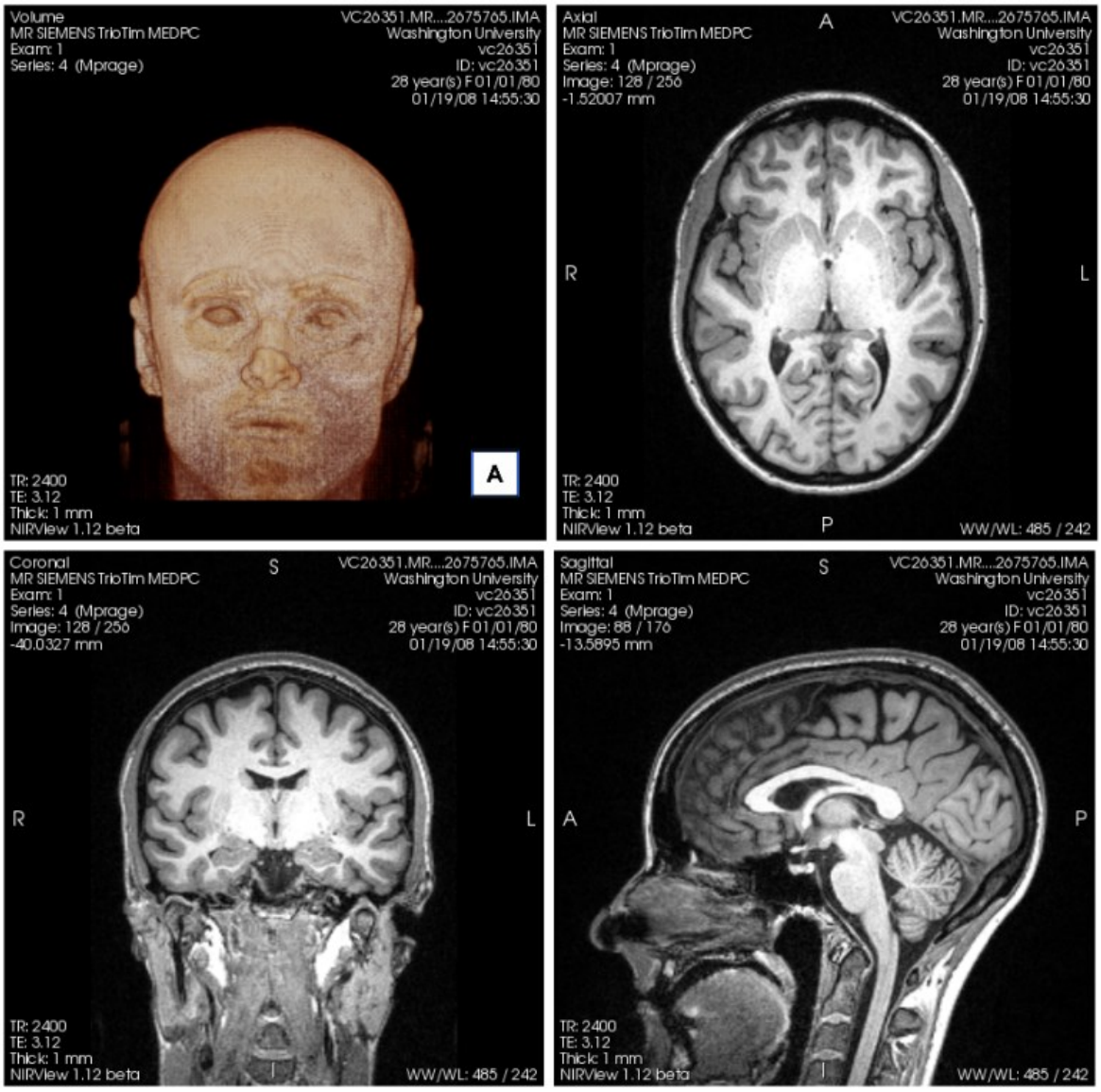

Figure 4.1. A set of 3D MRI head images from a healthy young adult and its 3D rendering.

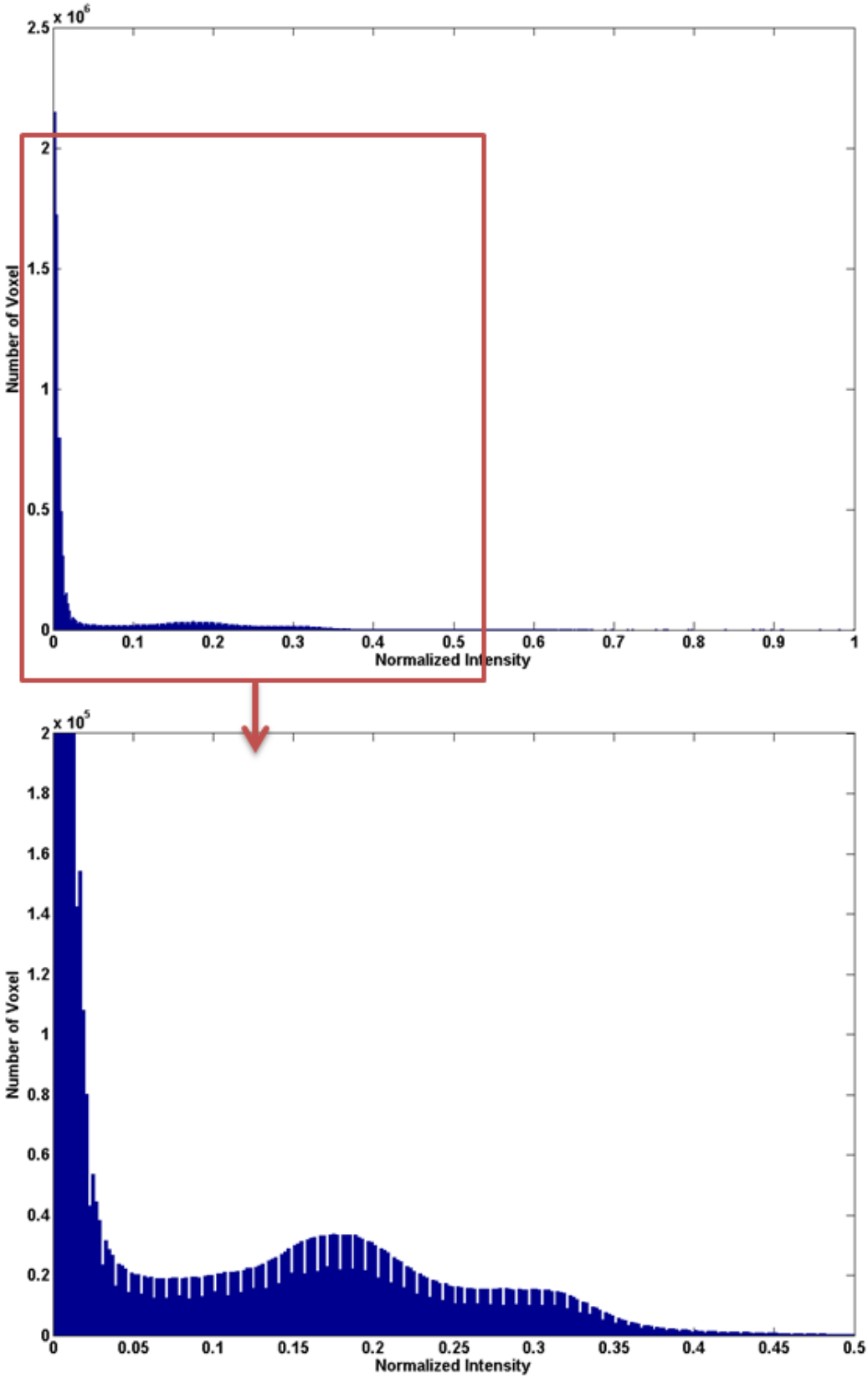

Figure 4.2. Histogram of normalized image intensity of the MRI head image in Figure 4.1.

Intensity based segmentation can be processed both manually and automatically. Manual segmentation can have the highest segmentation accuracy among all segmentation methods and is often used as a reference in the evaluation of other segmentation methods [187, 188]. Automatic and semi-automatic segmentation methods based on intensity have been created using several different techniques. Edge detection based segmentation [189], thresholds based segmentation [190] and k-means clustering based segmentation [191] are introduced in this part. Intensity based segmentation for multiple subjects is also presented [192].

4.2.1.1 Intensity based segmentation with single subject

4.2.1.1.1 Manual segmentation

Manual segmentation of a single subject usually classifies tissue regions in a voxel-by-voxel basis. Basic internal structure information and the intensity distribution pattern and personal expertise on the anatomical structures of human head are involved in the manual segmentation. Compared to other segmentation processes, manual segmentation can achieve relatively high accuracy when segmented by people with professional knowledge of human brain such as a neurologist or a neurosurgeon, and it has been used as the reference for evaluation of other segmentation methods [187, 188]. However, manual segmentation is case-by-case, so tissue classification for multiple subjects is not time efficient [193]. Even for a single subject, manual labelling of each voxel is also extremely time-consuming. Moreover, the difference between adjacent tissue types is not always significant. The segmentation accuracy of this method is highly dependent on the personal expertise (in terms of brain structure) of the operator [187, 193].

4.2.1.1.2 Automatic and semi-automatic segmentation

If tolerance anatomical error in structural details is relatively high, intensity-based segmentation can also be generated automatically and semi-automatically. Automatic and semi-automatic segmentation of head images relies on the distinguishable difference in image properties between different tissues types. This segmentation can be processed using several different modalities.

Automatic edge detection based segmentation is one of the semi-automatic segmentation methods, and it relies on edge detection of different tissue regions [179, 189]. It extracts the boundary of each tissue region based on changes in image intensity between different tissue types and the connected structure of each tissue region. Firstly, a seed point inside each brain tissue region is manually selected. Secondly, automatic edge detection is performed to extract the boundary of each tissue type. Thirdly, the segmentation result is corrected by morphological operations based on basic structural information. The edge detection segmentation has been improved by dividing the segmentation process into two steps, which are 1) segmentation between brain and non-brain tissue (also known as brain extraction) and 2) segmentation of the brain tissue into white matter, gray matter and cerebrospinal fluid [194, 195]. However, this segmentation may contain errors because of the small differences in image density between some adjacent tissue types and it may not be able to segment all the fine structure. Since the seed points are selected manually, the segmentation result can be affected by human interactions.

Another semi-automatic segmentation process is based on a group of thresholds [179, 190]. Firstly, tissue labels are assigned manually to a few voxels based on the anatomic structure of the subject. Secondly, a group of image intensity thresholds is created based on

the selected voxels, and the intensity range of each tissue type is generated based on the thresholds. Thirdly, the images are segmented based on the intensity range. An example of threshold based image segmentation is shown in Figure 4.3. Since the threshold-based segmentation method only relies on differences in the image intensity between tissue types and regions at a distant locations with similar intensity can be assigned as the same tissue type, therefore the threshold based segmentation normally requires some correction, which for example can be done manually correction after the segmentation step [196].

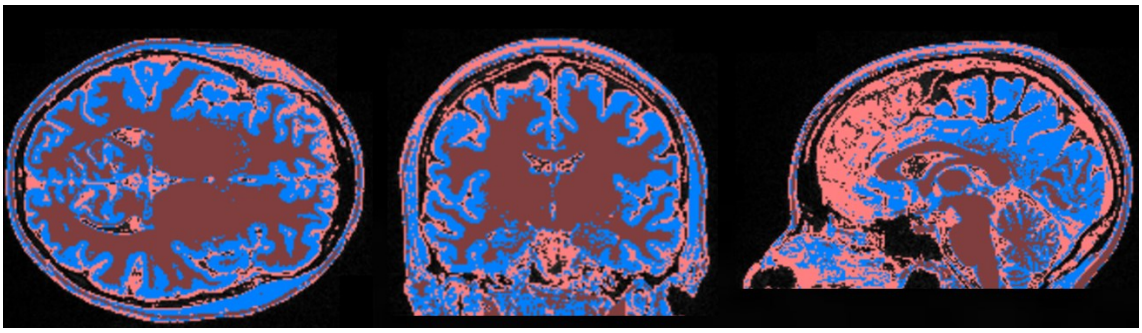

Figure 4.3. Threshold-based segmentation without post-segmentation correction of MRI images in Figure 4.1.

The image intensity based segmentation can also be processed fully automatically based on cluster methods such as the k-means clustering [191]. Since the human head contains five different tissue types (skin, skull, CSF, gray matter and white matter), head images can be divided into six groups by k-means clustering for the five tissue types and the background. An example of k-means clustering based image segmentation is shown in Figure 4.4. However, because of the complexity of the brain structure and the small intensity differences between some brain regions, the basic k-means clustering based segmentation method does not provide an accurate segmentation result [197].

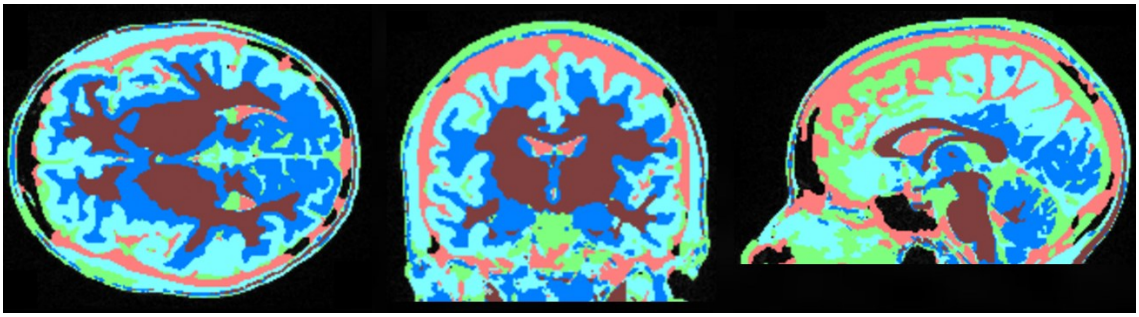

Figure 4.4. K-means-based segmentation of MRI images in Figure 4.1 without post-segmentation correction (k=6).

4.2.1.2 Intensity-based segmentation for multiple subjects

The intensity-threshold-based segmentation relies only on the intensity of the brain images without any information from the brain anatomical structure. It is possible to apply the same thresholds to multiple subjects. When imaged under the same circumstances (same system setting, same imaging environment etc), the same tissue region such as gray matter from different subjects have similar image intensity distribution. Therefore, the same thresholds can be applied to these images to derive an anatomical segmentation [187]. In this segmentation process, one of the subjects is selected as the reference, and the reference subject is segmented by the thresholds-based segmentation approach described in section 4.2.1.1.2.Secondly, the thresholds for the segmentation of the reference subject are extracted and used as thresholds for other subjects. Thirdly, images of all the other subjects are then segmented based on the same thresholds. The segmentation approach for multiple subjects can be processed within seconds, and it can provide similar accuracy as the threshold-based segmentation of individual subject.

4.2.2 Registration based segmentation

Since normal human brains have a similar internal structure, segmentation of head images can also be processed based on registration with a brain atlas [188, 198]. The brain atlas,

specifically the tissue classification maps of the brain atlas, is a set of brain images with distribution information for the different tissue regions. An example of a brain atlas is shown in Figure 4.5. Brain atlases can be generated based on a single subject or multiple subjects. Based on different subject groups, a brain atlas can represent the anatomical structure of the general population or a specific subject group defined by age, racial or disease type [199, 200]. For registration based segmentation, a brain atlas is registered to the subject head images. Each voxel of the subject images is then labelled as a tissue type based on the registered atlas. Registration based segmentation relies on the internal structure of the brain atlas and the registration between the atlas and the subject. Compared to intensity-based methods, it has the potential to be fully automatic with less post-segmentation correction.

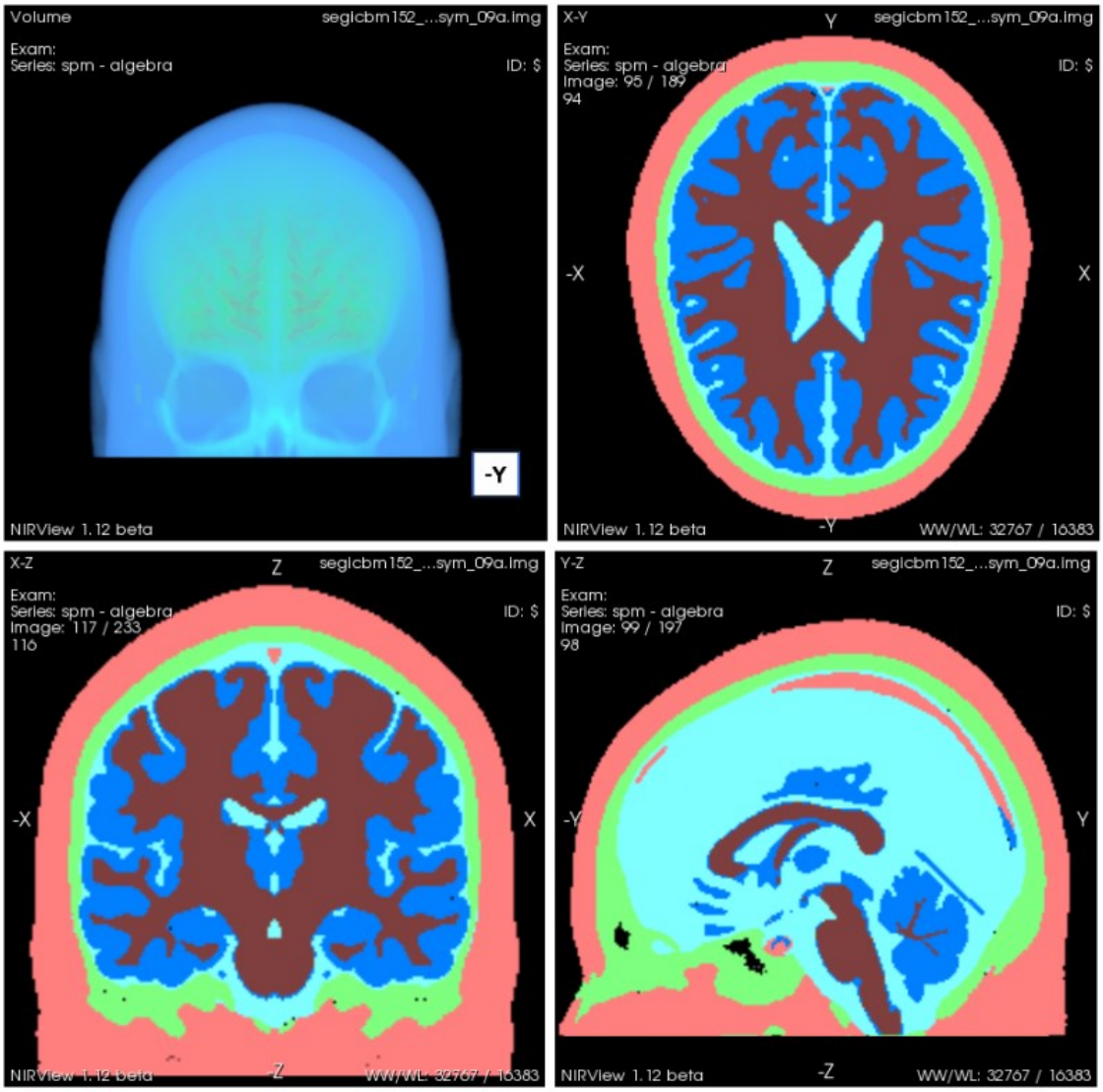

Figure 4.5. Tissue classification map of the ICBM152 atlas with five tissue regions and its 3D rendering. In the bottom figures, Pink region: skin (non-brain soft tissue). Green region: skull. Light blue: CSF. Dark blue: gray matter. Dark red: white matter. Black: background.

4.2.2.1 Segmentation based on a pre-segmented reference subject

The accuracy of registration based segmentation is determined by the registration accuracy and the difference in the internal structure between the atlas and the subject. In group studies of brain imaging, subjects from the same group often share one or more common factors such as age and disease type. A customized brain atlas generated from one or more selected subjects in the target group can reduce the internal structural difference

between the atlas and the subjects [188].The customized brain atlas is created based on tissue classification of a single subject or co-registered multiple subjects. This tissue classification is normally generated by a manual segmentation process or a segmentation process involving manual correction to ensure segmentation accuracy. Segmentation based on a pre-segmented reference subject has the potential to achieve better segmentation accuracy. However, this segmentation process is more time-consuming than other atlas-based segmentation methods, and selection of the reference subject may affect the registration result.

4.2.2.2 Segmentation based on a single general atlas

Segmentation of a brain image can also be generated based on an existing atlas. Atlas-based segmentation is one of the most commonly used segmentation methods for head MRIs and it can be processed automatically or with minimal human interaction [121]. An example of atlas based segmentation result is shown in Figure 4.6. A typical atlas-based segmentation process is divided into three steps. Firstly, a 3D tissue classification map is selected or generated based on intensity-averaged MRI scans of the atlas. Secondly, intensity-averaged atlas MRI scans are registered to the subject, and the tissue classification map is transformed based on the registration result. Thirdly, each voxel in the subject MRI scans is labelled as a tissue type based on the registered tissue classification map.

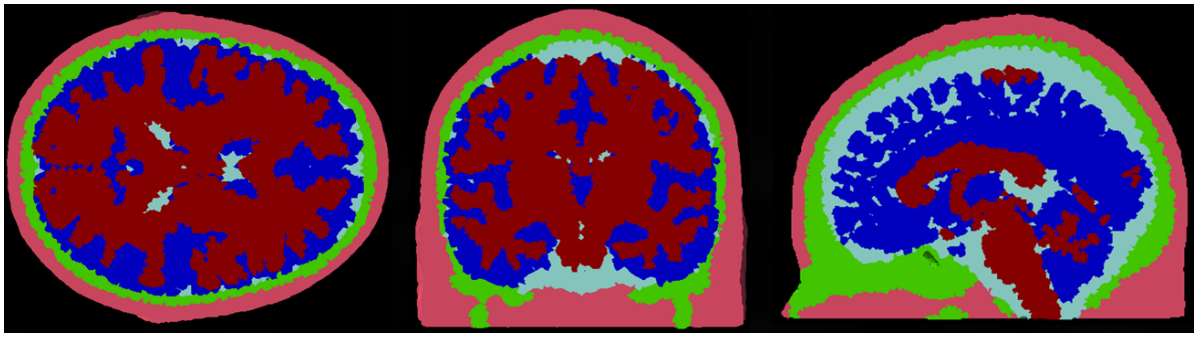

Figure 4.6. atlas-based segmentation of MRI images in Figure 4.1 based on the ICBM152 atlas in figure 4.5. The colour labels are the same as figure 4.5.

Previous studies in atlas-based segmentation have been focused on improving the segmentation accuracy [19, 188]. Different registration methods, both rigid and non-rigid, are proposed and evaluated. Other improvements in segmentation which increase the structural accuracy of the atlas or reduce errors caused by the structural difference between the atlas and the subjects are also investigated. Klein et al segments the subject head into brain and non-brain regions and applies decision fusion rules to improve the identification of large cortical structure volumes [201]. Instead of a definite tissue classification map, a tissue probabilistic map is applied to the segmentation to reduce the segmentation error causing by the structural difference between the subject and the atlas [202]. Prior information from one or multiple subjects can also be used to guide a general atlas-based segmentation [203]. The modified atlas-based segmentation procedure has been used in the generation of some segmentation databases such as the Internet Brain Segmentation Repository (IBSR) [204]and the LONI Probabilistic Brain Atlas [205].

4.2.2.3 Segmentation based on multiple atlases

In the last few decades, brain atlases have been created by different research groups based on both the general population and subject groups with certain limitations such as age and disease type. This provides the opportunity to segment head images based on multiple atlases, and this segmentation method has the potential to reduce the segmentation error from structural inaccuracy of the atlas or internal differences between the atlases and the subjects [18, 206]. The segmentation process-based on multiple atlases is similar to the single atlas based segmentation. Firstly, a tissue classification map with the same tissue labels is selected or generated based on intensity-averaged MRI scans from each atlas. Secondly, intensity-averaged MRI scans from each atlas are registered to the subject, and the corresponding tissue classification map is transformed based on the registration. Thirdly, the tissue type labels of

each tissue classification map are transformed to the subject based on nearest-neighbour interpolation to generate a propagated subject label volume. Each voxel in the subject MRI scans is labelled using vote-rule-based decision fusion on the propagated label volumes from multiple atlases.

When multiple atlases are not available, a similar segmentation approach can be achieved based on a single atlas and multiple reference subjects [18, 188]. Firstly, reference subjects are segmented based on the atlas. Secondly, a temporary atlas is generated based on the segmentation of each reference subject. Thirdly, the target subject is segmented based on the temporary atlases generated from the previous step. This segmentation method has the potential to reduce the segmentation error from internal differences between the atlas and the subjects. However, it is more time-consuming and requires multiple subjects from the same reference subject group.

Multi-atlas-based segmentation has proved to be more accurate than some single atlas-based segmentation processes, because specific errors associated with any single atlas are reduced in this process. However, not all atlases are appropriate for a specific subject. Involving an unsuitable atlas such as an atlas based on different age ranges may increase the segmentation error. Since the segmentation process includes registration of multiple atlases, it is more computationally expensive.

Registration based segmentation requires at least one set of atlas MRI scans and its corresponding tissue classification map. It is a fully automatic segmentation process and some post-segmentation correction based on image intensity can be applied to the segmentation result. Modified registration based segmentation is divided into three steps: firstly, a reference subject or atlas is registered to the target subject and the tissue classification map is

transformed based on the registration result. Secondly, the tissue label of each voxel in MRI scans of the target subject is selected automatically based on the registered tissue classification map. Thirdly, the classification is adjusted based on intensity distributions by a mixture of Gaussians or by weighting the classification according to Bayes rule [195].Therefore the segmentation can be processed based on both image intensity and the atlas.

4.2.3 Segmentation approach in SPM software based on both image intensity and an atlas

Segmentation methods combining image intensity distributions and a brain atlas have been developed to improve the segmentation accuracy. SPM is a software package designed for analysis of MRI images and the segmentation approaches in SPM are based on both image intensity and the ICBM152 atlas [154]. An optimised voxel-based morphometry (VBM) [207]is used in the SPM segmentation approach and the segmentation approach is processed iteratively [208]: firstly, MRI scans of the target subject are normalized into the MNI space. Since non-brain tissue in the human head such as the muscles have higher structural variability than the brain tissue, the spatial normalisation of the subject is only based on the gray matter. Secondly, the normalized subject or the updated segmentation result is registered to the atlas, and initial segmentation is generated based on tissue probability maps [209] in the atlas. Thirdly, the tissue labels from the second step are adjusted by applying Bayes rule to the voxel intensities and the adjusted segmentation result is used as the updated segmentation result in the next iteration. The last two steps are processed iteratively until reaching a pre-set number of iteration or minor changes are made compared to the previous iteration. The SPM segmentation approach is fully automatic. An example of SPM based image segmentation is shown in Figure 4.7. Since both image intensity and the anatomical structure from an atlas are

used in the segmentation process, the SPM segmentation approach provides better results than the segmentation approaches only based on an atlas or image intensity.

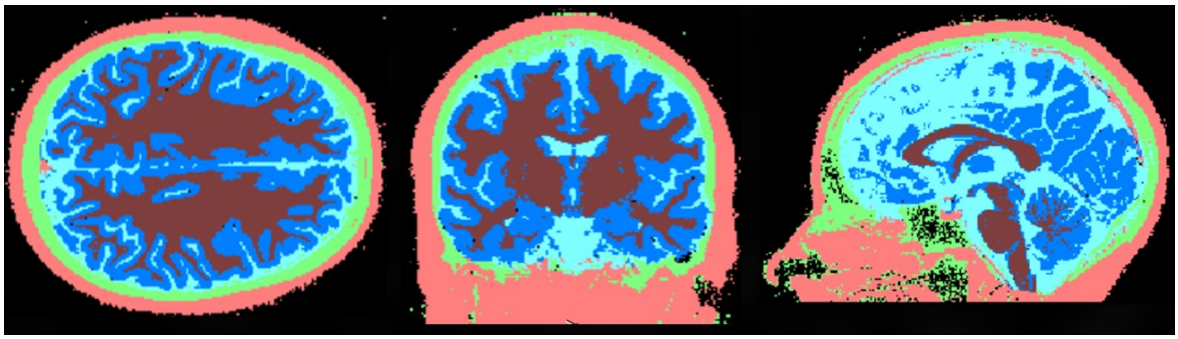

Figure 4.7. SPM-based segmentation of MRI images in Figure 4.1.

4.3. Comparison of the segmentation result based on an example subject

Segmentation methods for head MRI scans are divided into three categories: image intensity-based segmentation, registration-based segmentation and a combination of the first two approaches. Most of the segmentation approaches contain post-segmentation manual correction. However, since the fully manual segmentation approach is extremely time-consuming and requires some expertise on the detail of the anatomic structure of the human brain, it is not a suitable segmentation method for this work which involves multiple subjects. For comparison of the segmentation approaches in the three categories, one segmentation approach from each category is selected and compared based on segmentation of an example subject [Figure 4.1]. Subject specific anatomical T1-weighted MP-RAGE [echo time (TE)=3.13 ms, repetition time (TR)=2400 ms, flip angle=8 deg, $1\times1\times1$ mm^3 isotropic voxels] scans are used as MRI scans of the target subject. Five tissue types: skin (non-brain soft tissue), skull, CSF, gray matter and white matter, and the background are used as tissue labels for the segmentation. The k-means clustering based segmentation approach in the Nirfast/Nirview software package [68, 109] is used as an example of image intensity based

segmentation. The tissue label for each cluster is assigned based on basic knowledge of the structure of the human head such as that the central tissue region of human head is white matter. A rigid-registration based approach with the ICBM152 atlas [Figure 4.5] is used as the example of a registration-based segmentation method. Landmarks based on EEG10/20 location [210] (details in chapter 5 section 5.2.1.1) are extracted manually from the subject and atlas surface are used in the registration. Tissue labels of the subject images are assigned based on nearest neighbour of the registered atlas. The SPM segmentation approach described in part 2.3 is used as the combined segmentation approach. All the segmentation approaches include no manual correction during or after the segmentation to reduce human influence. The results of the segmentation approaches are shown in Figure 4.8.

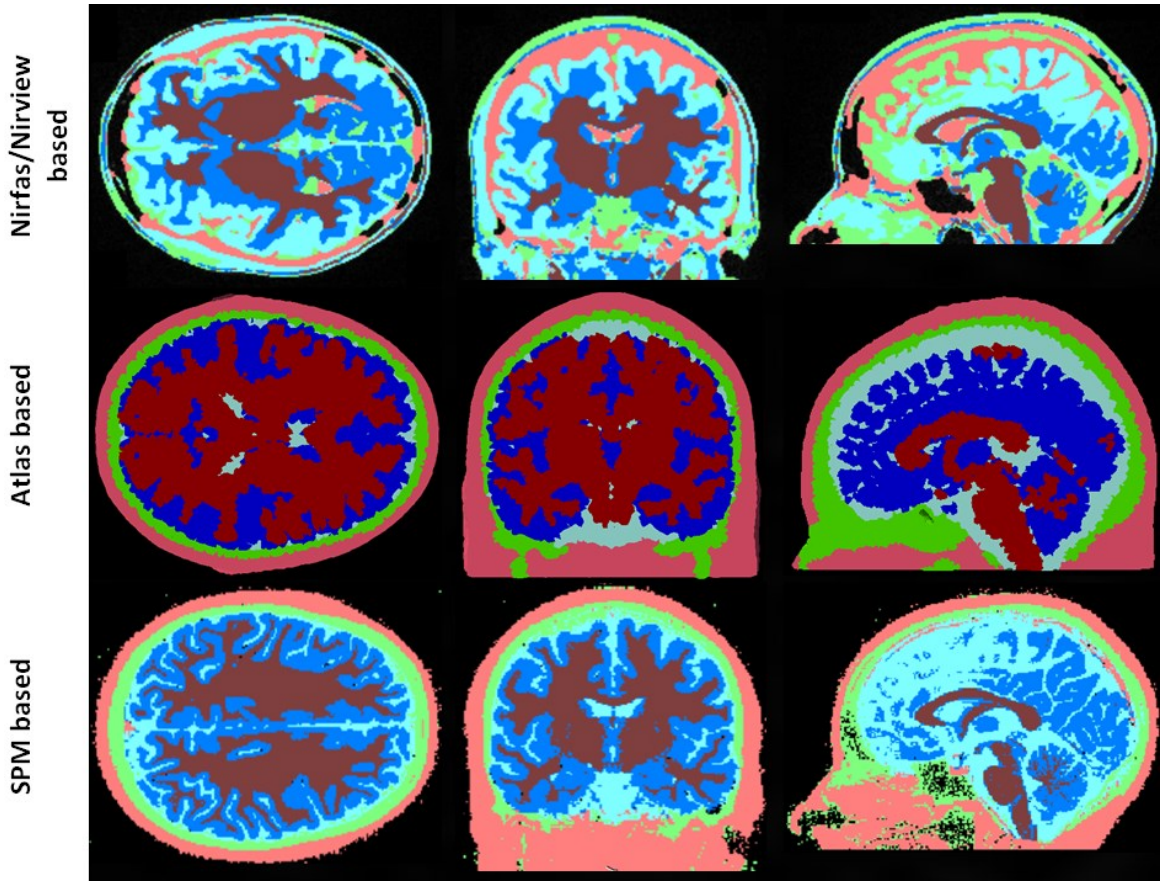

Figure 4.8. Tissue region labels based on K-mean clustering based segmentation in Nirfast/Nirview software package, atlas-based segmentation with landmark-based registration, and SPM segmentation approach for the head MRI scans in Figure 4.1.

In figure 4.8, SPM based segmentation shows the most accurate segmentation result among the three segmentation approaches. The Nirfast/Nirview based segmentation provided five tissue regions based only on the subject image. However, it cannot identify some regions properly such as the CSF region and it also fails to distinguish some non-brain soft tissue from brain tissue. The atlas-based segmentation clearly distinguishes the five tissue types. However, since the tissue label is only assigned based on the registered atlas, the segmentation result lacks some details of the subject-specific structure. The SPM based segmentation approach clearly distinguishes the five tissue types with subject-specific structural detail. Although it is the most time consuming approach of the three automatic segmentation approaches, it has higher segmentation accuracy than the other approaches.

A manual correction step can be processed after the tissue classification to remove some noise and errors such as noise in the background. The segmentation results after the manual correction of the SPM based segmentation are shown in Figure 4.9. It is a clear improvement to the fully automatic segmentation with fewer artefacts and background noise.

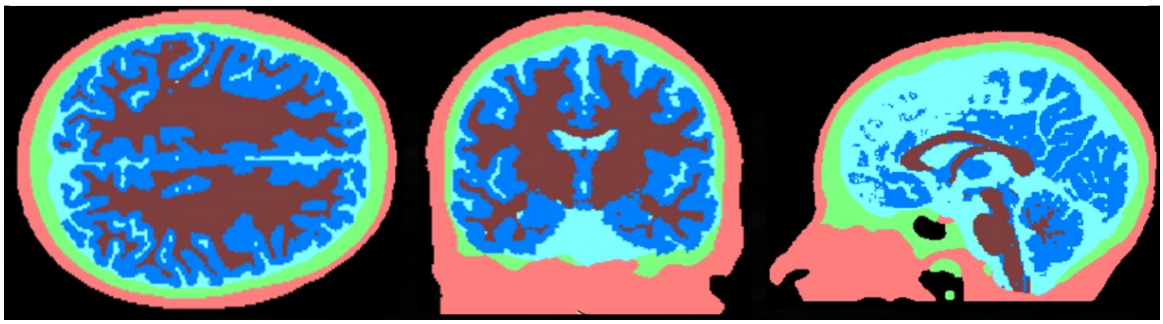

Figure 4.9. Segmentation result after manual correction of the SPM based segmentation in figure 4.8.

Since internal structural information can be extracted based on the segmentation result, a MRI scans based generation approach for five tissue layers mesh is designed based on the SPM segmentation approach with manual correction [Figure 4.10]. This generation approach is divided into three steps. First, MRI scans are segmented into five regions and the background based on the SPM based segmentation approach with manual corrections. Second, masks for the five tissue regions are generated from the segmented scans using the Nirview software package. Third, a five layer finite element mesh is generated using the Nirfast software package based on the five masks. This segmentation-meshing approach is near automatic, and the whole process can be performed within ~15 minutes. All the meshes of human heads used in this work are generated based on this approach.

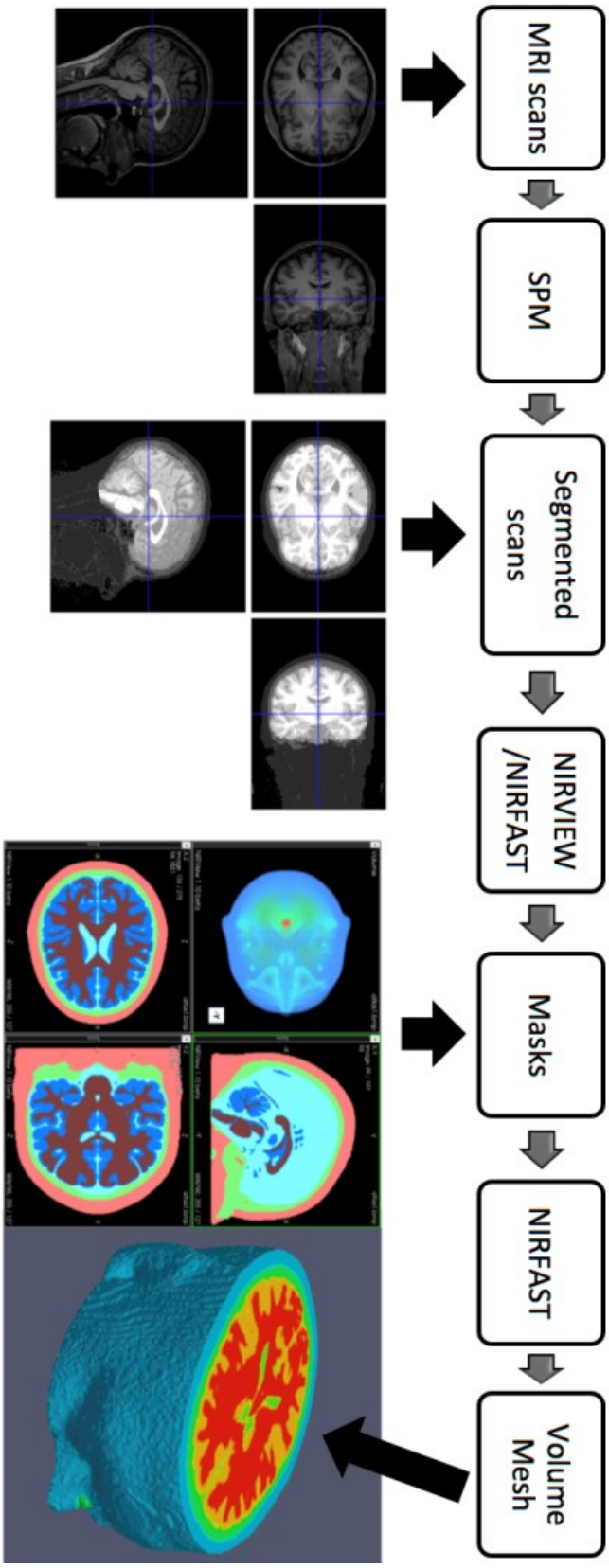

Figure 4.10. Workflow of the near automatic layered subject mesh generation approach.

4.4. Summary

DOT recovery of a human brain relies on a subject specific model with internal structural information. One of the main processes in the generation of the subject model is the segmentation of tissue regions based on head images. Segmentation methods for head MRIs are divided into three categories: intensity-based segmentation, registration-based segmentation and the combination of the first two approaches. They are evaluated based on the accuracy of the classification, whether additional information is required in the segmentation process and the process time (table 4.1).

Table 4.1: Summary of different segmentation methods

Segmentation methods	Advantages	Disadvantages	Examples
Intensity-based	• Can be processed fully automatically • Time efficient • Does not require any additional structural information.	• Possible errors in the classification of brain tissues from the non-brain soft tissue	• Threshold [190] • K-means cluster [191]
Registration-based	• Better segmentation accuracy • Can be processed automatically	• Requires additional brain atlas with internal structural information • Lacks the structural details specific to the target subject	• Segmentation based on rigid registration [201]
Intensity and registration-based	• Can achieve better segmentation accuracy • Contains structural detail specific to the target subject.	• Requires additional brain atlas with internal structural information	• SPM segmentation [208]

Results from the fully automatic segmentation approach in SPM contain some noise and errors. They may be caused be the image quality of the subject, structural inaccuracy of the atlas, differences in the structure between the atlas and the subject and errors in optimisation during the iteration process. Some of the noise and errors such as the noise in the background and the mislabelled single voxel in a tissue region may jeopardise the meshing process and they can be removed easily based on a manual correction. Therefore it is necessary to include the manual correction step in the segmentation approach.

A near automatic layered subject mesh generation process is designed based on the discussion above. This segmentation-meshing approach is built with SPM based segmentation including manual corrections and a Nirfast/Nirview based meshing process. The whole approach proves a subject mesh with acceptable accuracy within ~15 minutes.

The registration process is the main component in the atlas-based segmentation, and it is also used in generation of the forward model in the atlas-based DOT. Different registration methods for the human head are discussed in the following chapter.

CHAPTER 5: REGISTRATION METHOD FOR HUMAN HEAD MODEL

5.1. Introduction

Image registration of 3D subjects transforms one object (source object) to the best alignment with another object (reference object). It defines a 3D transformation *t(x)* at each position *x* of the source subject *Is* and transforms the source subject into the space of the reference subject *Ir* to generate a transformed source subject *Its=Is(x+t(x))*, so that the transformed source subject *Its* has the maximum similarity to the reference subject *Ir* [211]. In the past decades, 3D image registration has been applied to medical imaging for clinical and non-clinical application. The optimal choice of registration algorithm depends on whether the registration is inter/intra-subject, or inter/intra-modality.

Intra-subject registration in medical imaging aligns images of the same subject acquired at different times, with different subject status or by different imaging systems or imaging modalities. Intra-subject intra-modality registration aligns images of the same subject from the same imaging modality acquired at different times. In previous studies, functional activation in the human brain during stimulation or in the resting state is monitored based on registration of serial MRI scans of the same subject acquired at different times [13, 14]. Another application of this registration is in the identification of subtle pathological shape changes such as the development of a hematoma, a tumour or multiple sclerosis (MS) lesions [212]. It has been used to assist the diagnoses of some injuries and diseases and to assess and evaluate the treatments [129, 211, 213]. Intra-subject registration has also been applied to track organs or specific regions in an organ during movements, for example tracking the

position and shape of the human lung during breathing [214, 215] in order to guide treatments such as external beam radiotherapy for cancer [216].

Intra-subject inter-modality registration [217] aligns images of the same subject from different imaging modalities or different imaging system settings. This registration combines the information from different imaging modalities and provides the potential to obtain a more accurate structural and functional distribution of the subject. It has been applied to improve tissue classification of the subject based on characteristics of different image modalities. For example, the registration of CT and MR brain images has been applied to skull-base surgery [218, 219]. It integrates bone structures from CT images and soft tissue structures from MR images and tracks the location of soft tissue regions during the surgery based on CT scans and the registration between CT and MRI scans.

Inter-subject registration in medical imaging aligns images from different subjects or atlases for group studies and statistical analysis. Inter-subject intra-modality registration [220] aligns images of different subjects from the same imaging modality. It has been applied to study states of organs during physical activities such as cardiac motion during a heartbeat [221] and the position of joints during movements [222] and to identify differences in organ states for different subjects [223]. It is also used for investigation of the aging process in a healthy human such as the growth of children and young adult's brains [136]. Developments of some diseases such as Alzheimer's disease [19, 129] have also been analysed based on this registration method and it provides a better understanding of disease progression by reducing the influence of subject-specific anatomical structure. An average model for different organs, also known as an atlas, can be generated based on the registration of a group of subjects, and organ atlases for specific subject groups such as age-specific and disease-specific brain atlas

have been created [112, 116, 130]. Registration of a group of subjects is also an important process in the quantitative comparison between different subjects.

Inter-subject inter-modality registration [217, 224] aligns images of different subjects from different imaging modalities or different imaging system settings. This registration is normally divided into two steps: images of the same subject from different imaging modalities or different imaging system settings are registered together, and then the registered multi-modality images of different subjects are co-registered to a common space. Registration between functional and anatomical images from multiple subjects has contributed to relating structural regions with function regions in the human brain [225, 226]. Another application of this registration type is atlas-based segmentation [18]. The atlas is a set of average brain images that contain structural and functional information such as the tissue classification, region distribution, location of fiducial markers and specific structures such as specific sulci and gyri. Segmentation of tissue types or structural and functional regions and extraction of fiducial markers or specific structures can be generated based on a registration between the image of the target subject and the atlas and the distribution maps in the atlas such as tissue classification maps. This segmentation is one of most commonly used segmentation methods for tissue classification of the human brain. Further discussion is in the previous chapter.

An image registration process typically consists of three components: similarity measurement, transformation model, and optimization method [214]. The similarity measurement determines the geometry or image characteristics (such as image intensity) for analysing the similarity between the registered source subject and the reference subject. The transformation model specifies transformation parameters for the alignment of the source subject into the space of the reference subject. The optimization method generates the optimal transformation parameters based on maximization of the similarity. Different registration

methods are generated based on different similarity measurements, transformation models, or optimization methods and discussed in the following part.

5.2. Similarity measurements

Since the purpose of image registration is to generate a transformed source subject which has the maximum similarity to the reference subject, the measurement of similarity is an important component in the registration process. The similarity measurements are divided into two categories: feature-based approaches and intensity-based approaches [227]. The feature-based approach, also known as geometry-based approach, generates similarity of the two subjects based on features of the subject such as anatomical landmarks and structures [228]. The intensity-based approach, also known as the image-based approach, generates similarity directly from the image intensity of the two subjects [229].

5.2.1 Feature-based similarity measurements

Feature-based similarity measurements calculate similarity between the two subjects based on a common set of anatomical elements. Based on different types of anatomical elements, measurements of similarity are divided into three main categories: landmark-based approaches, curve-based approaches and surface-based approaches. These elements are typically extracted from structurally or functionally important features to ensure transformation based on this similarity measurement has biological validity [214, 230].

5.2.1.1 Landmark-based similarity measurement

The landmark-based similarity measurement extracts fiducial markers from the source subject and the target subject and determines the corresponding relationship between the two landmark sets. Similarity of the two subjects is measured based on the distance between the

two landmark sets. An example of the landmark system is shown in Figure 5.1. The landmarks can be extracted from the subjects before the imaging process based on external adhesive fiducial markers or implantable fiducial markers. Landmarks from this extraction method are accurate and consistent across different imaging modalities. However, this procedure of extraction is sometimes highly invasive and using non-invasive landmarks attached to the subject surface is not always achievable in the clinical situation. Moreover, both external adhesive fiducial markers and implantable fiducial markers use a set of physical markers placed onto the subject which cannot be consistently applied in order to acquire images over extended periods of time, therefore this landmark extraction method has limited application in clinical use.

Imaging landmarks can also extracted from subject images based on anatomical information such as the prominences of the skull, and geometrical information such as the intensity distribution. Extraction of these landmarks can be processed manually or automatically. Manual extraction of the landmarks is based on anatomical and geometrical information about the subject. Although expert experience is not required for the extraction, it can improve the accuracy of the extraction. Manual extraction is a preferred approach for landmarks of the human brain [231, 232]. However it is more time consuming than the automatic process and it may contain some consistency issues in locating landmark systems across subjects. Semi-automatic extraction processes extract landmarks based on a few manually extracted landmarks and landmarks extracted automatically are generated based on spatial or geometrical patterns of the landmark system.

EEG 10/20 landmark systems are a set of the most common landmark systems for registration of the human head [159, 233]. The electroencephalography (EEG) 10/20 system describes the location of scalp electrodes in an EEG test. This system is based on distances

between adjacent electrodes and distances between electrodes and the basic anatomical landmarks. The four basic anatomical landmarks from the four landmarks system above are used for the essential positioning of the EEG 10/20 system. Other landmarks are then extracted from the surface of the head based on the distance from the four anatomical landmarks and the landmarks that have been extracted. For example, the landmark near the left ear is extracted from the midline of the head determined by the two temple anatomical landmarks. The distance from this landmark to the left temple along the midline is 10% of the total distance between two temples. Using the same methods, landmark sets of different density can be extract from the surface. Number of landmarks from the EEG 10/20 systems vary from nineteen to over a hundred. In this work, EEG 10/20 systems with 19 landmarks and 40 landmarks are used for the registration.

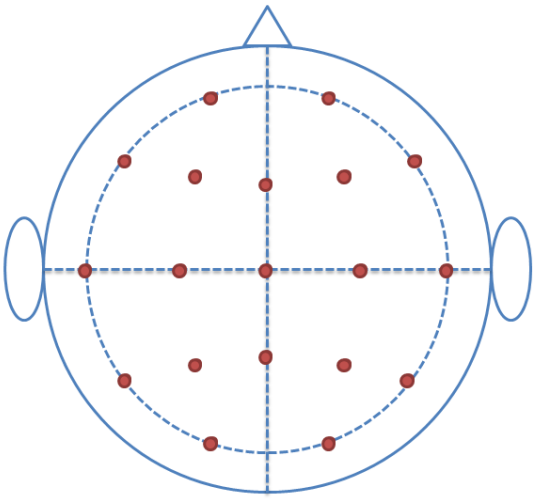

Figure 5.1. EEG 10/20 landmark system. (Top view) Red points are the landmarks, and blue dotted line are the auxiliary line in the EEG 10/20 system.

Landmark extraction can also be processed fully automatically based on pattern recognition of anatomical structures such as aortic and major veins [22]. However, it is not always achievable for inter-modality registration and it is extremely time consuming for a dense landmark systems [234].

Since the landmark-based similarity measurements only enquiries the spatial information of the fiducial points instead of the whole subject, and it can be applied to noisy data [235]. For the registration of 3D subjects, at least three pairs of corresponding landmarks are required to extract from the two subjects. Registration based on a dense landmark system has the potential to achieve higher registration accuracy than registration based on a sparse landmark system. However, increasing the number of landmarks leads to a more time and computationally consuming registration process. All three categories of feature-based similarity measurements rely on corresponding features from the source subject and the reference subject. However, this corresponding relationship is not always available in inter-subject registration and inter-modality registration, or even for the same subject with the same imaging modality. For example, the corresponding relationship is not always available when monitoring the development of a disease or analysing the growth of organs in infants. Another issue for feature-based similarity measurements is accuracy of similarity. Transformation of the source subject can achieve a maximized feature-based similarity, but still contains major errors such as folding or tearing in the areas away from the feature [214].

5.2.1.2 Curve-based similarity measurement

A curve-based similarity measurement is similar to a landmark-based approach. It extracts the same set of curves of anatomical structures such as gyrus and sulci in the human brain (figure 5.2) from images of the two subjects [22, 211], and the similarity is measured based on the corresponding curves from the source subject and the reference subject. An example of the curve system is shown in Figure 5.3. Similarity measurements based on landmarks and curves are both relatively computationally efficient and curve-based similarity measurements involve more anatomical information in the registration process than the landmark based approach. However, a dense curve system can be hard to generate, especially for inter-

modality registration, as not all anatomical structures are distinguishable in all imaging modalities.

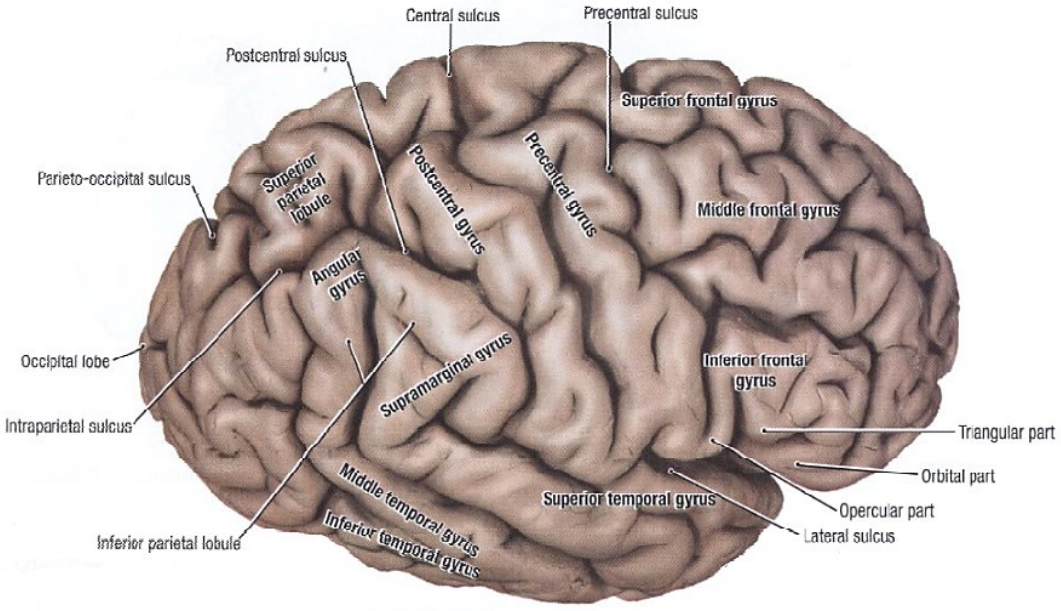

Figure 5.2. illustration on the four division lobes and their associated gyri [25].

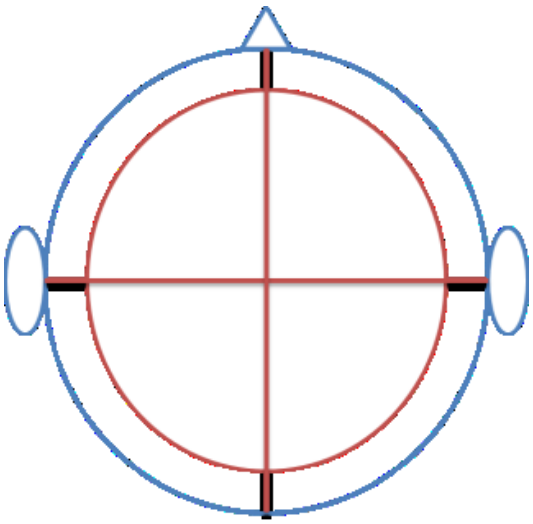

Figure 5.3. A curve system of the human brain consisting of three external curves. (Top view) The red lines are the curves.

5.2.1.3 Surface-based similarity measurement

The surface-based similarity measurement extracts the surface of the target organs or the surfaces of anatomical structures such as the ventricle or the cerebral cortex in the region of interest, and measures the similarity for the registration based on the corresponding surfaces. Normally, the surfaces are represented by a set of dense surface points from contours of the subject organs or anatomical structures. Surface points in the two subjects do not necessarily have one-to-one corresponding relationships as in the landmark-based approach and the curve-based approach. Since surface-based registration contains a large number of points compared to other feature-based approaches, it is more computationally expensive and may find a local minimum in the optimization. A two-step-registration approach is designed for the surface-based registration. Firstly, a coarse surface point system is created and registration between the two subjects is processed based on the coarse surface point system. The source subject and its surface landmarks are transformed based on the registration result. Secondly, the transformed subject is then registered to the reference subject based on the transformed dense surface points system. Surface-based methods have been proved to give good accuracy in the regions near the boundary, but are less accurate in the deeper regions because of lack of internal information [228, 236, 237].

5.2.2 Intensity-based similarity measurement

The intensity-based similarity measurement uses the subject images directly and measures the similarity based on intensity similarity of the whole image. Since an intensity-based similarity measurement involves intensity information from the whole subject, it keeps the maximum amount of information and tends to be more computationally expensive than the feature-based approaches. It is a fully automatic process which does not require any feature

extraction. For inter-modality registration, intensity-based registration [238] can be processed in two steps: firstly, images from all image modalities are transformed to simulate a common image modality based on anatomical structural information; Secondly, simulated images are registered based on the image intensity, and the original images are transformed based on the registration result.

5.3. Transformation models

The transformation model defines the deformation of the source subject into the space of the reference subjects and transformation parameters are generated based on an optimization process. Transformation models of 3D subjects are classified into two categories: rigid transformation and non-rigid transformation models [239]. Rigid transformation considers the source subject and reference subject as rigid objects with similar internal structure and the transformation is processed globally. Non-rigid transformation is applied when the internal structure varies between the two subjects and the transformation is processed both globally and locally [240].

5.3.1 Rigid transformation

Rigid transformation considers the subject as a rigid object and performs a whole subject alignment based on nine transformation parameters (three translation parameters, three rotation parameters, and three scaling parameters). Affine transformation is similar to the rigid transformation with three additional shear parameters. Since rigid transformation is not sufficient to register localized changes, it is normally applied to intra-subject registration or subjects with similar internal structure. However, rigid transformation is not ideal for intra-subject registration with major structural abnormalities such as swelling and bone fractures.

This transformation is usually applied to feature-based similarity measurements and it is a time efficient approach with processing time between a few seconds and a few minutes [214].

5.3.2 Non-rigid transformation

Non-rigid transformation aligns the source subject using both global transformation and localized transformation. It is used when the two subjects contain some localized structure differences. This transformation is applied to both feature-based similarity measurements and intensity-based similarity measurements [214, 241].

Different non-rigid transformation models are selected based on tissue characteristics or simulation measurements. For example, a thin plate spline model is applied to a landmark-based approach [242]. One of the mostly commonly used non-rigid transformation models is the spline-based transformation models [243]. It is a control point-based transformation and it is generated based on the physical bending energy field simulated by a thin metal plate placed under the control points. For a "thin-plate" spline, all the landmarks have influences on the global transformation. For B-splines, each landmark only affects its local region. It is considered a non-rigid transformation with "local support" [214].

Some non-rigid transformation models are designed to mimic the state of the subject tissue. The elastic model considers the subject as a linear, elastic solid under a force from image similarity measurements [244, 245]. The fluid model considers the object as a continuous fluid and allows highly localized transformation [244, 246]. Different transformation models can be applied to the same subject simultaneously. For example, in some registration of a human head, soft tissue such as brain tissue is considered as an elastic model, bone as a rigid model and cerebrospinal fluid (CSF) as a fluid model [214, 247].

Non-rigid transformation can take up to several hours to generate and it is usually more time consuming than rigid transformation [214, 248]. Also, an optimization result of a non-rigid transformation may contains errors from local minimization [231]. A modified non-rigid transformation approach is designed by using a rigid transformation as the initial alignment and then the non-rigid transformation is processed based on the registration result from the rigid registration. It has proved to be more efficient than the non-rigid transformation approach without initial alignment in some circumstances [249, 250].

5.3.3 Interpolations

One of the main applications of registration is quantitative comparison between the two objects, and it requires image data of the two subjects presented with the same image resolution or the same image points, therefore interpolation is a necessary step in some of the registration process.

Three of the most commonly used interpolation methods are presented in this chapter. The nearest neighbour interpolation is the simplest interpolation approach [251]. It determines the value of an image point/voxel by its nearest image point/voxel. This is the most time efficient approach and the original image value is preserved during the process, however it may reduce the image resolution. Another commonly used interpolation approach is tri-linear interpolation [252]. It is generated by a series of linear interpolations in three dimensions and the value of an image point/voxel is determined by sum of the image values of its surrounding points/voxels weighted by the linear distance. This approach is computationally inexpensive and provides higher accuracy than the nearest neighbour approach, but it still reduces the image quality during the process [251]. Sinc Interpolation [253] is similar to the tri-linear approach but it determined the image value by summing the image values of its surrounding

points/voxels weighted by the sinc function. Sinc interpolation can resample the image data with few errors introduced during the process [212].

5.4. Optimization

Image registration is aimed at finding the optimal transformation to achieve the maximum similarity of two subjects. The maximum similarity of two subjects is achieved by minimize the difference between the two subjects. For the source subject *Is*, reference subject *Ir* at a set of points *x* and its transform *t*, the difference between two subject is defined as *F(Ir, Is)* and the cost of the transformation is defined as *G(t(Φ))*. The generation of transformation parameter *Φ* is based on the minimization of the following function [254]:

$$\Phi_{\text{opt}} = \text{argmin}\big(F(I_r(x), I_s\big(t(x, \Phi)\big) + G(t(\Phi)\big) \tag{5.1}$$

Without considering the cost of transformation, the optimization process becomes the maximization of the similarity.

Image registration can be processed fully manually by optimizing the transformed subject using visual alignment [255]. A user interface has been developed to provide visual feedback during the registration. The user registers the images by adjusting (translating and rotating) the source subject to fit the reference subject. This adjustment is processed iteratively on each individual slice until a good visual alignment is achieved. This registration relies purely on the understanding of subject images from the user and is extremely time consuming. Therefore fully manual registration is not ideal for 3D image registration. An optimization method for semi-automatic and automatic registration is discussed in the following part.

5.4.1 Optimization for feature based similarity measurement

The feature-based similarity measurement is generated based on distance between the two feature sets from the source subject and the reference subject. Distance between curve sets and surface sets can be generated based on different methods such as the closest point distance and the Euclidean distances [256].

The iterative Closest Point algorithm (ICP) [257] is widely used among the feature-based registration methods. It optimizes the transformation parameter by minimizing the distance between the landmark from the source subject and its closest landmark from the reference subject. Since this method does not require a one-to-one corresponding relationship between landmarks, it can be applied to surface-based registration [231]. Other optimization methods can also be applied to feature-based similarity measurements, such as the Downhill Simplex Method (DSM) [240, 258], which is a gradient based local optimization method, and Genetic Algorithms (GAs) [240, 259], which are a gradient based global optimization method

Feature-based similarity measurements used with a non-rigid registration algorithm may have issues with the physical validity of the registration results. Continuity of subject between features is not included in the similarity measurement, which can lead to folding or tearing in the transformed subject [254, 260]. However, continuity is not always achievable for a physically valid registration such as an inter-subject brain registration between a healthy subject and a subject with a large extrinsic tumour.

5.4.2 Optimization for intensity based similarity measurement

Many optimization methods have been applied to the intensity based similarity measurements. The simplest method is based on measuring similarity by the sum of the squared differences (SSD) [214, 261] of image intensity in each voxel.

$$SSD = \frac{1}{N}\sum_N (I_r(x) - I_s(t(x)))^2 \quad (5.2)$$

Where *SSD* is the similarity measurement based on SSD, $I_r(x)$ is the image intensity at location *x*. $I_s(t(x))$ is the corresponding image intensity of the transformed source image based on transformation *t, N* is the number of voxels in the ROI.

The correlation coefficient [214, 262] also measures similarity based on corresponding voxels and it assumes that there is a linear relationship between similarity and corresponding intensities [Equation 5.3]. These two similarity measures are suitable for intra-modality registration.

$$\mathrm{CC} = \frac{\sum_N (I_r(x) - \bar{I_r}) \cdot \sum_N (I_s(t(x)) - \bar{I_s})}{\sqrt{\sum_N (I_r(x) - \bar{I_r})^2 \cdot \sum_N (I_s(t(x)) - \bar{I_s})^2 \cdot}} \quad (5.3)$$

Where *CC* is the similarity measurement based on the correlation coefficient.

Since image intensity patterns vary in inter-modality registration, there is not a linear relationship between similarity and corresponding intensities and the similarity measurement cannot be generated based on the image intensity directly. Other measurements such as mutual information (MI) [214, 263] measurement have been applied to inter-modality registration. Mutual information is an information-theoretic measure, which assumes there is a probabilistic relationship instead of linear relationship between similarity and corresponding intensities.

$$MI = H_r + H_s - H_{rs} \quad (5.4)$$

where $H_r = -\sum_i P_i log\, P_i$, $H_s = -\sum_j P_j log\, P_j$, $H_{rs} = -\sum_{ij} P_{ij} log\, P_{ji}$, P_i is probability of intensity *I* occurring in source or reference subject.

Intensity-based image registration is more computationally expensive than feature-based registration. Non-rigid Intensity based image registration suffers from inaccurate results because of local minimum issues. For intensity-based image registration of the human brain, the registration accuracy may decrease when the two subjects are misaligned by over 45 degree rotation and over 20mm translation before registration [212]. Pre-registration alignment based on features can improve intensity based registration. The feature-intensity based registration process is divided into two steps: first, the source subject is aligned with the reference subject based on feature-based rigid registration. Second, the aligned source subject is registered with the reference subject based on intensity based non-rigid registration [249, 250].

5.5. Evaluation of the registration methods

The registration method is normally evaluated based on the similarity measurements in the optimization process. However, it may not fully represent the accuracy of the registration because of the inverse crime (in this case, using the same set of parameters to calculate and evaluate the registration result). Moreover, folding and tearing errors as discussed above are not analysed within these evaluation criteria. The most accurate evaluation method is designed based on a set of test subjects for which the transformation is known [214, 264]. The registration methods are evaluated by comparison with the standard registration. However, evaluation requires a set of test subjects which are not always available. Another evaluation method is created based on the similarity measurements from different registration methods, for example, an intensity based registration is evaluated by the distances between a set of curves from anatomical structures such as gyri and sulci [22, 265]. This method requires accurate extraction of subject features.

In this work, the main application of 3D registration is to register brain tissue maps from an average template (atlas) to the subject space. Since the internal structure of the subject is not available in the atlas-based DOT recovery and extraction of the whole head surface requires additional image system, feature-based registration, specifically external-landmark based registration is used for atlas based DOT imaging. Although there are some non-rigid regions in the human head such as skin and muscles, since landmark-based non-rigid registration of different subjects only provides high accuracy in the area around landmarks, it cannot provide good accuracy in the cortex region based on external-landmark. Rigid registration is applied to brain images. Therefore, external-landmark based rigid registration is used for registration in atlas-based DOT brain imaging in this work. This rigid registration is evaluated based on the similarity measurement of another registration method such as the surface based registration. Three surface-based evaluation methods are designed for this registration.

5.5.1 Surface-based evaluation methods

The accuracy of the landmark-based registration methods for a head model is evaluated based on surface error defined as the distance between the surfaces of the registered subject and reference models. Three evaluation methods are compared in this chapter.

5.5.1.1 Corresponding-node evaluation method

The Corresponding-Node evaluation method [261, 265] is the most accurate evaluation method based on surface nodes and the evaluation method calculates the surface error based on the distances between each corresponding surface nodes pair of the registered and reference models [Figure 5.4]. This method calculates the distance of each nodes pair accurately but it requires a node to node correspondence between every node on the surfaces

of the two models. Surface error parameter *E* is defined as the average surface distance between the two models and is calculated by the average distance between the pairs of corresponding nodes using:

$$E = \frac{1}{n}\sum_{i=1}^{n} ||Sub_i - Ref_i|| \quad (5.5)$$

Where *E* is the surface error parameter, Sub_i is the surface node of the registered subject model, Ref_i is its corresponding nodes from the reference surface, and *n* is the number of surface nodes pair.

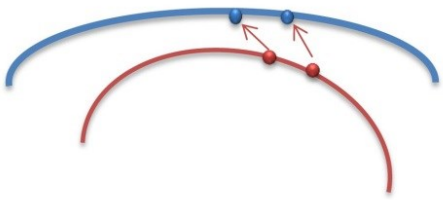

Figure 5.4. Schematic diagram of the correspond relationship in Corresponding-Node evaluation method. Blue line: Surface of the reference subject. Blue points: Surface nodes of the reference subject. Red line: Surface of the registered subject. Red point: Surface nodes of the registered subject.

5.5.1.2 Closest Nodes evaluation method

The Corresponding-Node evaluation method requires a node to node correspondence between every pair of nodes on the surfaces of the two models, which is not always available especial for inter-subject registration. The Closest-Nodes [257, 266] evaluation method is an acceptable alternative to the corresponding-node evaluation method. The surface error parameter *E* is defined as the average surface distance between the two models in this method. It is calculated by average of the distance between each node on the surface of the registered model and its closest node on the surface of reference model [Figure 5.5] using:

$$E = \frac{1}{n}\sum_{i=1}^{n} ||Sub_i - Ref_{ci}|| \quad (5.6)$$

where E is the surface error parameter, Sub_i is surface node of the registered subject model, Ref_i is its closest nodes from the reference surface and n is the number of surface nodes.

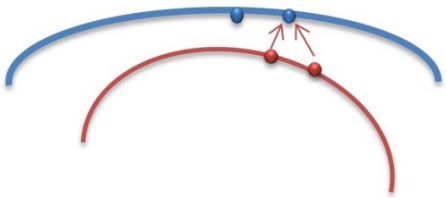

Figure 5.5. Schematic diagram of the correspond relationship in the Closest-Node evaluation method. Legend is the same as Figure 5.4.

Although the Closest-Node evaluation method has lower accuracy than the Corresponding-Node evaluation method, it does not require node to node correspondence between every pair of nodes, therefore it has a wider application.

5.5.1.3 Hausdorff distance evaluation method

The Hausdorff distance [267, 268] evaluation method is one of the most commonly used evaluation methods based on surface points and it defines the surface error as the Hausdorff distance between the surfaces of the registered subject and reference models [Figure 5.6]. The Hausdorff distance between the two curves is defined by their longest distance. The Hausdorff distance between curve A and curve B is represented in the following equation;

$$d_H(A,B) = \max(sup_{a\in A} \inf_{b\in B} d(a,b), sup_{b\in B} \inf_{a\in A} d(a,b)) \quad (5.7)$$

where $d_H(A,B)$ is the Hausdorff distance between curve A and curve B, a is the node from curve A, b is the node from curve B.

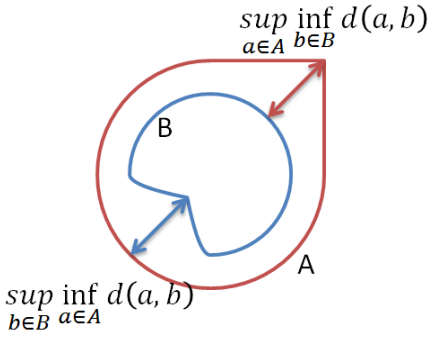

Figure 5.6. Hausdorff distance between curve A and curve B.

In this example, a uniform grid with 400 nodes is plotted on the surfaces of the two models and surface points are based on this grid. The Hausdorff distance between the two surfaces is generated and applied for the evaluation of the registration result.

5.5.2. Comparison between the three evaluation methods

Examples of three evaluation methods are presented based on one testing subject and three feature-based registration methods. The testing subject contains a point cloud of the head surface with ~4000 nodes, and a reference subject which is generated based on a random transformation of the testing subject. Registration between the two subjects is based on three feature-based rigid registration methods: basic-4-landmark based non-iterative point to point registration, EEG 10/20 system landmark based non-iterative point to point registration, and 3-curve based registration [Figure 5.7].

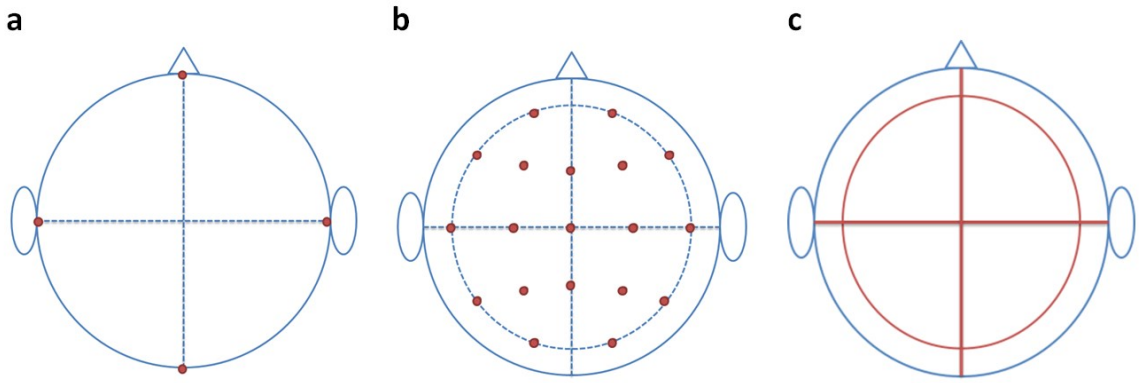

Figure 5.7. Three feature-based registration methods: a.basic-4-landmark based registration, b.EEG 10/20 system landmark based registration, and c.3 curve based registration.

The distance between each surface node in the reference subject and registered subject are presented in Figure 5.8. Basic-4-landmark based registration has the highest surface distance among the three registration methods based on both Corresponding-Node evaluation and Closest-Node evaluation and the EEG 10/20 system landmark-based registration method has the lowest node distance based on both evaluation methods. Although Closest-Node evaluation has a lower surface distance in some regions than Corresponding-Node evaluation for basic-4-landmark registration, Corresponding-Node distance and Closest-Node distance have similar distributions for all three registration methods.

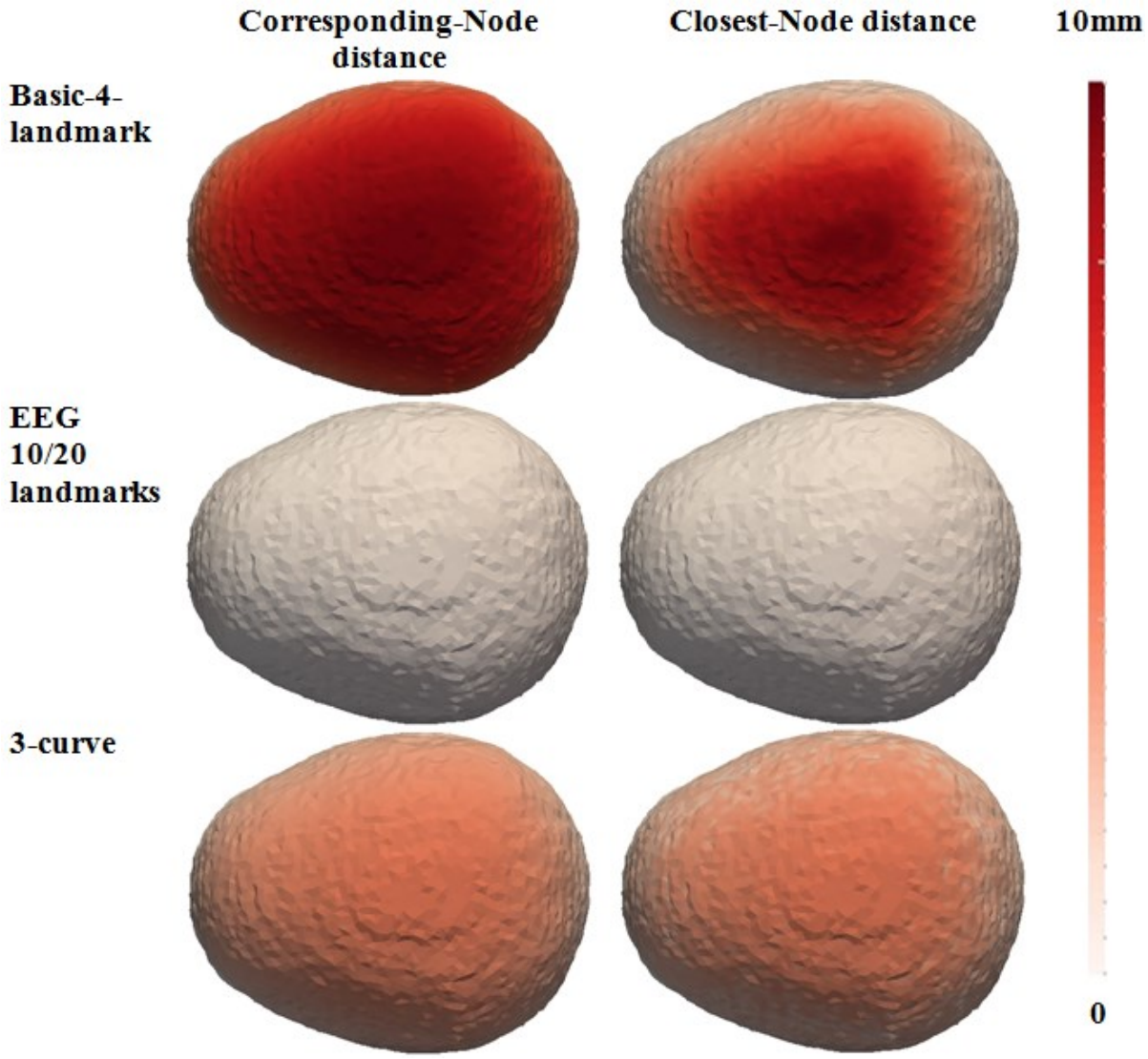

Figure 5.8. Corresponding-Node distance and Closest-Node distance based on result from three feature-based registration method: basic-4-landmark based registration, EEG 10/20 system landmark based registration, and 3-curve based registration.

The average surface error of the three evaluation methods for the three registration methods are shown in table 5.1 and Figure 5.9. Based on the Corresponding-Node evaluation method, Average surface errors of all three registration methods are lower than 5 mm. The basic-4 landmark registration method with a 4.6 mm surface error is considered the least accurate registration method, and the EEG 10/20 system landmark registration method with a 0.3 mm surface error is considered the most accurate registration method. The Closest-Node evaluation method shows consistent results with the Corresponding-Node evaluation method.

Based on the Closest-Node evaluation methods, the surface errors of all three registration methods are lower than 3 mm. The basic-4 landmark registration method with a 2.9 mm surface error is considered the least accurate registration method, and the EEG 10/20 system landmark registration method with a 0.3 mm surface error is considered the most accurate registration method. The Hausdorff distance evaluation method shows result consistent with the Corresponding-Node evaluation and Closest-Node evaluation methods. Based on the Hausdorff distance evaluation methods, the surface errors of all three registration methods are lower than 6.5 mm. The basic-4 landmark registration method with a 6.2 mm surface error is considered the least accurate registration method, and the EEG 10/20 system landmark registration method with a 0.6 mm surface error is considered the most accurate registration method.

Table 5.1. Quantitative evaluation of the three evaluation methods for the three registration methods.

Whole surface average	Hausdorff distance/mm	Corresponding-Node distance/mm	Closest-Node distance/mm
Basic-4-landmark	6.22	4.61	2.92
EEG 10/20 landmarks	0.55	0.28	0.28
3-Line-fitting	3.56	2.18	2.04

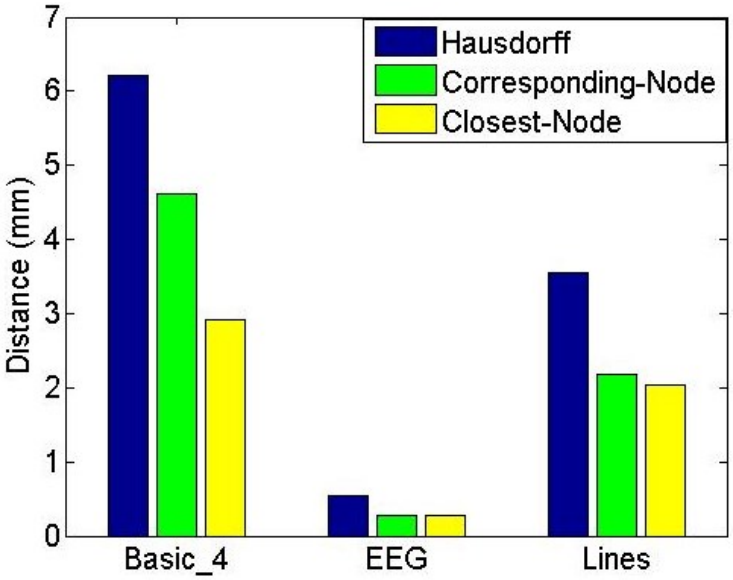

Figure 5.9. Quantitative evaluation of the three evaluation methods for the three registration methods.

Similar comparison of the three evaluation methods is also processed based on five subjects and 11 registration methods. For each subject, five different random affine deformed meshes are generated and used as testing data. Each deformed mesh is registered to its reference mesh based on the corresponding nodes of the head surfaces. 11 registration methods (basic-4-landmark Non-iterative Point to Point registration, EEG 19 landmark based registration with iterative Point to Point algorithm (P2P), EEG 19 landmark based registration with Non-iterative Point to Point algorithm (NP2P), EEG 19 landmark based registration with Iterative Closest Point algorithm (ICP), EEG 40 landmark based P2P registration, EEG 40 landmark based NP2P registration, EEG 40 landmark based ICP registration, Full-head landmark based P2P registration, Full-head landmark based NP2P registration, Full-head landmark based ICP registration, and 4-curve based registration) are used in this experiment and described in detail in the next chapter. The errors are calculated based on result of the 11 registration methods using the three evaluation methods outlined above. Average surface error is generated based on the surface error from the five mesh set for evaluation and comparison. The results of the evaluation are shown in Figure 5.10.

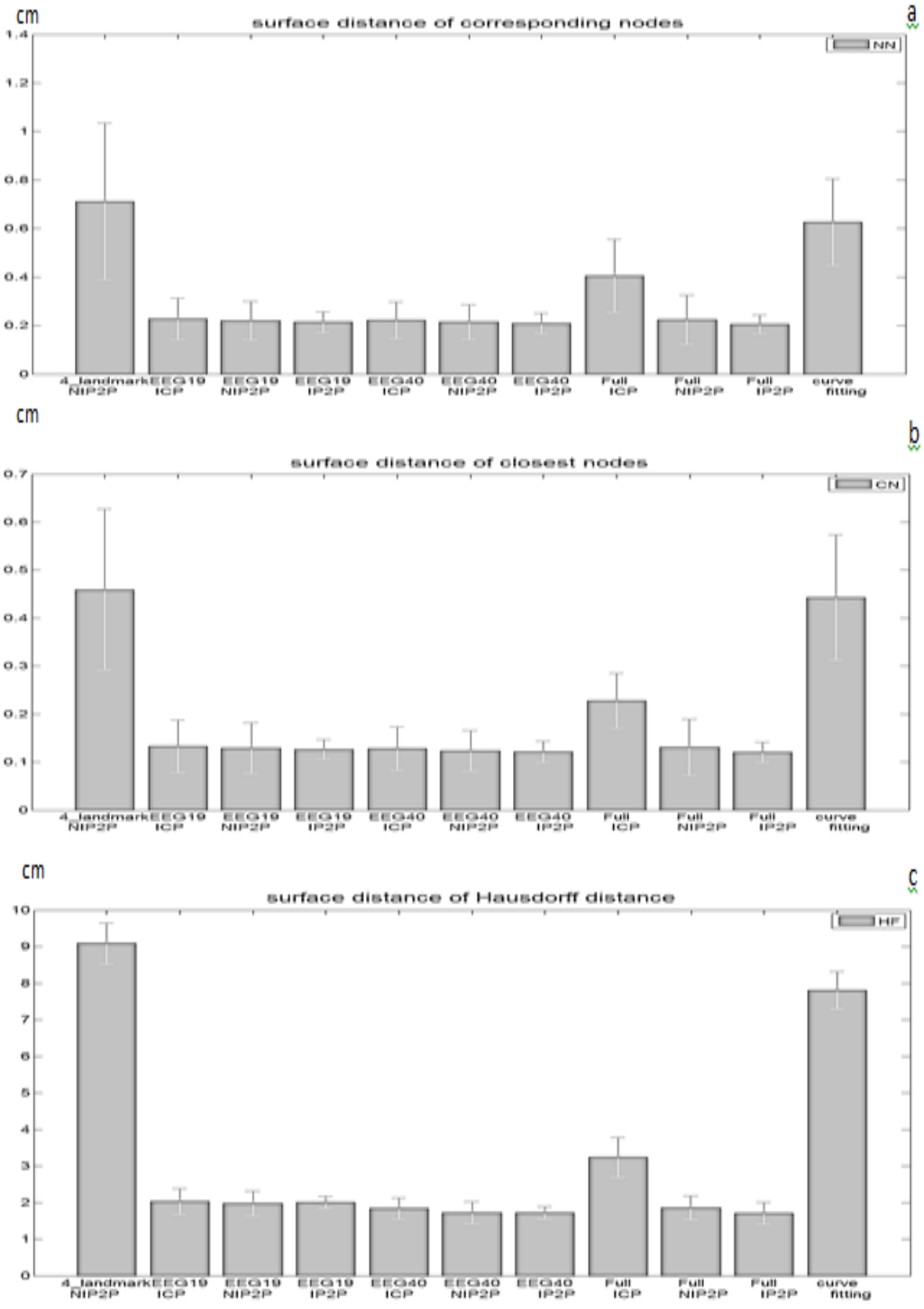

Figure 5.10. three quantitative evaluation of the 11 registration methods

Based on Corresponding-Node evaluation methods (Figure 5.10.a), surface errors of all 11 registration method are lower than 8mm. The four landmark registration method with a 7mm surface error is found to be the least accurate registration method, and the whole head

landmark system with P2P algorithm with a 2mm surface error is found to be the most accurate registration method. The surface errors of the whole landmark system with ICP algorithm and Curve Fitting registration are higher than 4mm. The other seven registration methods have similar surface errors of approximately 2.5mm.

Evaluation using the Closest-Node evaluation method (Figure 5.10.b) shows consistent results with Corresponding-Node method. Based on Closest-Node evaluation methods, surface errors of all 11 registration method are lower than 5mm. The four landmark registration method with a 4.6mm surface error is found to be the least accurate registration method, and the whole head landmark system with P2P algorithm with a 1.2 mm surface error is found to be the most accurate registration method.

The Hausdorff distance evaluation (Figure 5.10.c), method shows consistent result with Closest-Node and Corresponding-Node method. Based on Hausdorff distance evaluation methods, surface errors of all 11 registration method are lower than 10cm. The four landmark registration method with a 9cm surface error is found to be the least accurate registration method, and the whole head landmark system with P2P algorithm with a 2cm surface error is found to be the most accurate registration method.

In this study, there is a node to node correspondence between the testing subject and the reference subject, and the corresponding nodes evaluation is the most accurate. However this correspondence normally is not available especially for the registration in atlas-based DOT recovery. Since the three evaluation methods above provide similar results. The Closest-Node evaluation is an acceptable alternative of the Corresponding-Nodes evaluation method. All the geometrical error evaluation in this work is based on Closest-Node evaluation.

5.6. Summary

Image registration of 3D subjects transforms the source subject to constitute the maximum similarity to the reference subject. An image registration process typically consists of three components: a similarity measurement, a transformation model, and an optimization method. Registration methods are categorised based on the similarity measurement and the transformation model (table 5.2), and the optimization method is determined based on these two components.

Table 5.2: Summary of different registration methods

Category	Type of registration		Advantages	Disadvantages
Similarity measurements	Feature-based	Landmark-based	• Most robust to image noise • Can be applied to inter-modality registration	• Difficult to maintain consistency of the landmark location among different subjects and image modalities
		Curve-based	• Involves more anatomical information during the registration than the landmark-based approach • Can achieve better accuracy	• Difficult to maintain consistency of curves among different subjects
		Surface-based	• Surfaces are easier to extract than landmarks and curves which can be extracted automatically	• More computationally expensive

	Intensity-based		• Does not require the correspondence of image features between source and reference subjects • Can be processed automatically	• Less accurate and more computationally expensive
Transformation model	Rigid		• Time efficient	• Usually only applied to feature-based similarity measurements • Not ideal for non-rigid regions
	Non-rigid		• Can be applied to both similarity measurement • Can be used in inter-subject registration	• Not ideal for rigid regions • Time consuming

The optimal registration method varies for specific problems and is selected based on the registered objects. Registration between objects with large differences such as registration of images from different subjects or different imaging modalities, typically requires a computationally expensive registration method such as registration based on dense landmark system. Although registration methods can be evaluated based on the optimization result, the most accurate evaluation method is designed based on a set of test subjects for which the transformation is known. Normally, the evaluation is generated based on the similarity measurements associated with the different registration methods. For example, landmark-based registrations of head models are evaluated based on surface distance. Three evaluation methods based on surface distance: namely Corresponding-Node, Closest-Nodes and the Hausdorff distance evaluation methods are compared in this chapter based on 11 registration

methods of five subjects. Although the Corresponding-Node evaluation method is the most accurate method, it provides similar results to the other two methods. Therefore, the Closest-Node evaluation is an acceptable alternative if the corresponding nodes evaluation method is not available.

The registration in atlas-based DOT is between an atlas and the subject surface. Since the internal structure of the subject is not available and extraction of the whole head surface requires additional image system, external-landmark is used as the similarity measurement in the registration. Since brain image recovery is focused on the cortex region and external-landmark based non-rigid registration has low accuracy in the internal region, rigid registration is used as the transformation model. Therefore, external-landmark based rigid registration is used for registration in atlas-based DOT brain imaging in this work. All the geometrical accuracy of this registration is evaluation by the Closest-Node evaluation.

Registration between an atlas and the subject is the main process in the generation of forward model in atlas-based DOT. Quantitative evaluation of 11 registration methods based on geometrical accuracy of the registration result, accuracy of light propagation and recovery accuracy of brain activations is presented in the following chapter.

CHAPTER 6: QUANTITATIVE EVALUATION OF ATLAS-BASED DOT FOR IMAGING OF THE HUMAN VISUAL CORTEX

6.1. Introduction

Diffuse optical tomography (DOT) as described in chapter 2 is a functional imaging modality [269]. It has been applied to imaging functional activations in the adult brain [4, 14, 23] and neonatal brain [3, 17, 92]. For adult subjects, fMRI as described in chapter 2 is one of the most commonly used hemodynamic-based neuroimaging modality, and it suffers from relative high cost, fixed scanner locations and physical constraints during imaging which limit its translation as a bedside clinical tool [66]. DOT has shown a strong potential in clinical application specifically for neonate and long-term bedridden patients [1] .

In the recovery process of brain activations using DOT, it is important that the forward model accurately represents the subject being imaged as the propagation of light within tissue is a non-linear function of both shape, size and internal structure and (often assumed) underlying optical properties. Where available, the forward model is generated based on a subject-specific anatomical head model from other imaging modalities such as structural MRI [6, 177]. When subject-specific models are not available, a registered (atlas based) anatomical head model can be used as an alternative [9-11]. The ICBM152 atlas is used to provide internal structural information as well as an approximation of the external head shape in this work.

Registration between the atlas and the subject being imaged is one of the main steps in atlas-based DOT of the human brain and therefore the evaluation of the accuracy of the

registration methods themselves has been of great importance. Different registration methods are described in chapter 5. In previous studies (table 6.1), a surface based rigid registration method for human brain has been utilised by Huppertz et al [256] for EEG and MRI data by matching the surface from a 3D scanning device to the surface extracted from MRI images. Using this method the average error was found to be 0.3 mm based on the location error of fiducial points of the head surface, namely, the location of electrodes in EEG system. The size and distribution of fiducial points used for registration is also an important aspect which was investigated by West et al. which focused on fiducial point-based registration for cranial neurosurgery [270]. This study showed that the landmarks must be narrower than 4 mm to get a registration with an acceptable error while increasing the number of fiducial points and avoiding near-collinear configurations also improved the registration accuracy. Singh et al developed a fiducial point-based registration method that registered multichannel, multi-subject NIR data to the MNI space which used 19 fiducial points from EEG 10/20 landmark system and an iterative closest point algorithm for the optimization [159]. The accuracy of the method was evaluated by the closest surface points on the registered model and the atlas with the location error found to be within 4.7 to 7.0 mm.

Non-rigid registration is most commonly used to register subject-specific data to an average model or reference space such as MNI space for analysis. For example, Crum et al. divided the non-rigid registration into geometric approaches (registration methods based on anatomical information) and intensity approaches (registration methods based on intensity patterns) which demonstrated that combining geometric and intensity approaches is a more robust method for registration of human brain image [271]. There are a number of different toolboxes available publicly to allow non-rigid deformation and three of these were compared by Ardekania et al. using brain MRI scans [211]. The algorithms compared were the

Automatic Image Registration (AIR), the Statistical Parametric Mapping (SPM8), and the Automatic Registration Toolbox packages (ART). These comparisons showed that all algorithms provide accuracy within geometrical error of less than 2.0 mm. Klein et al. focused on the evaluation and comparison between 14 non-rigid and 1 rigid registration method based on calculated overlay between different brain regions from an average head and registered subject models from different subjects [22]. It was shown that non-rigid registration is more accurate providing an average accuracy of 75% in overlay. However, non-rigid methods often require both surface information and internal structure of the subject head, while rigid methods can be used when the internal information is not available, which is a common problem faced with atlas based image recovery in DOT.

Table 6.1: Summary of previous studies in registration of brain imaging

Category	Investigated registration method	Authors	Aim of the study
Rigid registration	Surface based	Huppertz et al [256]	Geometrical accuracy of the registration methods
	Fiducial point-based	West et al [270]	Locating the fiducial point
	Fiducial point-based	Singh et al [159]	Accuracy of the registration from subject-specific data to the MNI space
Non-rigid registration	Registration methods with geometric and intensity approaches	Crum et al [271]	Robustness of the registration method
	Registration methods from commonly used toolboxes (AIR,SPM,ART)	Ardekania et al [211]	Comparison of geometrical accuracy of the registration methods
	14 non-rigid and one rigid	Klein et al [22]	Comparison of geometrical accuracy of the registration methods

Previous studies in utilisation of atlas based DOT are focused on evaluation of the accuracy in reconstruction result directly (table 6.2）. In these studies, accuracy of the recovered images is evaluated by comparison between a reference and the atlas-based reconstruction with the evaluation criteria typically generated mostly based on the localization error or overlapping percentage of the two reconstructed areas. Custo et al. compared the DOT recovery of the same brain activation based on subject-specific models and the corresponding registered atlas [11]. The atlas was registered to each individual subject based on a rigid registration using fiducial points from EEG 10/20 system. 3 subjects were used in the study and the results from the subject and the registered atlas based model showed ~70% overlay. Cooper et al. also focused on comparison of DOT recovery using subject-specific and registered models using the same registration method as Custo et al. but using simulated data from 32 subjects [9]. Accuracy of the recovery result was evaluated based on mean Euclidean, mean geodesic and mean Hausdorff error. Localization error of atlas based DOT was approximately 18 mm in Euclidean space, and 9 mm for DOT with subject-specific model. Based on this study although the atlas based DOT demonstrated larger reconstruction errors, it was deemed as an acceptable alternative when subject-specific model is not available. Ferradal et al. used a similar landmark system after adjusting the fiducial location that concentrate on the region of interest being imaged (visual cortex) [10]. Subject specific and atlas based DOT with linear registration and a non-linear registration method based on a B-spline transformation were compared to fMRI data for comparisons using a group analysis. For the group analysis, each subject was registered to the standard atlas and the reconstructed activation was generated based on statistical tests. Atlas-based DOT had an average localization error of 2.7mm compared to subject-specific model, and 6.6mm to fMRI. Although all of these studies are focused on evaluation of the recovered activations (images)

from a ‘single’ registration method, they show that in their respective studies, the reconstructions based on an atlas model have acceptable accuracy using both simulated and experimental data and can be considered as an alternative when subject specific anatomical mesh is not available.

Table 6.2: Summary of previous studies in accuracy of DOT brain activation reconstruction

Author	Registration method	Utilized data	Aim of the study
Custo et al [11]	Fiducial points-based rigid	Brain activations measured by DOT and MRI	Accuracy of the DOT recovery based on comparison with MRI
Cooper et al [9]	Fiducial points-based rigid	Simulated brain activations measured by DOT and MRI	Accuracy of the DOT recovery based on comparison with simulated activation
Ferradal et al [10]	Fiducial points-based rigid and non-rigid	Brain activations measured by DOT and MRI	Comparison of the DOT recovery based on different registration methods

The previous works in atlas based DOT discussed above are focused on investigation and comparison of the registration method based on a ‘single’ fiducial points system in terms of geometrical error and/or the recovered activation. To date, the effect of registration algorithm or fiducial number and location on atlas-based DOT data quality have yet to be fully evaluated. As model-based image recovery in DOT relies on accurate models for light propagation, no work to date has investigated the effect of registration errors on consequent errors in the light model, which directly affects the parameter recovery accuracy. Optical properties of human head can be modelled with five major layers, skin, skull, bone, CSF, gray matter and white matter. In ‘rigid’ registration methods that rely only on external markers these layers are also rigidly transformed. It is therefore important to not only consider the external geometry error, but also the consequent error on the light model within the layered

tissues. In summary, atlas-based DOT can be divided into three steps: 1) registration between the atlas model and the subject, 2) generation of the light propagation model using the registered atlas, and 3) recovery of brain activations. All three steps are evaluated in the presented work.

Full-head anatomical 3D images from 24 subjects are used to evaluate the accuracy of three different rigid registration methods, each using a combination of ~5 different landmark system, giving rise to 11 different algorithms. The accuracy of each algorithm is investigated by evaluating the error of the light propagation model thereby considering the quality of not just the external registration, but also effects of registration of the internal structures. Finally to demonstrate the overall consequence on parameter recovery, each of the 11 algorithms are evaluated using simulated functional activation data from the visual cortex for all 24 subjects.

6.2. Methods

Image recovery in DOT using measured NIR data from a human subject involves data calibration (data-pre-processing) as well as model based image reconstruction. Data calibration is a critical aspect of image reconstruction regardless of the modelling method utilized and is covered in detail elsewhere [23]. Regardless of whether using subject specific or atlas-based models, the domain of interest needs to be segmented and meshed, which is achieved using NIRVIEW [109]. For model based image reconstruction, different models of light propagation in tissue can be utilized; in this work we use a finite element model (FEM) of the head using NIRFAST [68].

6.2.1 Subject specific models

Generation of subject specific models for image recovery can be summarized using the flowchart shown in Figure 4.10. Specifically, MRI data from a given subject is segmented by the SPM-based segmentation for chapter 4 section 4.2.3 [208, 272]. Segmented images of the five tissue types (skin, skull, CSF, gray and white matter) are generated, which is then used together with NIRVIEW and NIRFAST to create masks and layered volumetric FEM meshes. The optical properties used for each layer are typically accepted to be subject specific, but throughout this work, the values shown in Table 6.3 are used [6, 108, 273, 274].

Table 6.3. Head tissue optical properties at 750 nm

	μ_a (mm^{-1}) / μ'_s (mm^{-1}) / Refractive Index
Scalp	0.0170 / 0.74 / 1.33
Skull	0.0116 / 0.94 / 1.33
CSF	0.004 / 0.3 / 1.33
Gray Matter	0.0180 / 0.84 / 1.33
White Matter	0.0167 / 1.19 / 1.33

6.2.2 Atlas based models

Registration for DOT recovery using atlas based models can be summarized using the flowchart in Figure 6.1. Specifically, for atlas based DOT there are three major steps: 1) Registration of the atlas: affine transformation matrices are generated based on fiducial points extracted from surfaces of the atlas model and the subject head. These transformation matrices are then applied to the atlas model to generate the registered atlas based light model in the subject specific space. All transformed FEM models are then checked for consistency and accuracy using NIRFAST. 2) Generation of the forward model where NIR light

propagation through the domain is simulated based on the registered atlas model. The internal structures of the head are provided by the registered atlas, based entirely on registration of the external surface. 3) Recovering the activation maps: The model of light from step 2 is used to calculate the sensitivity matrix which is then used to calculate the optical property changes based on simulated (or measured) subject specific data.

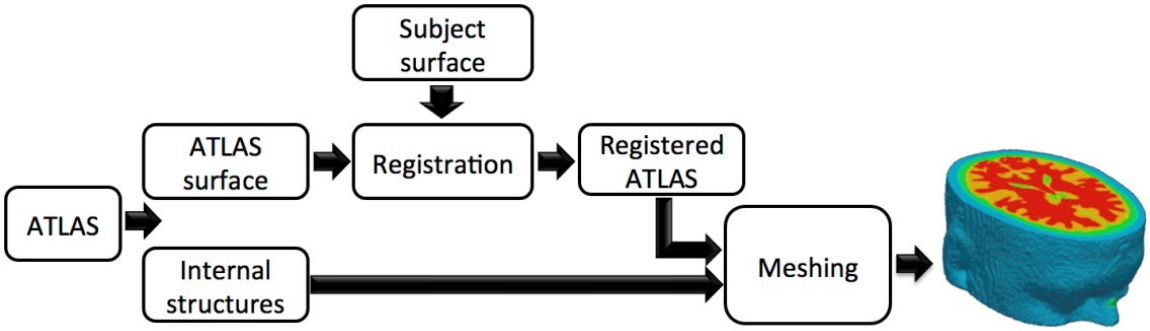

Figure 6.1.Workflow of creating atlas based models using registration methods.

6.2.2.1 Registration methods

Landmark-based registration is a common rigid registration method for the human heads. It can be used to generate an affine transformation matrix for the atlas model based on specific fiducial points as extracted from the atlas and subject head. There are two major steps in the registration process: 1) Fiducial points are extracted separately from surfaces of the atlas and subject head based on the same landmark system. 2) An affine transformation matrix is then generated and optimized by minimizing the distance between these two sets of landmarks. In order to provide a comprehensive comparison, 11 different rigid registration methods are studied and applied for the atlas based model for 24 subjects as summarized in Table 6.4 and Figure 6.2.

Table 6.4. Rigid registration methods as well as different types of landmark systems used.

Method	Basic 4	EEG 19	EEG 40	Full head	Line fitting
ICP		×	×	×	
IP2P		×	×	×	
NP2P	×	×	×	×	
Line fitting					×

6.2.2.2 Optimisation algorithms

The second step of the registration consists of the generation of the affine transformation matrix that is optimized based on an algorithm which minimizes the distance between landmark pairs from subject and atlas models. Three algorithms are used in this work: 1) iterative Point to Point algorithm (P2P), 2) Non-iterative Point to Point algorithm (NP2P), and 3) Iterative Closest Point algorithm (ICP).

In the P2P optimisation algorithm, there is a one-to-one corresponding relationship between landmarks from the subject and atlas model since the two landmarks sets are extracted based on the same landmark system. The P2P algorithm pairs corresponding landmarks from the subject and the atlas, and optimises the affine transformation matrix by minimizing the distance between the set of corresponding landmark pairs. The optimisation progresses iteratively through two steps:

1) Generation of an affine transformation matrix based on minimisation of the mean square error (MSE) between the paired landmarks:

$$T = arg_T min \sum_{i=1}^{n} \left\| T * Atlas_i - Sub_i \right\| \tag{6.1}$$

where T is the affine transformation matrix, n is number of pairs in the landmark system, $Atlas_i$ is a landmark from atlas model and Sub_i is the corresponding landmark of $Atlas_i$ from subject *i*.

2) Generation of the registered atlas model by applying the affine transformation matrix to the atlas and as well as the landmarks set:

$$Atlas_i^k = T_k Atlas_i^{k-1} \tag{6.2}$$

where $Atlas_i^k$ is the landmark from subject surface from iteration k and T_k is the corresponding affine transformation matrix. The registered model is then used as the atlas model in the next iteration. These processes are then repeated until the difference between iterative changes in the mean squared error is below some threshold.

The NP2P optimisation algorithm is similar to P2P except the two steps of optimisation are only processed once. Compared to the iterative process, the Non-iterative process has a shorter processing time.

The ICP optimisation algorithm is also similar to P2P except that a different pairing function is utilised [275]. Specifically, in the ICP algorithm the landmarks from the atlas model are paired with their closest landmarks from the subject, and the landmark pairs are reselected after each iteration based on their closest pairs.

6.2.2.3 Landmark systems

Four different landmark systems are investigated in this work. The first landmark system is basic-4 landmark system, Figure 6.2(a), which contains landmarks from four anatomically specified points: the nasion, which is the depressed area between the eyes and above the

bridge of the nose; the inion, which is the most prominent point at the back of the head; and the two temples which are the area on the scalp above the ears. These four landmarks can be easily extracted manually from surface of heads. Since there are only four fiducial points in this basic-4-landmark system, only the NP2P algorithm is applied to this system, as further iterations do not provide additional improvements.

Second and third landmark systems are EEG-19 and EEG-40 landmark systems Figure 6.2(b)&(c). They both extract landmarks based on the location of scalp electrodes as defined by the EEG10/20 landmark systems [210, 276, 277]. Landmarks locations in these systems are selected based on distances among adjacent landmarks as well as the distances between these and the four basic anatomical landmarks. These two landmark systems are similar except for the density of fiducial points. EEG-19 landmark system is an EEG10/20 landmark system with 19 fiducial points for each subject, and EEG-40 is an EEG10/20 landmark system with 40 fiducial points. All three optimization algorithms are applied to these two landmark systems.

The fourth landmark system is a full-head landmark, Figure 6.2(d), which places a high-density grid on the surface of the head based on the basic-4 landmarks and extracts landmarks uniformly from the grid, excluding facial features. This landmark system contains 700 fiducial points evenly distributed across the whole scalp covering the cerebral cortex. All three optimization algorithms are applied to this landmark system.

A line-fitting-based registration is also used, which generates and optimizes the affine transformation matrix by fitting curves extracted from the surface of the atlas model with those from the subject head surface Figure 6.2(e). Three surface curves are extracted based on the basic-4 landmarks system above and an affine transformation matrix is then optimised by

minimizing the differences on a set of discrete points along each of the lines, which is processed iteratively between two steps similar to that of P2P optimisation algorithm.

Based on these landmark systems and the optimization algorithm outlined above, a comprehensive set of 11 different registration methods, Table 6.4, are evaluated in this work.

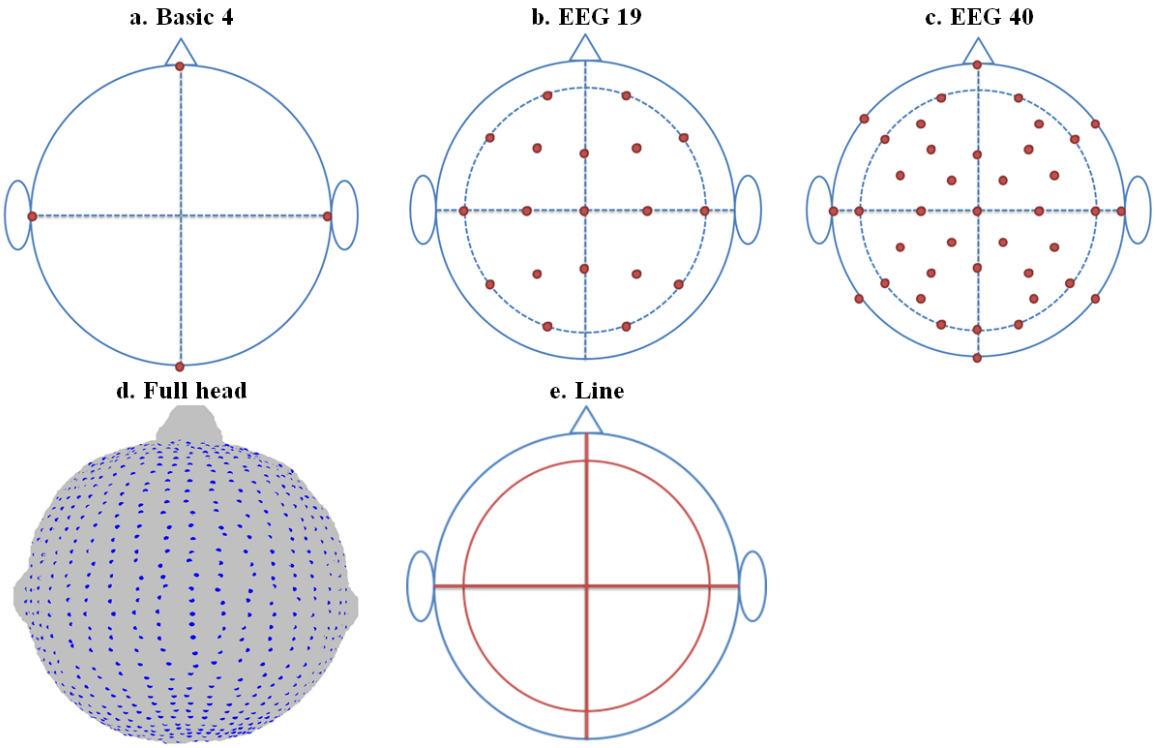

Figure 6.2. Set of five different Landmark systems used for registration.

6.2.3 Geometrical error analysis

Subject specific head meshes are generated from 24 different subjects using subject specific MRIs. The atlas head mesh is generated from the ICBM152 head atlas. The atlas mesh is then registered to each of the subject specific meshes individually using the 11 registration methods listed in Table 6.4. Evaluation of the geometrical error of the registered atlas model against the subject specific model is calculated with the surface distance, defined

as distance from each surface node of the subject's mesh to its closest surface node of the registered atlas' mesh.

6.2.4 Sensitivity matrix error analysis

A high density 24 source and 28 detector pad as described elsewhere [278] is placed on the surface of the head mesh, locations of which are determined by placing centre of pads on the inion of the head, so that the whole pad is on the scalp directly above the visual cortex. The registered atlas meshes share the same location of the pad centre with their corresponding subject meshes. Sensitivity matrices are then generated based on all 24 subject meshes and 264 registered atlas meshes (24 subjects × 11 registrations) using the NIRFAST software package. In the presented work, a single wavelength model based at 750 nm is considered and all the relevant optical properties for each layer within the head are given in Table 6.3. Relative error of the sensitivity matrices is calculated as percentage difference between sensitivity matrices generated from registered atlas models and those of the corresponding subject specific model.

6.2.5 Focal activation error analysis

Four individual focal activations are simulated in the four quadrants of the visual cortex for each subject. Each simulated activation has a radius of 7 mm and is limited at most to 3 mm depth from the surface of the brain (cortex). In the simulated activation region, a 24% change in optical parameter (absorption only) is set to cause at most a 5% change in the measured signal from the detectors [28]. In line with our current in vivo performance, 0.12%, 0.15%, 0.41% and 1.42% Gaussian random noise was added to first (13mm), second (30mm), third (40mm) and fourth (48mm) nearest neighbour measurements to provide realistic data [279]. Only the first to fourth nearest neighbours for each source are used for image recovery.

Simulated activations are then reconstructed using the subject mesh as well as the registered atlas mesh from each of the 11 registration methods. All presented results are limited to a region of interest (ROI) defined as the region under the imaging pad to a depth of 30 mm which has been determined the maximum possible imaging depth of the visual cortex for our imaging setup [6]. For parameter recovery, a spatially-varying regularisation is used.

$$\Delta\mu = \tilde{\quad}\ \tilde{\quad}\tilde{\quad}\ \Big)^{-1}\Delta y \tag{6.3}$$

$$\tilde{J} = \frac{J}{diag\left(\sqrt{diag(J^T J)+\beta\left(max\left(diag(J^T J)\right)\right)}\right)} \tag{6.4}$$

where $\propto$ is the Tikhonov regularisation parameter, β is the spatial regularisation factor, with $\propto = 0.01, \beta = 0.01$ and J is the sensitivity matrix. Δμ is the recovered change in optical properties and Δy is the change in boundary data due to the modelled focal activation. Additionally, to reduce artefacts in the reconstructions, a voxel-based Gaussian smoothing function (mean of 0 and standard deviation of 5 mm) is utilised. The recovered activation regions are then selected by thresholding the smoothed recovered changes based on either 50% or 70% of the maximum recovered changes.

The location error for the recovered activations D_c is given as Equation 6.5.

$$D_c = \sqrt{(x_r - x_s)^2 + (y_r - y_s)^2 + (z_r - z_s)^2} \tag{6.5}$$

$$x_r = \frac{\sum_{i=1}^{nodes}\left(x_{ni} * \mu_{ani}\right)}{\sum_{i=1}^{nodes}\left(\mu_{ani}\right)} \tag{6.5.1}$$

$$y_r = \frac{\sum_{i=1}^{nodes}\left(y_{ni} * \mu_{ani}\right)}{\sum_{i=1}^{nodes}\left(\mu_{ani}\right)} \tag{6.5.2}$$

$$z_r = \frac{\sum_{i=1}^{nodes}(z_{ni} * \mu_{ani})}{\sum_{i=1}^{nodes}(\mu_{ani})} \tag{6.5.3}$$

where (x_r, y_r, z_r) are the coordinates of the centre of mass of the recovered activation; x_s y_s z_s are the coordinate of centre of target simulated activation; *nodes* are number of nodes in activation region; x_{ni} y_{ni} z_{ni} are the coordinate of node *i* in the region and μ_{ani} is recovered optical parameter of node *i*. The relative recovered volume of the region v_{per} is given as Equation 6.6.

$$v_{per} = \frac{v_r}{v_s} * 100\% \tag{6.6}$$

where v_r is volume of the recovered activation; v_s is volume of the target simulated activation. The relative percentage overlay of the recovered region $v_{ov}$is given as Equation 6.7.

$$v_{ov} = \frac{v_{overlay}}{v_s} * 100\% \tag{6.7}$$

where $v_{overlay}$ is volume of overlay between simulated activation and recovered activation; v_s is volume of the target simulated activation. Finally, the average contrast in the recovered activation μ_r is given as Equation 6.8.

$$\mu_r = \frac{\sum_{i=1}^{nodes}(\mu_{ani}) \big/ nodes}{\mu_{sim}} \tag{6.8}$$

where μ_{ani} is recovered change of optical parameter of node i, nodes is number of nodes in activation region. μ_{sim} is simulated change of optical parameter.

6.3. Results and Discussions

The aim of this work is to evaluate the errors due to atlas based image reconstruction in DOT for the visual cortex. Therefore, all presented results are limited to this ROI which is directly covered by the imaging pad. To provide a qualitative example of the calculated surface distance error, results from three different registration methods for a given subject are shown in Figure 6.3. Although in this example the basic-4 landmark registration has high surface distance error on the top most part of the head (>10 mm), it has the lowest surface distance within the ROI (over the visual cortex). However, although both the EEG19ICP and FullnP2P registration have higher errors over the visual cortex, they provide a better match when considering the entire head.

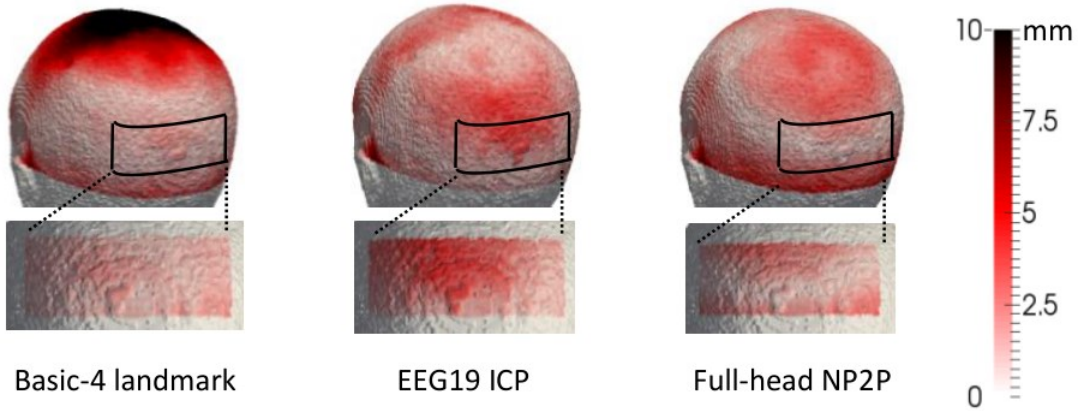

Figure 6.3. Examples of calculated surface distance errors for three different registration methods. ROI is shown in black box is used for all quantitative analysis.

In order to provide a more detailed analysis from different registration methods over all 24 subjects, whisker/box plots of the mean surface errors within the ROI are shown in figure 6.4. The outliers of different registration methods are not always the same subjects. It may be caused by the asymmetrical structure in the area around landmarks. Since different landmark systems are applied to these registration methods, the outliers are not always the same subject

for all the registration methods. It can be seen that all registration methods have on average ~7mm surface distance error and no greater than 11 mm within the ROI. For the same landmark system, NP2P and P2P methods have a slight advantage over the ICP method. Basic-4 landmark registration, line-fitting and full-head landmark registration, with NP2P and P2P show a slight advantage over other registration methods.

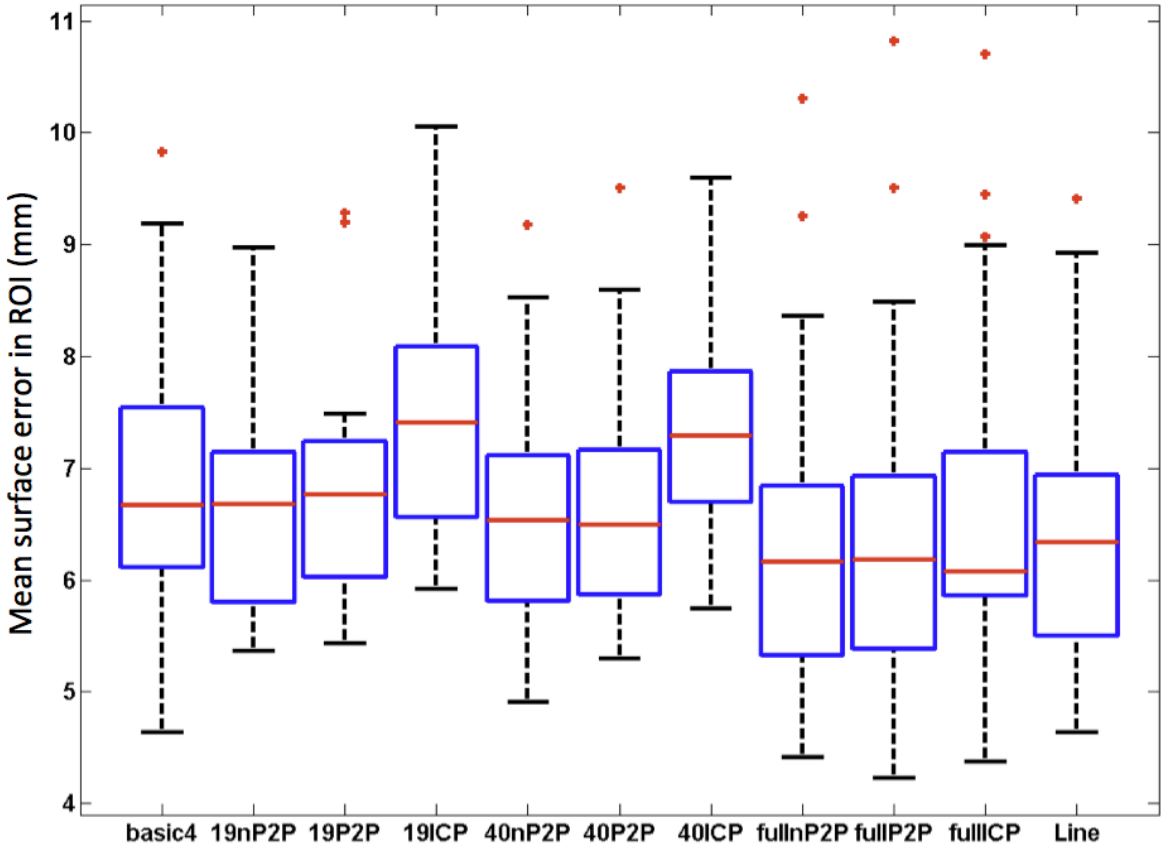

Figure 6.4. Surface geometry error for different registration methods for all 24 subjects. The central (red) lines represent the median, the box plots represent the 25th and 75th percentiles, whereas the whiskers present +/- 2.7 standard deviations. Outliers are presented as red crosses.

All of the utilised registration methods rely on external landmarks for registration on to the subject model and all tissue types are deformed rigidly to provide the best match. The internal tissue structural information therefore relies only on external landmarks. Specifically in this work, since the recovery of focal activations are expected from the cortical surface of the brain, it is necessary to evaluate the registration error not only to the external surface but

also to internal structures. Figure 6.5 provides a qualitative example of the calculated surface distance error of the cortex from three different registration methods for the given subject. It can be seen that generally the geometric error is less than 5 mm, with the maximum error seen in the folds of the brain as expected. These errors are calculated for each registered atlas models individually, but plotted on the subject cortex.

To investigate the accuracy of registration of internal structures once registered on to the subject, it is possible to calculate the joint-histogram of the subject specific mesh against the registered mesh [Figure 6.6]. To achieve this, the subject specific mesh and the registered atlas mesh are interpolated to the same voxel-based grid ensuring that each node in the grid has region labels (white matter, gray matter, CSF, skull, skin and air) from the two meshes. A region difference map is then generated based on the difference between the two labels and the joint histogram is calculated. Each region is normalized based on the number of nodes in the subject specific model to allow a fair comparison and only data from the ROI is shown. It can be seen that the joint histogram of fully registered meshes (i.e. subject specific versus subject specific) provides a unit diagonal plot, indicating that all the nodes from a given region in one model matched exactly with the same nodes in another. Conversely, if two models do not match exactly, some blurring (cross-talk) between nodes of different regions will be expected. It is evident that for the example shown in Figure 6.6, for all registration methods, there exists a cross-talk between air/skin tissue as well as gray/white matter. More importantly, CSF is not well registered and has a strong cross-talk with neighbouring tissue types.

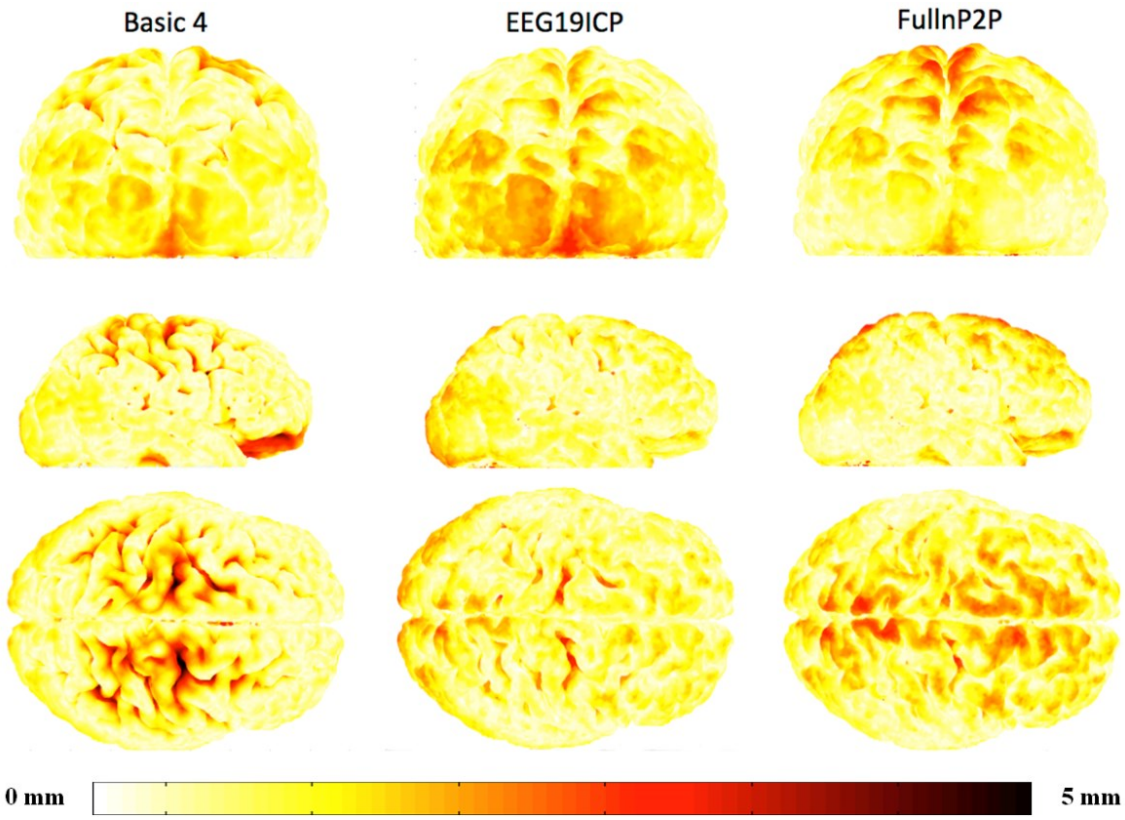

Figure 6.5. Examples of calculated cortex surface errors for three different registration methods. Top row: Back view. Middle row: Side view. Bottom row: Top view.

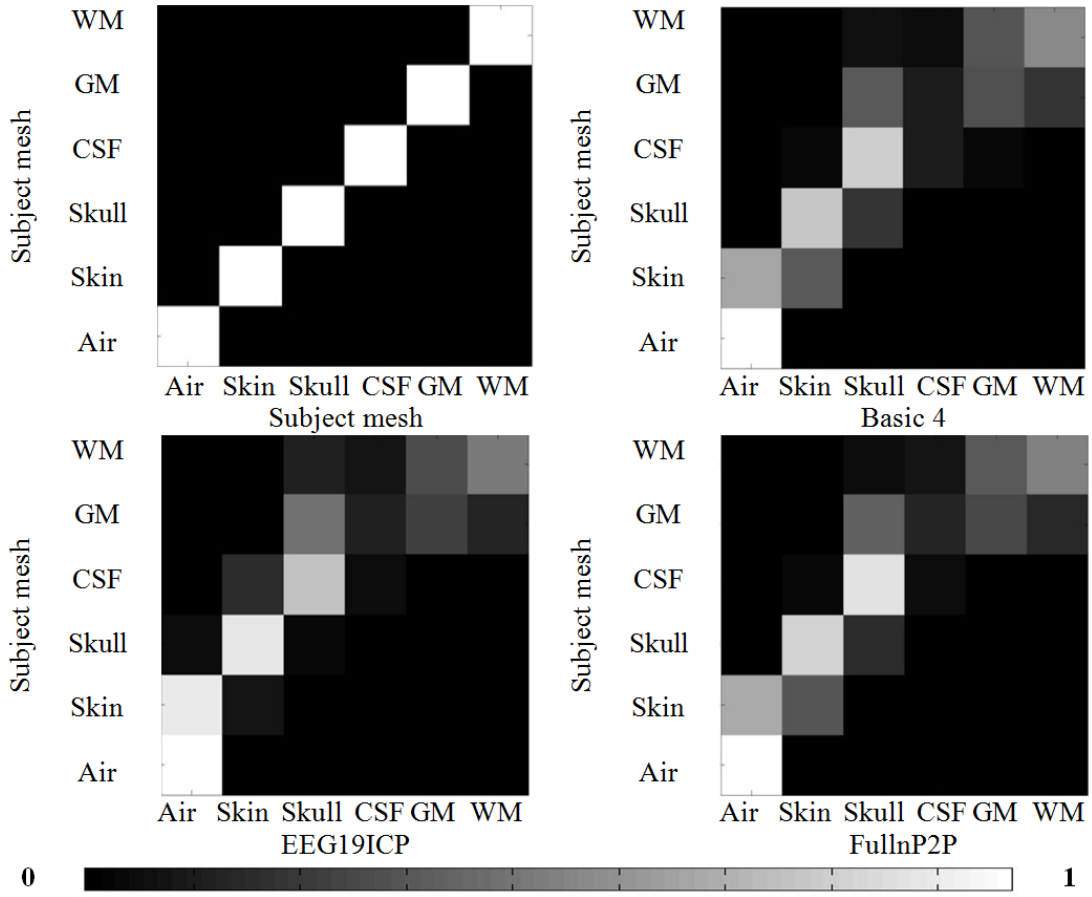

Figure 6.6. Joint histograms of a single subject with different registration algorithms.

The calculation of light propagation within the head, for model based DOT, relies not only on structural information about tissue layers, but also on the accuracy of the underlying optical properties. To quantitatively demonstrate the percentage error of assumed optical properties throughout the head based on different registration methods, a spatial map of tissue absorption error is shown for a given subject in Figure 6.7. This is an axial slice through the entire head, mid-way within the imaging pad. It can be see that the largest error is at the CSF/Brain interface as well as CSF/Bone. There also exists an error at the skin layer, where as expected from Figure 6.5, there exists a geometric registration error on the external surface.

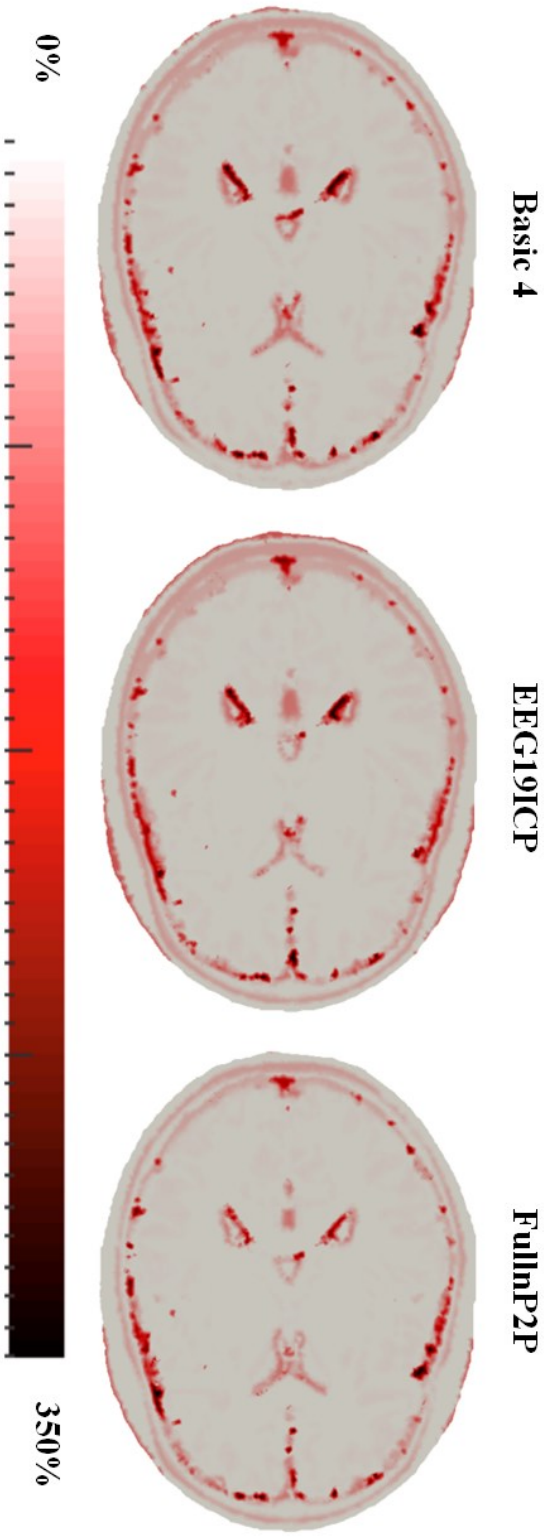

Figure 6.7. Spatial map of error in tissue absorption at 750nm for a given subject for different registration methods. This is an axial slice through the registered atlas mesh, mid-way within the measurement pad.

To provide a qualitative example of error of the sensitivity matrices, results from the three registration methods for a given subject are shown in Figure 6.8. The mean relative error of the sensitivity matrices for all subjects within the ROI are used for quantitative evaluation of the inaccuracy of sensitivity matrices [Figure 6.9]. The relative errors of sensitivity matrices in ROI vary from less than 20% to more than 300%. For the same landmark system, NP2P and P2P methods have a slight advantage over the ICP method. Basic-4 landmark registration, line-fitting registration and full-head landmark registration with NP2P and P2P show an advantage over other registration methods which is consistent with the evaluation result of the surface geometry error.

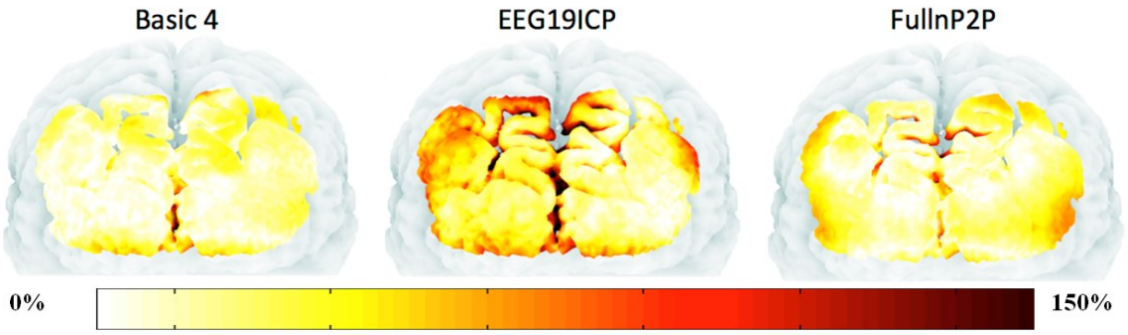

Figure 6.8. Example of relative error of sensitivity matrices on the cortex. Note that only the regions with a total sensitivity greater that 1% of the maximum value are shown.

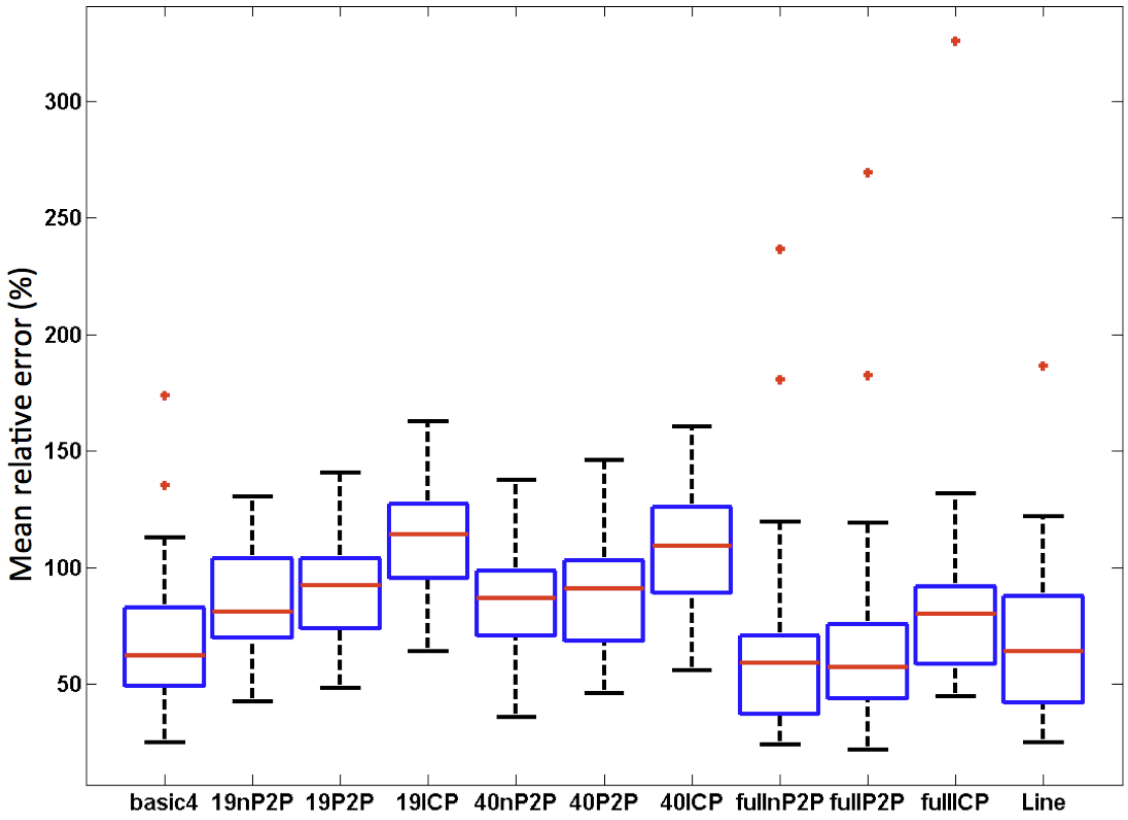

Figure 6.9. Mean relative sensitivity error for different registration methods for all 24 subjects. The central (red) lines represent the median, the box plots represent the 25th and 75th percentiles, whereas the whiskers present +/- 2.7 standard deviations. Outliers are presented as red crosses.

In order to evaluate the correlation of these results with the geometric error data, the average mean error (for all 24 subjects) of both parameters (surface error versus sensitivity at the cortex) is plotted for each registration method in Figure 6.10. It is seen that based on the average error, across all 24 subjects, there is a strong correlation between surface geometry error and cortex sensitivity error. The basis-4 landmark system is an anomaly, which can be explained by the fact that one of the four landmarks placed over the back of the head is providing a strong fiducial for registration. Ignoring the data from the basic-4 landmark system the calculate R^2 value is 0.97, indicating that the surface geometry error can be used as a surrogate for approximating the error for sensitivity at the cortex surface.

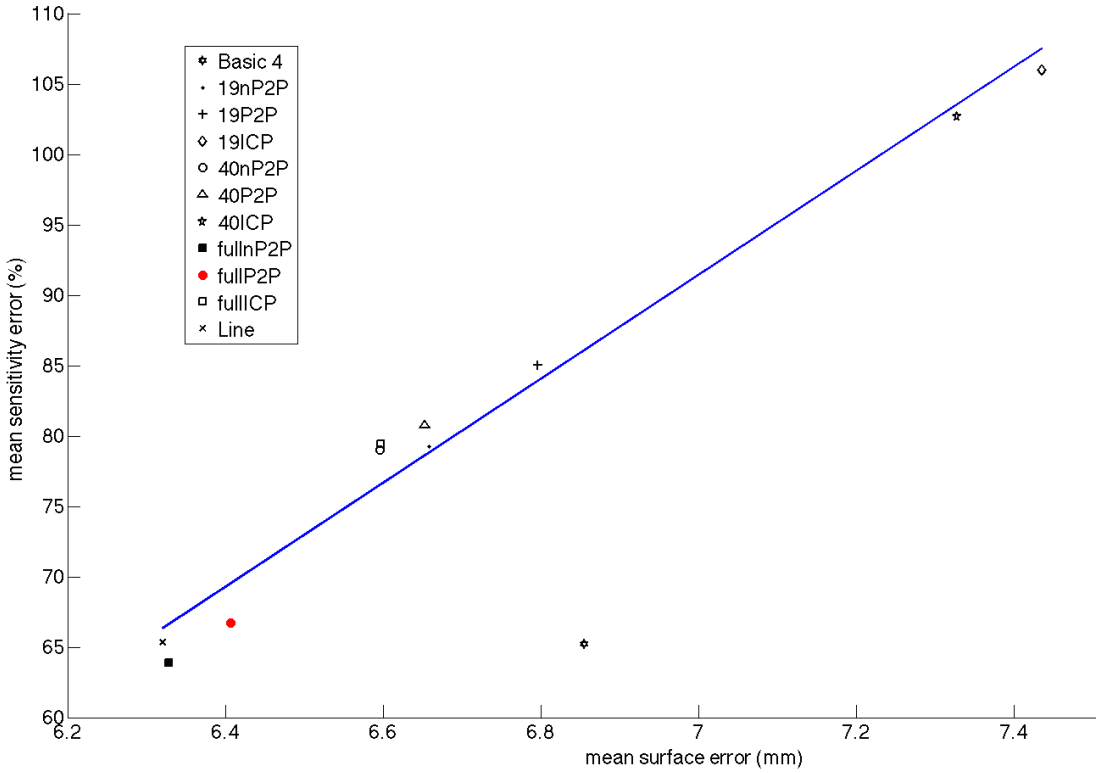

Figure 6.10. Mean relative sensitivity error 24 subjects versus mean surface error. Note that the 4 basic landmark data is not considered for the R2 value or the best fit line.

Evaluation of simulated focal activation result from all 24 subjects is based on the accuracy of recovered activation region. As an example, simulated activations of a given subject and the recovery result based on three registered atlas models as well as the subject specific model are shown in Figure 6.11. Quantitative evaluations of the results from both the subject specific and registered atlas models are shown in Figure 6.12. The most striking result is that although it has been shown that geometric surface error (and hence) sensitivity error (light propagation error) can be substantial depending on different types of registration algorithms, no single algorithm is providing errors greater than 4.5 mm in location error. This is perhaps expected as in most functional DOT imaging experiments, we are concerned with dynamic (often referred to temporal or difference) imaging, whereby rather than recovering an absolute image of optical properties, we are only concerned with recovery of changes with respect to a baseline and this type of image recovery has shown to be less prone to geometric

and model errors as compared to static (absolute) imaging [24, 280, 281]. The relative overlay depends (as expected) on the threshold value and is closer to the expected 100% using the 70% threshold. Nonetheless, all atlas based models overestimate the volume of the recovered activation ranging from 120% to ~200%. Conversely, the relative overlay is much better with 50% threshold (as expected) at the expense of larger volume being recovered. The recovered contrast for all models is approximately the same with ~16% for 50% threshold and ~18% for 70% threshold.

The subject specific mesh provided the best results with a 1.2 mm average location error and provides the most accurate recovery in terms of volume recover and overlay, regardless of whether 50% or 70% threshold is used. Basic 4 landmark registration, line-fitting registration and full-head landmark registration with NP2P and P2P show the best results using the atlas based models which is consistent with previous results.

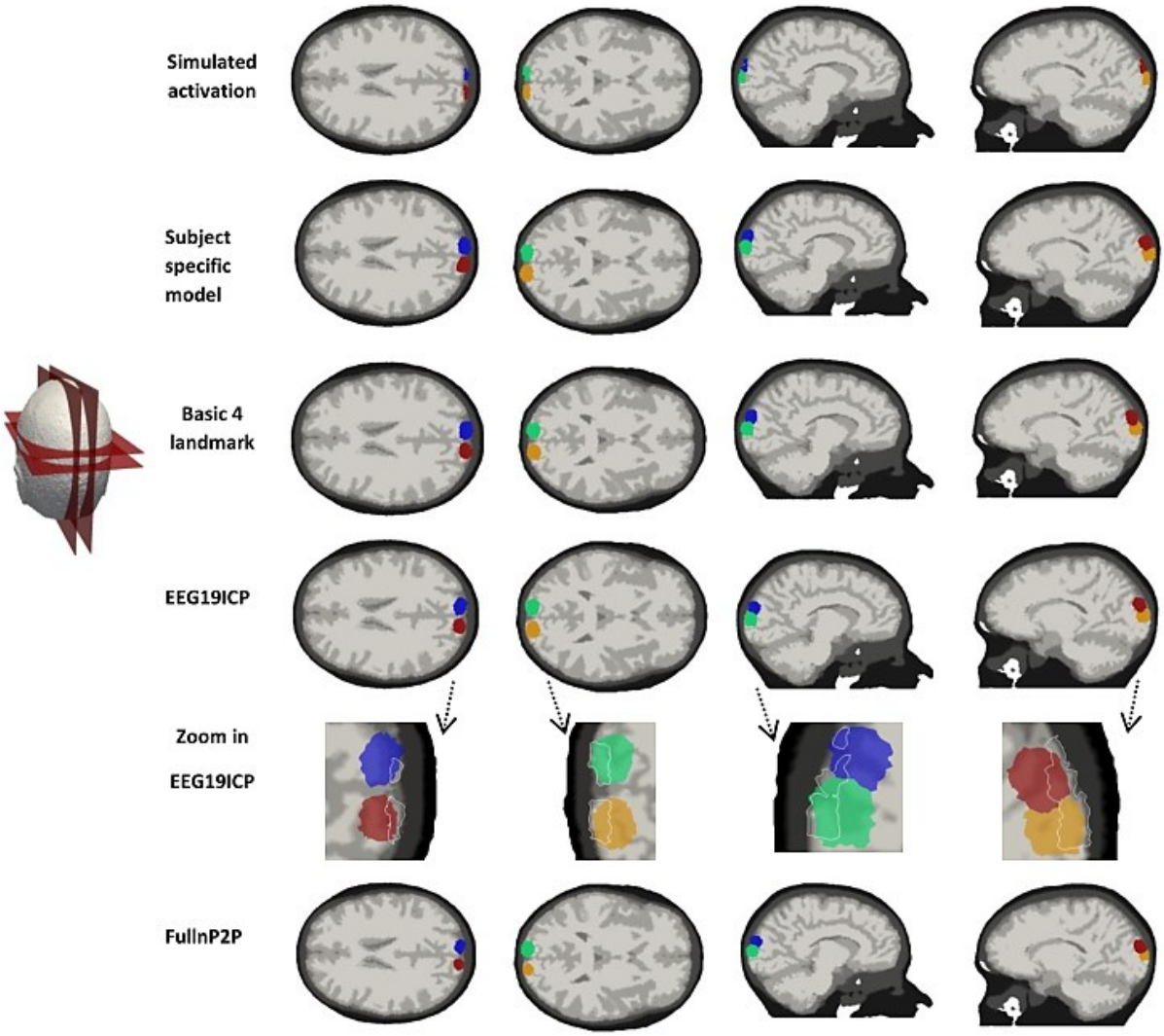

Figure 6.11. Example of focal activation recovery result for a single subject based on subject specific model and three registered atlas models. Note that each individual activation is color-coded and represent an individual simulation. White lines in the zoomed in plots represent the simulated activation.

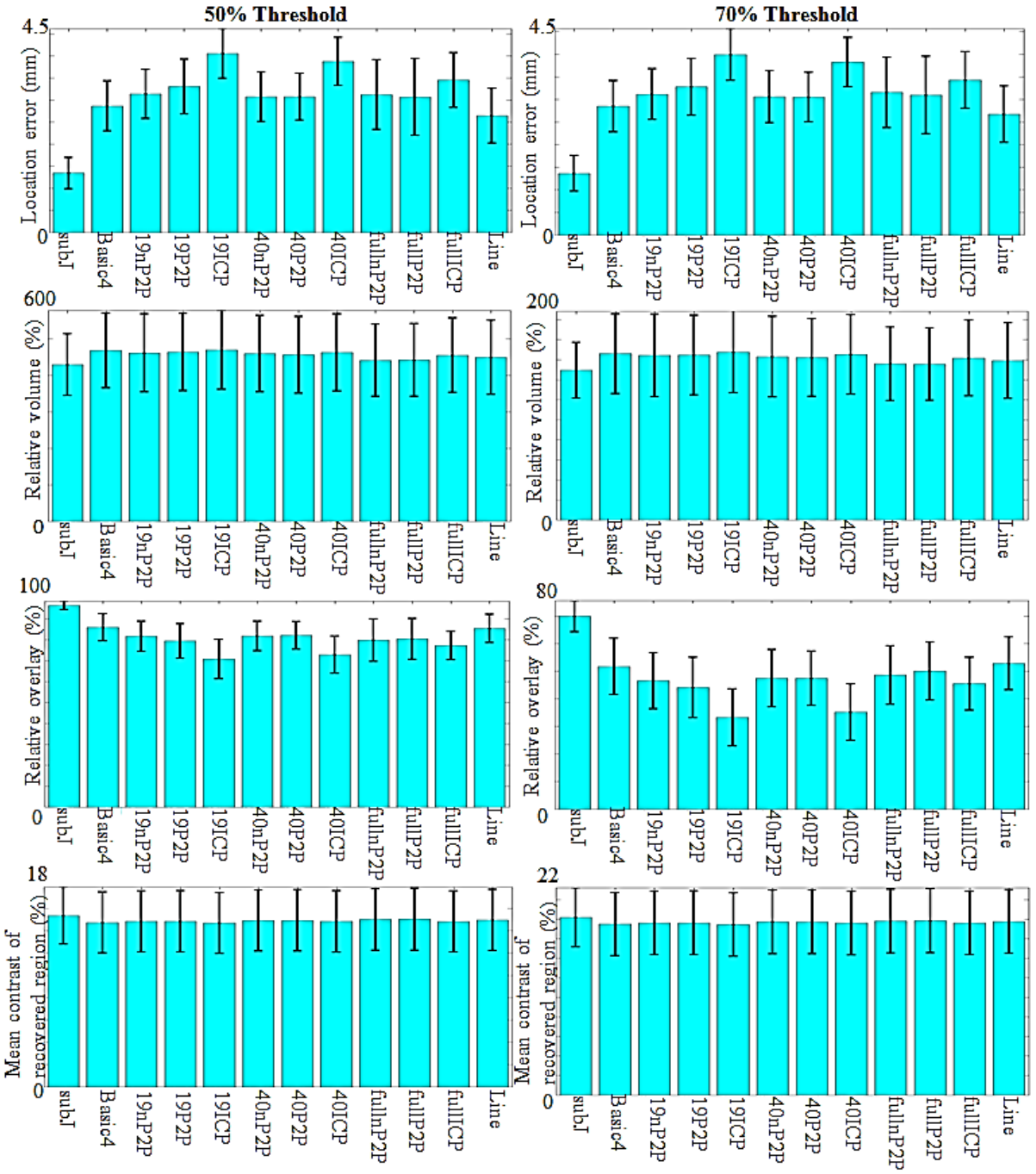

Figure 6.12. Evaluation of focal activation recovery for all registration methods across all 24 subjects.

6.4. Conclusion

In this work, a detailed workflow for the utilisation of atlas based models for image recovery in DOT is demonstrated with strong emphasis on High Density DOT of the visual cortex. In contrast to previously published work, 11 different registration algorithms have

been utilised, using 24 different subjects. Additionally, the presented work has concentrated not only on analysing the geometrical match between different registration models, or evaluation of recovered focal activations, but also provides a quantitative evaluation of induced errors in estimated of internal tissue structural distributions and their effect on the accuracy of the light propagation model.

It has been shown that all the registration methods provide recovery results for activations in visual cortex, which are less than 4.5 mm in localisation error. Although the difference in accuracy between different registration methods is not significant, the overall comparison of accuracy of all the three steps (registration, light propagation model and image recovery) are consistent, which indicates that the accuracy of registration has a direct effect on accuracy of the corresponding sensitivity matrix and hence the corresponding recovery result. Comparing different algorithms, registration methods with NP2P and P2P optimization algorithms demonstrate a slight advantage over ICP optimization algorithms using the same landmark system on geometry errors, accuracy of the sensitivity matrices and the focal recovery. This is because point to point optimization algorithms aim to register corresponding landmark pairs specifically instead of closest landmark pairs which is more accurate. Basic-4 landmark registration, line-fitting registration and full-head landmark registration with NP2P and P2P show an advantage over other registration methods. The improved accuracy of the full-head landmark registration is primarily due to the high- density of landmark sets utilised.

The basic-4 landmark registration method has shown better accuracy in the visual cortex comparing to other registration method. This may be because one of the four landmarks is extracted from the inion which is on the surface of scalp directly above visual cortex, which is similar for the line-fitting algorithm. Basic-4 landmark registration may not be one of the

most accurate registration methods if the study is of other regions of the brain, for example the motor cortex, for which other landmark systems may provide a better accuracy.

Focal activation recovery results from the 50% and 70% thresholds have almost the same location error, with basic-4 landmark, line-fitting and full-head landmark registration using NP2P and P2P demonstrating better results. All models have a similar average contrast, though it is slightly higher for the 70% threshold. All proposed rigid registration methods show a similar accuracy on the recovery of the activated area in the visual cortex. However, with more landmarks needed for the registration, the landmark extraction and computational process become more complex and the iterative process tends to increase the calculation time. For non-iterative processes, the computation time is usually a few seconds, but for an iterative process, it can be up to few minutes. Considering these two aspects, for recovery of focal activations in visual cortex, a registration method based on basic-4 landmark system is the most efficient method among the studied algorithms for atlas based DOT. However, other landmark systems may provide better accuracy when considering regions other than the visual cortex. The region based quantitative evaluation of the registration methods are presented in the following chapter.

CHAPTER 7: EVALUATION OF RIGID REGISTRATION METHODS FOR WHOLE HEAD IMAGING IN DOT

7.1. Introduction

Functional brain imaging techniques as described in chapter 2 can measure the physiological activities within the human brain to localise functional activation in response to, for example, visual or auditory stimuli [93, 282-284] or at rest-state [285, 286]. The cortex can be divided into different functional regions, such as visual and motor areas, and the functional connectivity between regions can be computed as the correlation between the time courses of the various brain regions [93, 287, 288]. This has become an important tool for the study of brain organization and development in health and disease and is applicable to subjects who are unable to respond to tasks such as infants or unconscious patients.

Previous studies have shown that brain activation tasks such as the inhibiting reflexive saccades task and hierarchical language tasks are correlated across multiple brain regions [12, 13]. Some neurodevelopmental disorders such as Alzheimer's disease, schizophrenia and adolescent depression have also been shown to be related to distributed brain networks [289-292]. Functional connectivity brain imaging is focused on the correlation between diverse brain regions and mapping of the functional networks. Traditional task-based functional imaging may not be suitable for some subjects such as unconscious patients and infants. Resting-state functional connectivity imaging provides a task-less approach to analysing correlation between diverse brain regions during spontaneous activity and mapping the resting state networks [13, 14]. Wide field imaging assesses brain activation in multiple functional

regions simultaneously and can be used for both task-based functional connectivity and resting-state functional connectivity imaging.

PET and fMRI are two of the most commonly used imaging techniques for quantitative recovery of brain activity. As described in chapter 2, PET is contraindicated in paediatric patients because of the exposure to ionizing radiation [282, 288, 293, 294], and fMRI is not permitted with pacemakers and cochlear implants because of the exposure to strong magnetic fields [93, 283, 295]. Additionally, the conventional imaging unit of PET and fMRI may cause discomfort for some patients with claustrophobia and may not be suitable for extremely obese patients.

Functional near-infrared spectroscopy (fNIRS) is a near-infrared light (NIR) based technique which can be used to monitor and map activations in human brain by measuring the tissue hemodynamic and oxidative metabolism in the cortex area [296]. The accuracy of fNIRS recovery including the effect of the registration methods in fNIRS have been investigated in previous studies [233, 297-299]. However, fNIRS generally lacks spatial information, which is a clear limitation in the analysis of brain activation and human cortex. Diffuse Optical Tomography (DOT) , as described in chapter 2, is a 3D NIR based imaging technique that has shown its ability to recover brain function of an adult within 30mm depth of the cortex surface [279]. DOT is a non-ionizing imaging technique with portable and low-cost instrumentation that can be applied to infants and hospitalized patients and has the potential to monitor the brain activities in real time [13].

DOT brain image recovery relies on a forward model which simulates the light propagation in the head. As described in chapter 5, atlas-based head models are used as the forward model for atlas-based DOT, the accuracy of which can directly affect the recovery of

brain activation. In DOT brain activation recovery, the measured NIR data on the surface of the head is related linearly to the small changes in internal optical properties via a Sensitivity matrix (details in chapter 2). The analysis of this sensitivity map within the head model can be used to evaluate the accuracy of the forward model for atlas-based DOT. Previous studies of whole head sensitivity analysis in DOT have included the effect of the source-and-detector location on the sensitivity of NIR data to different brain regions. Cooper et al's study on whole head sensitivity analysis uses a source-and-detector array, which covers the visual, auditory and motor functional brain regions [9] to distinguish the highly sensitive areas of the subject's brain accessible to the source-and-detector array. Giacometti et al's study on whole head sensitivity analysis uses a whole head source-and-detector cap based on EEG 10/5 landmark system and evaluates the overall sensitivity of the whole cortex and the sensitivity in different brain regions based on a contrast-to-noise ratio (CNR) analysis [276]. This study showed that most brain regions have a relatively high sensitivity (>50%) for DOT, though some regions presented lower sensitivity due to the variation in skull and scalp thickness.

In this chapter, a whole head sensitivity analysis of DOT is used for the evaluation of atlas-based DOT. The atlas-based head models are generated using a number of different rigid registration methods. The overall sensitivity of the whole adult cortex within the field of view (typically 30 mm deep given the high density source-detector configuration used in this work) and the sensitivity value in different brain regions using the atlas-based model and subject-specific model are evaluated and compared. The correlations of the geometrical and sensitivity accuracy for different regions are evaluated.

7.2. Methods

The simulation of NIR light propagation in the human head can be achieved using an anatomical model of the subject. In this work, a finite element model (FEM) of the head having multiple regions is used as the forward model, using the NIRFAST software package which uses the diffusion approximation with index-mismatched type III boundary conditions [68]. A subject-specific model requires anatomical information of the subject head, often obtained from structural MRI. When the MRI are not available, the geometry and internal structures from an atlas-based model can be used as an alternative [9-11], generated by registering an atlas model to the subject.

7.2.1 Layered head mesh

For both subject-specific and atlas based models, the forward model is generated using a segmenting-meshing process of the MRI of the subject or the atlas. The segmenting-meshing process can be divided into three steps. First, MRI scans from the atlas model or a given subject are segmented into five tissue types (skin, bone, CSF, gray and white matter) by the Statistical Parametric Mapping (SPM) software package based on tissue distribution probability maps and the pixel intensity of the MRI scans [208, 272]. Second, five masks are generated based on the five-region-segmented scans using the NIRVIEW [109] and NIRFAST software packages [68]. Third, layered FEM volumetric meshes are created based on the five masks by NIRFAST and the optical properties are assigned to each node in the mesh, based on its tissue type. Although the optical properties for each tissue type may vary for individual subjects, the same set of heterogeneous optical properties is applied to all of the individual meshes in this work to ensure the consistency of the evaluation and comparison.

The set of optical properties used in this work at 750 nm are based on previous works which are commonly used as shown in table 6.3 in chapter 6.

7.2.2 Atlas based models

The generation process of atlas-based models in this work relies on a surface-based rigid registration of the atlas mesh to the subject and is summarized in Figure 7.1. Based on the segmenting-meshing process outlined above, an atlas mesh and a subject-specific mesh from each subject MRI scan are generated separately. The surfaces of the two meshes are then extracted and registered together. The registered atlas mesh is then transformed by applying the affine transformation matrix generated in the registration process to the original atlas mesh. The registered atlas mesh is then used as the atlas-based head mesh in this work.

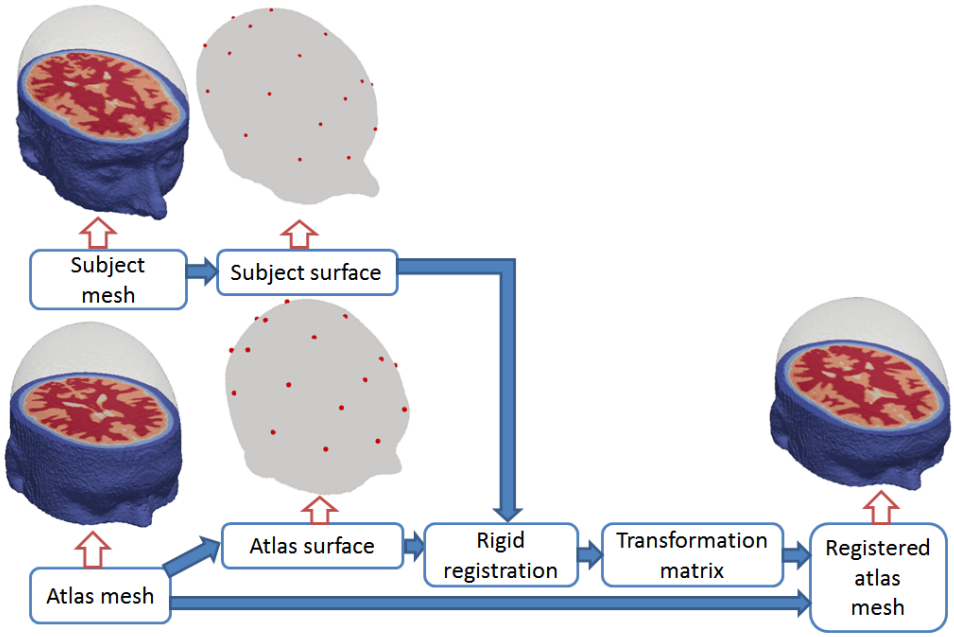

Figure 7.1. Workflow of creating a registered atlas-based mesh.

Registration methods used in this work are focused on the head surface based rigid registration. Although non-rigid registration methods have also been used for the registration of atlas-based DOT brain imaging, most require some internal structural information of the

subject, which is not often available. Non-rigid registration methods can also be applied using external landmarks, however since non-rigid registration is more localized than rigid registration, it tends to require more fiducial markers and it can be more computationally intensive [10, 22]. Therefore rigid registration methods based only on external landmarks are used in this work. The registration process can be divided into two steps. First, external fiducial point sets (landmarks) are extracted from the surfaces of the atlas and the subject mesh, based on the same landmark system. Second, the minimization of the distance between the two landmark sets is processed based on an optimization algorithm. The affine transformation matrix which is used to transform from the atlas space to the subject space is generated for the registration process.

Different registration methods can be used based on different landmark systems or different optimization algorithms. The registration methods used specifically in this work are created based on four different landmark systems and three different optimization algorithms as well as one line-fitting based registration, Figure 6.2. The basic-4-landmark system contains fiducial points extracted manually from four anatomically specified points: the nasion, the inion, and the two temples. EEG 19 and EEG 40 landmark systems contain 19 and 40 landmarks extracted based on EEG 10/20 system and EEG 10/5 system. The full-head-landmark system contains 700 landmarks extracted uniformly across the whole head surface area under the source and detector cap (details in section 7.2.4). The basic-4-landmark based registration method generates the transformation matrix based on a non-iterative optimization algorithm using the corresponding relationship between the two sets of landmarks from the subject and the registration target (the non-iterative point to point (nP2P) optimization algorithm). The nP2P algorithm is also used in the registration algorithm based on EEG 19, EEG 40 and full-head landmark systems. An iterative optimization algorithm using the

corresponding relationship between landmarks sets (point to point (P2P) optimization algorithm) and an iterative optimization algorithm based on closest point (iterative closest point (ICP) optimization algorithm) is additionally used for EEG 19, EEG 40 and full-head landmark systems. The line-fitting based registration method generates the transformation matrix by optimizing the fitting of three curves (a temple to temple curve, a nasion to inion curve and a circumferential line connecting all four points) as extracted from the head surfaces of the subject and the target. This gives rise to 11 registration methods consisting of basic-4-landmark, EEG 19 nP2P, EEG 19 P2P, EEG ICP, EEG 40 nP2P, EEG 40 P2P, EEG 40 ICP, Full-head-landmark nP2P, Full-head-landmark P2P, Full-head-landmark ICP and line-fitting registration methods, further details of which are covered in depth elsewhere [300].

Additionally, a spherical coordinate landmark system has also been used which defines a spherical coordinate system based on three fiducial points (the nasion and the left and right temple points) and extracts arbitrary points from the subject scalp as landmarks based on the spherical coordinates (figure 7.2). This approach may be considered practically easier to apply than those outlined above [301-303]. For this purpose, 19 spherical coordinate landmarks using nP2P, P2P and ICP (Figure 7.3(f)) are also used for the registration of the atlas model (named SpnP2p, SpP2p and SpICP respectively) and are evaluated and compared with the 11 registration methods outlined above.

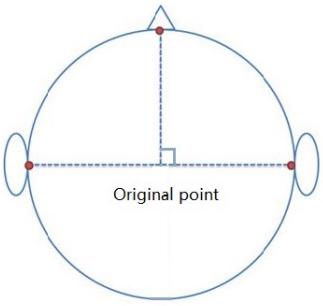

Figure 7.2. Original point in the spherical landmark coordinate system.

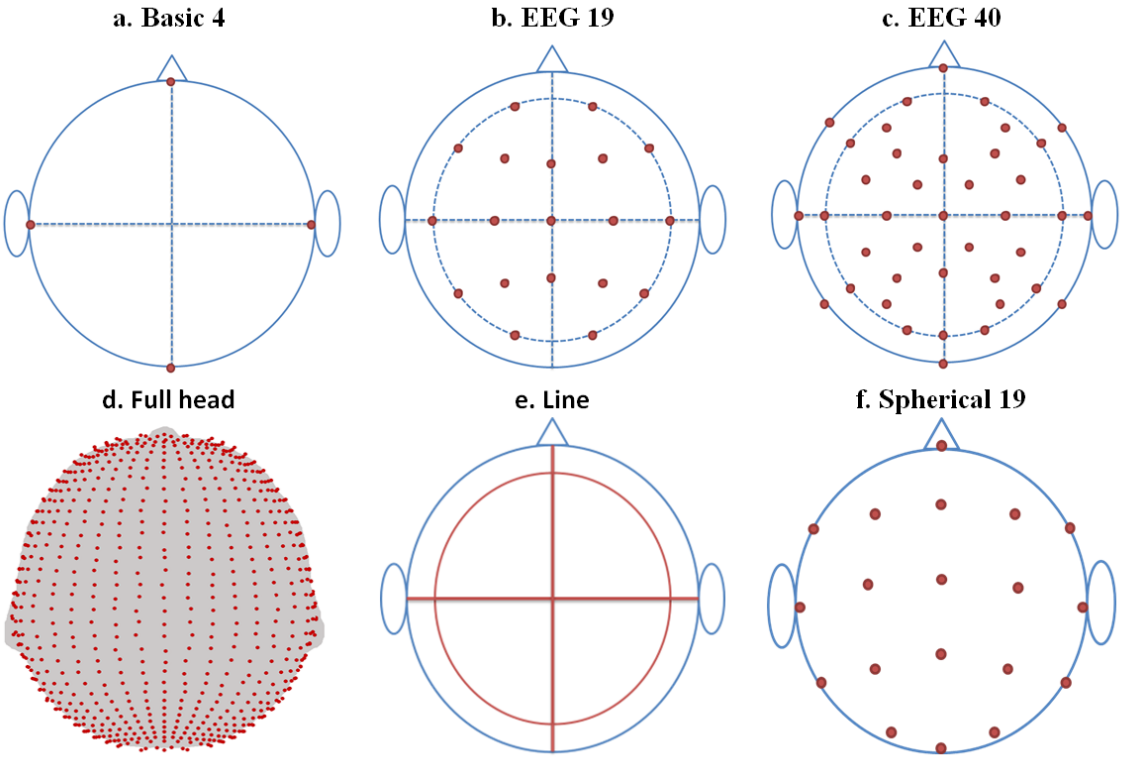

Figure 7.3. Set of different Landmark systems used for registration.

7.2.3 Sensitivity matrix for image recovery

The model based light propagation for brain DOT relies on a forward model which contains the internal structure and optical properties of the subject. The accuracy of the light propagation can be evaluated based on the spatially varying sensitivity of NIR boundary data to the spatially varying optical property. The sensitivity matrix contains the sensitivity of the NIR boundary data of each measurement to the optical property of each mesh node. The sensitivity of NIR boundary data to the optical property can be represented as:

$$J\Delta\mu = \Delta\Phi \tag{7.1}$$

where $\Delta\mu$ is the changes in tissue property, $\Delta\Phi$ is the change in boundary data, and J is the sensitivity matrix. For continuous wave (CW) DOT, the sensitivity matrix is defined as:

$$J = \begin{bmatrix} \frac{\partial lnI_1}{\partial \mu_{a1}} & \frac{\partial lnI_1}{\partial \mu_{a2}} & \cdots & \frac{\partial lnI_1}{\partial \mu_{aNN}} \\ \frac{\partial lnI_2}{\partial \mu_{a1}} & \frac{\partial lnI_2}{\partial \mu_{a2}} & \cdots & \frac{\partial lnI_2}{\partial \mu_{aNN}} \\ \cdots & \cdots & \cdots & \cdots \\ \frac{\partial lnI_{NM}}{\partial \mu_{a1}} & \frac{\partial lnI_{NM}}{\partial \mu_{a2}} & \cdots & \frac{\partial lnI_{NM}}{\partial \mu_{aNN}} \end{bmatrix} \tag{7.2}$$

where *ln I* is the log amplitude of boundary data, μ_a is the absorption property, *NN* is the number of nodes and *NM* is the number of measurement. The total sensitivity of all measurements at each spatial point of the model is used for the evaluation and comparison of sensitivity accuracy in this work, which is defined as:

$$J_{total,n} = \sum_{i=1}^{NM} J_{i,n} \tag{7.3}$$

where $J_{total,n}$ is the total sensitivity value at node *n* for all measurements and $J_{i,n}$ is the sensitivity value of measurement *i* and node *n*.

7.2.4 Simulation experiments

For the evaluation of the rigid registration methods for the atlas based whole head DOT, a simulation experiment is designed based on 14 female and 10 male individual subjects with mean age of 26(+/-4) and using the ICBM 2009a Nonlinear Symmetric T1w modality atlas model [112, 117]. Subject specific anatomical T1-weighted MPRAGE (echo time (TE) = 3.13 ms, repetition time (TR) = 2400 ms, flip angle = 8°, 1 x 1 x 1 mm isotropic voxels) scans were acquired for each subject (subsequently referred to as T1). All subjects passed MR screening to ensure their safe participation. Informed consent was obtained and the research was approved by the Human Research Protection Office at Washington University School of Medicine. The five-layer-head meshes with ~400000 nodes corresponding to ~2390000 linear

tetrahedral elements are generated based on the T1 MRI data of the 24 subjects to provide the subject specific meshes. The atlas model is then utilised to generate the atlas-based mesh to be used for registration. The atlas mesh is registered to each subject individually using the rigid registration methods outlined above. The optical properties of the five tissue regions in Table 6.3 in chapter 6 are then applied to all of the 336 registered atlas meshes (24 subjects × 14 registration methods). A high-density (HD) source-detector cap with 158 sources and 166 detectors cap (Figure 7.4) is then placed on the surface of all meshes where the sources and detectors in the cap are uniformly distributed on the surfaces of the head and cover the entire surface area above the brain. For all 360 meshes (336 atlas based and 24 subject specific), the sensitivity matrices are then calculated using the first to fourth nearest neighbour measurements at 1.0, 2.2, 3.0, and 3.6 cm source-detector distance respectively on the HD source-detector cap [7].

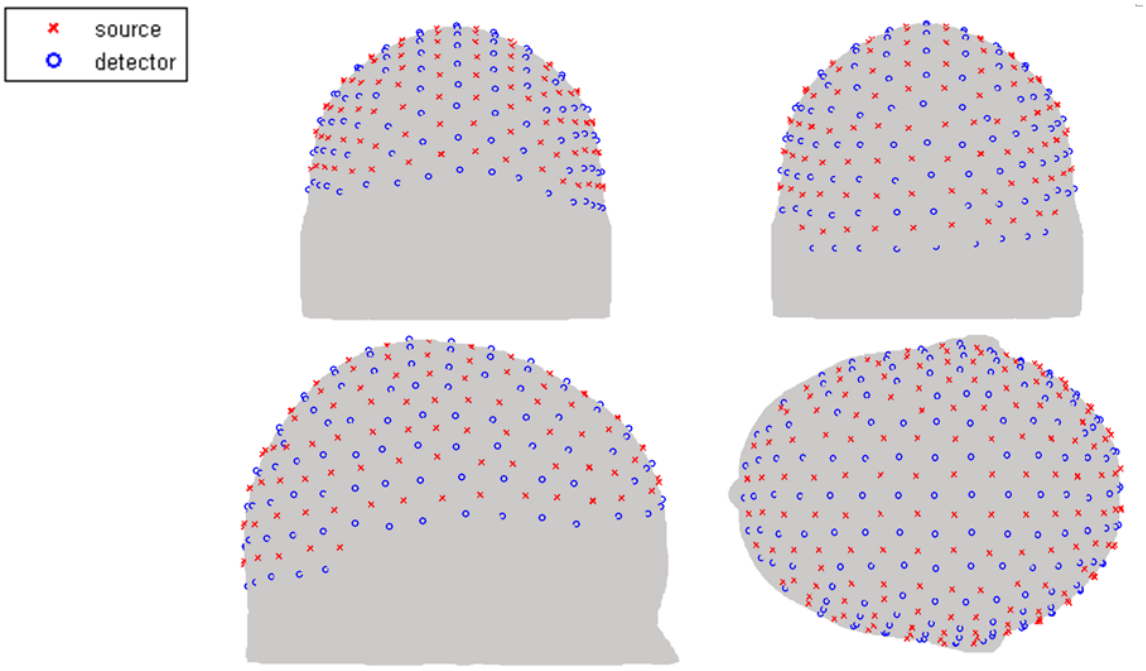

Figure 7.4. High-density source and detector cap for an example head surface.

The accuracy of the registration methods can be evaluated by the geometrical accuracy of the registered atlas mesh as compared to the subject specific mesh. The geometrical accuracy is calculated by the distance from each surface node of the subject specific mesh to its closest surface node of the registered atlas mesh. The surface region under the HD cap is considered as the region of interest (ROI) for the analyses. The average distances across the head surface within the ROI are calculated based on the registered atlas mesh for all 14 registration methods for all 24 subjects.

The accuracy of the light propagation is evaluated by the accuracy of the sensitivity matrix for each registered atlas mesh. The sensitivity accuracy is calculated by the comparison of sensitivity matrices between the registered atlas mesh and the subject specific mesh. Specifically, for the evaluation, the sensitivity matrices are generated based on registered atlas and the subject specific mesh separately for the HD source-detector cap and then the values within the ROI are selected by utilising only the sensitivity values on the surface of the cortex which are higher than 1% of the maximum value [304]. The total sensitivity is then calculated for all source/detector measurements (equation 7.3) and these are then mapped to the same uniform grid using a linear interpolation function. The total sensitivity values from these two matrices are then compared on this voxel basis.

The correlation of the geometrical and sensitivity error is also evaluated in this work for the analysis of the registration method on the accuracy of the light propagation model. Different regions of the head can have different geometry-sensitivity correlation, therefore a unified analysis based on the EEG 10/20 system region segmentation is used for the evaluation [276]. This region segmentation is divided into three steps: Firstly, 19 landmarks are extracted from the surface of each head mesh based on EEG 10/20 system and numbered as 1 to 19. Secondly, distance from each node within the mesh to all of the 19 landmarks is

calculated and the closest landmark of each node is selected. Thirdly, all the nodes are then labelled based on their closest landmarks and nodes with the same label are considered as the same region. 19 regions are then generated based on the EEG 10/20 system. The geometrical and sensitivity error are then calculated for each region separately and the correlation are compared for each region.

7.3. Results

7.3.1 Evaluation of the geometry accuracy

Each of the considered registration methods is evaluated by the use of geometrical accuracy analysis of the registered atlas mesh onto the subject specific mesh. The geometrical accuracy is defined as the external surface distances between the registered atlas and the subject-specific mesh on every surface node within the ROI. The geometrical error of three registration methods (basic-4-landmark registration, EEG19ICP registration and full-head-landmark registration) for the same subject is shown in Figure 7.5 as an example. As evident, qualitatively, the basic-4-landmark registration method has the highest geometrical error (~10 mm) among the three shown registration methods. For all shown registration methods, the error varies spatially: Using the basic-4-landmark registration method the upper middle surface area has relatively high geometrical error while the back and temple surface areas have relatively low error. For the EEG 19 ICP registration method, the upper middle and the back surface area have relatively high geometrical error while the front surface area has a relatively low geometrical error. For full-head-landmark system nP2P registration method, the upper front and upper back surface areas have relatively high geometrical error while the lower side surface area has a relatively low geometrical error.

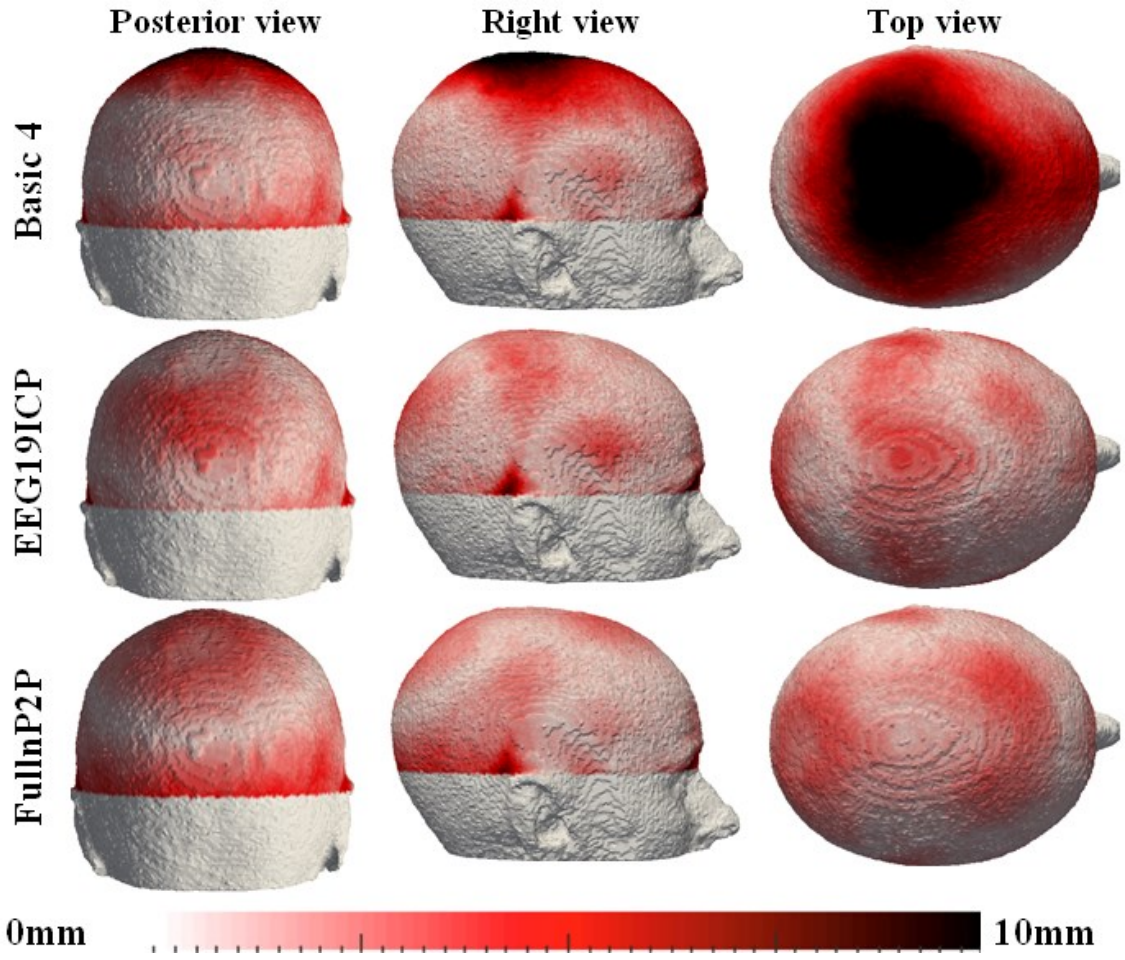

Figure 7.5. An example of geometry error based on 3 registration methods for an example subject.

The complete evaluation of the registration accuracy is based on the average surface distance of the registered atlas mesh for all 24 subjects as compared to the subject specific mesh [Figure 7.6]. Of the utilised 14 registration methods, the full-head-landmark nP2P registration method with 1.5 (+/- 0.5) mm average surface distance has the best average geometrical accuracy while the basic-4-landmark registration with 4 (+/- 1) mm average surface distance has the worst accuracy. The three 19 spherical coordinate landmarks based registration with 3.2 (+/- 0.5) mm average surface distance are the second least accurate registration methods. The line fitting registration has 2.3(+/- 0.5) mm average surface distance. The full-head-landmark P2P and ICP registration methods have 2.2 mm average surface distance, but they show a variation of 1.5 mm which is the largest difference among all

subjects. The other 6 registration methods (EEG 19 and 40 landmark system with nP2P, P2P and ICP registration methods) are less accurate with 2 (+/- 0.5) mm average surface distance.

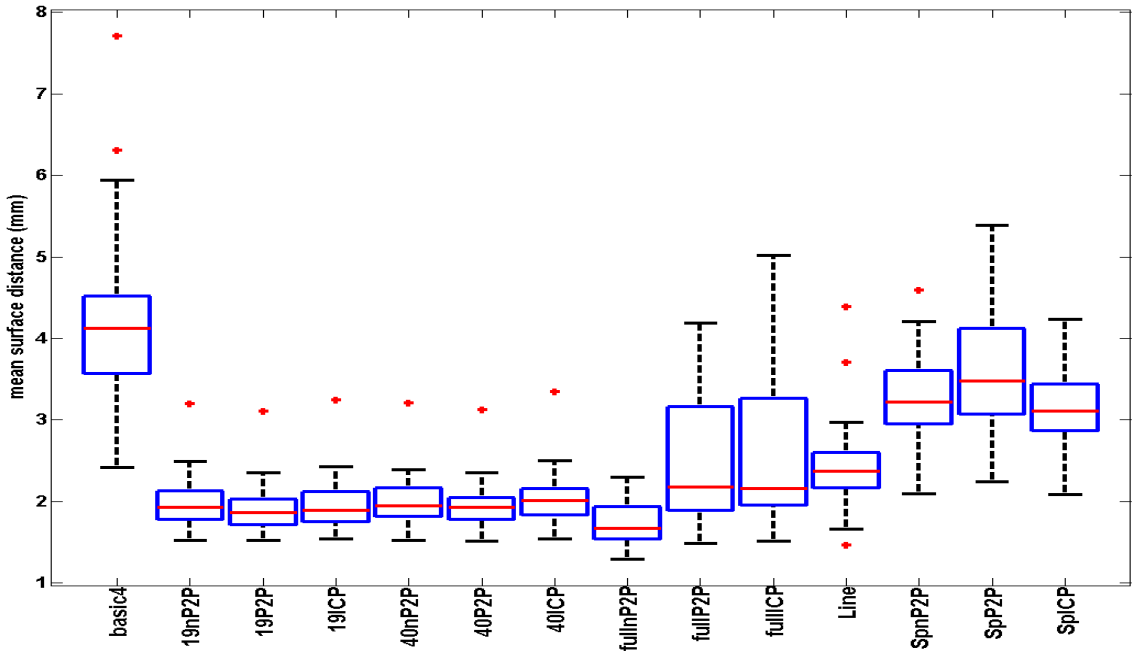

Figure 7.6. Evaluation of geometrical errors based on 24 subjects. The central (red) lines represent the median, the box plots represent the 25th and 75th percentiles, whereas the whiskers present +/- 2.7 standard deviations. Outliers are presented as red crosses.

7.3.2 Geometry accuracy of the gray matter

Because of the error from the registration methods and the underlying differences between the internal structures of the atlas and subject-specific model, the final registration of the internal structure of the registered atlas mesh can also be inaccurate. This inaccuracy of the internal structure can be evaluated based on the geometrical analysis of gray matter registration itself. The geometrical accuracy of the gray matter is defined as the geometric distance between gray matter surfaces of the registered atlas mesh and the subject specific mesh on each surface (gray matter) node. The surface nodes of the gray matter are selected for both the registered atlas mesh and the subject specific mesh and the Euclidean distance is then calculated by the distance from each gray matter surface nodes of the subject specific mesh

and its closest gray matter surface node on the registered atlas mesh. As the geometrical accuracy varies in different areas of the gray matter a structural regional map based on previous studies and landmark structure such as the central sulcus and the lateral fissure is used on the cortex to aid spatial discrimination of the error seen in different areas [Figure 7.7] [305, 306]. This brain regional map contains 4 different lobes: the Occipital, Temporal, Parietal, and Frontal Lobes, and it is used for a better analysis of the gray matter geometrical accuracy for different brain areas.

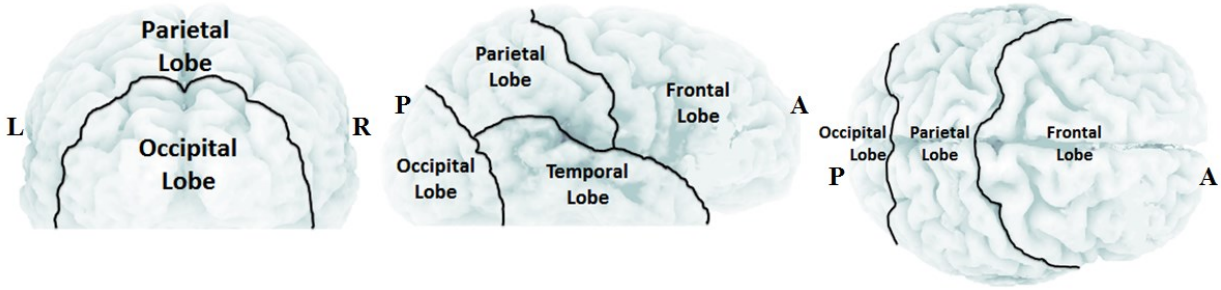

Figure 7.7. Brain regions used for geometrical representation. (a) posterior view, (b) right view, and (c) top. view.

The geometrical accuracy of the gray matter registration for an example subject, based on three registration methods (basic-4-landmark, EEG19ICP and full-head-landmark) is shown in Figure 7.8. For the entire gray matter surface within the ROI, the basic-4-landmark registration method has the lowest accuracy among the three registration methods with 5 mm maximum surface distance. For all three registration methods shown, the geometrical accuracy of gray matter varies for different functional areas of the brain. For the basic-4-landmark registration method, the brain areas near temporal, prefrontal and occipital cortex regions have better accuracy as compared to others whereas the areas near central cortex region (area adjoining frontal and parietal cortex regions) have lowest accuracy. For the EEG 19 landmark system with ICP registration method, the areas near temporal and prefrontal cortex region have the best accuracy as compared to other parts of the cortex whereas the

areas near the occipital cortex region have lowest. For the full-head-landmark system with nP2P registration method, the areas near the occipital and temporal cortex region have the best accuracy whereas the areas near superior frontal and superior parietal cortex regions have lowest. However due to the complex structure of the gray matter (such as the gyri), the gray matter surface accuracy may not fully represent the geometrical accuracy of the cortex registration itself.

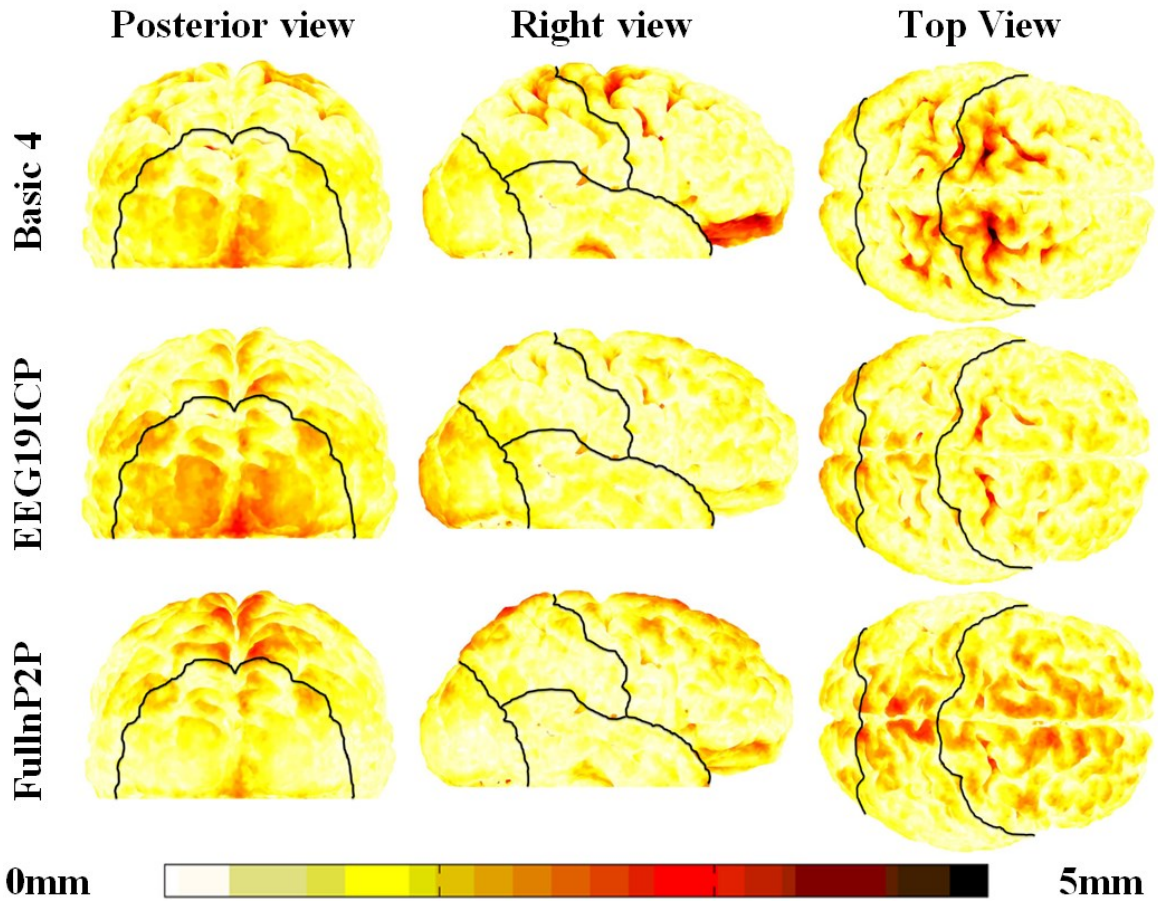

Figure 7.8. An example of gray matter geometry errors based on 3 registration methods for an example subject.

7.3.3 Evaluation of the sensitivity accuracy

The accuracy of light propagation of the registered atlas mesh is evaluated based on the comparison between the sensitivity matrices from the subject-specific and the registered atlas

mesh. The ROI for this evaluation is selected as the region within the gray matter with a sensitivity value higher than 1% of the maximum. Since the geometry of the subject-specific gray matter and the registered atlas gray matter will differ, some areas are excluded in the registered atlas mesh since there will be no common overlap in these areas. For the comparison therefore, the sensitivity values of the registered atlas mesh which have been excluded are set as zero.

As shown above, since the accuracy of geometrical registration varies for different brain regions, the sensitivity accuracy could also vary for different regions. The sensitivity errors of the cortex for one example subject, based on three different registration methods are shown in Figure 7.9. For all brain regions, the basic-4-landmark registration has the overall lowest sensitivity accuracy: the occipital cortex region has better accuracy as compared to other regions and the areas near central cortex region have the lowest accuracy. For EEG 19 landmark system with ICP registration method, the areas near temporal and prefrontal cortex region show better accuracy as compared to other regions whereas the areas near occipital and superior parietal cortex region have lower accuracy. For the full-head-landmark system with nP2P registration method, the areas near temporal cortex region have better accuracy as compared to other regions whereas the areas near superior frontal and superior parietal cortex regions have lower accuracy. It is worth noting that the sensitivity accuracy distribution for different brain regions is similar to the geometrical accuracy distribution.

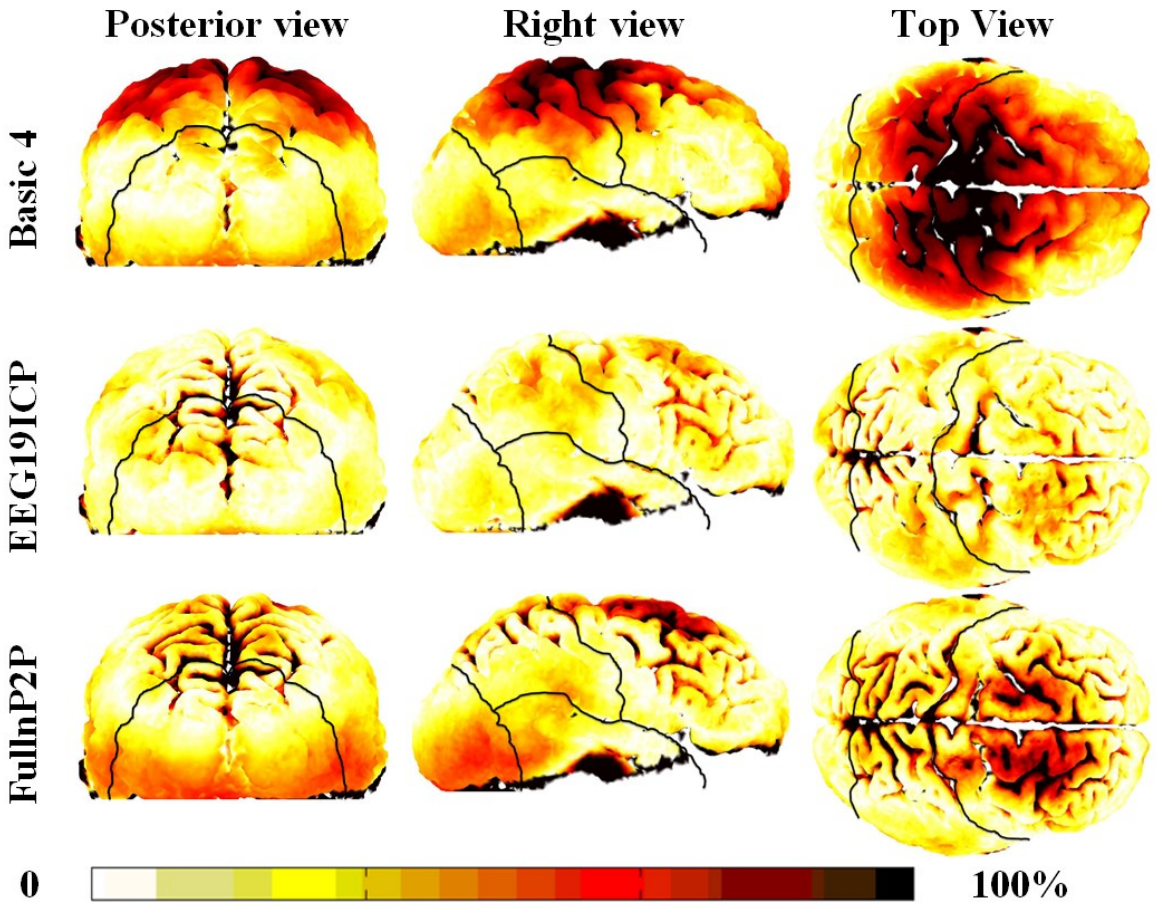

Figure 7.9. An example of sensitivity percentage error of the cortex based on 3 registration methods for an example subject.

To fully quantify the evaluation of the sensitivity error for all 14 registration methods based on all 24 subjects, the sensitivity error across all brain regions is shown in Figure 7.10. All registration methods have on average a sensitivity error of no more than 50%. The full-head-landmark nP2P registration method has a 32(+/- 8)% average sensitivity error, which is the most accurate registration method based on the sensitivity accuracy. Line fitting registration and basic-4-landmark registration have 50(+/- 10)% average sensitivity error, which are the least accurate methods. The three 19 spherical coordinates landmarks based registrations have 50(+/- 15)% average sensitivity error and have lower accuracy as compared to the other registration methods. The full- head-landmark P2P and ICP registration methods have 40(+/-20)% average sensitivity error, which show the largest difference among all

subjects. The other six registration methods (EEG 19 and 40 landmark system with nP2P, P2P, ICP registration methods) have similar accuracies with 35(+/-5)% average sensitivity error, which are more accurate than the full- head-landmark P2P and ICP registration methods.

Compared to other registration methods, the basic-4 landmark registration and three 19 spherical coordinates landmarks registration methods have a clear disadvantage on both geometrical and sensitivity accuracies. Therefore, for the remainder of the analysis, the three 19 spherical coordinates based landmarks registration methods are not considered, but since the basic-4 landmark registration relies on minimum required landmarks it will be included for analysis.

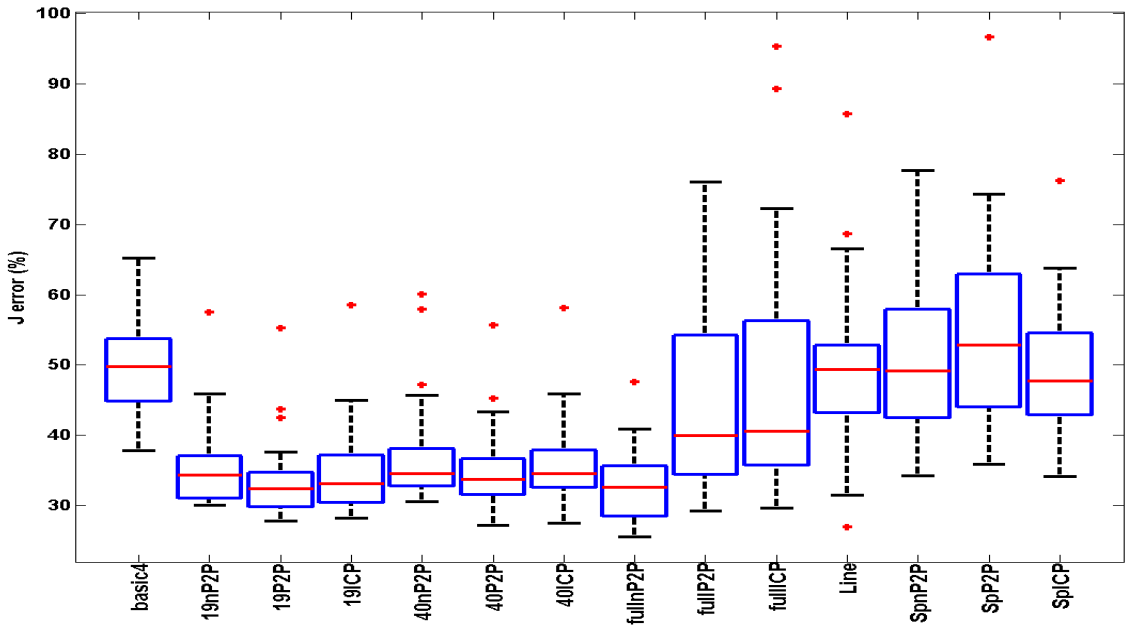

Figure 7.10. Evaluation of sensitivity errors of the cortex based on 24 subjects.

7.3.4 Correlation between geometry and sensitivity accuracy

Based on the analyses of the geometrical and sensitivity accuracy on the 24 subjects, there may be some correlation between these measures. A correlation analysis is performed for the registration methods between the geometrical and sensitivity accuracy on the whole head

using the average surface distance error and the average sensitivity error [Figure 7.11]. As evident, there is no strict linear relationship between the geometrical and sensitivity accuracy, however, the accuracy of the registration methods can be further classified. The full head landmark nP2P registration is considered as the most accurate method for both the geometrical and the sensitivity accuracy, and the basic-four landmark registration is considered as the least accurate method. The full-head-landmark P2P and ICP registration and line-fitting registration methods have the worse accuracy as compared to the other registration methods.

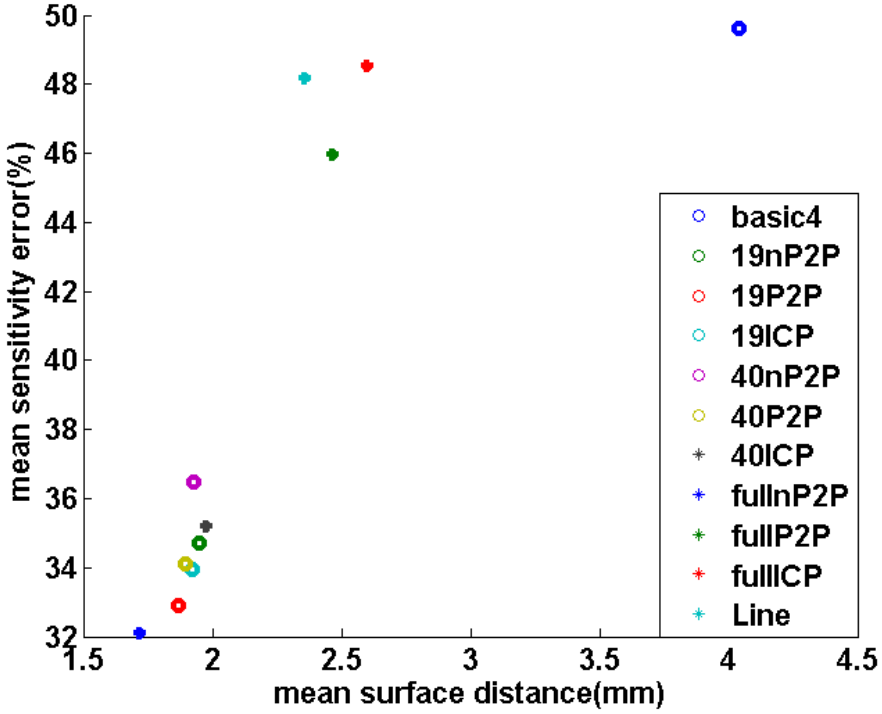

Figure 7.11. Correlation between geometry error and sensitivity errors of the whole head region based on 24 subjects and registration methods.

The analysis based on one example subject has shown that the geometrical and sensitivity accuracy can vary for different regions of the human brain. Therefore, there may be some classification for the correlation between these parameters on different brain regions. The 19 head regions within the ROI, based on the EEG 10/20 system are used for the classification of

the correlation of all 24 subjects [Figure 7.12]. The average geometrical and sensitivity accuracy for each subject is used for each region, separately, for all registration methods for all subjects and the correlation and strength (strength meaning magnitude, i.e. higher strength would mean that a small change in one parameter will result in a large change in the other) between the geometrical and sensitivity accuracy are generated for each region. An example of these errors in a relatively highly correlated and low correlated region is shown in Figure 7.13 and 7.14. For the high correlation region (region 2) with R^2=0.95, the basic-4-landmark registration and full head landmark nP2P registration have the lowest geometrical error (~2 +/- 0.5mm). They also have the lowest sensitivity error (~35 +/- 7 %). Line fitting registration has the highest geometrical error (~3 mm) and sensitivity error (~60%). For this region, there is a clear linear relationship between the geometrical and the sensitivity accuracy for each of the registration methods. For the low correlation region (region 6) with R^2=0.78, full head landmark nP2P registration have the lowest geometrical error (~1.5mm) and the lowest sensitivity error (~30%). But the EEG 19 and 40 landmark based registration methods also have a relatively low geometrical error (~1.7mm) and sensitivity error (~30%). In this region, there are no significant advantage in the accuracy of the geometrical and sensitivity among the registration methods. The full head landmark P2P and ICP registration and the line-fitting registration have a ~1.7 (+/- 1) mm geometry error and ~40 (+/- 20) % sensitivity error showing the largest accuracy difference across all of the 24 subjects. The basic-4 landmark registration with the highest geometrical error (~6.2 mm) and the highest sensitivity error (~68%) has a clear disadvantage among all of the registration methods. However there is no clear linear relationship between geometrical and the sensitivity accuracy from the registration methods.

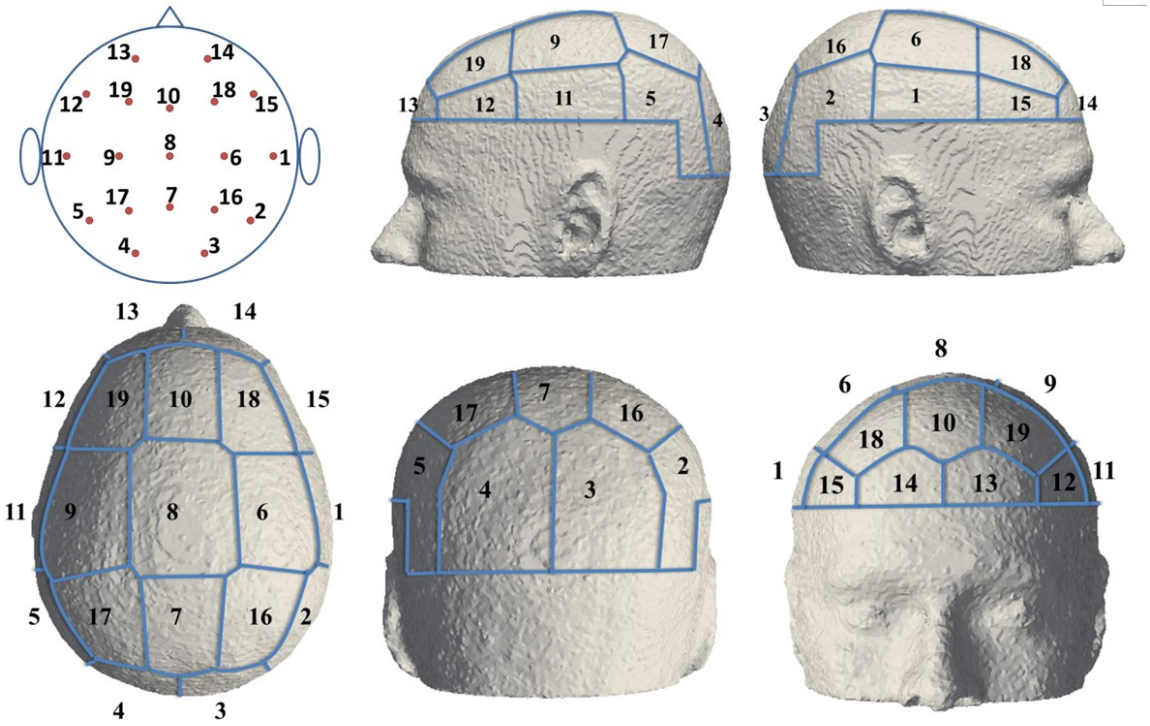

Figure 7.12. Outline of the EEG 10/20 based head regions within the ROI for geometrical and sensitivity analysis.

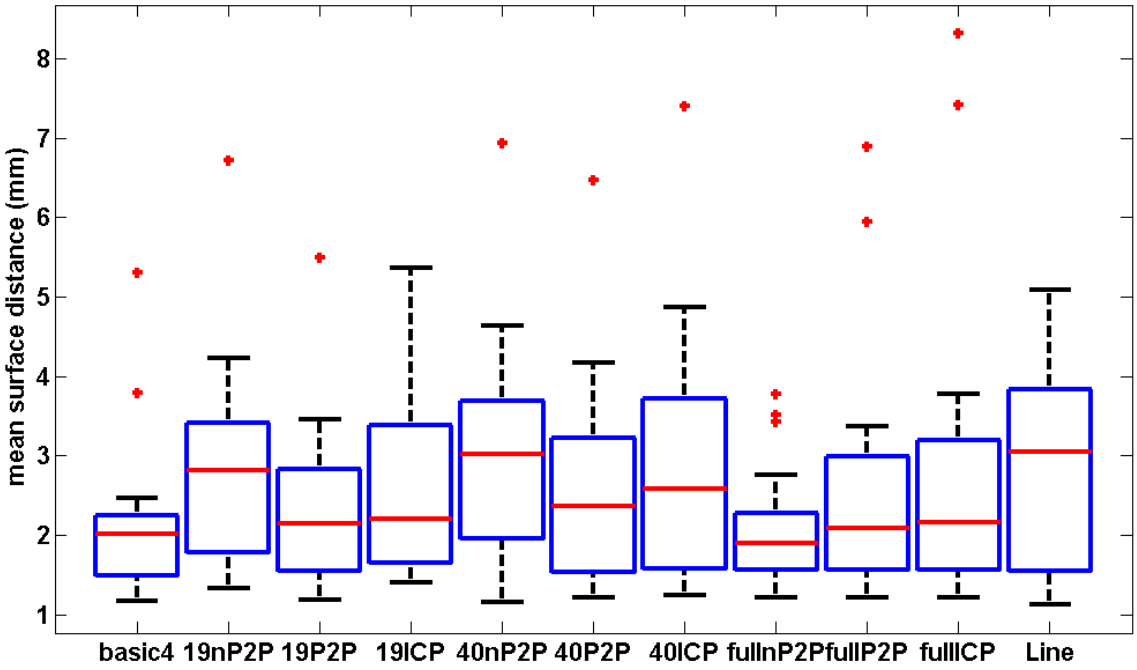

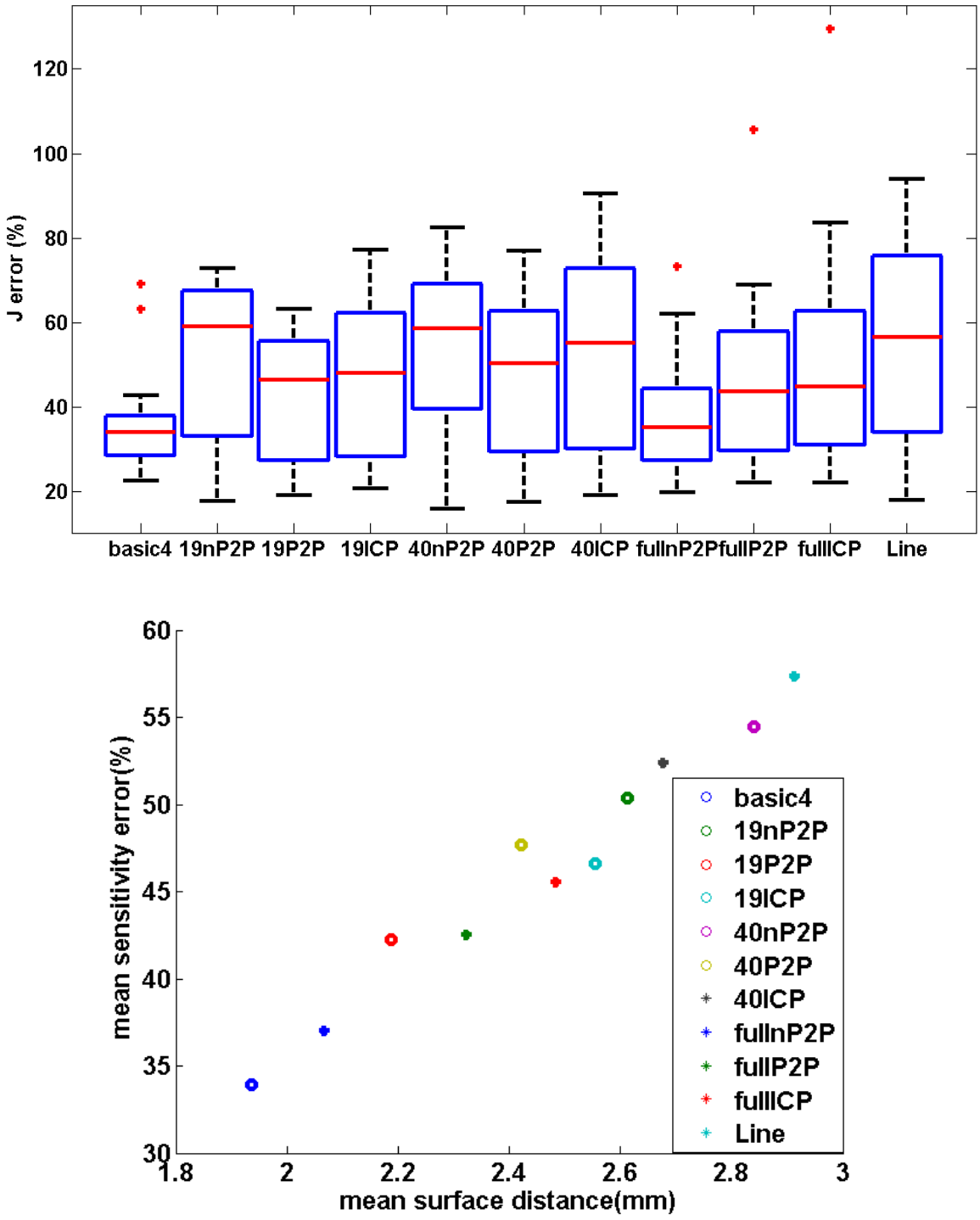

Figure 7.13. Region 2 variation based on Fig 11, showing a high correlation and medium strength (slope). (a) Evaluation of geometrical errors in region 2, (b) Evaluation of sensitivity errors of the cortex in region 2, and (c) Correlation between geometry error and sensitivity errors in region 2.

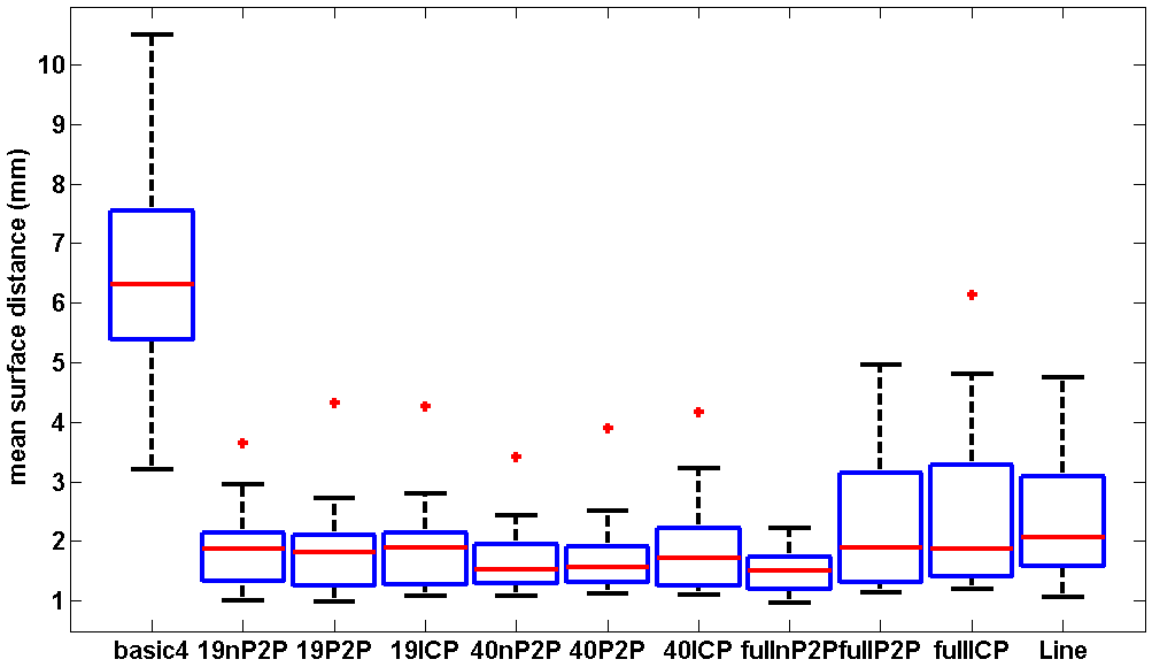
mean surface distance (mm)
10
9
8
7
6
5
4
3
2
1
basic4
19nP2P
19P2P
19lCP
40nP2P
40P2P
40lCP
fullnP2P
fullP2P
fulllCP
Line

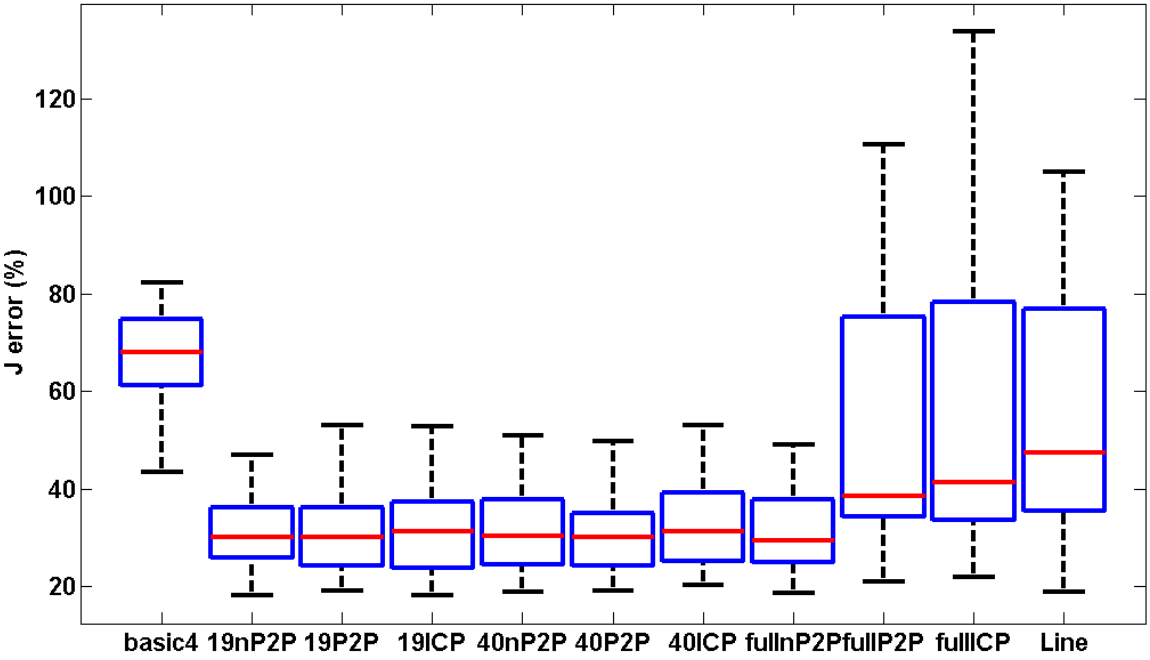
J error (%)
120
100
80
60
40
20
basic4
19nP2P
19P2P
19lCP
40nP2P
40P2P
40lCP
fullnP2P
fullP2P
fulllCP
Line

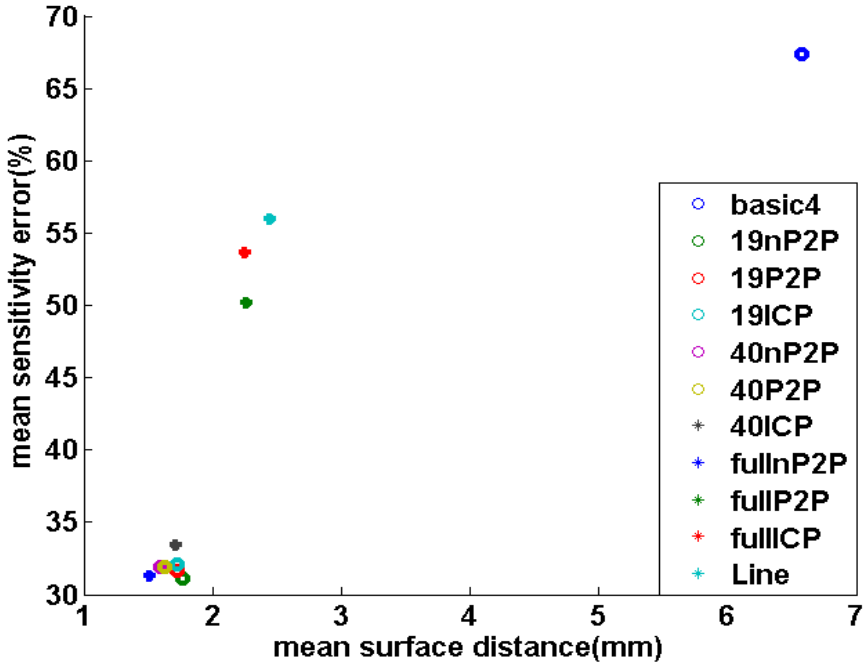

Figure 7.14. Region 6 variation based on Fig 11, showing a low correlation and high strength (slope). (a) Evaluation of geometrical errors in region 6, (b) Evaluation of sensitivity errors of the cortex in region 6, and (c) Correlation between geometry error and sensitivity errors in region 6.

The correlation and strengths of all the 19 brain regions based on all of the 24 subjects with 11 of the registration methods are shown is Figure 7.15 and 7.16. The correlation for the 19 regions varies from $R^2 = 0.7$ to $R^2 = 0.98$ and the strength for 19 regions varies from 4 to 26 (higher the strength, higher the sensitivity error for a given geometrical error). Regions around the top of the head which is near to the central cortex region and the forehead which is near the prefrontal cortex region have lower correlation and lower strength as compared to other head regions. Region 8 in the top middle part of the head has a correlation of $R^2 = 0.78$ and strength of 4 and it is one of the low correlation and low strength regions. Regions around the temples which are near temporal cortex region have higher correlation and higher strengths as compared to other head regions. Region 2 near the right temple has correlation of $R^2 = 0.98$ and a strength of 26 and it is one of highest correlation and high strength regions.

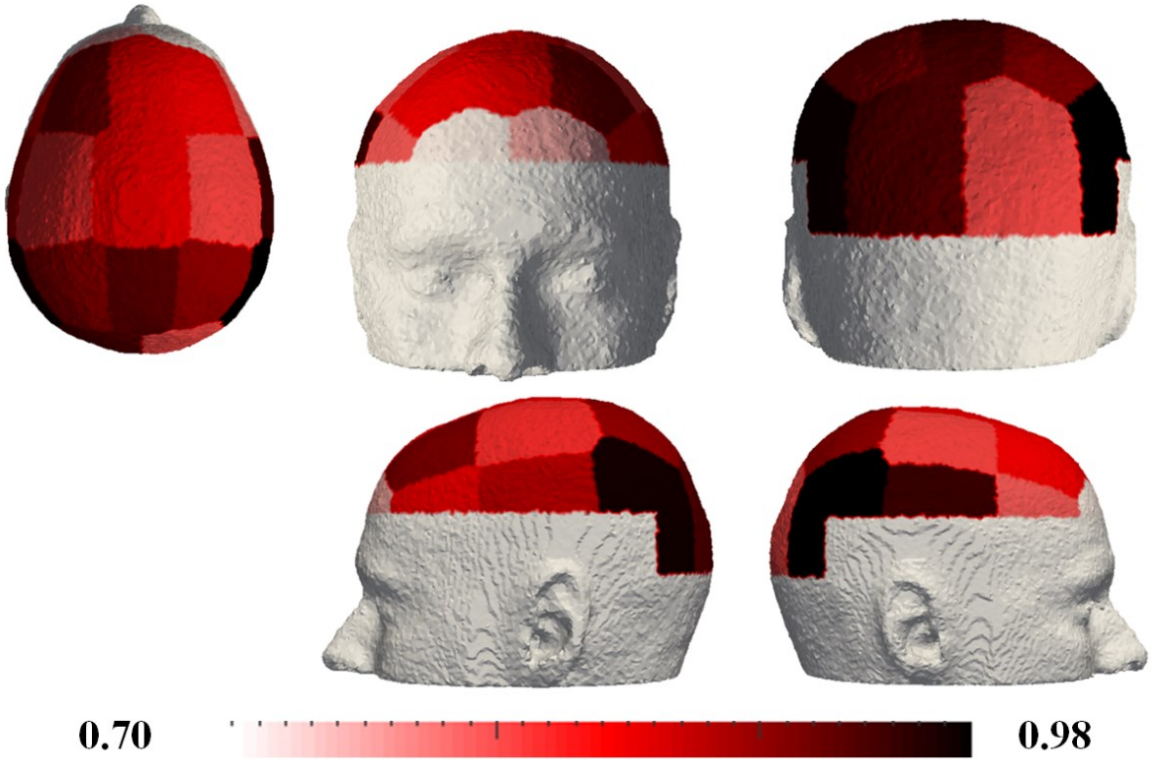

Figure 7.15. Correlation between geometrical and sensitivity errors in all EEG10/20 based head regions.

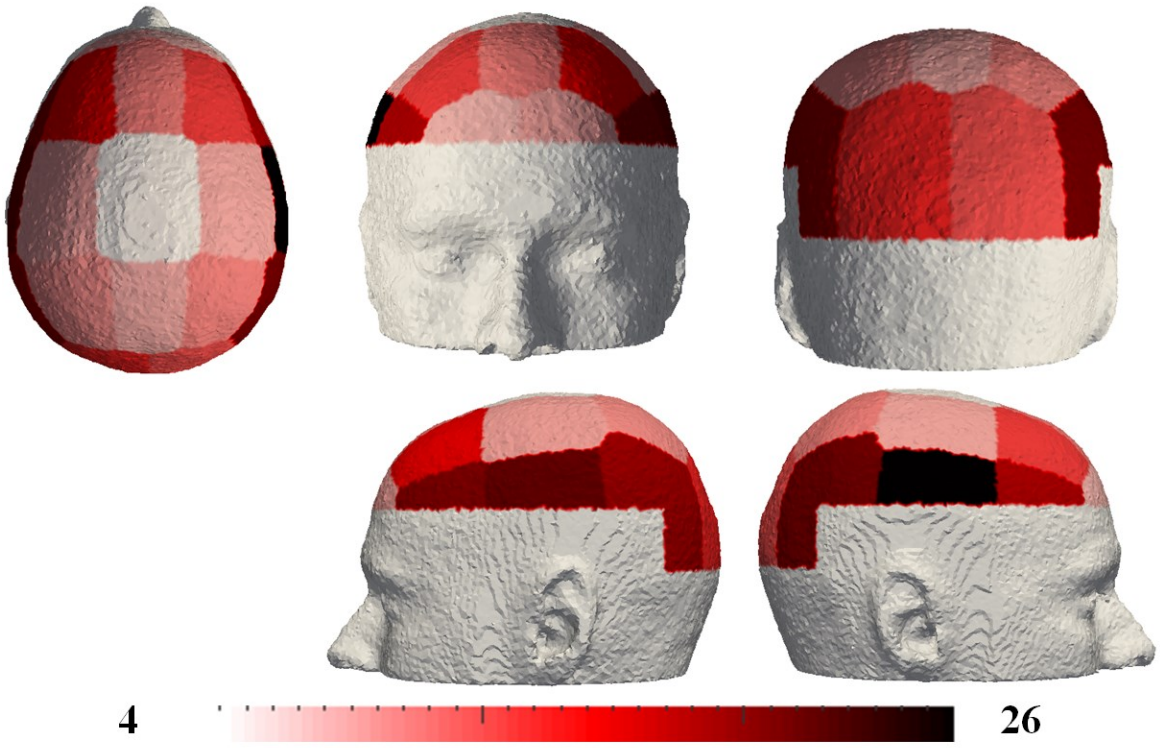

Figure 7.16. Strength of geometrical and sensitivity errors in all EEG10/20 based head regions.

7.4. Discussion

Atlas-based DOT requires a subject-specific model based on the registration of the atlas model. The accuracy of the registration can directly affect the accuracy of the atlas based model, and therefore affect the accuracy of the simulated light propagation. Accuracy of the registration is evaluated using the geometrical accuracy of the registered atlas, and the accuracy of the light propagation is evaluated by the accuracy of the sensitivity matrix as generated from the registered atlas model.

Quantitative evaluation based on the whole head within the source and detector cap region using a high density cap was performed on 24 subjects and different rigid registration methods. Of these registration methods, 11 were based on either basic-4 or EEG-based landmarks and three based on spherical coordinates as derived from three landmark systems. Of these two different methods, generally the spherical coordinate landmark registration methods, even though in a practical setting may be easier to define, did not perform as well as the EEG-based algorithms when considering the geometrical surface errors as well as the calculated sensitivity errors. This could be primarily due to the fact that using the spherical coordinates based algorithms, landmarks as chosen arbitrarily, may not be best suited for registration as compared to well defined EEG-based landmarks.

The full-head-landmark nP2P registration method has the most accurate method on both parameters (geometry and light propagation) among all registration methods. Line fitting registration and basic-4-landmark registration have the least accurate methods on the sensitivity with line fitting registration showing little advantage over basic-4-landmark registration. The full-head-landmark P2P and ICP registration methods show the largest difference among different subjects for both parameter evaluated. All other registration

methods show similar accuracies and they are more accurate than either the full-head-landmark P2P or ICP registration methods based on both evaluation.

The accuracy of the registration is not uniformly distributed through different brain regions. The difference of accuracies between the regions can be caused by the distribution of the landmarks which is the only basis of the optimization in the registration process. For example, the occipital cortex region contains one of the four landmarks in the basic-4-landmark system (the inion) which holds 25% of all landmarks in the registration. Because of this clear advantage over other regions, the occipital cortex region is one of the most accurate registered regions based on the registration method with basic-4-landmark system. However, the occipital cortex region does not show such advantage when using a uniformly distributed landmark system such as the EEG19 landmark system. In the EEG19 landmark system, the occipital cortex region contains two of the 19 landmarks which holds only 10.5% of all landmarks in the registration and it does not show a clear advantage over other regions. Furthermore, the location and extraction of the EEG 19 landmark can introduce additional spatial estimation errors [277, 307], which can also decrease the registration accuracy.

Although there is no clear linear relationship between the accuracies of geometry and light propagation, there are some similarities between the registration methods on both evaluation criteria. The results from the region-based correlation analyses of the two measures of accuracies shows that the correlation value R^2 varies from 0.7 to 0.98 through all of the defined 19 brain regions with most regions having a relatively high correlation. Therefore, the most suitable registration methods based on ROI can be selected based on the geometrical registration accuracy in ROI. The two regions on the forehead show the lowest correlation value as these two regions contain some features which are hard to register. This can increase the geometrical inaccuracy in this region without large effects on the sensitivity accuracy.

Based on the analysis above, the most appropriate registration method varies for activities located in different functional brain regions. For example, full-head-landmark nP2P registration method is the most accurate method for the central cortex region while basic-4-landmark registration method is the most accurate method for the temporal cortex region. Therefore the registration method should be selected based on the location of the brain activities. For the whole cortex recovery, the full- head-landmark nP2P registration method is the most accurate method. However the extraction of the full-head-landmark and the registration process are more time consuming than the other registration methods. Since the EEG19 registration based methods with small disadvantage in the registration accuracy is more efficient as compared to the full-head-landmark nP2P registration method, it is the most appropriate registration method for the whole cortex recovery. Although there is little difference in the accuracy between EEG19 ICP, EEG19 P2P and EEG19 nP2P registration methods, the iterative algorithms are more computationally demanding than the non-iterative algorithms. Therefore EEG19 nP2P registration method is a more efficient method as compared to EEG19 P2P and EEG19 ICP registration methods. We have previously shown that an error of ~30% within the sensitivity matrix was acceptable for the recovery of focal activations from the visual cortex with less than 4.5 mm accuracy in localisation [34]. It is therefore expected that similar results can be achieved for the whole cortex imaging using the EEG19 nP2P registration method.

7.5. Conclusions

Atlas-based DOT in brain activation recovery which is not constrained by the information of internal structure of the subject and relies only on the NIR data is an emerging functional neuroimaging technology. The registration accuracy and its effect on the recovery result have been investigated in the past few years, which have been focused on the registration accuracy

and recovery accuracy in localized areas [9-11]. There are also studies of the comparison between non-rigid registration and rigid registration methods for human head [22, 211]. In this chapter, 19 rigid registration methods are evaluated and compared with the registration and the sensitivity accuracies analysed based on the whole head. It is shown that DOT recovery based on atlas model and surface landmark can provide recovery result with acceptable accuracy for the whole human cortex. It also demonstrates that a typical landmark based registration method such as EEG19 nP2P registration has an acceptable accuracy over the whole cortex region. But appropriate registration methods with higher accuracy for the recovery of certain brain activation under investigation should be selected based on the functional brain regions involved, and the appropriate registration methods can be selected based on the geometrical registration accuracy in ROI.

Both Chapter 6 and Chapter 7 are evaluation and comparison of registration methods for DOT recovery of brain functional activation. Chapter 6 is focused on selecting an optimal registration method for recovery brain activation within a single cortex region whereas chapter 7 evaluated the registration methods based on the whole cortex region. Based on the comparison between different brain regions from chapter 7 and the comparison between the three evaluation methods from chapter 6, the surface geometrical error can be used as a selection criterion for the optimal registration method based on most brain regions.

Since only activations in the visual cortex region is recovered and evaluated in this study, it would be of benefit to investigate the recovery accuracy of activations in other cortex region based on different registration methods. The connected cortex regions are sometime imaged simultaneously during function brain imaging. It would be of benefit to evaluate registration methods based on several connected cortex region.

DOT recovery process of the whole cortex activation is extremely time and memory consuming. The convention sensitivity generation process for the subject meshes used in this chapter with ~400,000 nodes and ~3500 source/detector pairs can takes ~ 15 hours and ~10 GBytes memory, and for a typical head mesh with ~235,000 nodes and ~3500 source/detector pairs can takes ~ 3 hours and ~6 GBytes memory. An efficient sensitivity generation which increases the time and storage efficiency is presented in the following chapter.

CHAPTER 8: A FAST AND EFFICIENT IMAGE RECONSTRUCTION FOR HD DOT IMAGING

8.1. Introduction

Real-time imaging of the human brain is an important technique within neuroimaging which has been used in the study of brain activation during interactive tasks [308, 309], analysis of networks between different functional brain regions during complex movements and emotions [310-313], and monitoring whole brain state for spontaneous activation such as sleep, and changes between tiredness and alertness [314]. It provides the opportunity of observing brain processes during physical and mental experience, guiding medical and behavioural therapies and assisting the rehabilitation of some disorders and diseases such as depression, schizophrenia, and stroke [16, 315, 316]. Since immediate feedback is available during the imaging process, some brain–computer interfacing (BCI) systems are designed based on real time brain imaging [311, 317-319]. The BCI systems analyse brain activity data and react to the findings in real-time. It is an alternative communication and environment control tool for disabled patients.

EEG and NIRS, as described in chapter 2 and chapter 7, are the most commonly used real-time brain imaging modalities. They have been used to track and classify brain activities during complex motor tasks, such as alternating bilateral self-paced finger tapping task; monitoring brain activation during different stages of sleep [4]; and develop BCI environmental control systems [317, 318]. However, EEG and NIRS lack spatial information, and have limitations on the region-based analysis. Real-time fMRI as described in chapter 2 has been used to observe the self-regulation of activity in circumscribed regions and emotion

networks, and has also been used to analyse the neuro-feedback of treatment for patients with attention deficit and hyperactivity disorder (ADHD) [312, 319-323]. However, since MRI is not suitable for patients with electronic implants such as pacemaker and has some limitations for infants and patients with claustrophobia, the application of real-time fMRI is also limited.

Diffuse optical tomography (DOT) ,as described in chapter 2 6 and 7, is a low-cost, portable imaging system as compared to other brain imaging techniques and can be used for infants and hospitalised patients [3, 7]. Currently, the DOT recovery process for the whole head can take several hours and becomes more computationally expensive as the size of the region of interest (domain) and number of source and detectors increases. Real-time DOT imaging therefore relies on the reduction of processing time and previous studies of fast DOT recovery have been largely focused on the inverse process. The reduction of recovered parameter density based on a coarse reconstruction basis and adaptive meshing algorithms have been shown to increase the time-efficiency for the recovery process [324-327]. A sensitivity matrix reduction method (where the sensitivity matrix is defined in chapter 2) for the inverse process has also been used to reduce the processing time [304]. Since the inverse problem is highly under-determined, gradient-based optimisation schemes and modified singular value decomposition are also used to increase the efficiency in inverse processing [21, 285, 286, 328]. Parallelisation is one of the most common time reduction methods with efficient DOT recovery with both CPU and GPU based parallelisation were analysed previously [20, 101, 329, 330] highlighting their advantage providing a systematic method of their incorporation is utilised. Although most previous studies are focused on reducing the calculation time of the inverse process, the generation of the forward model and its associated sensitivity matrix for parameter recovery are also worth investigating.

This work is focused on a unique and efficient generation of the sensitivity matrix using the forward model for image reconstruction (inverse model). Two efficient generation processes are developed and evaluated based on a reduced sensitivity matrix and the parallelisation of the calculation process. Time and memory efficiency of these novel efficient generation processes are evaluated based on comparison with the conventional generation process.

8.2. Methods

8.2.1 Sensitivity Matrix

As described in chapter 2, model-based image reconstruction in DOT relies on the use of a model, typically a numerical model based on the FEM to simulate the NIR light propagation within a medium. The volumetric mesh generation of a FEM of the human head [109, 300] , such as the mesh generation approach present in chapter 4, are shown to be achievable on a relatively fast (typically minutes) time-scale. Through the use of a HD-DOT system for the imaging of the whole surface of the cortex, typically FEM with meshes containing over 230,000 nodes are needed to capture, in sufficient detail, the geometry and internal structures of the head. Additionally, our current whole-head clinical system contains ~3500 source/detector pairs for each wavelength (750 and 850 nm) of operation which using conventional techniques (discussed below) are very computationally expensive, as maps of brain activation are derived through the direct calculation and approximate inversion of a wavelength dependant sensitivity matrix [13] .

The sensitivity matrix, as described in chapter 2, contains a set of sensitivity values which are defined as the sensitivity of NIR boundary data of each measurement to a small change in

optical property of each mesh node. For continuous wave (CW) DOT, the sensitivity matrix is defined as:

$$J = \begin{bmatrix} \frac{\partial lnI_1}{\partial \mu_{a_1}} & \frac{\partial lnI_1}{\partial \mu_{a_2}} & \cdots & \frac{\partial lnI_1}{\partial \mu_{a_{NN}}} \\ \frac{\partial lnI_2}{\partial \mu_{a_1}} & \frac{\partial lnI_2}{\partial \mu_{a_2}} & \cdots & \frac{\partial lnI_2}{\partial \mu_{a_{NN}}} \\ \cdots & \cdots & \cdots & \cdots \\ \frac{\partial lnI_{NM}}{\partial \mu_{a_1}} & \frac{\partial lnI_{NM}}{\partial \mu_{a_2}} & \cdots & \frac{\partial lnI_{NM}}{\partial \mu_{a_{NN}}} \end{bmatrix} \tag{8.1}$$

where *lnI* is the log amplitude of boundary data, μ_a is the absorption property at a given wavelength, *NN* is the number of nodes in the FEM mesh and *NM* is the number of measurement. Since DOT is a highly under-determined and ill-posed problem (*NN* >> *NM*), the image recovery step can be defined as:

$$\Delta\mu = \tilde{j}^T(\tilde{J}\tilde{j}^T + \alpha I)^{-1}\Delta y \tag{8.2}$$

Where

$$\tilde{J} = \frac{J}{diag\left(\sqrt{diag(J^TJ) + \beta\left(max\left(diag(J^TJ)\right)\right)}\right)}$$

$\propto$ is the Tikhonov regularisation parameter, β is the spatial regularisation factor, with $\propto = 0.01, \beta = 0.01$ and *I* is the identity matrix [13, 23, 278].

The Jacobian is formed using the Adjoint method [331], which takes advantage of reciprocity to construct the matrix entries from the forward model fluence calculations, and is highly efficient as compared to perturbation methods [332] . Using this approach and assuming a continuous wave (CW) system, for a given source (*i*) and detector (*j*) pair, for all nodes (*r*) of a given FEM mesh, the sensitivity for intensity measurements due to absorption can be calculated as [331]

$$J(j,i,r) = \left[\sum_{k|N_k \epsilon \tau(r)} \Phi_k^i \, u_k(r)\right] \times \left[\sum_{k|N_k \epsilon \tau(r)} \Phi_{Adj,k}^j \, u_k(r)\right] \quad (8.3)$$

where Φ^i is the fluence due to source *i* at nodes *k* of an element τ associated with a mesh node *r* and Φ_{Adj}^j is the corresponding Adjoint fluence due to detector *j* with u_k being the associated finite element basis (shape) function. If the forward solution is obtained on a regular voxel grid, where all the FEM nodal spacing is equal and the FEM elements area/volume are also constant, this expression can be simplified to:

$$J(j,i,r) = \Phi^i(r) \times \Phi_{Adj}^j \quad (8.4)$$

However, for a FEM mesh consisting of non-uniform element size and basis functions, this calculation cannot be simplified and the summation as outlined in equation 8.3 must be calculated for all nodal sensitivity values taking into account the finite element basis function for each node; a computationally time consuming task, as it will involve repeated summation and multiplication for each FEM nodal sensitivity calculation. Nonetheless, this simplification (equation 8.4) can be utilized to provide an approximation of the sensitivity values to allow the determination of an effective Region of Interest (ROI) for image reconstruction, as it only involves a point by point multiplication for each nodal value calculations.

Previous studies have shown that only nodes within the region being imaged, which have sensitivity values higher than 1% of the maximum absolute value can affect the DOT recovery [22]. Based on this criterion, it is therefore possible to use the approximation (equation 8.4) to provide the 'effective' ROI for which the more accurate sensitivity matrix can be calculated (equation 8.3) for only the required ROI, therefore dramatically reducing the computational burden. This assumption can be used when the FEM mesh resolution and

element area are such that the created mesh is near-uniform in element size, which is the case in our models using our meshing algorithms outlined elsewhere [109].

Consider, for example a single source/detector pair on a full head model (optical properties shown in Table 6.3 in chapter 6) and the associated sensitivity matrix calculated using both equations 8.3 and 8.4, referred to as ‘Original’ and ‘Approximated’ matrices respectively, Figure 8.1. For each sensitivity distribution, contour plots of relative magnitude based on maximum absolute magnitudes ranging from 10 – 0.0001% is shown. The discrepancies between the two sensitivity matrices are largest for the higher threshold of 10% and smallest for the lower threshold of 0.0001%.

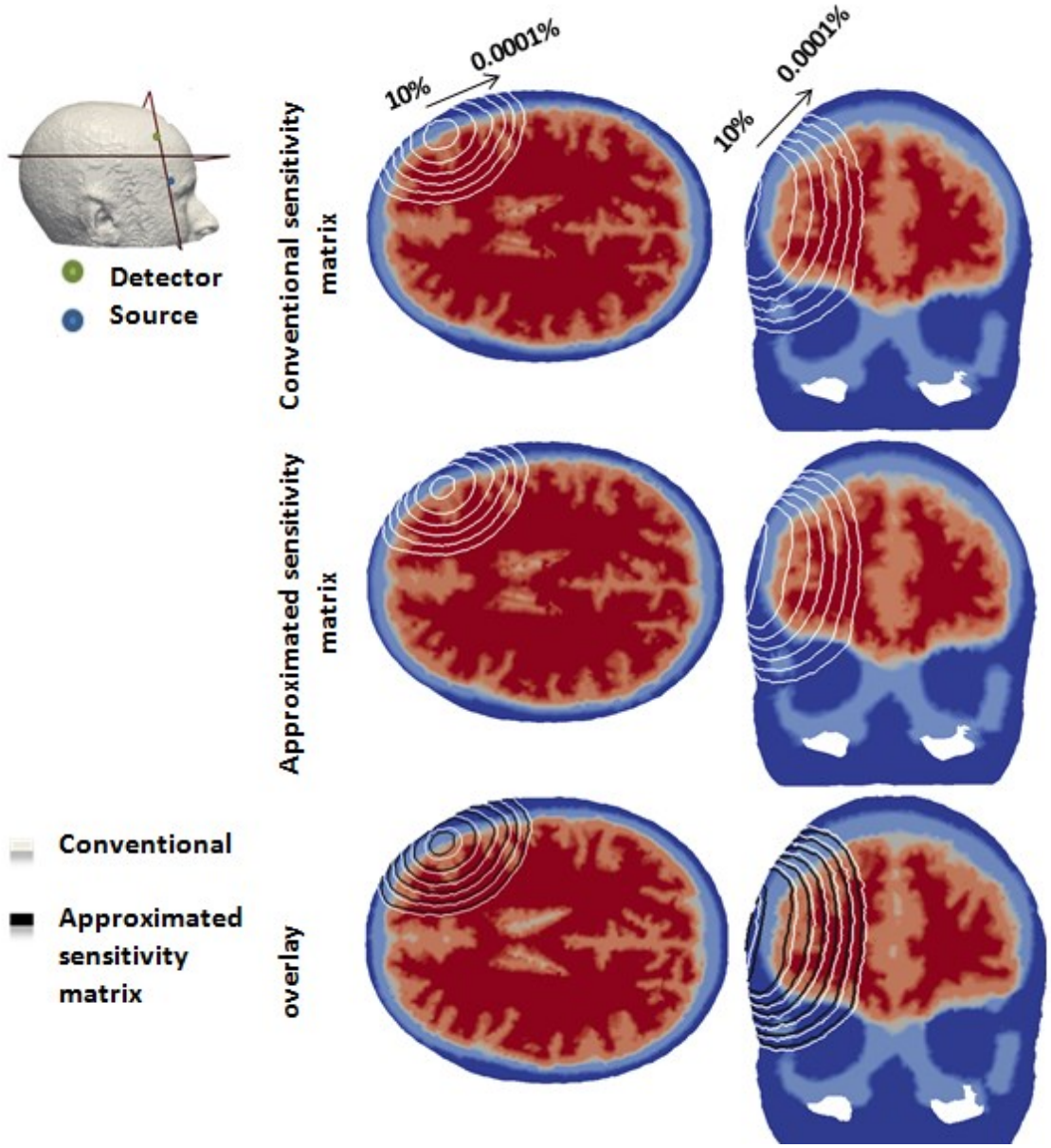

Figure 8.1. An example of the sensitivity calculated for a given source/detector pair on a full head model using conventional and approximated method. Each contour line represents 10 – 0.0001 % of the maximum absolute sensitivity value.

8.2.2 Efficient Sensitivity Matrix

In order to calculate the sensitivity matrix in an efficient framework, without loss of information while reducing the computational burden, an efficient sensitivity matrix calculation can be summarised using the following steps (figure 8.2):

1) For all source/detectors, calculate the fluence (the so called direct and adjoint fields)

2) For all source/detector pairs, calculate the sensitivity values for all nodes using equation 8.4. Note that this is computationally efficient, given that it is a simple point by point multiplication.

3) Determine common nodes within the ROI for all source/detector pairs, within the FEM mesh that have sensitivity above a chosen threshold value.

4) Calculate the absolute sensitivity value for all nodes within the ROI using equation 8.3.

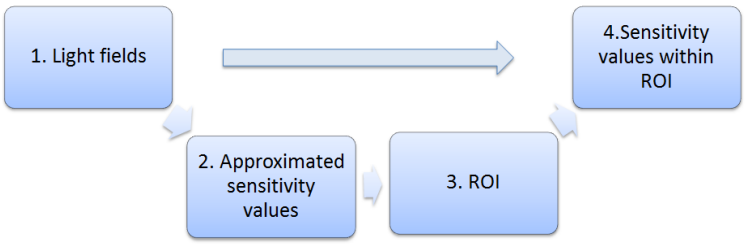

Figure 8.2. A schematic of the generation process of the reduced sensitivity matrix

It is important to point out however, that although using this method, only a portion of the Sensitivity matrix is calculated, which will be shown to be the only effective region for this application of HD-DOT, it still requires the full head fluence calculations due to the complex light propagation in scattering tissue.

8.2.3 Sparse representation

Using the scheme outlined above and given that the majority of nodes within the FEM mesh will have zero contribution to the sensitivity matrix, one further advantage can be taken for the storage of this otherwise large matrix, using ‘sparse matrix’ representation. Given that only a certain portion of the FEM mesh nodes will have a ‘sensitivity’ contribution for each source/detector pair, only such values need to be stored within the memory for the inverse

problem, equation 8.2, where only the row/column index and value for each non-zero entry are stored, thus significantly reducing the memory requirements for an HD-DOT imaging set-up. Consider for example, a FEM head mesh containing ~320,000 nodes with ~3,500 measurement pairs. The sensitivity matrix, using conventional non-sparse representation, (equation 8.1) will require 8.4 GBytes of RAM for storage where the sensitivity of all nodes within the FEM mesh are calculated and stored, regardless of their contribution to the source/detector pairs. However, using the approximation scheme outlined above, together with sparse representation, the same Sensitivity matrix can be stored using sparse representation, where only nodal values above a certain threshold are stored using only ~0.8 GBytes of RAM. Additionally, sparse matrices also have significant advantages in terms of computational efficiency. Unlike operations with full matrices, operations with sparse matrices do not perform unnecessary low-level arithmetic, such as zero-adds. The resulting efficiencies can lead to dramatic improvements in execution time for algorithms working with large amounts of sparse data.

8.2.4 Parallelisation in the sensitivity generation process

Parallelisation, which computes multiple processes simultaneously, is one of the most common methods to reduce the processing time. For example, a fully-parallelisable process distributed over 10 Central processing units (CPU) is ten times faster than based on single CPU. The generation of the sensitivity matrix can also benefit from parallelisation. There are two main calculations within the forward model to which parallelisation can be applied to: 1) The calculation of light fields (direct and adjoint) is processed for each sources and detector separately, therefore calculations for multiple sources and detectors can be run in parallel simultaneously and 2) The calculation of the sensitivity matrix which itself is based on light

fields (equation 8.3) is also processed on a measurement pair basis and can hence also be parallelised.

Both the parallelisation and the reduction based on the ROI (using equation 8.4) for the calculation of the sensitivity matrix can increase the efficiency of the calculation process. Therefore the two ways to increase the efficiency of the calculation of the sensitivity matrix based on the two factors are: 1) The calculation of the reduced sensitivity matrix without parallelisation and 2) the calculation of a reduced sensitivity matrix with parallelisation on sources and detectors for light fields and sensitivity values calculations. The accuracy and efficiency of these two processes are evaluated and compared with the conventional sensitivity generation process.

8.2.5 Simulated study

8.2.5.1 Mesh resolution model accuracy

Throughout this work, we have utilised NIRFAST, an open source light propagation model and image reconstruction toolbox (www.nirfast.org), which utilised linear 3D tetrahedral elements based on the Diffusion Approximation [68, 109]. A feature of FEM based image reconstruction and light propagation models is that the accuracy of the fluence is a function of the chosen mesh resolution and the corresponding finite element basis function. In theory, the solution of FEM approaches the true solution as the area of each FEM elements nears zero; therefore for a given model, the mesh with highest nodal resolution should be more accurate. The problem of mesh resolution versus computational model then becomes two folds: for a complex multi-layered mesh, whereby fine structural features need to be represented, a high density FEM mesh is required, but for fast computational models, a low density mesh is better suited. Numerical errors due to FEM mesh resolutions have previously

been discussed together with algorithms which take into account such numerical model errors as unknown and recoverable parameters [333]. For the purpose of this work, and to highlight the need for high density meshes together with fast and efficient computational models, a multi-layered high density mesh with ~400000 nodes corresponding to ~2450000 linear tetrahedral elements is used as the ground truth. Additionally, eight multi-layered FEM meshes with different node densities are generated based on the same subject containing a total of ~50000 to ~320000 nodes corresponding to ~290000 to ~1930000 linear tetrahedral elements (table). Each model contains five tissue regions (skin, skull, CSF, gray matter and white matter) with the optical properties for each tissue type assigned based on a single wavelength (750 nm) model, Table 6.3. A high-density (HD) source-detector cap is placed on the surface of each head mesh covering the entire cortex [Figure 7.4] containing 158 sources and 166 detectors which are distributed uniformly across the source-detector cap. This gives rise to 3478 measurements, where the 1st to 4th nearest neighbour measurements corresponding to 1.0, 2.2, 3.0, and 3.6 cm source-detector distance respectively are used for the sensitivity matrix calculation [7]. The sensitivity matrices for each model using equation 8.3 and 8.4 are generated based on the same subject and compared to the high resolution (ground truth mesh) sensitivity matrix to calculate percentage accuracy on a nodal basis. The region of interest (ROI) for this evaluation is limited to the gray matter region only and the sensitivity values are mapped onto a high resolution uniform grid using linear interpolated functions for analysis.

Table 8.1. Spatial resolution of the eight meshes

Total nodes	50000	70000	100000	140000	200000	235000	270000	320000
spatial resolution (mm)	3.75	3.39	2.98	2.67	2.35	2.24	2.17	2.02

8.2.5.2 Threshold value

The calculation of the reduced sensitivity matrix is based on the chosen threshold for the effective ROI. A simulation experiment is designed for the determination and selection of a suitable threshold. A layered mesh with ~320000 nodes, corresponding to ~1930000 linear tetrahedral elements is generated based on an MRI scan of a subject head which contains five tissue regions (skin, skull, CSF, gray matter and white matter) with the optical properties for each tissue type assigned based on a single wavelength (750 nm) model [Table 6.3 in chapter 6] As in previous case, a high-density (HD) source-detector cap is placed on the surface of the head mesh covering the entire cortex [Figure 7.4] containing 158 sources and 166 detectors which are distributed uniformly across the source-detector cap giving 3478 measurement pairs.

The sensitivity matrix as outlined in Section 8.2.2 is calculated based on five different thresholds (10%, 1%, 0.1%, 0.01% and 0.001%) and is stored as a sparse matrix. The conventional full sensitivity matrix is also calculated to allow a direct comparison of accuracy which is determined as the percentage error between the new sensitivity matrix (outlined in section 8.2.2) and the conventional full sensitivity matrix.

8.2.5.3 Full-field imaging and parameter recovery

For the analysis of the recovery result based on the reduced sensitivity matrix, a simulation experiment is designed for the recovery of brain activity within the whole cortex. Whole cortex activation, which here is a simulated brain activation that models the same changes in optical coefficients throughout the entire cortex region, is simulated within the same subject mesh as the previous experiment. Boundary data are generated based on the same HD-DOT source-detector cap with noise added to simulate a clinical situation. The brain activation which is modelled as a unit change in optical property (Δy in Equation 8.2) is

reconstructed (Using equations 8.2) based on either the original sensitivity matrix or the reduced sensitivity matrix with a threshold of 0.001%. The recovered results from the two sensitivity matrices, $\Delta\mu$, are evaluated and compared.

8.2.5.4 Computational speed and memory requirements

The final simulation experiment is designed for the evaluation of the time and memory efficiency of the two efficient sensitivity matrix generation processes outlined in section 8.2.4. Eight multi-layered FEM meshes with different node densities are generated based on the same subject. The eight meshes contain a total of ~50000 to ~320000 nodes corresponding to ~290000 to ~1930000 linear tetrahedral elements. The original and the reduced sensitivity matrices are generated for each mesh and the computational speed and memory requirements using each specific technique is calculated. All computational models are performed using MATLAB R2012b on a Workstation running 64 bit Linux (Ubuntu 12.04 LTS) with 16 GBytes RAM using 2 six-core AMD Opteron Processors at 800 MHz.

Memory efficiency of the sensitivity calculation processes as proposed, are evaluated based on the comparison of required memory of the reduced sparse sensitivity matrices and the original sensitivity matrices from the eight meshes. Time efficiency of the proposed sensitivity calculations are also evaluated based on the comparison of average processing times as compared to the conventional sensitivity generation process. For each mesh, all the sensitivity generation processes are performed five times, and the average processing time of each is calculated. Reductions in processing time and memory storage requirements are presented.

8.3. Result and Discussions

Quantitative evaluation of the accuracy of the sensitivity matrix is analysed based on eight different resolution meshes generated from the same subject. The eight meshes each have a different density with the number of nodes varying from 50000 to 320000. The sensitivity matrix is generated for each mesh and used together with a reference sensitivity matrix as generated from a high-density mesh with ~400000 nodes based on the same subject. The accuracy of the sensitivity matrices for each of the eight meshes is evaluated based on the comparison with the reference sensitivity matrix, defined as:

$$J_{err} = \frac{|J_{subj} - J_{ref}|}{J_{ref}} * 100\% \tag{8.5}$$

where J_{err} is error of the sensitivity matrix, J_{subj} is sensitivity matrix of the subject mesh and J_{ref} is the reference sensitivity matrix.

The ROI for this evaluation is defined as the gray matter region of the reference high-resolution sensitivity matrix. The nodal average sensitivity errors in ROI for the eight meshes are shown in Figure 8.3. The accuracy of the sensitivity matrix increases as the density of the nodes in the mesh increases. The sensitivity matrix based on mesh with 320000 nodes has the smallest sensitivity error (~4%) and the sensitivity matrix based on mesh with 50000 nodes has the largest sensitivity error (~10%). This highlights the need for the use of high resolution meshes for model-based HD-DOT and hence the requirement in improving the computational speed.

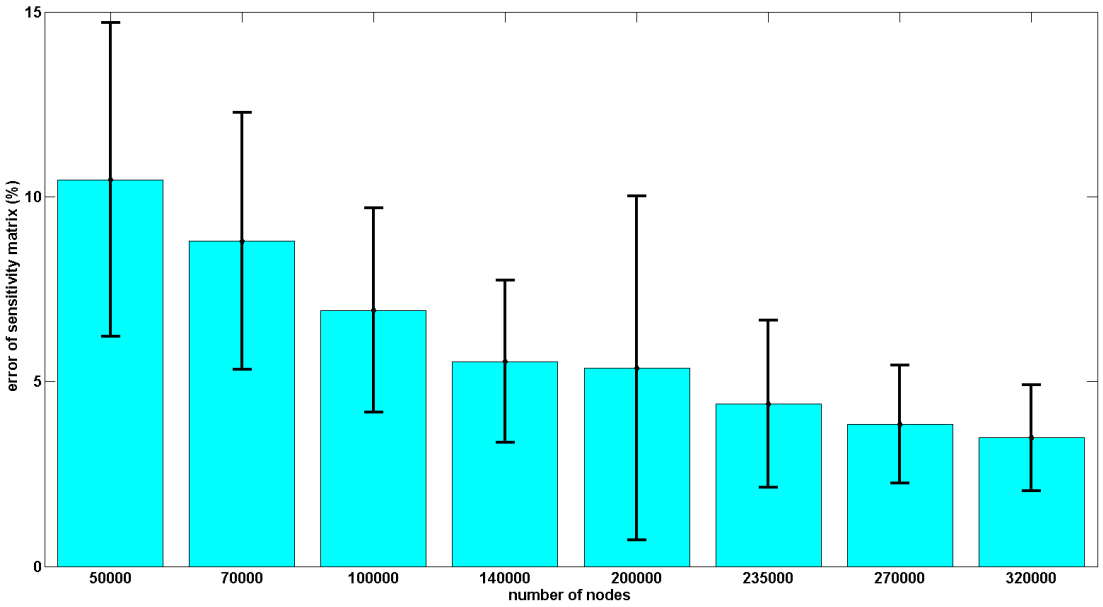

Figure 8.3. Accuracy of the sensitivity matrix as a function of FEM mesh nodal density with respect to ground truth (high density mesh). The accuracy is calculated on a node by node basis and error bars represent the variation across the whole model with the ROI.

Calculation of the reduced sparse sensitivity matrix relies on the approximate sensitivity matrix (equation 8.4) and the associated threshold value chosen to find the nodes within the ROI. The accuracy of this reduced and sparse sensitivity matrix is evaluated based on the HD source and detector cap with multiple measurements, as compared to the full conventional matrix for different threshold values. Five reduced and sparse sensitivity matrices based on different thresholds (10%, 1%, 0.1%, 0.01% and 0.001% of the maximum sensitivity value) and the original sensitivity matrix, are generated using the same mesh. The accuracy of the sensitivity matrices as a percentage error (on nodal basis) using different threshold are calculated with respect to the original matrix and shown in Figure 8.4. For all five reduced sparse sensitivity matrices, deeper tissue such as the gray matter has higher sensitivity error than shallower tissue such as the skin. The maximum sensitivity error in the ROI decreases as the threshold for the reduced sensitivity matrix decreases. Reduced sensitivity matrix based on the 10% threshold has a 100% maximum sensitivity error in the ROI and reduced sparse sensitivity matrix based on 0.001% threshold has a 0.8% maximum sensitivity error. Note that,

as shown in Figure 8.1, the total sensitivity diminished as a function of depth and therefore all area deep within the head, where the total sensitivity due to all source/detector combinations was less than 1% of the absolute maximum sensitivity was not considered to be within the ROI and represented as ‘NaN’ for this analysis.

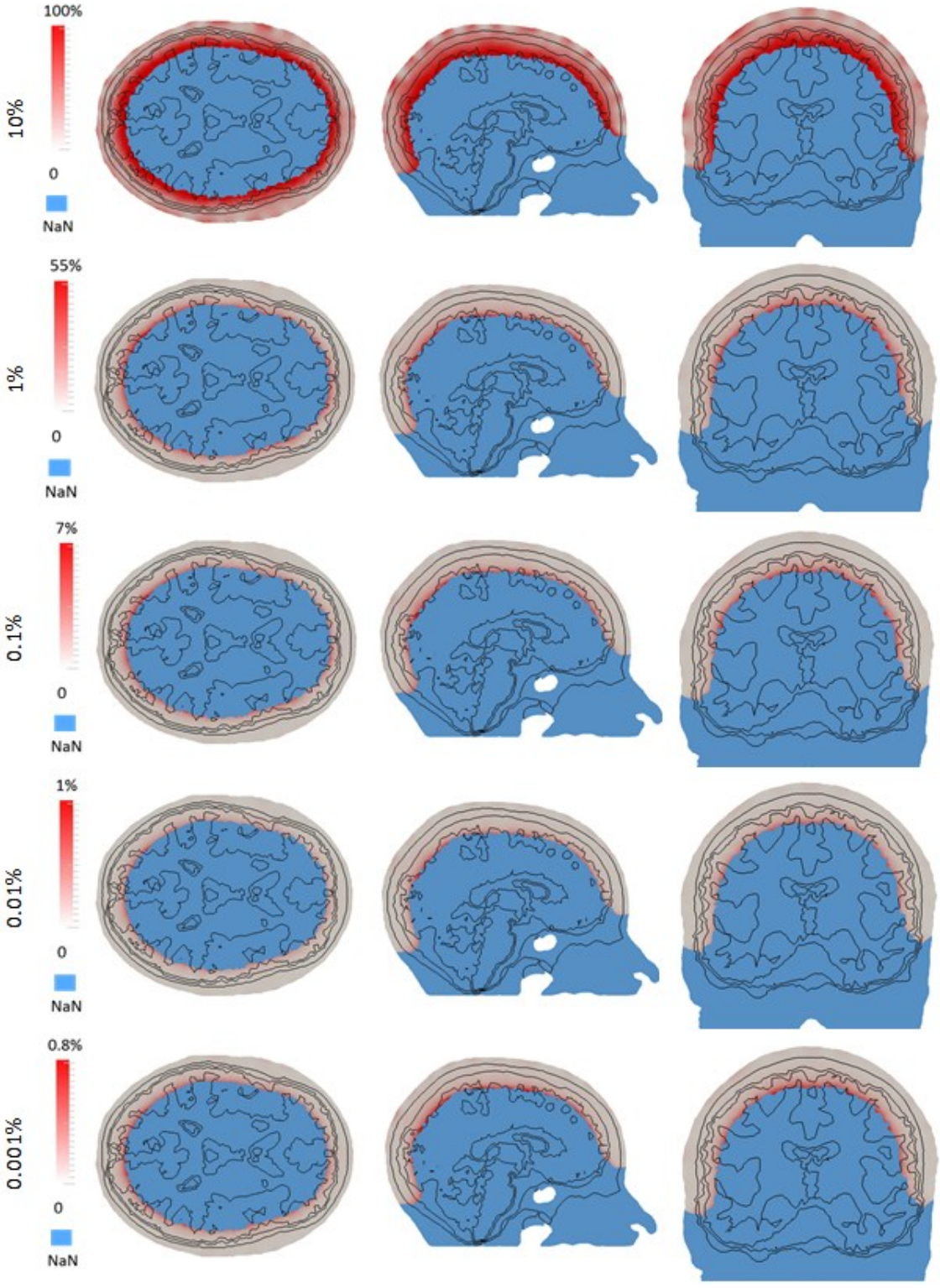

Figure 8.4. An example of sensitivity error for reduced sparse sensitivity matrices with different thresholds as compared to conventional full matrix.

The average sensitivity errors of the five reduced sensitivity matrices for the gray matter within the ROI are shown in Figure 8.5. The average sensitivity error within the ROI (effectively of the gray matter) decreases as the threshold chosen for the calculation of the reduced sparse sensitivity matrix decreases. The reduced sparse sensitivity matrix, based on 10% threshold, has ~65% average sensitivity error and is the least accurate sensitivity matrix. The most accurate of the five reduced sensitivity matrices is the reduced sensitivity matrix based on 0.001% threshold, which has ~0.02% sensitivity error. To ensure the sensitivity values in the entire effective region are accurate, a threshold of 0.001% of the maximum absolute sensitivity value is therefore used for the generation of reduced sensitivity matrix in this work.

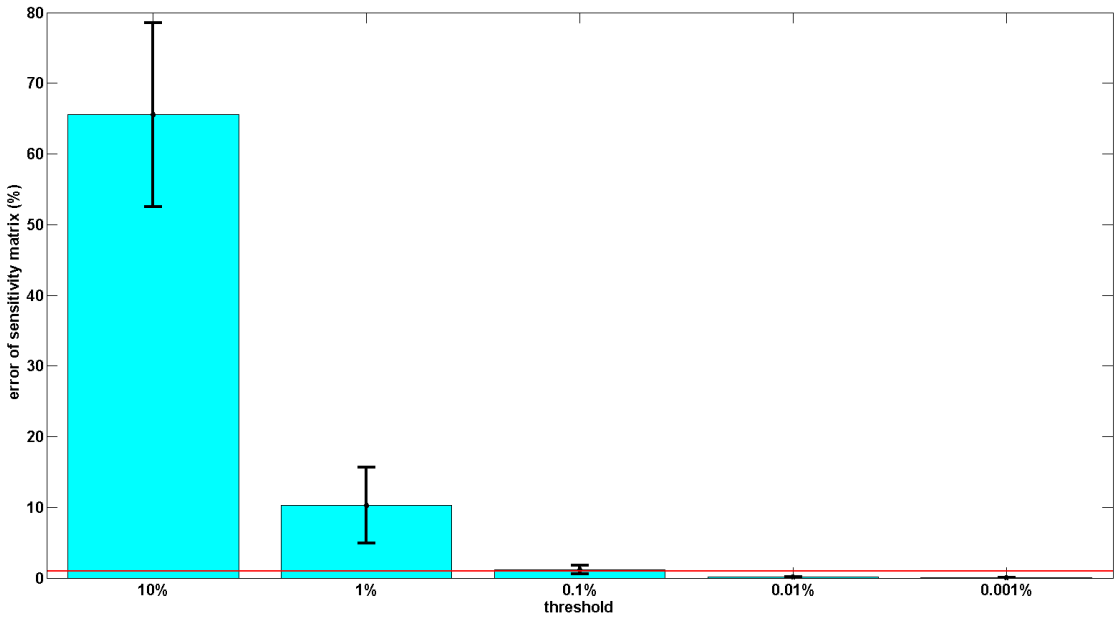

Figure 8.5. Accuracy evaluation of the reduced sparse sensitivity matrices with different thresholds as compared to conventional full matrix. The red line represents the 1% sensitivity threshold.

For the evaluation of the recovery accuracy of the reduced sparse sensitivity matrix, whole cortex activation is simulated and recovered using both the proposed reduced sparse sensitivity matrix and the original sensitivity matrix. The normalized recovery results based on these two sensitivity matrices are shown in Figure 8.6. Recovery results based on the

original sensitivity matrix and reduced sensitivity matrix are visually the same, and they are located in the same region as the simulated activations demonstrating that the reduced sensitivity matrices can be an acceptable alternative for the original sensitivity matrices.

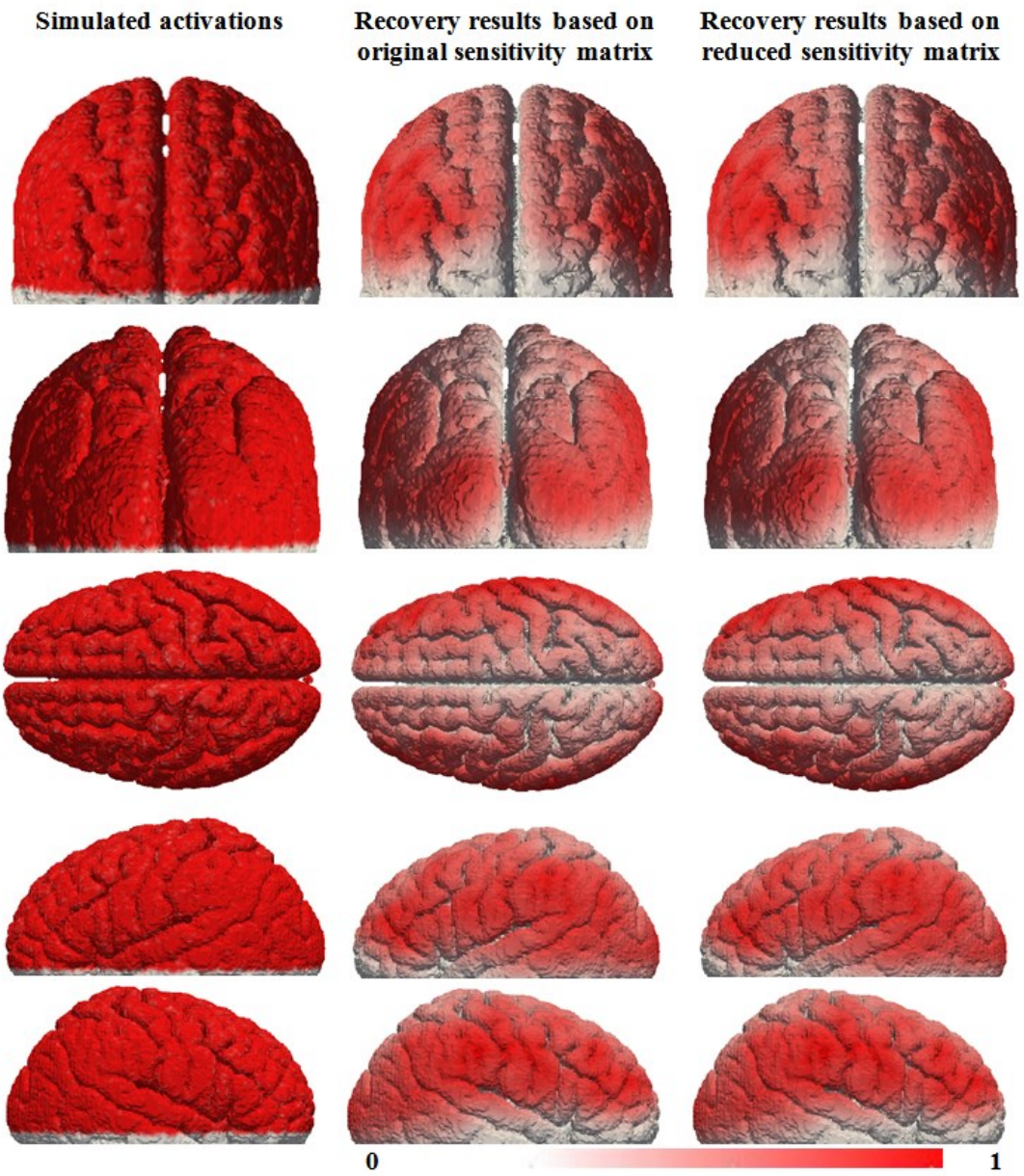

Figure 8.6. Recovery result of whole cortex.

Memory efficiency of the proposed sparse sensitivity calculation is evaluated based on storage memory reduction of the reduced sparse sensitivity matrix as compared to the full

conventional matrix. This is performed based on the reduced sparse sensitivity matrices from the eight different resolution meshes and the comparison with the original sensitivity matrix from the same corresponding mesh, shown in Figure 8.7. For both sensitivity matrices, storage memory increases as the number of nodes in the mesh increases. The mesh with 320000 nodes has the largest RAM requirements for storage with the original sensitivity matrix requiring ~8.4 GBytes and the corresponding largest reduced sensitivity matrix requiring ~0.7 GBytes. The percentage memory reduction of the reduced sensitivity matrixes based on the eight meshes is shown in Figure 8.8. The memory reductions of all eight meshes are higher than 1000% and with the reduction increasing as the number of nodes in the mesh increases. The reduced sensitivity matrix based on the mesh with 320000 nodes has the largest reduction factor amongst the eight meshes (~1240%) and the reduced sensitivity matrix based on mesh with 50000 nodes has the smallest reduction factor (~1020%). Therefore the reduced sensitivity matrix is more memory efficient compared to the original sensitivity matrix, based on the same mesh.

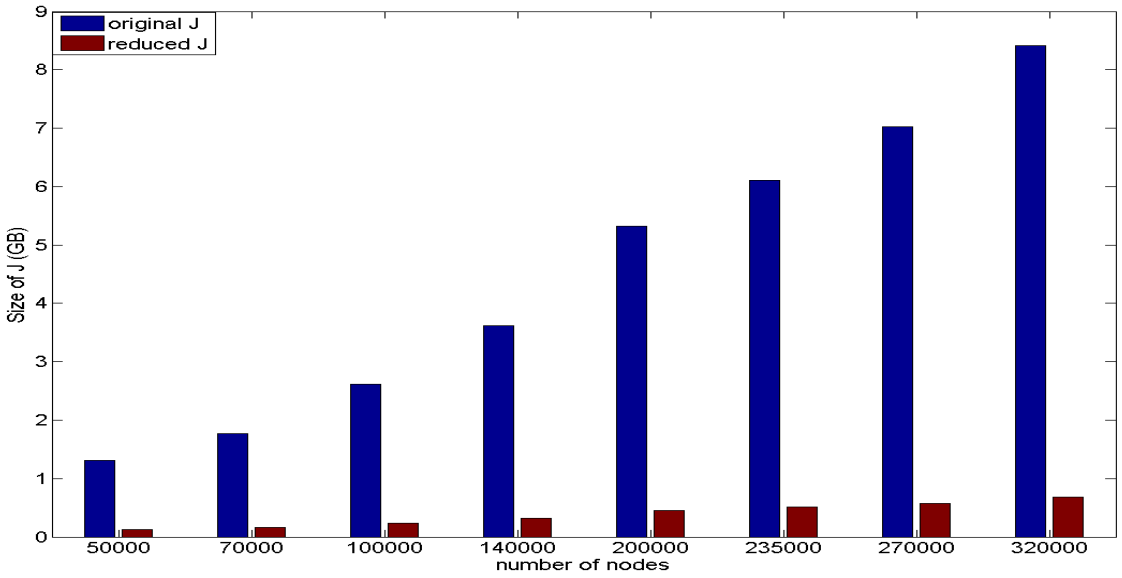

Figure 8.7. Size of the sensitivity matrix for eight meshes.

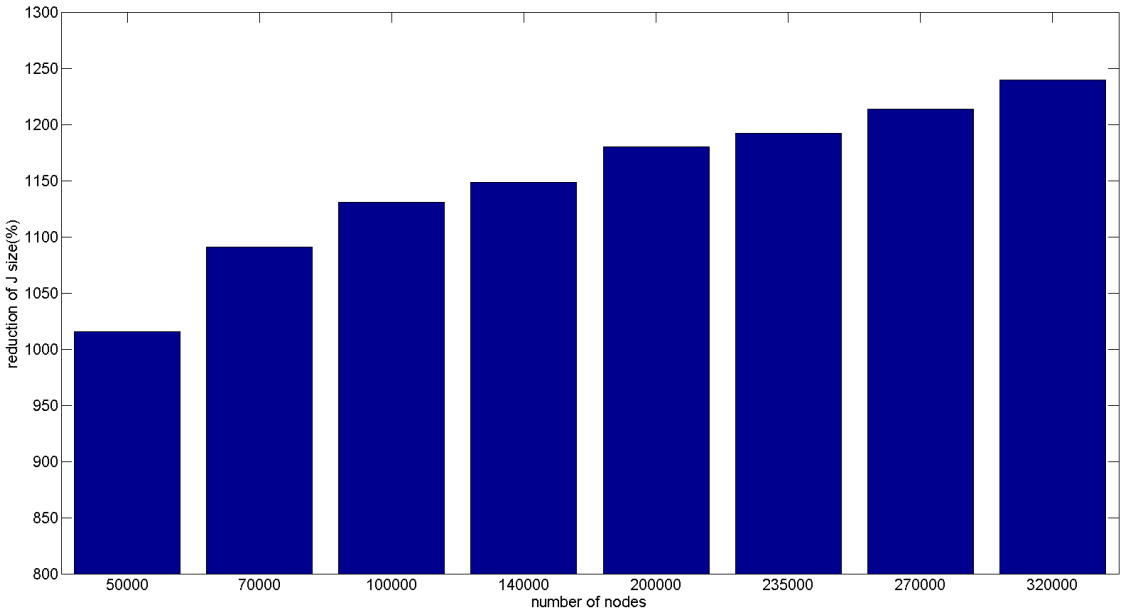

Figure 8.8. Reduction of size of the sensitivity matrix for eight meshes.

The reduced sensitivity matrix utilising parallelisation in the calculation process has also been investigated. Computational processing time for both the light field calculations as well as the sensitivity matrix generation are evaluated separately based on the eight meshes outlined above. Using parallelisation for the generation of light field only, Figure 8.9, the process time varies from <5 minutes to ~1.5 hours and tends to increase as the node density of the mesh increase and the utilization of parallelisation on generation of light fieled has ~300% reduction on processing time for high density meshes. For the generation of the sensitivity matrix, once the light fields have been calculated, the processing time using conventional methods varies from <20 minutes to ~6 hours, Figure 8.10, and it increases as the node density of the meshes increases. The calculation of the reduced sparse sensitivity matrix has ~230% reduction on process time as compared to the conventional full matrix calculation and utilization of parallelisation provides an additional ~200% reduction on processing time.

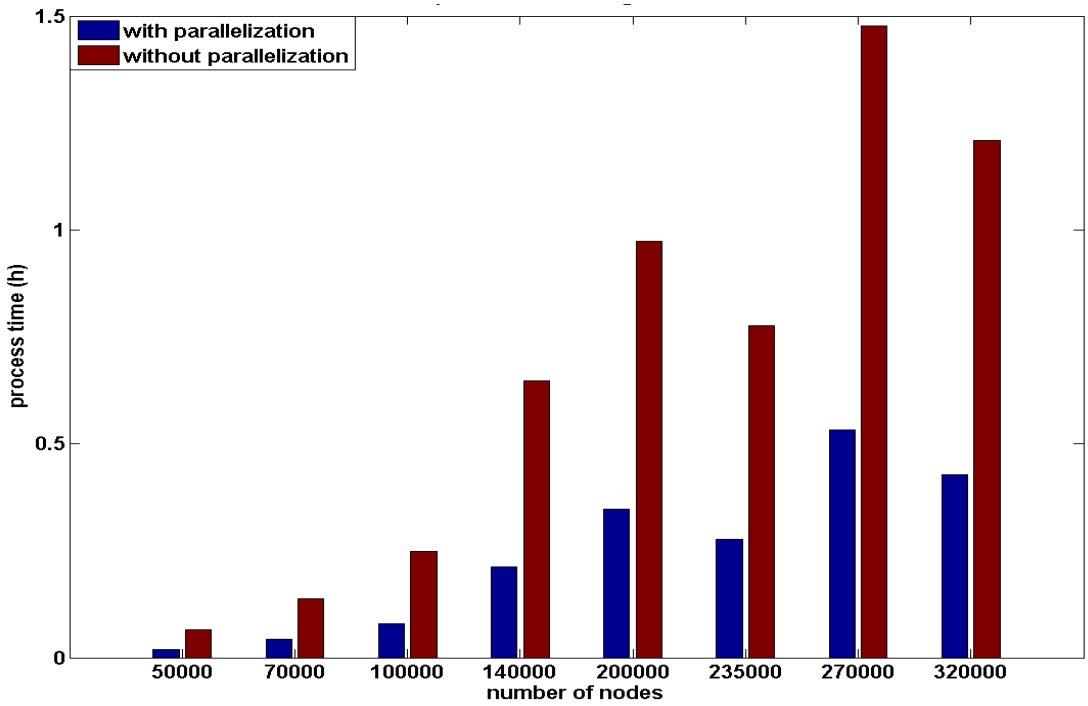

Figure 8.9. Processing time of the light field generation.

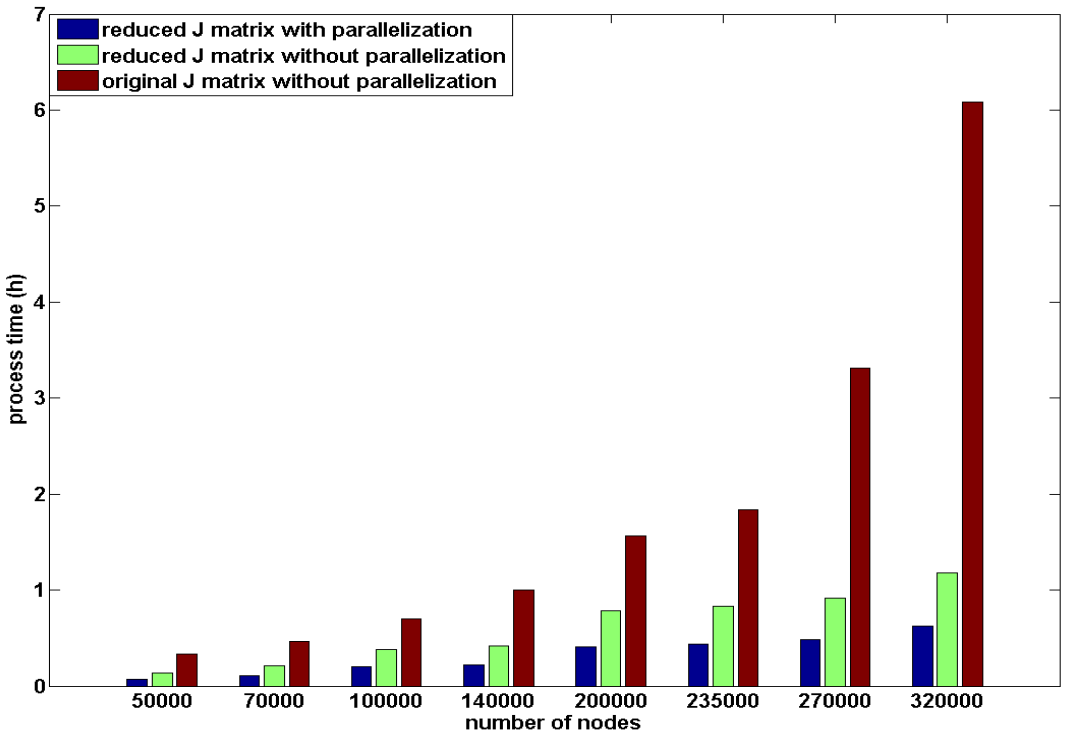

Figure 8.10. Processing time of the sensitivity matrix generation only from calculated light fields and the reduction based on parallelisation and reduced sensitivity matrix.

The utilisation of parallelisation for the field calculations, as well as sensitivity matrix calculation, together with application of the proposed reduced sparse calculations, are compared with conventional non-parallelised calculations, Figure 8.11 to provide an overall whole model computational analysis. For each mesh density, the reduced sparse sensitivity calculations using both parallelisation or not, are more time efficient than the conventional generation process. For the same sensitivity matrix generation process, processing time increases as the node density of the mesh increases. Since the storage memory of the original sensitivity matrix using meshes with 270000 nodes and 320000 nodes are close to the hardware memory limitation of the machine, processing time of the original sensitivity matrices increased dramatically due to memory swap allocations. The mesh with 320000 nodes has the longest processing time for the conventional generation process (~470 minutes) and for the efficient proposed process with parallelisation is ~65 minutes. The mesh with 50000 nodes has the shortest processing time for the conventional generation process (~30 minutes) and ~7 minutes using the proposed process.

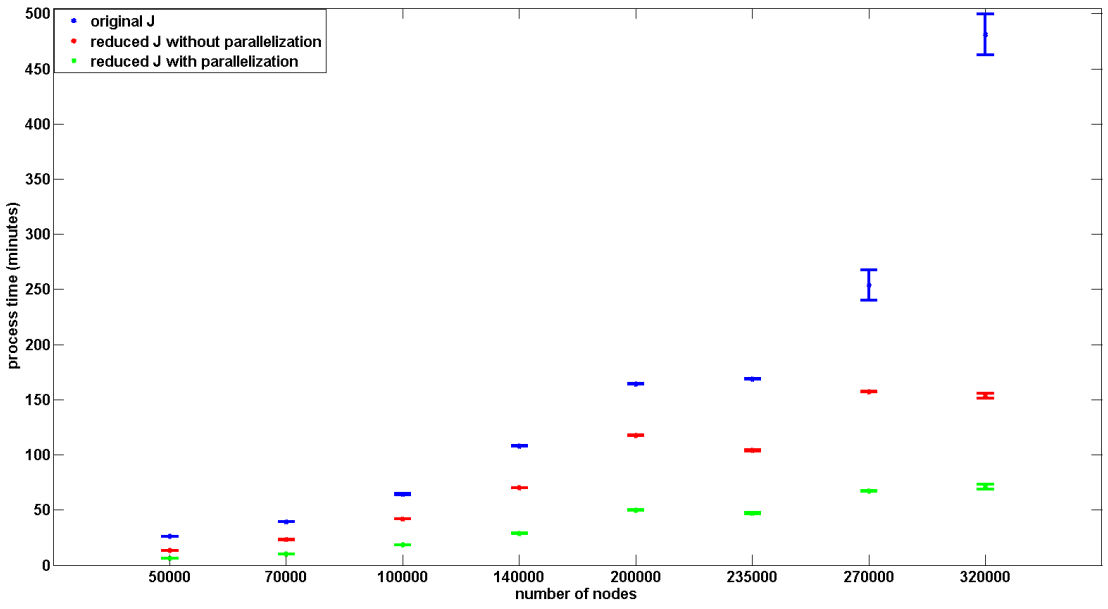

Figure 8.11. Total processing time of sensitivity generation processes.

There isn't a clear linear relationship between the reduction in processing time and the nodes density of the meshes. Except for the mesh with 270000 nodes and 320000 nodes which approach the memory limitation of the machine during the conventional sensitivity generation process, a 25 fold reduction of the processing time of each mesh (five reduced sensitivity generation processes × five conventional generation processes) are similar for each sensitivity generation process. For all eight meshes, the efficient sensitivity generation process without parallelisation has ~170% reduction of process time and the efficient sensitivity generation process with parallelisation has ~400% reduction of process time. Therefore, the proposed sensitivity generation process with parallelisation is the most time efficient generation process.

8.4. Conclusion

Efficient sensitivity generation processes as outlined here rely on the reduced sparse sensitivity matrix representation and parallelisation in the generation process. One of the main steps in the generation of the reduced sensitivity matrix is the selection of the approximate efficient regions. Every node in the ROI should have a sensitivity value higher than the 1% of the maximum absolute sensitivity value and the approximated ROI should cover the entire efficient region as defined by this criterion, since any nodes with less than 1% contribution are not likely to contribute to parameter recovery. Approximate ROIs are selected based on threshold of an approximated and computationally fast sensitivity matrix (equation 8.4), therefore the threshold value can affect the accuracy of the reduced sensitivity matrix. Based on evaluation results, accuracy of the reduced sparse sensitivity matrix increases as the threshold decreases. Compared to the original sensitivity matrix, the reduced sparse sensitivity matrix based on 0.001% threshold has less than 0.8% maximum sensitivity error in the ROI and ~0.02% average sensitivity error within gray matter, which is the sampled area

using our HD-DOT setup. To ensure the sensitivity accuracy in the ROI the reduced sensitivity matrix based on 0.001% threshold is therefore used in this work.

The effect of FEM mesh resolution on accuracy of the sensitivity matrix is also presented. It is shown that as the node density of the mesh increases, the numerical accuracy of the sensitivity matrix also increases, highlighting the need for use of high resolution meshes for model based parameter recovery. The sensitivity matrices based on the mesh with 320000 nodes has the smallest sensitivity error (~4%) and the sensitivity matrices based on the mesh with 50000 nodes have the biggest sensitivity error (~10%).

The effect of using a reduced sparse sensitivity matrix on brain activation recovery is evaluated based on simulated whole cortex (flat field) activation. Recovery results based on the original sensitivity matrix and the reduced sparse sensitivity matrix are compared for the whole cortex, and there is no visual difference on the recovery results based on the two matrices. Therefore, the reduced sparse sensitivity matrix is an acceptable alternative to the original sensitivity matrix.

Compared to the original sensitivity matrix, the reduced sparse sensitivity matrix has clear advantages in the memory and computational time efficiency for the generation process. Based on eight meshes of varying node resolution, storage memory of the original sensitivity matrix and the reduced sparse sensitivity matrix both increase as the node density of the mesh increases. The memory reduction of the reduced sensitivity matrix is higher than 1000% for all eight meshes and it increases as the node density of the mesh increases. The mesh with 320000 nodes has the biggest original sensitivity matrix (~8.4 GB) and the biggest reduced sparse sensitivity matrix (~0.7 GB), yet providing the largest reduction in memory

requirements (~1240%), such that it is possible to calculate and store these matrices for parameter recovery on simple hardware.

Two efficient calculations of the reduced sparse sensitivity matrix are also investigated based on parallelisation within the generation process itself. Processing time for meshes of different resolutions, for both light field calculations as well as the sensitivity matrix calculations have shown that, as expected, parallelisation based on multiple CPUs provide an enhanced computational speed. For all example meshes of varying resolution, the process time increases as the node density of the mesh increases, but there is no linear relationship between the node density of the mesh and the reduction of the processing time, which in part is due to hardware limitation and the use of swap memory in extreme cases. The mesh with 320000 nodes has the longest processing time for the conventional calculation (~470 minutes) and longest processing time for the proposed calculation process with parallelisation (~65 minutes). The mesh with 50000 nodes has the shortest processing time for the (~30 minutes) and shortest processing time for the proposed process with parallelisation (~7 minutes). For all eight meshes, the reduction of the processing time is ~170% using the proposed process without parallelisation and ~400% with parallelisation. The parallelisation approach does not achieve a full 10x speedup because not all calculations in the sensitivity generation process are parallelizable. To be specific, only calculation of the light field values for source and detector and calculation of sensitivity values from light field are parallelised in this study. Therefore, further reduction of calculation time may be achieved by parallelizing more processes in the generation approach**.** Since there are some delicate structures in human brain such as the small folds in the gyri that cannot be represented by low density meshes, the structure of the meshes can become more complex when reaching certain limitations of the node density, again highlighting the need for the utilisation of high density FEM meshes for

model based parameter recovery. Therefore, the process time is not increase monotonically with the number of nodes.

CHAPTER 9: SUMMARY AND FUTURE WORK

This work in general is about atlas-based Diffuse Optical Tomography brain imaging for human adults. DOT brain imaging is a neuroimaging modality which recovers optical properties and monitors functional brain activations by measuring NIR light propagation in the subject. The recovery process of DOT is divided into two steps: generation of the forward model and the inverse processing of the forward data. The subject-specific forward model is usually generated based on brain images of the same subject from an additional imaging modality and the segmentation of these images. A registered atlas model is an acceptable alternative for the subject-specific models. The forward model in the atlas-based DOT recovery is generated based on the tissue classification of the registered atlas model. This work focuses on evaluation of registration methods for atlas-based DOT brain imaging and design of an efficient approach for the generation of sensitivity matrix based on the FEM mesh.

9.1. Summary

This thesis consists of 9 chapters.

Chapter 1 is the introduction of the work undertaken. It presents the three problems addressed in this work: 1) finding the most suitable registration method for atlas based DOT of a certain cortex region; 2) determining whether the most suitable registration method varies based on region of interest; and 3) designing an efficient recovery approach for DOT recovery. It also shows that these three problems are unique and worth investigating based on related previous studies.

Chapter 2 is a review of different neuroimaging modalities and a brief introduction to DOT brain imaging and the recovery approach of DOT used in this work. From the comparison with other neuroimaging modalities, DOT is a low cost and portable imaging modality which can be used for long-term monitoring of brain activation of subjects such as infants and hospitalised patients. FEM and linear optimization inverse method with Tikhonov regularization are selected in this chapter as suitable methods for the recovery of brain activation in this work. This recovery process is shown to be time efficient with acceptable accuracy for recovery of the complex subjects such as the human brain.

Chapter 3 is the introduction and comparison of commonly used human brain atlases. It presents several atlases in MRI brain imaging. Two single subject based atlases, two atlases for general population and two age-specific atlases are introduced in this chapter. The ICBM 152 atlas which is a MRI-based atlas for general population is selected for the generation of FEM in atlas-based DOT recovery in this work. This atlas is a high resolution model with classified tissue region maps which is suitable for the atlas model in DOT brain activations recovery.

Chapter 4 is the introduction and comparison of commonly used segmentation methods for human brain imaging data. In this chapter, the basic intensity-based segmentation methods, the basic registration-based segmentation methods, and the SPM segmentation method combining intensity and registration-based methods are introduced and compared. The SPM segmentation method is selected for the generation of layered subject head models in this work. A near automatic generation approach for MRI based layered FEM mesh using the SPM segmentation is also discussed in this chapter. This mesh generation approach is fast and user friendly and can be processed with ~15 minutes.

Chapter 5 is the introduction and comparison of commonly used registration methods for the human head. In this chapter, registration methods are presented in four categories based on two different similarity measurements and two different transformation models. Landmark-and curve-based rigid registration is selected for the generation of registered atlas models for atlas-based DOT recovery. Three evaluation methods are compared based on 11 registration methods, and the Closest-Node evaluation method is selected for the evaluation of registration result in this work. The surface landmark-based rigid registration and surface curve-based rigid registrations are suitable for register human brain with only the external geometrical information and Closest-Node evaluation is appropriate for registration between different subjects.

Chapter 6 is the evaluation of registration methods for atlas-based DOT recovery of the visual cortex. It evaluated 11 rigid registration methods based on three evaluation criteria and selected the most suitable registration method for atlas based DOT of the visual cortex, which solved the first problem in chapter 1. For the focal activations in the visual cortex, basic-4 landmark based registration method is the most efficient registration method.

Chapter 7 is the evaluation of registration methods for atlas-based DOT recovery based on the whole cortex and multiple brain regions across the whole head. It evaluated 11 rigid registration methods based on 19 brain regions and whole cortex with two evaluation criteria. It shows that optimal registration varies based on the ROIs for different brain activations, which solved the second problem in chapter 1. The EEG19 nP2P registration method is the suitable efficient method for the whole cortex activation studies, and the optimal registration method can be selected based on the geometrical accuracy of the registration in the ROI.

Chapter 8 presents an efficient generation method for the light propagation approximation based on a reduced sparse sensitivity matrix and parallelisation process. This efficient

generation process improves the storage efficiency by >1000% and time efficiency by ~400% comparing to the conventional approach, which provides a unique solution for the third problem in chapter1.

Chapter 9 (this chapter) is the summary of this work.

9.2. Future work

This work is about evaluation of the registration methods for atlas-based DOT brain imaging and design of an efficient approach for the generation of sensitivity matrix based on FEM mesh. In the study of registration methods for atlas-based DOT, 24 healthy young adults are used as subjects. Further study can be focused on age-specific or disease-specific subject groups where the recovery can be processed based on both general atlas and the specific atlas. The influence of the changes in atlas can be evaluated based on the recovery results. Since only rigid registration methods are evaluated and compared in this work, further comparison can also analysed based on multiple non-rigid registration methods and rigid registration methods. In the study of the efficient generation approach for sensitivity matrix, an efficient process is designed based on reduced sparse sensitivity matrix representation and parallelisation. Further study of the efficient recovery process can investigate the efficient inverse processing based on the reduced sparse sensitivity matrix representation and parallelisation. After the efficient methods for the sensitivity generation and the inverse processing are designed, an efficient recovery approach for the DOT brain imaging can be created.

Besides of the registration accuracy between the atlas model and the subject, difference of the internal structures between the atlas model and the subject also influence the accuracy of recovery result of atlas-based DOT. Different atlas models have been discussed in chapter

4. Recovery of brain activation from DOT can be investigated based the different atlas models such as age-specific atlases in the future work. Since there always exist some inaccuracy in the registration processes, differences in the internal structure of the atlas models may not have significant effect on the recovery result. It is worth investigating that whether using an atlas model from a specific subject group can improve the recovery results further. Human brain atlases have some fine structure in regions such as the cortical sulci which increases the processing time of mesh generation and the recovery process. It is also worth investigating that whether using a simplified atlas model such as a layer model with less structural details can provide acceptable recovery results, while being more computational efficient.

Another important application of atlas in brain analysis is to provide a common space such as MNI space that data from different subjects can be evaluated and compared. With the development in inter-imaging modality analysis, the evaluation and comparison between different subjects and different imaging modalities has become possible. Normally, the imaging data from the same subject with different imaging modalities are first registered to a common imaging modality such as MRI. Then different subjects are registered to the atlas space based on the common imaging modality, which requires at least one common imaging modality for all subjects, which may not be available. A multi-modality atlas which contains data from multiple imaging modalities for the same atlas can be designed in the future, so that each imaging data can be registered to the atlas space directly and the common imaging modalities is not required for the inter-subject inter-modality analysis.

The inter-imaging modality analysis has the potential to increase the image resolution. Since DOT is relatively robust to motions during imaging and can be applied in long-term studies with low financial cost, combining DOT with other imaging modalities such as CT and US may be able increase the spatial resolution and expand the image field. Combining

long-term DOT imaging with a single MRI may be able to reduce the expense of monitoring. The combination of DOT and other imaging modalities are worth investigating.

APPENDIX: STEP-BY-STEP GUIDES OF THE MESH GENERATION PROCEDURE AND TWO MATLAB GUI DESIGNED IN THIS WORK

A1: A step-by-step guide of the near automatic generation approach for layered FEM mesh based subject MRI

A layered FEM mesh can be generated from the subject MRI scans based on the near automatic generation approach in chapter 5. Here attached a step-by-step guide for the generation approach.

Download SPM8 from the SPM website: http://www.fil.ion.ucl.ac.uk/spm/software/

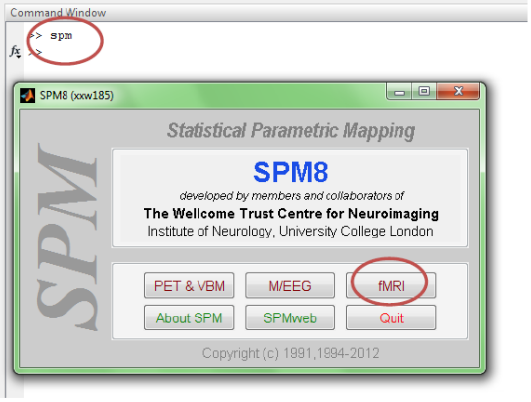

Start SPM8 for MRI by typing: 'spm' into Matlab command and click button 'fMRI'

2. Load MR images

Load MR images by DICOM Import function:
1. Click on the 'DICOM Import'
2. Choose all the DICOM Image
3. Choose an output directory.

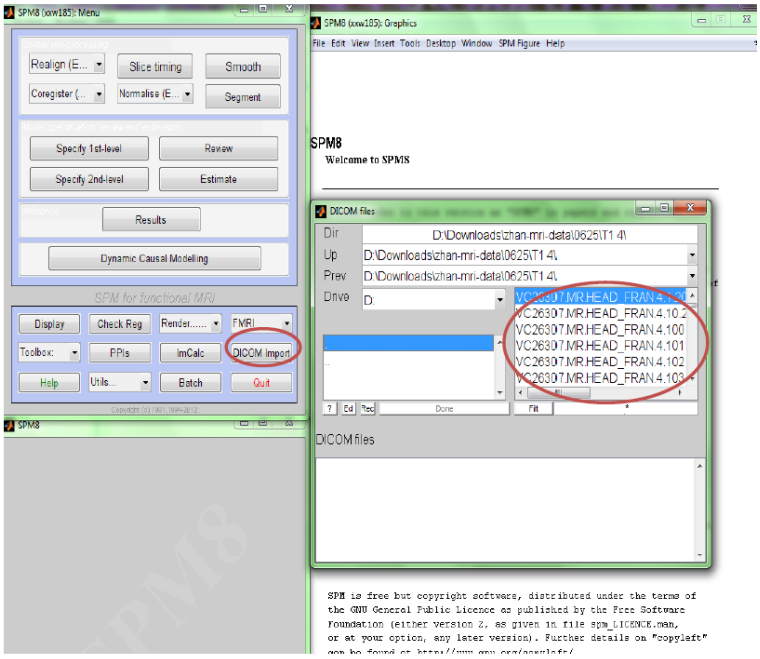

3. View 3D image

Loaded DICOM image is saved as .hdr and .img file. Display and Chesk Reg function can be used for viewing the 3D image.

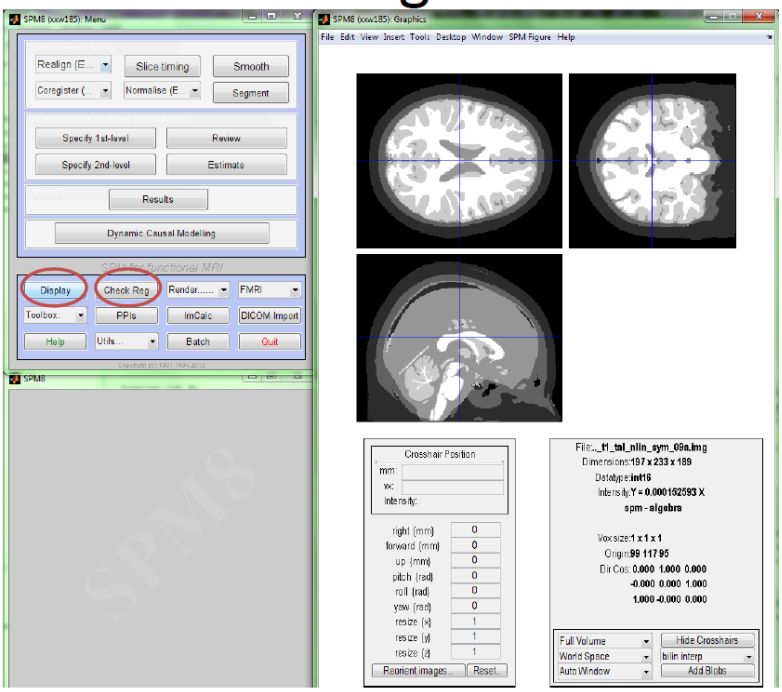

4. Segmentation

Segment brain MRI images by ‘New segment function’. Click ‘Batch’—’SPM’ —’Tools’ —’New segment’

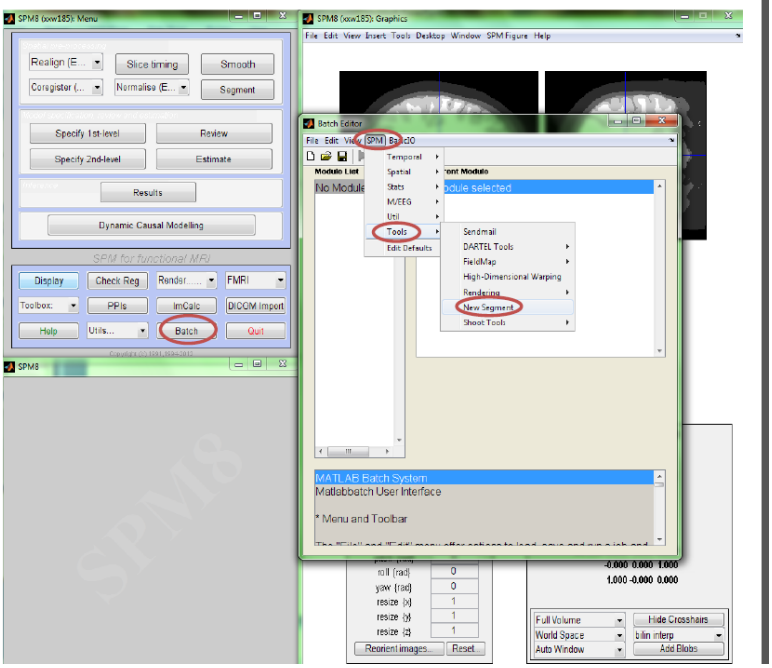

4. Segmentation

Choose the brain MRI image for ‘Data-Channel-volume ‘ and click run. It will create five tissue probability maps for gray matter white matter CSF Skin and Skull by default.

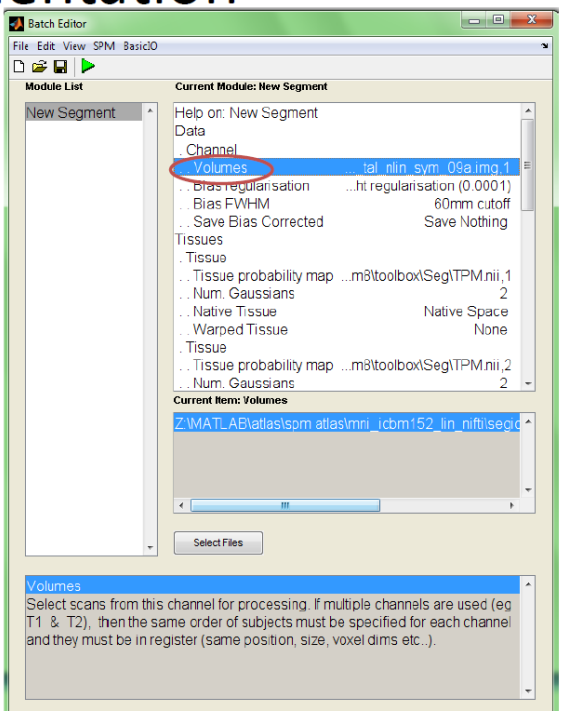

4. Segmentation result

Five tissue probability maps (Gray matter. White matter, CSF ,Skull, Skin) of the subject are generated by the segmentation. 'Check Reg' function can be used to display all 6 image (5 tissue probability maps and the MRI image) together.

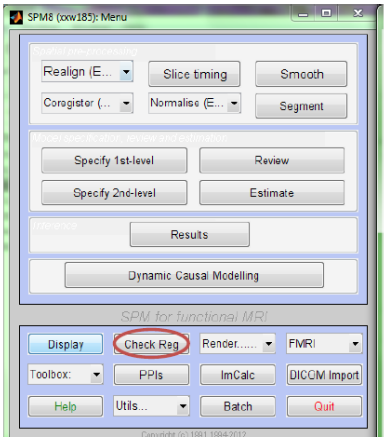

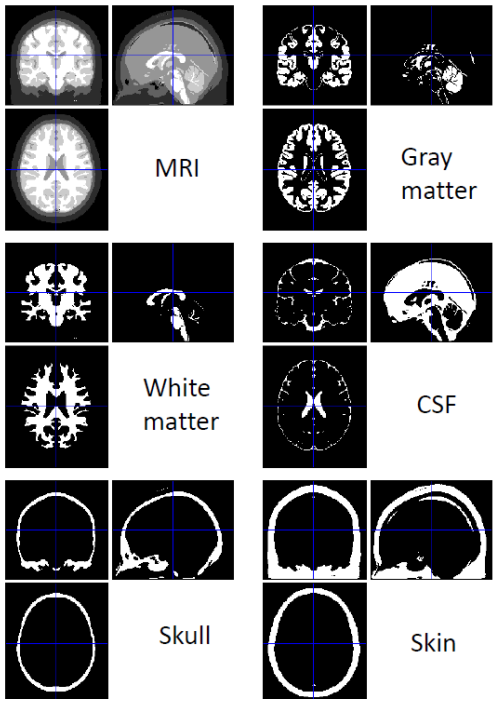

5. Generate segment image

Segment image can be generated based on the 5 tissue probability maps . Each tissue probability maps is threshold to determine the belonging of each pixel to the tissue regions. Each region can be set as different value and over-layered onto one single 3D image.

The threshold, valuing and over layering can be complied using the 'ImCalc' function.

1. For threshold, choose each of the tissue probability maps, set the Expression as 'i1>0.5'.
2. Process the threshold step for all of the 5 tissue probability maps .
3. For valuing and over layering, choose all five output file from the threshold step and set the Expression as 'i1.*5+i2.*4+i3.*3+i4.*2+i5'. It can generate a segment image

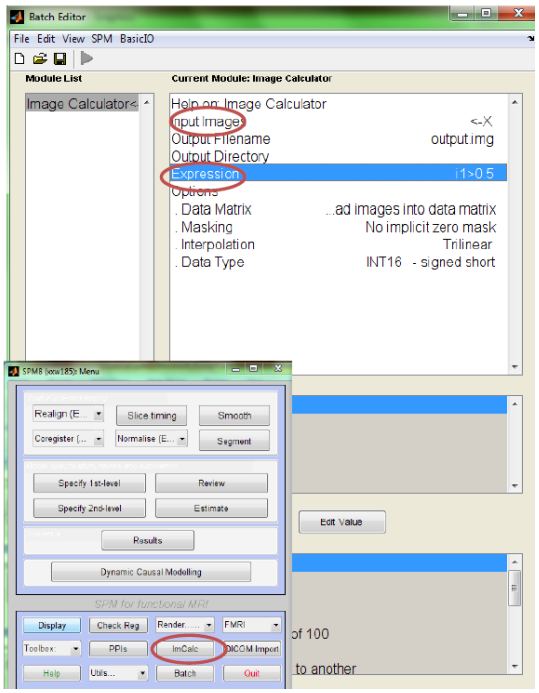

6. Output from SPM

Output the segment 3D image as 2D image series.
1. Display the segment image using 'Check Reg' function.
2. Right click on the image to turn off the crosshair.
3. Using 'Movie tool --- Run' to save image series. Choose the movie direction and set the interval and step size as default. Choose save as image series. It will generate a set of image series

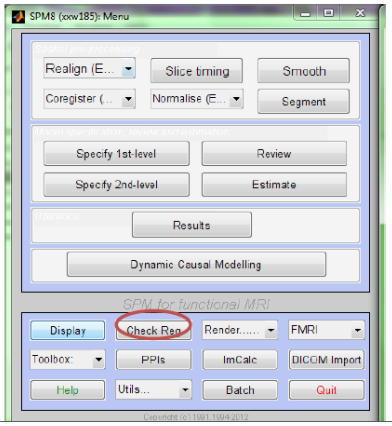

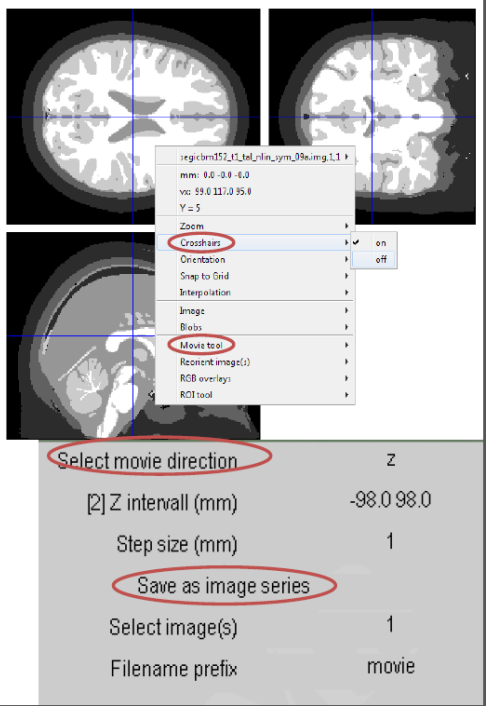

7. Load image series into Nirview

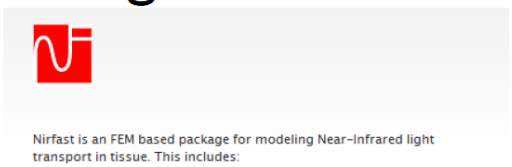

Download Nirview from Nirfast website: http://www.dartmouth.edu/~nir/nirfast/

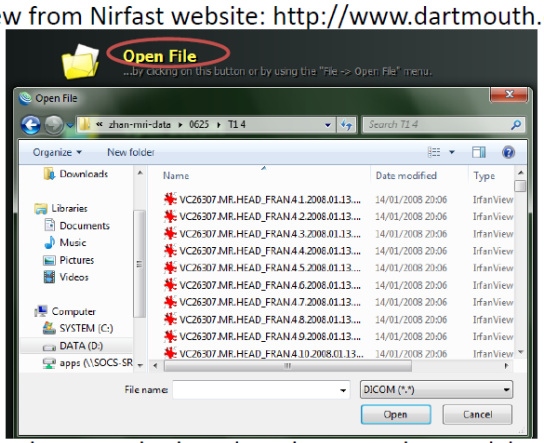

Transfer the .png image series into .bmp images using matlab.
Load bmp into Nirview using 'open file' function by selecting one of the bmp images and choose rest option as default .

8. Generated masks

Using 5 different threshold region to generate 5 Paintbrush. The threshold region used in this case are: [40 80], [80 120],[120 200],[200 250], [250 256].

Do some manually correction if necessary.

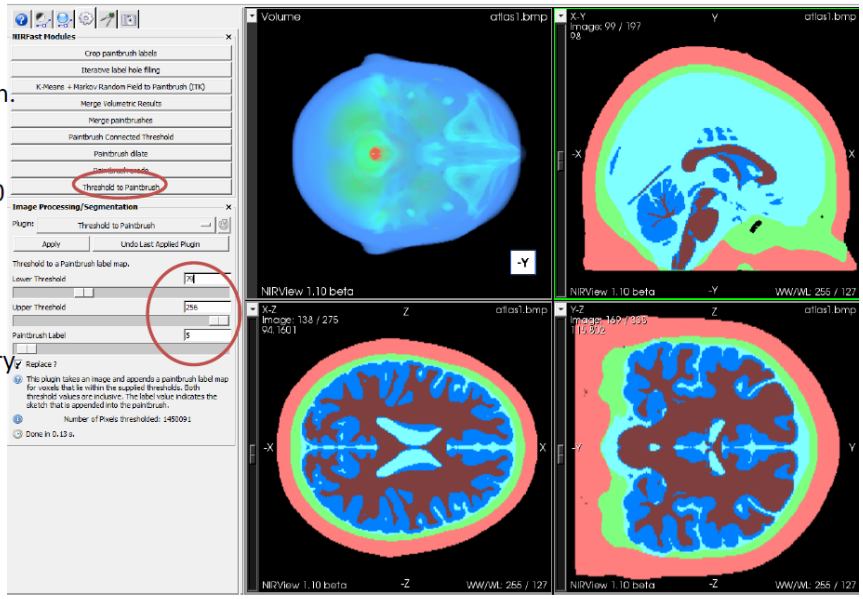

9. Output from Nirview

Set Fiducial as where source and detectors would be using the '+++' function.
Save the Fiducials as .txt file .

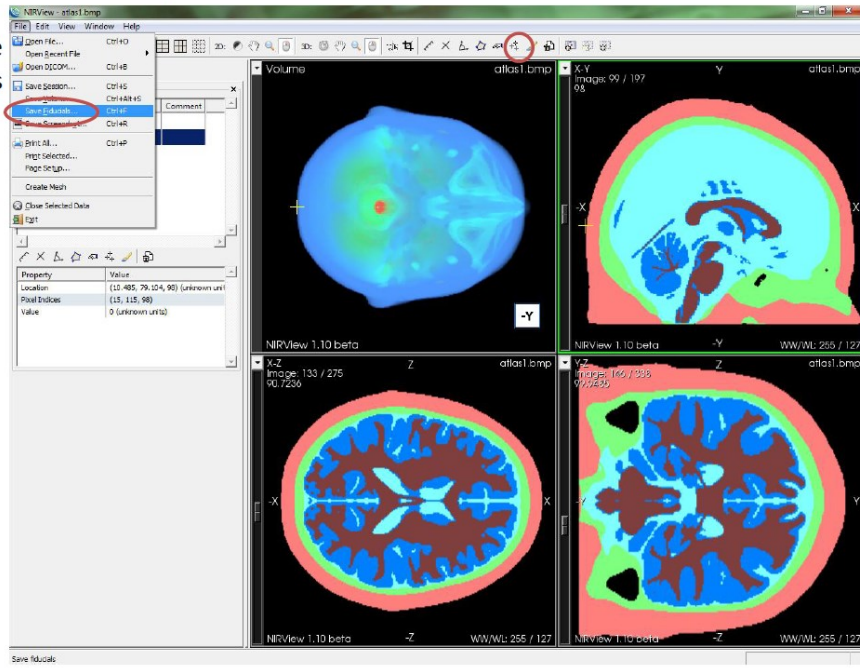

9. Output from Nirview

Save the 5 Paintbrushs as .mhd file under the same directory with 'Fiducial ' file and using the same name as Fiducial file.

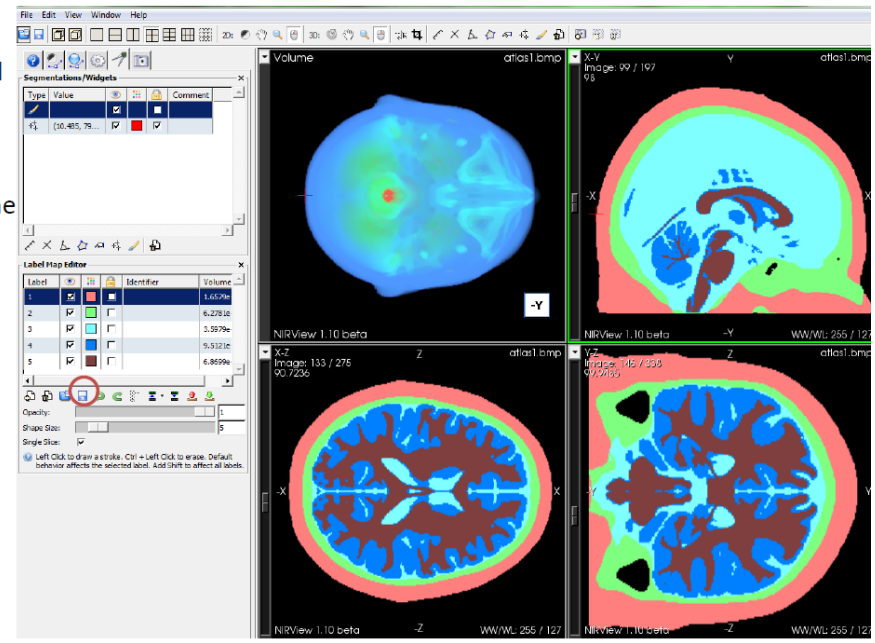

10. Generate mesh

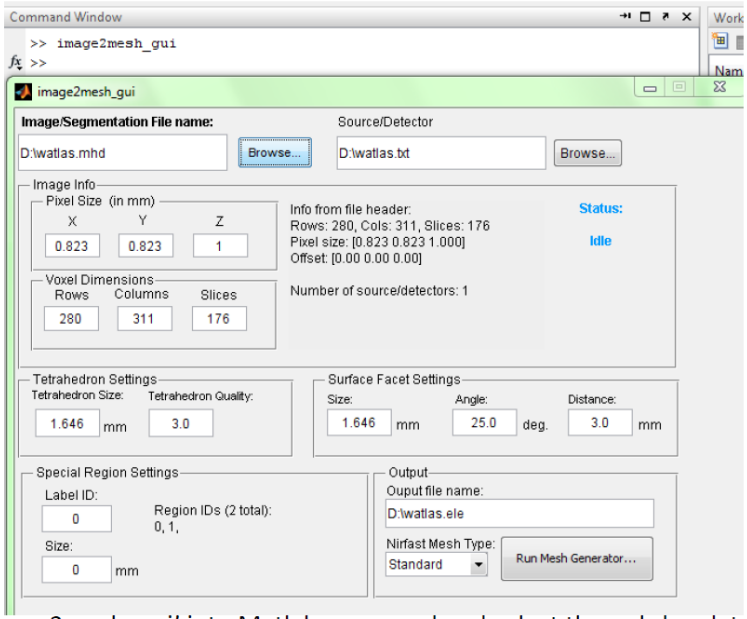

Typing: 'image2mesh_gui' into Matlab command and select the .mhd and .txt file generated in the previous step. It will generate a mask-based mesh for the subject head.

A2: Landmark extraction gui in matlab

One of the issues in landmark-based registration is the consistence of the landmarks from different subject. An automatic or semi-automatic landmark extraction approach is suitable to reduce the human influence during the extraction. A semi-automatic landmark extraction gui is designed in matlab. It can extract external landmarks of head surface based on four landmark systems with four per-extracted anatomical landmarks [Figure A.1].

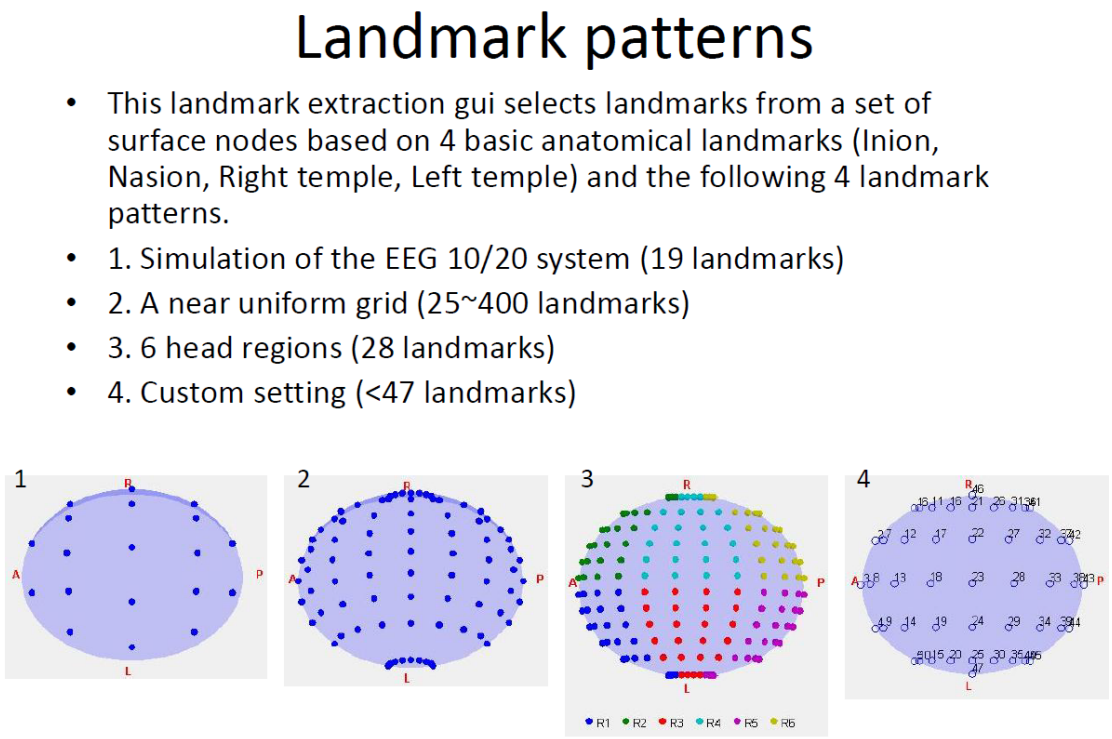

Figure A.1. 4 landmark systems for the landmark extraction gui.

1. Open landmark_extraction gui and upload dataset for surface nodes

- 1.Open the gui: type ***Landmark_Extraction*** in matlab command window
- 2. Load dataset (eg. testnodes.mat which contains a surface nodes matrix (4721*3) and a 4-landmark matrix (4*3)): Click ***Load*** and select the dataset for the subject

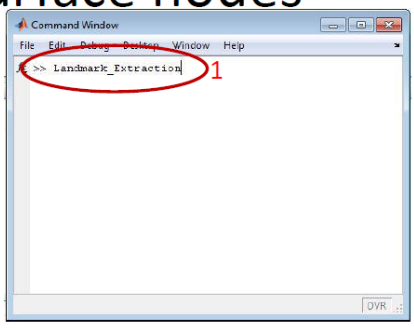

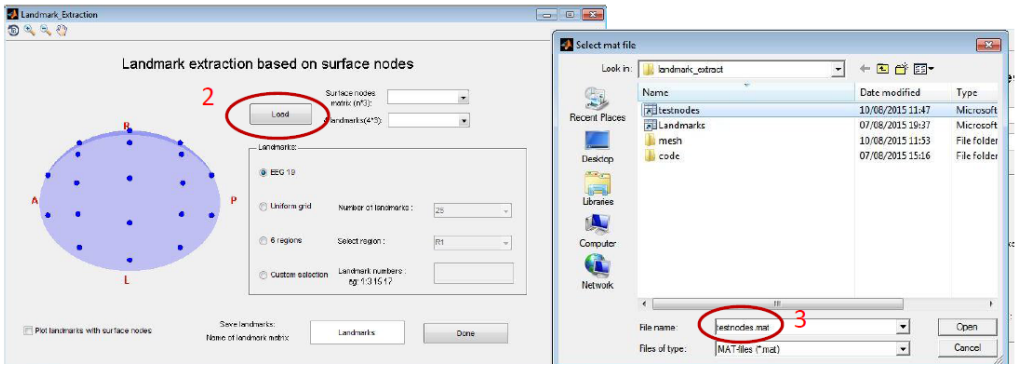

2. Load surface nodes and the 4 landmarks

- 1. Select the surface nodes matrix : click the ***down arrow*** and select a surface nodes coordinate matrix (eg. ***Surface_node***)
- 2. Select the 4 landmark matrix : repeat the previous step and select the 4 landmark coordinate matrix (eg. ***land4***)

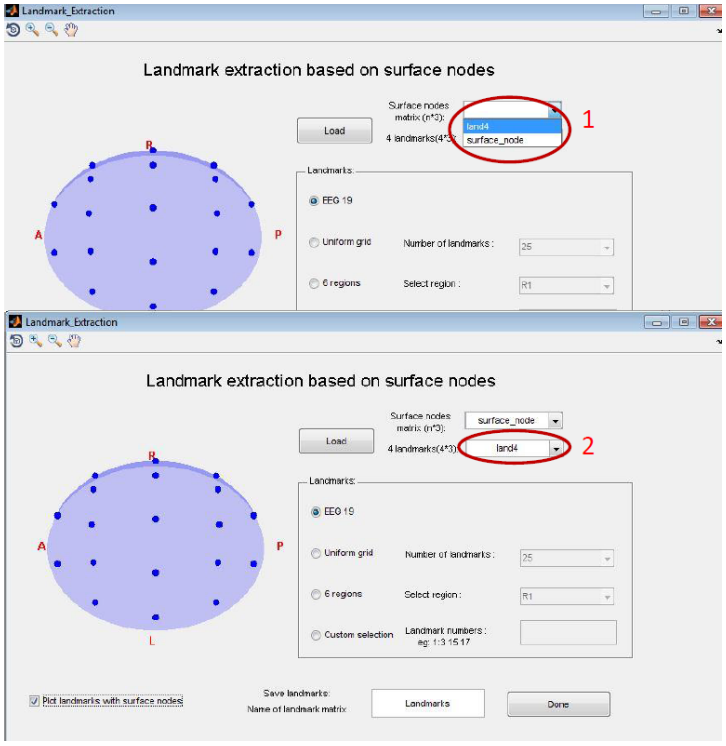

3.Choose a landmark pattern

- 1. choose a landmark pattern (the default choice is ***EEG 19*** -- the 19 landmarks simulates the EEG 10/20 system)

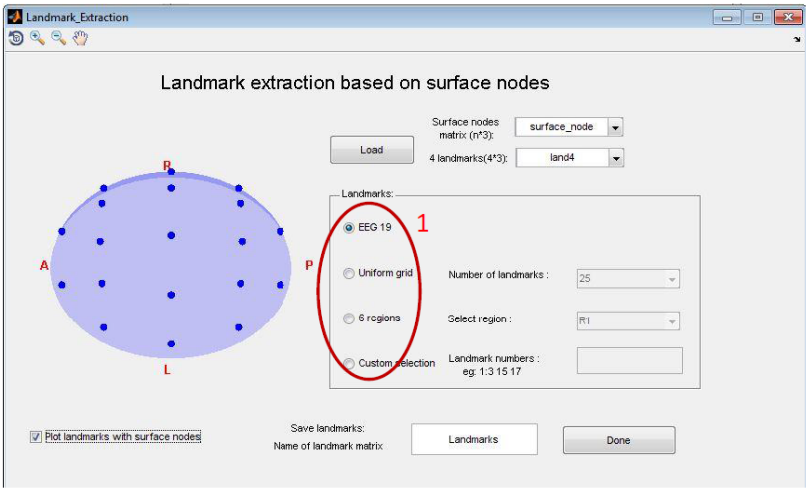

4. Extract 19 landmarks based on EEG 10/20 system

- 1. Choose a landmark pattern: select ***EEG 19***
- 2. View diagram of the landmarks: rotate and scale using the image ***toolbar*** (A: anterior, P:posterior, R:right,L:left)
- 3. Plot the extraction result: select ***Plot landmarks with surface nodes*** to plot the extracted landmarks with the surface nodes if necessary
- 4. Name the extracted landmark matrix and save the result: type a name for the landmark matrix (default: ***Landmarks***) and click ***Done***

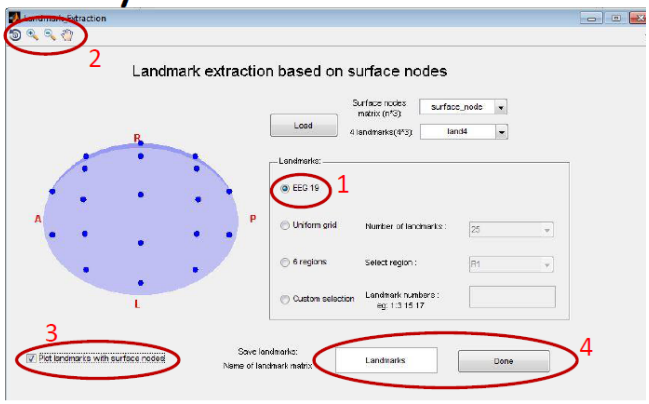

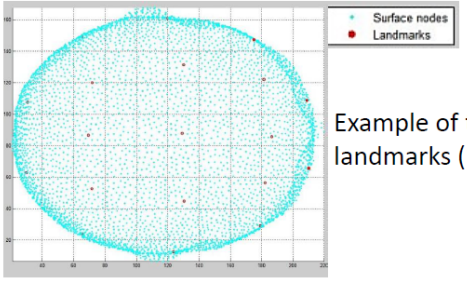

Example of the extracted landmarks (19 landmarks)

5. Extract landmarks based on a near uniform grid

- 1. Choose a landmark pattern: select ***Uniform grid***
- 2. Select number of landmarks for the extraction: click the ***down arrow*** and select from ***25*** to ***400***
- 3. View the diagram for a 81-landmark-grid: rotate and scale using the image ***toolbar***
- 4. Plot and save the extraction result: same as the ***step 3 and 4*** in the Extract 19 landmarks based on EEG 10/20 system

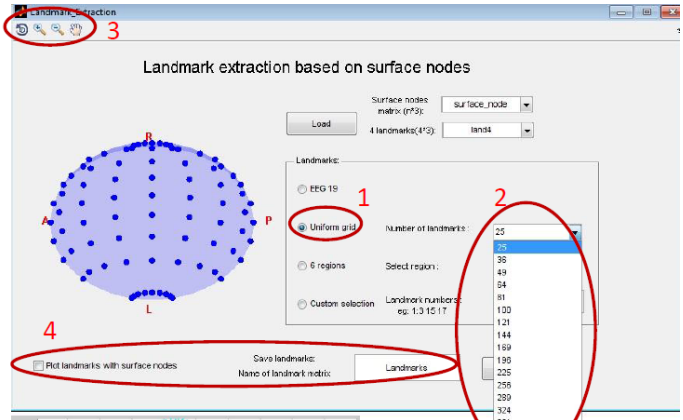

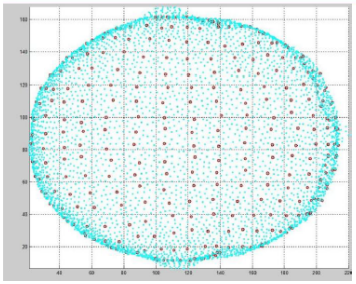

The extracted landmarks (324 landmarks)

6. Extract landmarks from one of the 6 regions

- 1. Choose a landmark pattern: select ***6 regions***
- 2. View the diagram of landmarks from the 6 regions: rotate and scale using the image ***toolbar***
- 3. Select the region for extracting landmarks : click the ***down arrow*** and select from ***R1*** to ***R6***
- 4. Plot and save the extraction result: same as the ***step 3 and 4*** in the Extract 19 landmarks based on EEG 10/20 system

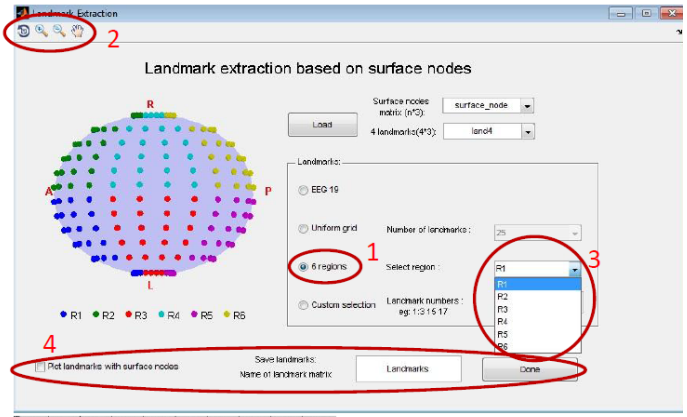

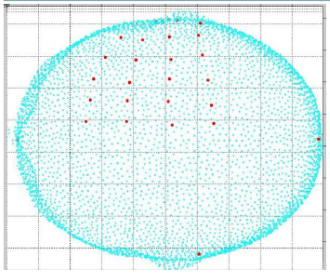

Example of the extracted landmarks (28 landmarks: 24 landmarks from region 4 and the original 4 landmarks)

7. Extract landmarks based on custom setting

- 1. Choose a landmark pattern: select ***Custom selection***
- 2. View the diagram of landmarks with numbered label : rotate and scale using the image ***toolbar***
- 3. Select landmarks based on the numbered label : type an array of landmark labels with integers between ***1*** and ***47***
- 4. Plot and save the extraction result: same as the ***step 3 and 4*** in the Extract 19 landmarks based on EEG 10/20 system

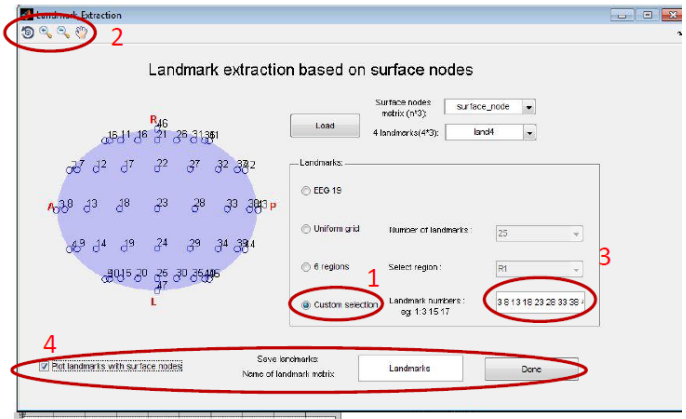

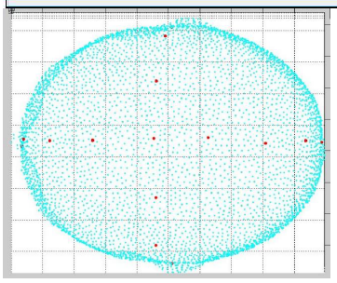

Example of the extracted landmarks (15 landmarks)

A3: Landmark and surface based registration gui in matlab

An automatic registration gui is designed for Landmark based registration and surface based registration. It can process a rigid register for subject point cloud based on a set of landmarks extracted before the registration or based or the surface point cloud. Workflow of the gui is shown in the figure A.2.

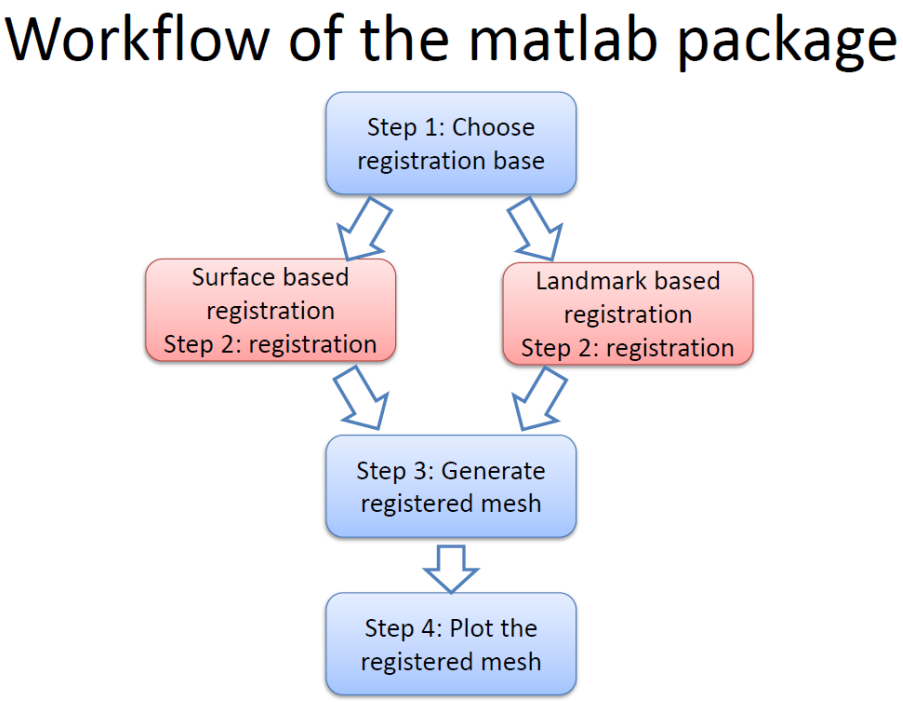

Figure A.2. Work flow of the Landmark and surface based registration gui.

Step 1: Choose registration base

- Type: *Nodes_based_rigid_registration in matlab* command window
- Choose *landmark nodes* or *surface nodes* based registration in the popup window
- Press *Go* and a popup window for step 2 will be open

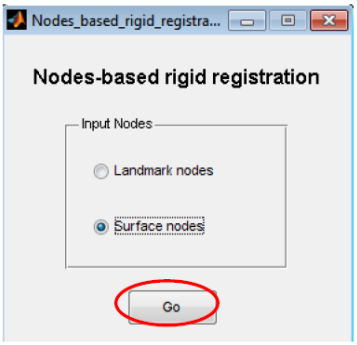

Surface based registration
Step 2: registration

- 1. Press *load* to load matlab files that contain surface nodes coordinates matrices

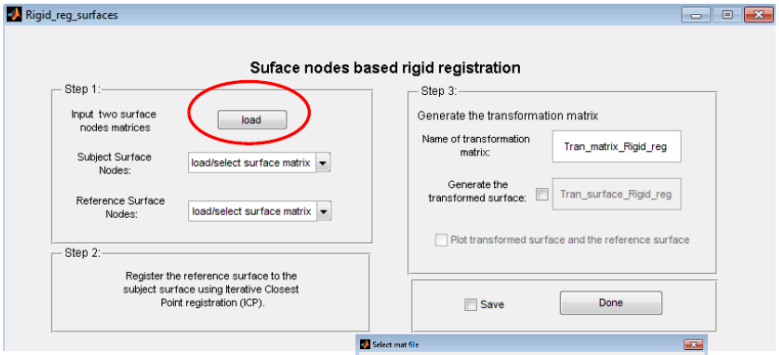

- 2. Choose the matlab files

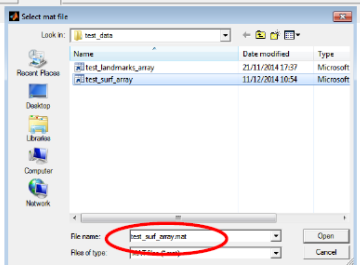

Surface based registration
Step 2: registration

- 3. Select n*3 coordinates matrices as subject and reference surfaces

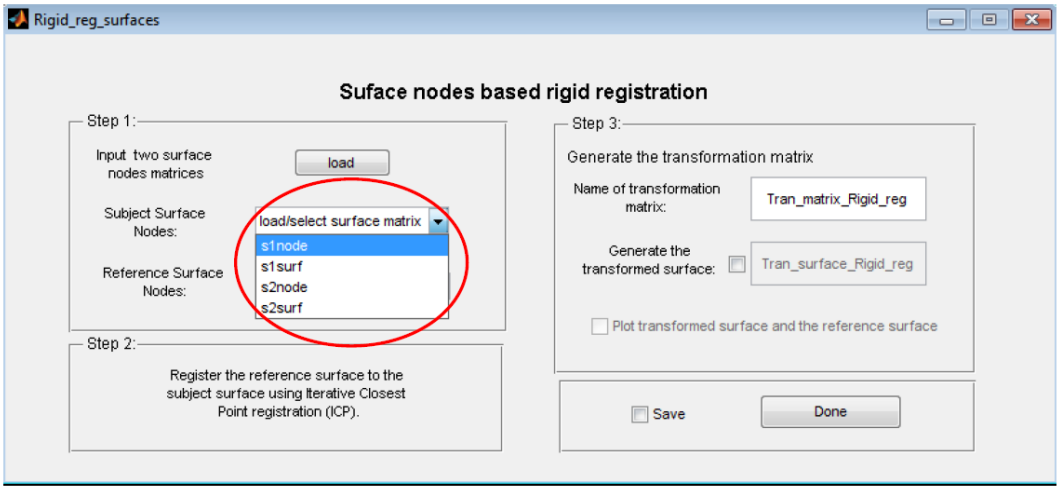

Surface based registration
Step 2: registration

- 4. Define name of the output transformation matrix. The default name is shown in image.
- Tick *save* to save the transformation matrix

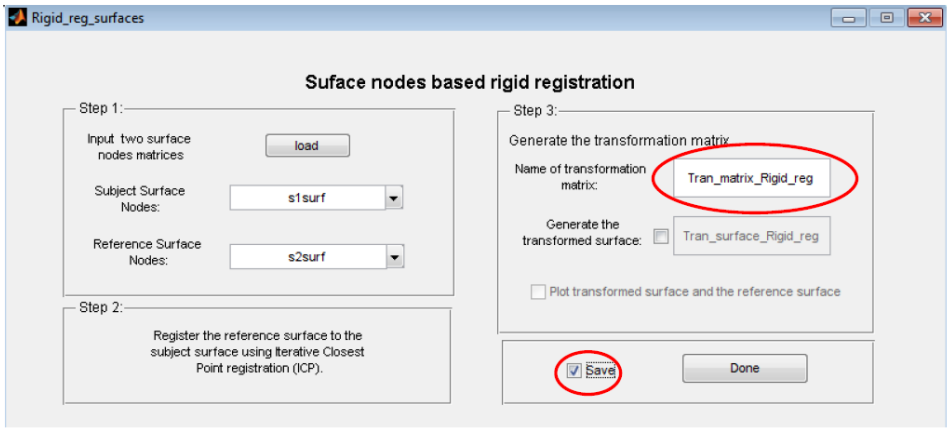

Surface based registration
Step 2: registration

- 5. Tick *generate the transformed surface* to generated the registered surface and define name of the output registered surface matrix
- Tick *save* to save the transformation matrix and registered surface
- 6. Tick *Plot* to plot the registered surface nodes and reference surface nodes
- 7. Press *done* to process the registration and open a window for step 3

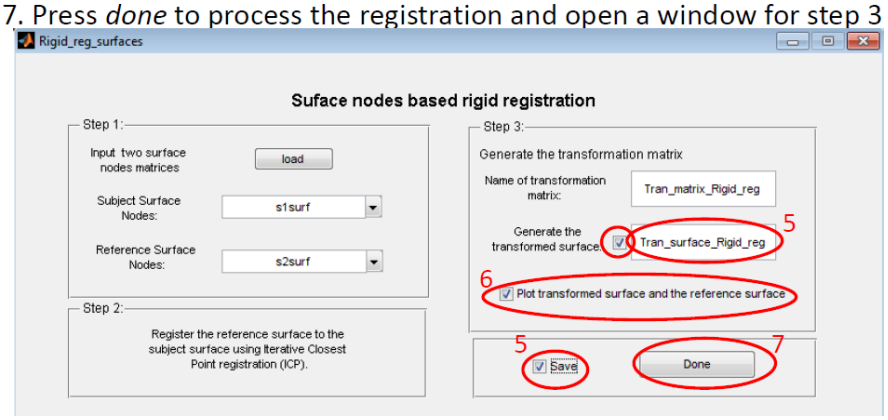

Surface based registration
Step 2: registration

- Plotted figure of the registered surface nodes and reference surface nodes

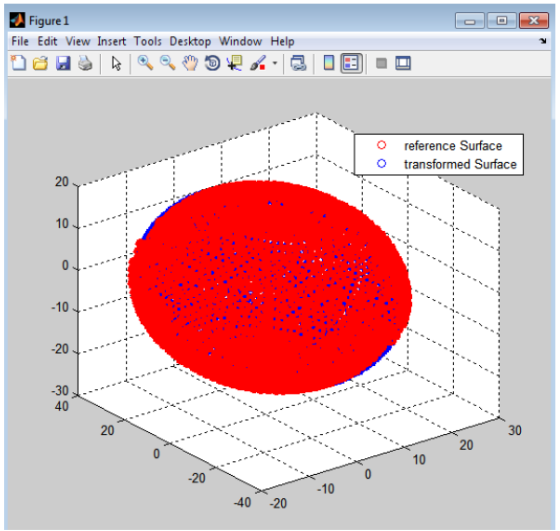

Step 3: Generate registered mesh

- 1. Tick *Registration transformation of the mesh* to generate the registered mesh nodes n*3 coordinates matrix
- 2. Select the *registration m*atrix generated in step 2. If matrix name is set as default in step 2, the registration matrix is automatically chosen.

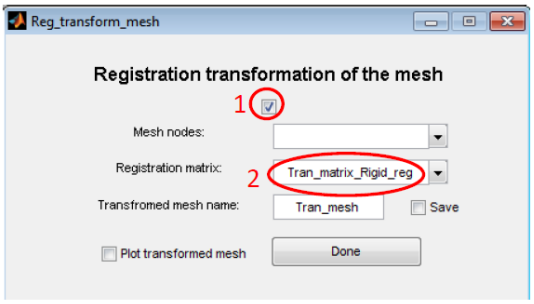

Step 3: Generate registered mesh

- 3. Select the mesh nodes n*3 coordinates matrix for the subject mesh

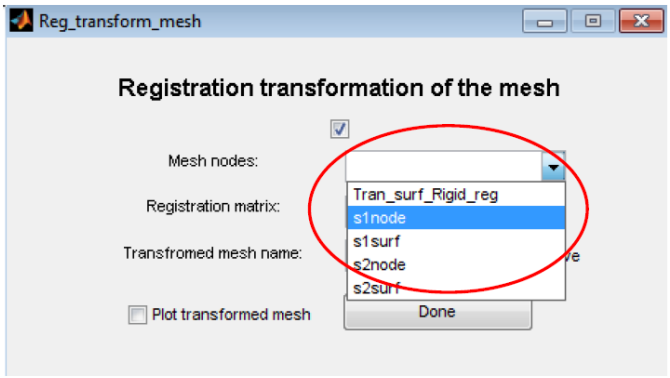

Step 3: Generate registered mesh

- 4. Define name of the output registered mesh, and tick *save* to save the mesh nodes coordinates matrix
- 5. Tick *Plot* to open window for step 4 and press *done* to process the generation.

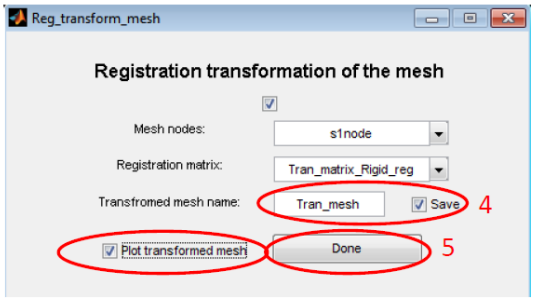

Step 4: Plot the registered mesh

- 1. Tick *Plot as points* to plot meshes nodes as a scattered point figure.
- Tick *Plot as surface* to plot meshes as surface

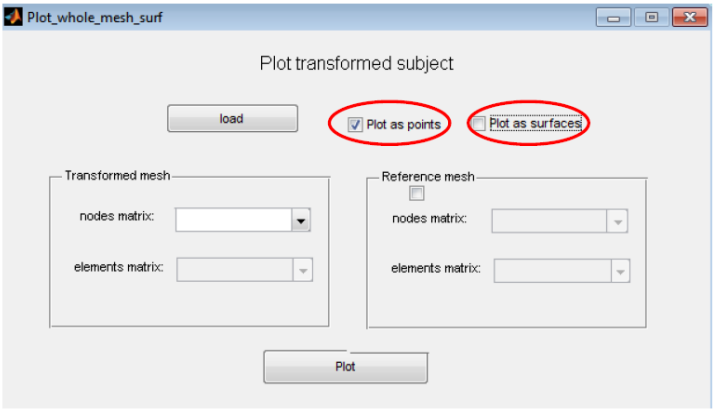

Step 4: Plot the registered mesh

- 2. Press *load* to load matlab files that contain registered mesh nodes coordinates matrices and if *Plot as surfaces* is chosen, load matlab files that contain n*4 mesh element matrices as well. This loading can be skipped if the matrices is already in the matlab workspace
- Select the matrices for the transformed mesh. If default name is used in step 3, select *Tran_mesh_Reigid_reg* as the nodes matrix of the transformed mesh.

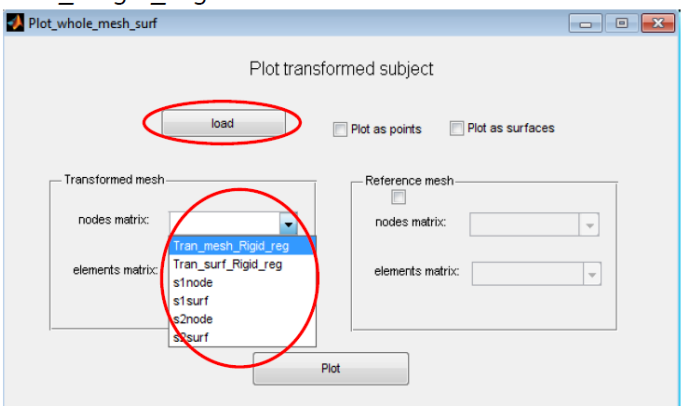

Step 4: Plot the registered mesh

- 3. Tick *Reference mesh* to plot the reference mesh with the registered mesh
- Select the mesh nodes matrix for the reference mesh, and select the element matrix of the reference mesh if *Plot as surfaces* id chosen.
- 4. Press Plot to plot the figures

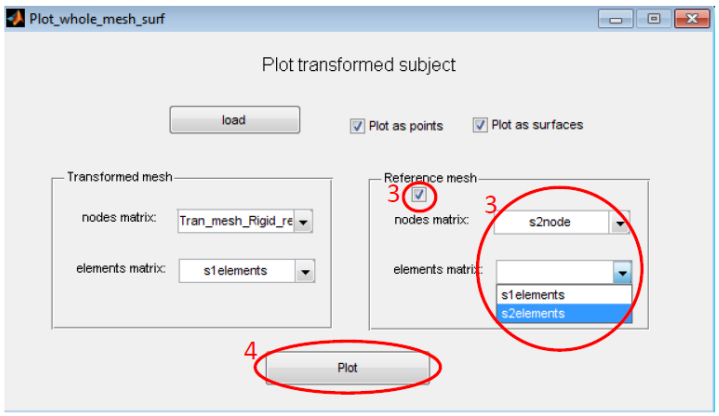

Step 4: Plot the registered mesh

- Plotted figure of the registered and reference meshes

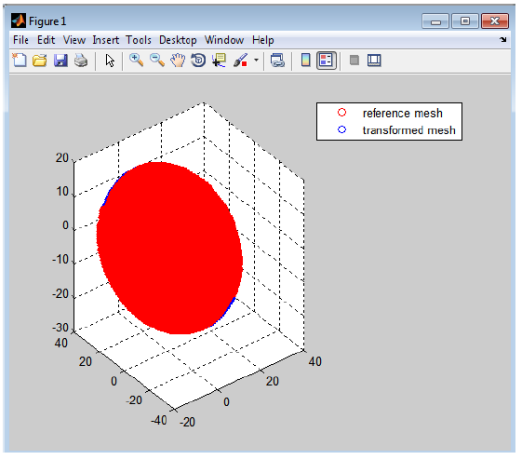

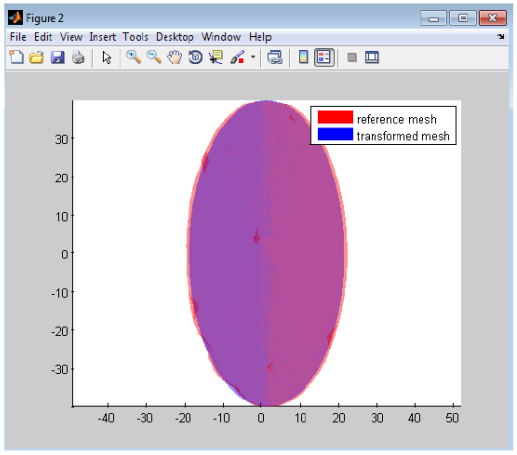

Landmark based registration
Step 2: registration

- 1. Press *load* to load matlab files that contain landmark coordinates matrices

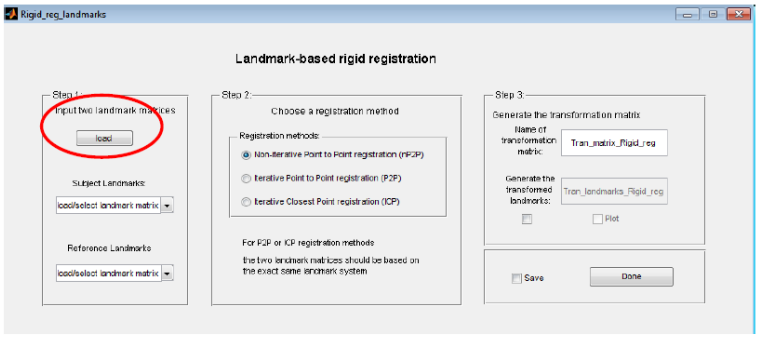

- 2. Choose the matlab files

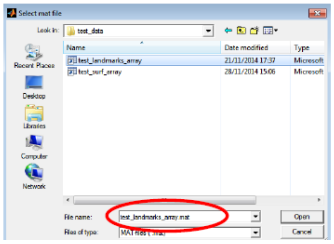

Landmark based registration
Step 2: registration

- 3. Select n*3 coordinates matrices as subject and reference landmarks

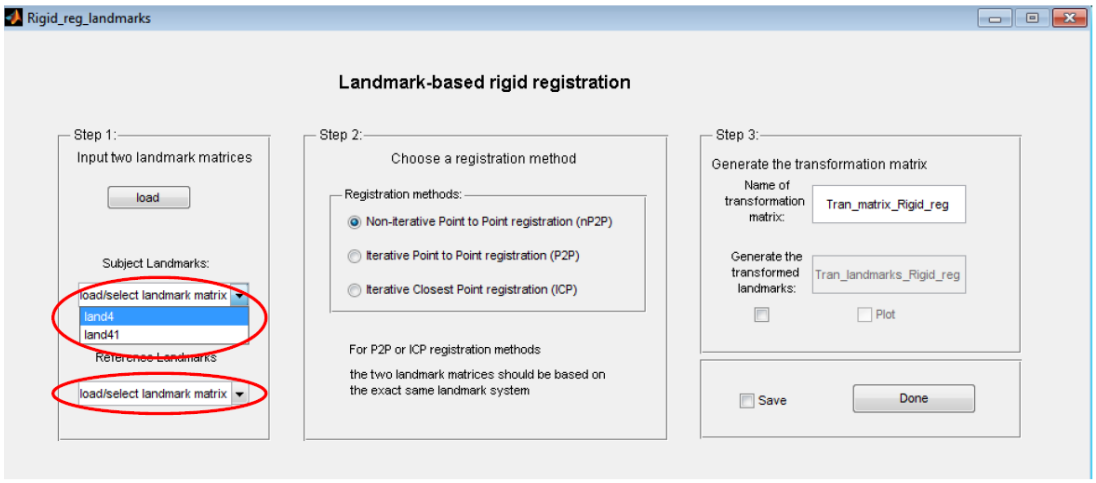

Landmark based registration
Step 2: registration

- 4. Choose a registration method

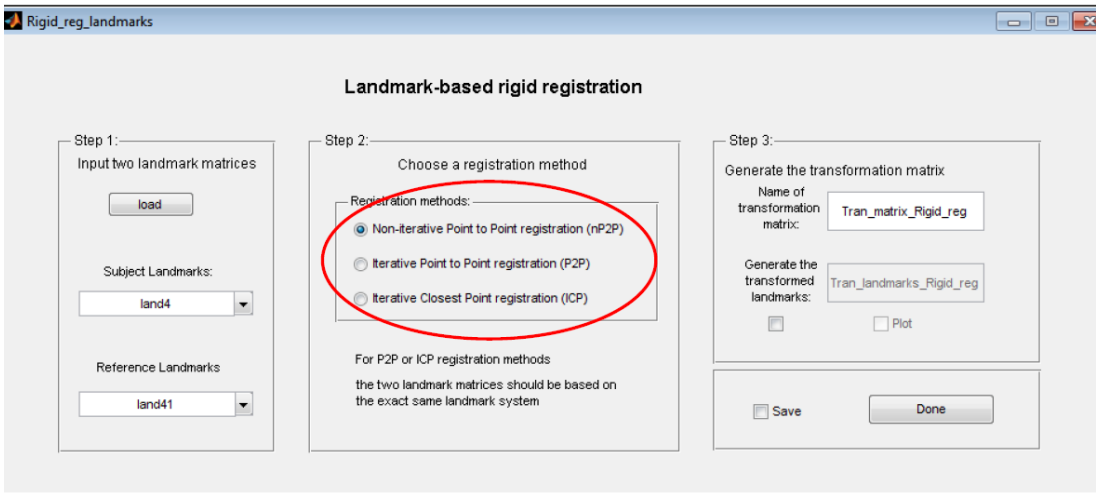

Landmark based registration
Step 2: registration

- 5. Define name of the output transformation matrix. The default name is shown in image.
- Tick *save* to save the transformation matrix

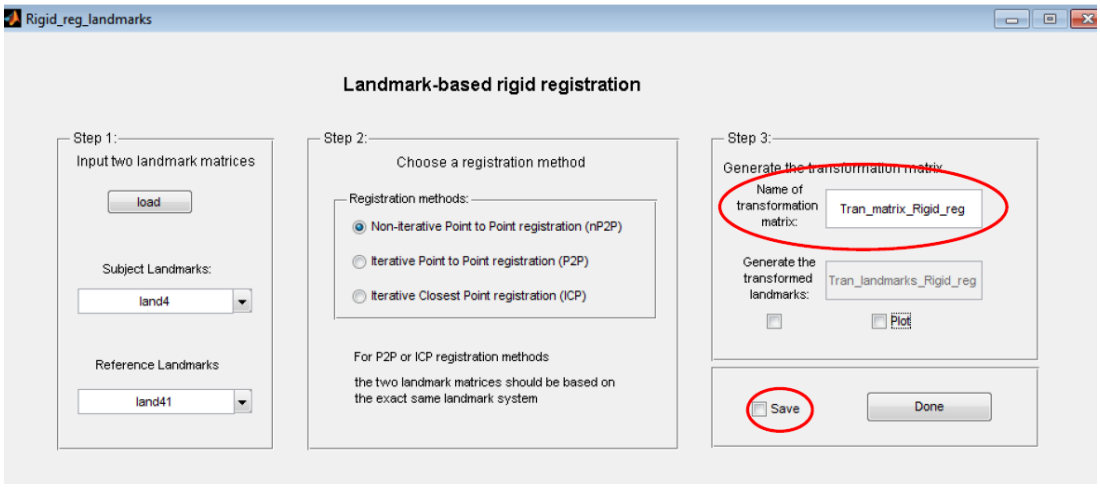

Landmark based registration
Step 2: registration

- 6. Tick *generate the transformed landmark* to generated the registered landmarks and define name of the output registered landmarks matrix
- Tick *save* to save the transformation matrix and registered landmarks
- 7. Tick *Plot* to plot the registered landmarks and reference landmarks
- 8. Press *done* to process the registration and open a window for step 3

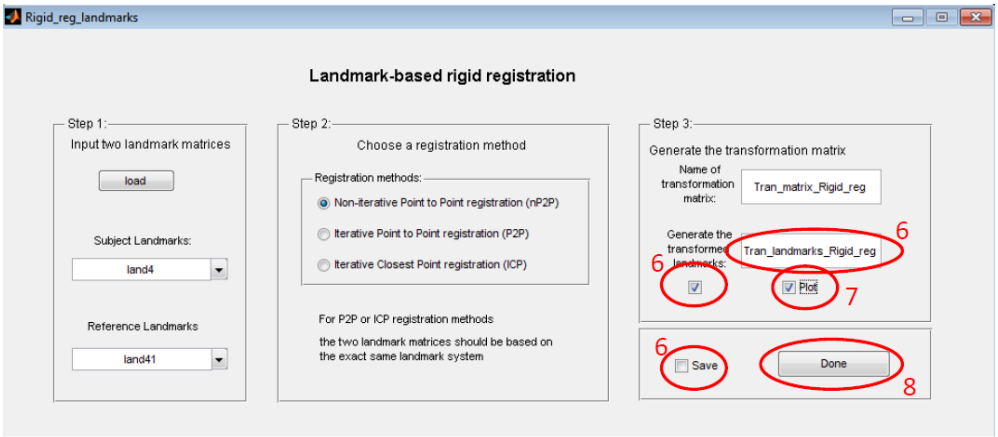

Landmark based registration
Step 2: registration

- Plotted figure of the registered landmarks and reference landmarks

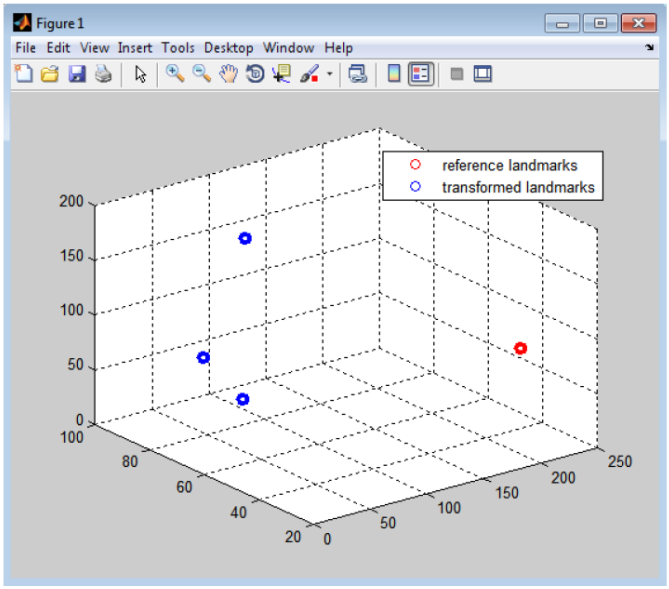

Reference

1. S. R. Hintz, D. A. Benaron, A. M. Siegel, A. Zourabian, D. K. Stevenson, and D. A. Boas, "Bedside functional imaging of the premature infant brain during passive motor activation," *Journal of perinatal medicine* **29**, 335-343 (2001).
2. S. R. Hintz, W. F. Cheong, J. P. Van Houten, D. K. Stevenson, and D. A. Benaron, "Bedside imaging of intracranial hemorrhage in the neonate using light: Comparison with ultrasound, computed tomography, and magnetic resonance imaging," *Pediatric research* **45**, 54-59 (1999).
3. S. M. Liao, S. L. Ferradal, B. R. White, N. Gregg, T. E. Inder, and J. P. Culver, "High-density diffuse optical tomography of term infant visual cortex in the nursery," *J Biomed Opt* **17**, 081414 (2012).
4. D. A. Boas, A. M. Dale, and M. A. Franceschini, "Diffuse optical imaging of brain activation: approaches to optimizing image sensitivity, resolution, and accuracy," *Neuroimage* **23 Suppl 1**, S275-288 (2004).
5. A. Corlu, R. Choe, T. Durduran, K. Lee, M. Schweiger, S. R. Arridge, E. M. Hillman, and A. G. Yodh, "Diffuse optical tomography with spectral constraints and wavelength optimization," *Appl Opt* **44**, 2082-2093 (2005).
6. A. T. Eggebrecht, B. R. White, S. L. Ferradal, C. Chen, Y. Zhan, A. Z. Snyder, H. Dehghani, and J. P. Culver, "A quantitative spatial comparison of high-density diffuse optical tomography and fMRI cortical mapping," *Neuroimage* **61**, 1120-1128 (2012).
7. S. L. Ferradal, S. M. Liao, A. T. Eggebrecht, J. S. Shimony, T. E. Inder, J. P. Culver, and C. D. Smyser, "Functional Imaging of the Developing Brain at the Bedside Using Diffuse Optical Tomography," *Cerebral Cortex* **bhu320**(2015).
8. S. R. Arridge and M. Schweiger, "Photon-measurement density functions. Part 2: Finite-element-method calculations," *Appl Opt* **34**, 8026-8037 (1995).
9. R. J. Cooper, M. Caffini, J. Dubb, Q. Fang, A. Custo, D. Tsuzuki, B. Fischl, W. Wells, 3rd, I. Dan, and D. A. Boas, "Validating atlas-guided DOT: a comparison of diffuse optical tomography informed by atlas and subject-specific anatomies," *Neuroimage* **62**, 1999-2006 (2012).
10. S. L. Ferradal, A. T. Eggebrecht, M. Hassanpour, A. Z. Snyder, and J. P. Culver, "Atlas-based head modeling and spatial normalization for high-density diffuse optical tomography: in vivo validation against fMRI," *Neuroimage* **85 Pt 1**, 117-126 (2014).
11. A. Custo, D. A. Boas, D. Tsuzuki, I. Dan, R. Mesquita, B. Fischl, W. E. Grimson, and W. Wells, 3rd, "Anatomical atlas-guided diffuse optical tomography of brain activation," *Neuroimage* **49**, 561-567 (2010).
12. T. Matsuda, M. Matsuura, T. Ohkubo, H. Ohkubo, E. Matsushima, K. Inoue, M. Taira, and T. Kojima, "Functional MRI mapping of brain activation during visually guided saccades and antisaccades: cortical and subcortical networks," *Psychiatry research* **131**, 147-155 (2004).
13. A. T. Eggebrecht, S. L. Ferradal, A. Robichaux-Viehoever, M. S. Hassanpour, H. Dehghani, A. Z. Snyder, T. Hershey, and J. P. Culver, "Mapping distributed brain function and networks with diffuse optical tomography," *Nat Photonics* **8**, 448-454 (2014).
14. B. R. White, A. Z. Snyder, A. L. Cohen, S. E. Petersen, M. E. Raichle, B. L. Schlaggar, and J. P. Culver, "Resting-state functional connectivity in the human brain revealed with diffuse optical tomography," *Neuroimage* **47**, 148-156 (2009).
15. R. J. Ilmoniemi, J. Virtanen, J. Ruohonen, J. Karhu, H. J. Aronen, R. Naatanen, and T. Katila, "Neuronal responses to magnetic stimulation reveal cortical reactivity and connectivity," *Neuroreport* **8**, 3537-3540 (1997).
16. S. Ruiz, S. Lee, S. R. Soekadar, A. Caria, R. Veit, T. Kircher, N. Birbaumer, and R. Sitaram, "Acquired self-control of insula cortex modulates emotion recognition and brain network connectivity in schizophrenia," *Human brain mapping* **34**, 200-212 (2013).

17. E. Gratton, S. Fantini, M. A. Franceschini, G. Gratton, and M. Fabiani, "Measurements of scattering and absorption changes in muscle and brain," *Philosophical transactions of the Royal Society of London. Series B, Biological sciences* **352**, 727-735 (1997).
18. P. Aljabar, R. A. Heckemann, A. Hammers, J. V. Hajnal, and D. Rueckert, "Multi-atlas based segmentation of brain images: atlas selection and its effect on accuracy," *Neuroimage* **46**, 726-738 (2009).
19. O. T. Carmichael, H. A. Aizenstein, S. W. Davis, J. T. Becker, P. M. Thompson, C. C. Meltzer, and Y. Liu, "Atlas-based hippocampus segmentation in Alzheimer's disease and mild cognitive impairment," *Neuroimage* **27**, 979-990 (2005).
20. X. Yi, X. Wang, W. Chen, W. Wan, H. Zhao, and F. Gao, "Full domain-decomposition scheme for diffuse optical tomography of large-sized tissues with a combined CPU and GPU parallelization," *Appl Opt* **53**, 2754-2765 (2014).
21. J.-J. Tsai, N.-J. Chen, W.-C. Fang, and J.-S. Chen, "Fast Image Reconstruction Algorithm For Continuous Wave Diffuse Optical Tomography," *IEEE/NIH Life Science Systems and Applications Workshop* **93**(2011).
22. A. Klein, J. Andersson, B. A. Ardekani, J. Ashburner, B. Avants, M. C. Chiang, G. E. Christensen, D. L. Collins, J. Gee, P. Hellier, J. H. Song, M. Jenkinson, C. Lepage, D. Rueckert, P. Thompson, T. Vercauteren, R. P. Woods, J. J. Mann, and R. V. Parsey, "Evaluation of 14 nonlinear deformation algorithms applied to human brain MRI registration," *Neuroimage* **46**, 786-802 (2009).
23. B. W. Zeff, B. R. White, H. Dehghani, B. L. Schlaggar, and J. P. Culver, "Retinotopic mapping of adult human visual cortex with high-density diffuse optical tomography," *P Natl Acad Sci USA* **104**, 12169-12174 (2007).
24. C. Habermehl, S. Holtze, J. Steinbrink, S. P. Koch, H. Obrig, J. Mehnert, and C. H. Schmitz, "Somatosensory activation of two fingers can be discriminated with ultrahigh-density diffuse optical tomography," *Neuroimage* **59**, 3201-3211 (2012).
25. P. H. Koh, " Methodology of Optical Topography Measurements for Functional Brain Imaging and the Development and Implementation of Functional Optical Signal Analysis Software," (University of London, 2007).
26. R. Vigario, J. Sarela, V. Jousmaki, M. Hamalainen, and E. Oja, "Independent component approach to the analysis of EEG and MEG recordings," *IEEE Trans Biomed Eng* **47**, 589-593 (2000).
27. R. D. Hoge, M. A. Franceschini, R. J. M. Covolan, T. Huppert, J. B. Mandeville, and D. A. Boas, "Simultaneous recording of task-induced changes in blood oxygenation, volume, and flow using diffuse optical imaging and arterial spin-labeling MRI," *Neuroimage* **25**, 701-707 (2005).
28. T. Durduran, G. Yu, M. G. Burnett, J. A. Detre, J. H. Greenberg, J. Wang, C. Zhou, and A. G. Yodh, "Diffuse optical measurement of blood flow, blood oxygenation, and metabolism in a human brain during sensorimotor cortex activation," *Opt Lett* **29**, 1766-1768 (2004).
29. A. Gevins, H. Leong, M. E. Smith, J. Le, and R. Du, "Mapping cognitive brain function with modern high-resolution electroencephalography," *Trends Neurosci* **18**, 429-436 (1995).
30. M. Lauritzen and L. Gold, "Brain function and neurophysiological correlates of signals used in functional neuroimaging," *J Neurosci* **23**, 3972-3980 (2003).
31. A. M. Dale and M. I. Sereno, "Improved Localizadon of Cortical Activity by Combining EEG and MEG with MRI Cortical Surface Reconstruction: A Linear Approach," *J Cogn Neurosci* **5**, 162-176 (1993).
32. A. M. Dale, A. K. Liu, B. R. Fischl, R. L. Buckner, J. W. Belliveau, J. D. Lewine, and E. Halgren, "Dynamic statistical parametric mapping: combining fMRI and MEG for high-resolution imaging of cortical activity," *Neuron* **26**, 55-67 (2000).
33. E. Rykhlevskaia, G. Gratton, and M. Fabiani, "Combining structural and functional neuroimaging data for studying brain connectivity: a review," *Psychophysiology* **45**, 173-187 (2008).

34. Y. Yang and A. Raine, "Prefrontal structural and functional brain imaging findings in antisocial, violent, and psychopathic individuals: a meta-analysis," *Psychiatry research* **174**, 81-88 (2009).
35. M. J. Paulus, S. S. Gleason, S. J. Kennel, P. R. Hunsicker, and D. K. Johnson, "High resolution X-ray computed tomography: an emerging tool for small animal cancer research," *Neoplasia* **2**, 62-70 (2000).
36. J. Ambrose, "Computerized x-ray scanning of the brain," *J Neurosurg* **40**, 679-695 (1974).
37. D. W. Roberts, J. W. Strohbehn, J. F. Hatch, W. Murray, and H. Kettenberger, "A frameless stereotaxic integration of computerized tomographic imaging and the operating microscope," *J Neurosurg* **65**, 545-549 (1986).
38. M. Khodaverdi, F. Pauly, S. Weber, G. Schröder, K. Ziemons, R. Sievering, and H. Halling, "Preliminary studies of a micro-CT for a combined small animal PET/CT scanner," *In Nuclear Science Symposium Conference Record IEEE* **3**, 1605-1606 (2001).
39. J. Merino-deVillasante and J. M. Taveras, "Computerized tomography (CT) in acute head trauma," *AJR. American journal of roentgenology* **126**, 765-778 (1976).
40. Y. S. Kwoh, J. Hou, E. A. Jonckheere, and S. Hayati, "A robot with improved absolute positioning accuracy for CT guided stereotactic brain surgery," *IEEE Trans Biomed Eng* **35**, 153-160 (1988).
41. W. Calvo, J. W. Hopewell, H. S. Reinhold, and T. K. Yeung, "Time- and dose-related changes in the white matter of the rat brain after single doses of X rays," *Br J Radiol* **61**, 1043-1052 (1988).
42. R. Naqi and M. Azeemuddin, "Naeglaeria infection of the central nervous system, CT scan findings: a case series," *JPMA. The Journal of the Pakistan Medical Association* **63**, 399-402 (2013).
43. H. T. Chugani, M. E. Phelps, and J. C. Mazziotta, "Positron emission tomography study of human brain functional development," *Ann Neurol* **22**, 487-497 (1987).
44. C. Catana, D. Procissi, Y. Wu, M. S. Judenhofer, J. Qi, B. J. Pichler, R. E. Jacobs, and S. R. Cherry, "Simultaneous in vivo positron emission tomography and magnetic resonance imaging," *Proc Natl Acad Sci U S A* **105**, 3705-3710 (2008).
45. M. S. Buchsbaum, J. Wu, L. E. Delisi, H. Holcomb, R. Kessler, J. Johnson, A. C. King, E. Hazlett, K. Langston, and R. M. Post, "Frontal-Cortex and Basal Ganglia Metabolic Rates Assessed by Positron Emission Tomography with [F-18] 2-Deoxyglucose in Affective-Illness," *Journal of affective disorders* **10**, 137-152 (1986).
46. W. M. R. B. Jagust, B. Reed, D. Mungas, W. Ellis, and C. Decarli, " What does fluorodeoxyglucose PET imaging add to a clinical diagnosis of dementia?," *Neurology* **69**, 871-877 (2007).
47. R. E. Coleman, J. M. Hoffman, M. W. Hanson, H. D. Sostman, and S. C. Schold, "Clinical application of PET for the evaluation of brain tumors. Journal of nuclear medicine: official publication," *Society of Nuclear Medicine* **32**, 616-622 (1991).
48. M. S. Judenhofer, H. F. Wehrl, D. F. Newport, C. Catana, S. B. Siegel, M. Becker, A. Thielscher, M. Kneilling, M. P. Lichy, M. Eichner, K. Klingel, G. Reischl, S. Widmaier, M. Rocken, R. E. Nutt, H. J. Machulla, K. Uludag, S. R. Cherry, C. D. Claussen, and B. J. Pichler, "Simultaneous PET-MRI: a new approach for functional and morphological imaging," *Nat Med* **14**, 459-465 (2008).
49. A. Martinez-Möller, M. Souvatzoglou, G. Delso, R. A. Bundschuh, C. Chefd'hotel, S. I. Ziegler, N. Navab, M. Schwaiger, and S. G. Nekolla, "Tissue classification as a potential approach for attenuation correction in whole-body PET/MRI: evaluation with PET/CT data," *Journal of nuclear medicine* **50**, 520-526 (2009).
50. S. Vandenberghe and P. K. Marsden, "PET-MRI: a review of challenges and solutions in the development of integrated multimodality imaging," *Phys Med Biol* **60**, R115-154 (2015).
51. P. N. Wells, "Ultrasound imaging," *Phys Med Biol* **51**, R83-98 (2006).
52. A. Fenster and D. B. Downey, "3-D ultrasound imaging: A review," *Ieee Eng Med Biol* **15**, 41-51 (1996).

53. D. Markov-Vetter, J. Muehl, D. Schmalstieg, E. Sorantin, and M. Riccabona, "3D augmented reality simulator for neonatale cranial sonography. , , ." *Comput Assist Radiol Surg* **1230**, 483-487 (2001).
54. T. M. O'Shea, S. J. Counsell, D. B. Bartels, and O. Dammann, "Magnetic resonance and ultrasound brain imaging in preterm infants," *Early Hum Dev* **81**, 263-271 (2005).
55. M. Balki, Y. Lee, S. Halpern, and J. C. A. Carvalho, "Ultrasound Imaging of the Lumbar Spine in the Transverse Plane: The Correlation Between Estimated and Actual Depth to the Epidural Space in Obese Parturients," *Anesth Analg* **108**, 1876-1881 (2009).
56. J. J. Niederhauser, M. Jaeger, R. Lemor, P. Weber, and M. Frenz, "Combined ultrasound and optoacoustic system for real-time high-contrast vascular imaging in vivo," *IEEE Trans Med Imaging* **24**, 436-440 (2005).
57. T. S. Sumanaweera, J. R. Adler, Jr., S. Napel, and G. H. Glover, "Characterization of spatial distortion in magnetic resonance imaging and its implications for stereotactic surgery," *Neurosurgery* **35**, 696-703; discussion 703-694 (1994).
58. I. L. Pykett, J. H. Newhouse, F. S. Buonanno, T. J. Brady, M. R. Goldman, J. P. Kistler, and G. M. Pohost, "Principles of nuclear magnetic resonance imaging," *Radiology* **143**, 157-168 (1982).
59. H. Cheng, G. Nair, T. A. Walker, M. K. Kim, M. T. Pardue, P. M. Thule, D. E. Olson, and T. Q. Duong, "Structural and functional MRI reveals multiple retinal layers," *Proc Natl Acad Sci U S A* **103**, 17525-17530 (2006).
60. B. J. Casey, J. N. Giedd, and K. M. Thomas, "Structural and functional brain development and its relation to cognitive development," *Biol Psychol* **54**, 241-257 (2000).
61. S. Ogawa, T. M. Lee, A. S. Nayak, and P. Glynn, "Oxygenation-Sensitive Contrast in Magnetic-Resonance Image of Rodent Brain at High Magnetic-Fields," *Magnetic resonance in medicine* **14**, 68-78 (1990).
62. S. Ogawa, T. M. Lee, A. R. Kay, and D. W. Tank, "Brain magnetic resonance imaging with contrast dependent on blood oxygenation," *Proc Natl Acad Sci U S A* **87**, 9868-9872 (1990).
63. P. M. Matthews, "Recent advances in technology: 53 functional magnetic resonance imaging," in *Basic clinical radiobiology*, M. C. Joiner and A. van der Kogel, eds. (CRC Press, 2016).
64. M. Aswendt, J. Adamczak, and A. Tennstaedt, "A review of novel optical imaging strategies of the stroke pathology and stem cell therapy in stroke," *Frontiers in cellular neuroscience* **8**(2014).
65. A. Torricelli, L. Spinelli, A. Pifferi, P. Taroni, R. Cubeddu, and G. Danesini, " Use of a nonlinear perturbation approach for in vivo breast lesion characterization by multiwavelength time-resolved optical mammography," *Optics express* **11**, 853-867 (2003).
66. D. K. Joseph, T. J. Huppert, M. A. Franceschini, and D. A. Boas, "Diffuse optical tomography system to image brain activation with improved spatial resolution and validation with functional magnetic resonance imaging," *Appl Opt* **45**, 8142-8151 (2006).
67. V. Ntziachristos, A. G. Yodh, M. Schnall, and B. Chance, "Concurrent MRI and diffuse optical tomography of breast after indocyanine green enhancement," *P Natl Acad Sci USA* **97**, 2767-2772 (2000).
68. H. Dehghani, M. E. Eames, P. K. Yalavarthy, S. C. Davis, S. Srinivasan, C. M. Carpenter, B. W. Pogue, and K. D. Paulsen, "Near infrared optical tomography using NIRFAST: Algorithm for numerical model and image reconstruction," *Communications in numerical methods in engineering* **25**, 711-732 (2009).
69. R. Weissleder, "A clearer vision for in vivo imaging," *Nat Biotechnol* **19**, 316-317 (2001).
70. S. Perrey, "Non-invasive NIR spectroscopy of human brain function during exercise," *Methods* **45**, 289-299 (2008).
71. Y. Yamashita, E. Watanabe, F. Kawaguchi, A. Maki, and H. Koizumi, "Development of Optical Topography for noninvasive measurement of human brain activity," *Medix* **29**(1998).
72. B. R. White and J. P. Culver, "Quantitative evaluation of high-density diffuse optical tomography: in vivo resolution and mapping performance," *J Biomed Opt* **15**, 026006 (2010).

73. M. S. Hassanpour, A. T. Eggebrecht, J. P. Culver, and J. E. Peelle, "Mapping cortical responses to speech using high-density diffuse optical tomography," *Neuroimage* **117**, 319-326 (2015).
74. J. P. Culver, R. Choe, M. J. Holboke, L. Zubkov, T. Durduran, A. Slemp, V. Ntziachristos, B. Chance, and A. G. Yodh, "Three-dimensional diffuse optical tomography in the parallel plane transmission geometry: evaluation of a hybrid frequency domain/continuous wave clinical system for breast imaging," *Medical physics* **30**, 235-247 (2003).
75. M. Guven, B. Yazici, X. Intes, and B. Chance, "Diffuse optical tomography with a priori anatomical information," *Phys Med Biol* **50**, 2837-2858 (2005).
76. A. P. Gibson, J. C. Hebden, and S. R. Arridge, "Recent advances in diffuse optical imaging," *Phys Med Biol* **50**, R1-R43 (2005).
77. A. J. Chaudhari, F. Darvas, J. R. Bading, R. A. Moats, P. S. Conti, D. J. Smith, S. R. Cherry, and R. M. Leahy, "Hyperspectral and multispectral bioluminescence optical tomography for small animal imaging," *Phys Med Biol* **50**, 5421-5441 (2005).
78. J. V. Frangioni, "In vivo near-infrared fluorescence imaging," *Curr Opin Chem Biol* **7**, 626-634 (2003).
79. G. Choy, S. O'Connor, F. E. Diehn, N. Costouros, H. R. Alexander, P. Choyke, and S. K. Libutti, "Comparison of noninvasive fluorescent and bioluminescent small animal optical imaging," *Biotechniques* **35**, 1022-1026, 1028-1030 (2003).
80. P. K. Yalavarthy, B. W. Pogue, H. Dehghani, C. M. Carpenter, S. Jiang, and K. D. Paulsen, "Structural information within regularization matrices improves near infrared diffuse optical tomography," *Optics Express* **15**, 8043-8058 (2007).
81. V. Quaresima, R. Lepanto, and M. Ferrari, "The use of near infrared spectroscopy in sports medicine," *Journal of sports medicine and physical fitness* **43**, 1 (2003).
82. G. Yu, T. Durduran, G. Lech, C. Zhou, B. Chance, E. R. Mohler, 3rd, and A. G. Yodh, "Time-dependent blood flow and oxygenation in human skeletal muscles measured with noninvasive near-infrared diffuse optical spectroscopies," *J Biomed Opt* **10**, 024027 (2005).
83. J. C. Hebden, A. Gibson, R. M. Yusof, N. Everdell, E. M. Hillman, D. T. Delpy, S. R. Arridge, T. Austin, J. H. Meek, and J. S. Wyatt, "Three-dimensional optical tomography of the premature infant brain," *Phys Med Biol* **47**, 4155-4166 (2002).
84. B. W. Pogue, S. P. Poplack, T. O. McBride, W. A. Wells, K. S. Osterman, U. L. Osterberg, and K. D. Paulsen, "Quantitative hemoglobin tomography with diffuse near-infrared spectroscopy: pilot results in the breast," *Radiology* **218**, 261-266 (2001).
85. H. Jiang, N. V. Iftimia, Y. Xu, J. A. Eggert, L. L. Fajardo, and K. L. Klove, "Near-infrared optical imaging of the breast with model-based reconstruction," *Acad Radiol* **9**, 186-194 (2002).
86. A. H. Hielscher, A. Y. Bluestone, G. S. Abdoulaev, A. D. Klose, J. Lasker, M. Stewart, U. Netz, and J. Beuthan, "Near-infrared diffuse optical tomography," *Dis Markers* **18**, 313-337 (2002).
87. S. Wray, M. Cope, D. T. Delpy, J. S. Wyatt, and E. O. Reynolds, "Characterization of the near infrared absorption spectra of cytochrome aa3 and haemoglobin for the non-invasive monitoring of cerebral oxygenation," *Biochimica et biophysica acta* **933**, 184-192 (1988).
88. C. E. Elwell, M. Cope, A. D. Edwards, J. S. Wyatt, D. T. Delpy, and E. O. Reynolds, "Quantification of adult cerebral hemodynamics by near-infrared spectroscopy," *J Appl Physiol (1985)* **77**, 2753-2760 (1994).
89. A. P. Gibson, T. Austin, N. L. Everdell, M. Schweiger, S. R. Arridge, J. H. Meek, J. S. Wyatt, D. T. Delpy, and J. C. Hebden, "Three-dimensional whole-head optical tomography of passive motor evoked responses in the neonate," *Neuroimage* **30**, 521-528 (2006).
90. H. Saitou, H. Yanagi, S. Hara, S. Tsuchiya, and S. Tomura, "Cerebral blood volume and oxygenation among poststroke hemiplegic patients: Effects of 13 rehabilitation tasks measured by near-infrared spectroscopy," *Archives of physical medicine and rehabilitation* **81**, 1348-1356 (2000).

91. S. P. Gopinath, C. S. Robertson, C. F. Contant, R. K. Narayan, R. G. Grossman, and B. Chance, "Early Detection of Delayed Traumatic Intracranial Hematomas Using near-Infrared Spectroscopy," *Journal of neurosurgery* **83**, 438-444 (1995).
92. T. Austin, A. P. Gibson, G. Branco, R. M. Yusof, S. R. Arridge, J. H. Meek, J. S. Wyatt, D. T. Delpy, and J. C. Hebden, "Three dimensional optical imaging of blood volume and oxygenation in the neonatal brain," *Neuroimage* **31**, 1426-1433 (2006).
93. J. W. Belliveau, D. N. Kennedy, Jr., R. C. McKinstry, B. R. Buchbinder, R. M. Weisskoff, M. S. Cohen, J. M. Vevea, T. J. Brady, and B. R. Rosen, "Functional mapping of the human visual cortex by magnetic resonance imaging," *Science* **254**, 716-719 (1991).
94. J. C. Hebden, S. R. Arridge, and D. T. Delpy, "Optical imaging in medicine: I. Experimental techniques," *Phys Med Biol* **42**, 825-840 (1997).
95. S. R. Arridge and M. Schweiger, "Image reconstruction in optical tomography," *Philosophical transactions of the Royal Society of London. Series B, Biological sciences* **352**, 717-726 (1997).
96. S. R. Arridge and J. C. Hebden, "Optical imaging in medicine: II. Modelling and reconstruction," *Phys Med Biol* **42**, 841-853 (1997).
97. J. C. Hebden and D. T. Delpy, "Enhanced time-resolved imaging with a diffusion model of photon transport," *Opt Lett* **19**, 311-313 (1994).
98. H. Dehghani, S. Srinivasan, B. W. Pogue, and A. Gibson, "Numerical modelling and image reconstruction in diffuse optical tomography," *Philosophical transactions. Series A, Mathematical, physical, and engineering sciences* **367**, 3073-3093 (2009).
99. S. R. Arridge, "Optical tomography in medical imaging," *Inverse Problems* **15**, R41-R93 (1999).
100. S. R. Arridge, M. Cope, and D. T. Delpy, "The theoretical basis for the determination of optical pathlengths in tissue: temporal and frequency analysis," *Phys Med Biol* **37**, 1531-1560 (1992).
101. E. Alerstam, T. Svensson, and S. Andersson-Engels, "Parallel computing with graphics processing units for high-speed Monte Carlo simulation of photon migration," *J Biomed Opt* **13**, 060504 (2008).
102. S. R. Arridge, "Photon-measurement density functions. Part I: Analytical forms," *Appl Opt* **34**, 7395-7409 (1995).
103. B. C. Wilson and G. Adam, "A Monte Carlo model for the absorption and flux distributions of light in tissue," *Med Phys* **10**, 824-830 (1983).
104. S. T. Flock, M. S. Patterson, B. C. Wilson, and D. R. Wyman, "Monte Carlo modeling of light propagation in highly scattering tissues. I. Model predictions and comparison with diffusion theory," *Biomedical Engineering, IEEE Transactions on* **36**, 1162-1168 (1989).
105. S. R. Arridge and J. C. Schotland, "Optical tomography: forward and inverse problems," *Inverse Problems* **25**, 123010 (2009).
106. B. W. Pogue, T. O. McBride, J. Prewitt, U. L. Osterberg, and K. D. Paulsen, "Spatially variant regularization improves diffuse optical tomography," *Appl Opt* **38**, 2950-2961 (1999).
107. H. Dehghani, B. W. Pogue, S. P. Poplack, and K. D. Paulsen, "Multiwavelength three-dimensional near-infrared tomography of the breast: initial simulation, phantom, and clinical results," *Appl Opt* **42**, 135-145 (2003).
108. A. Bluestone, G. Abdoulaev, C. Schmitz, R. Barbour, and A. Hielscher, "Three-dimensional optical tomography of hemodynamics in the human head," *Optics express* **9**, 272-286 (2001).
109. M. Jermyn, H. Ghadyani, M. A. Mastanduno, W. Turner, S. C. Davis, H. Dehghani, and B. W. Pogue, "Fast segmentation and high-quality three-dimensional volume mesh creation from medical images for diffuse optical tomography," *J Biomed Opt* **18**, 086007 (2013).
110. M. Schweiger and S. Arridge, "The Toast plus plus software suite for forward and inverse modeling in optical tomography," *J Biomed Opt* **19**, 040801 (2014).
111. T. H. Matsui, " An atlas of the human brain for computerized tomography," (1978).
112. J. Mazziotta, A. Toga, A. Evans, P. Fox, J. Lancaster, K. Zilles, R. Woods, T. Paus, G. Simpson, B. Pike, C. Holmes, L. Collins, P. Thompson, D. MacDonald, M. Iacoboni, T.

Schormann, K. Amunts, N. Palomero-Gallagher, S. Geyer, L. Parsons, K. Narr, N. Kabani, G. Le Goualher, D. Boomsma, T. Cannon, R. Kawashima, and B. Mazoyer, "A probabilistic atlas and reference system for the human brain: International Consortium for Brain Mapping (ICBM)," *Philosophical transactions of the Royal Society of London. Series B, Biological sciences* **356**, 1293-1322 (2001).

113. K. E. Pape, R. J. Blackwell, G. Cusick, A. Sherwood, M. T. Houang, R. J. Thorburn, and E. O. Reynolds, "Ultrasound detection of brain damage in preterm infants," *Lancet* **1**, 1261-1264 (1979).
114. S. B. Eickhoff, K. E. Stephan, H. Mohlberg, C. Grefkes, G. R. Fink, K. Amunts, and K. Zilles, "A new SPM toolbox for combining probabilistic cytoarchitectonic maps and functional imaging data," *Neuroimage* **25**, 1325-1335 (2005).
115. M. Brett, K. Christoff, R. Cusack, and J. Lancaster, "Using the Talairach atlas with the MNI template," *Neuroimage* **13**, 85-85 (2001).
116. A. C. Evans, A. L. Janke, D. L. Collins, and S. Baillet, "Brain templates and atlases," *Neuroimage* **62**, 911-922 (2012).
117. J. Mazziotta, A. Toga, A. Evans, P. Fox, J. Lancaster, K. Zilles, R. Woods, T. Paus, G. Simpson, B. Pike, C. Holmes, L. Collins, P. Thompson, D. MacDonald, M. Iacoboni, T. Schormann, K. Amunts, N. Palomero-Gallagher, S. Geyer, L. Parsons, K. Narr, N. Kabani, G. Le Goualher, J. Feidler, K. Smith, D. Boomsma, H. Hulshoff Pol, T. Cannon, R. Kawashima, and B. Mazoyer, "A four-dimensional probabilistic atlas of the human brain," *Journal of the American Medical Informatics Association : JAMIA* **8**, 401-430 (2001).
118. A. J. Schwarz, A. Danckaert, T. Reese, A. Gozzi, G. Paxinos, C. Watson, E. V. Merlo-Pich, and A. Bifone, "A stereotaxic MRI template set for the rat brain with tissue class distribution maps and co-registered anatomical atlas: application to pharmacological MRI," *Neuroimage* **32**, 538-550 (2006).
119. P. E. Roland, C. J. Graufelds, W. H. J, L. Ingelman, M. Andersson, A. Ledberg, J. Pedersen, S. Akerman, A. Dabringhaus, and K. Zilles, "Human brain atlas: For high-resolution functional and anatomical mapping," *Hum Brain Mapp* **1**, 173-184 (1994).
120. J. L. Lancaster, M. G. Woldorff, L. M. Parsons, M. Liotti, C. S. Freitas, L. Rainey, P. V. Kochunov, D. Nickerson, S. A. Mikiten, and P. T. Fox, "Automated Talairach atlas labels for functional brain mapping," *Hum Brain Mapp* **10**, 120-131 (2000).
121. M. Cabezas, A. Oliver, X. Llado, J. Freixenet, and M. B. Cuadra, "A review of atlas-based segmentation for magnetic resonance brain images," *Comput Methods Programs Biomed* **104**, e158-177 (2011).
122. L. W. Swanson, "Brain Maps: Structure of the Rat Brain (2nd edn)," *Nature* **363**, 347-350 (2004).
123. N. Kovacevic, J. T. Henderson, E. Chan, N. Lifshitz, J. Bishop, A. C. Evans, R. M. Henkelman, and X. J. Chen, "A three-dimensional MRI atlas of the mouse brain with estimates of the average and variability," *Cereb Cortex* **15**, 639-645 (2005).
124. E. Munoz-Moreno, A. Arbat-Plana, D. Batalle, G. Soria, M. Illa, A. Prats-Galino, E. Eixarch, and E. Gratacos, "A magnetic resonance image based atlas of the rabbit brain for automatic parcellation," *PloS one* **8**, e67418 (2013).
125. J. Szabo and W. M. Cowan, "A stereotaxic atlas of the brain of the cynomolgus monkey (Macaca fascicularis)," *The Journal of comparative neurology* **222**, 265-300 (1984).
126. M. Kuklisova-Murgasova, P. Aljabar, L. Srinivasan, S. J. Counsell, V. Doria, A. Serag, I. S. Gousias, J. P. Boardman, M. A. Rutherford, A. D. Edwards, J. V. Hajnal, and D. Rueckert, "A dynamic 4D probabilistic atlas of the developing brain," *Neuroimage* **54**, 2750-2763 (2011).
127. Y. Tang, C. Hojatkashani, I. D. Dinov, B. Sun, L. Fan, X. Lin, and A. W. Toga, "The construction of a Chinese MRI brain atlas: A morphometric comparison study between Chinese and Caucasian cohorts," *Neuroimage* **51**, 33-41 (2010).
128. K. A. Johnson and J. A. Becker, "Whole Brain Atlas" (1999), retrieved http://www.med.harvard.edu/aanlib/home.html.

129. P. M. Thompson, M. S. Mega, R. P. Woods, C. I. Zoumalan, C. J. Lindshield, R. E. Blanton, J. Moussai, C. J. Holmes, J. L. Cummings, and A. W. Toga, "Cortical change in Alzheimer's disease detected with a disease-specific population-based brain atlas," *Cerebral cortex* **11**, 1-16 (2001).
130. P. M. Thompson, Mega, M. S., & Toga, A. W. , "Disease-specific brain atlases," in *Brain Mapping III: The Disorders* J. C. Mazziotta and A. W. Toga, eds. (Academic Press, 2000).
131. "ICBM 152 Nonlinear atlases version 2009", retrieved http://www.bic.mni.mcgill.ca/ServicesAtlases/ICBM152NLin2009.
132. K. Zilles, R. Kawashima, A. Dabringhaus, H. Fukuda, and T. Schormann, "Hemispheric shape of European and Japanese brains: 3-D MRI analysis of intersubject variability, ethnical, and gender differences," *Neuroimage* **13**, 262-271 (2001).
133. T. D. Cannon, P. M. Thompson, T. G. van Erp, A. W. Toga, V. P. Poutanen, M. Huttunen, J. Lonnqvist, C. G. Standerskjold-Nordenstam, K. L. Narr, M. Khaledy, C. I. Zoumalan, R. Dail, and J. Kaprio, "Cortex mapping reveals regionally specific patterns of genetic and disease-specific gray-matter deficits in twins discordant for schizophrenia," *Proc Natl Acad Sci U S A* **99**, 3228-3233 (2002).
134. A. W. Toga, P. M. Thompson, M. S. Mega, K. L. Narr, and R. E. Blanton, "Probabilistic approaches for atlasing normal and disease-specific brain variability," *Anat Embryol (Berl)* **204**, 267-282 (2001).
135. M. Brett, I. S. Johnsrude, and A. M. Owen, "The problem of functional localization in the human brain," *Nature reviews. Neuroscience* **3**, 243-249 (2002).
136. V. S. Fonov, A. C. Evans, R. C. McKinstry, C. R. Almli, and D. L. Collins, "Unbiased nonlinear average age-appropriate brain templates from birth to adulthood," *NeuroImage* **47**, 102 (2009).
137. R. L. Buckner, M. E. Raichle, and S. E. Petersen, "Dissociation of human prefrontal cortical areas across different speech production tasks and gender groups," *J Neurophysiol* **74**, 2163-2173 (1995).
138. M. Krams, M. F. Rushworth, M. P. Deiber, R. S. Frackowiak, and R. E. Passingham, "The preparation, execution and suppression of copied movements in the human brain," *Exp Brain Res* **120**, 386-398 (1998).
139. T. Greitz, C. Bohm, S. Holte, and L. Eriksson, "A Computerized Brain Atlas - Construction, Anatomical Content, and Some Applications," *Journal of computer assisted tomography* **15**, 26-38 (1991).
140. V. M. Spitzer and D. G. Whitlock, "The Visible Human Dataset: the anatomical platform for human simulation," *Anat Rec* **253**, 49-57 (1998).
141. K. Höhne, M. Bomans, M. Riemer, R. Schubert, U. Tiede, and W. Lierse, "A 3D anatomical atlas based on a volume model," *IEEE Comput Graphics Appl* **12**, 72–78 (1992).
142. J. Talairach and P. Tournoux, *Co-planar stereotaxic atlas of the human brain. 3-Dimensional proportional system: an approach to cerebral imaging.* (Thieme Medical Publishers, New York, 1988).
143. C. J. Holmes, R. Hoge, L. Collins, R. Woods, A. W. Toga, and A. C. Evans, "Enhancement of MR images using registration for signal averaging," *Journal of computer assisted tomography* **22**, 324-333 (1998).
144. K. Brodmann and L. J. Garey, *Brodmann's: Localisation in the Cerebral Cortex* (Springer Science & Business Media, 2001).
145. J. L. Lancaster, L. H. Rainey, J. L. Summerlin, C. S. Freitas, P. T. Fox, A. C. Evans, A. W. Toga, and J. C. Mazziotta, "Automated labeling of the human brain: a preliminary report on the development and evaluation of a forward-transform method," *Hum Brain Mapp* **5**, 238-242 (1997).
146. A. C. Evans, D. L. Collins, and B. Milner, " An MRI-based stereotactic atlas from 250 young normal subjects," *Proc 22nd Annual Symposium, Society for Neuroscience* **18**, 408 (1992).
147. "Talairach Daemon", retrieved http://www.talairach.org/daemon.html.

148. P. T. Fox, S. Mikiten, G. Davis, and J. L. Lancaster, "BrainMap: a database of human functional brain mapping," *Functional Neuroimaging: Technical Foundations*, 95–106 (1994).
149. A. Laird, J. Lancaster, and P. Fox, "BrainMap: The social evolution of a functional neuroimaging database," *Neuroinformatics* **3**, 65-78 (2005).
150. D. L. Collins, P. Neelin, T. M. Peters, and A. C. Evans, "Automatic 3D intersubject registration of MR volumetric data in standardized Talairach space," *J Comput Assist Tomogr* **18**, 192-205 (1994).
151. A. C. Evans, D. L. Collins, S. R. Mills, E. D. Brown, R. L. Kelly, and T. M. Peters, "3d Statistical Neuroanatomical Models from 305 Mri Volumes," *Nuclear Science Symposium & Medical Imaging Conference, Vols 1-3*, 1813-1817 (1993).
152. B. Aubert-Broche, A. C. Evans, and L. Collins, "A new improved version of the realistic digital brain phantom," *Neuroimage* **32**, 138-145 (2006).
153. M. B. I. Centre, "Colin 27 Average Brain, Stereotaxic Registration Model, original 1998 version", retrieved http://www.bic.mni.mcgill.ca/ServicesAtlases/Colin27.
154. W. D. Penny, Friston, K. J., Ashburner, J. T., Kiebel, S. J.,, *Statistical parametric mapping: the analysis of functional brain images: the analysis of functional brain images*. (Academic press, 2001).
155. "FieldTrip: the MATLAB software toolbox for MEG and EEG analysis", retrieved http://www.fieldtriptoolbox.org/.
156. R. Oostenveld, P. Fries, E. Maris, and J. M. Schoffelen, "FieldTrip: Open source software for advanced analysis of MEG, EEG, and invasive electrophysiological data," *Comput Intell Neurosci* **2011**, 156869 (2011).
157. A. O. Nusbaum, C. Y. Tang, M. S. Buchsbaum, T. C. Wei, and S. W. Atlas, "Regional and global changes in cerebral diffusion with normal aging," *AJNR. American journal of neuroradiology* **22**, 136-142 (2001).
158. J. Diedrichsen, J. H. Balsters, J. Flavell, E. Cussans, and N. Ramnani, "A probabilistic MR atlas of the human cerebellum," *Neuroimage* **46**, 39-46 (2009).
159. A. K. Singh, M. Okamoto, H. Dan, V. Jurcak, and I. Dan, "Spatial registration of multichannel multi-subject fNIRS data to MNI space without MRI," *Neuroimage* **27**, 842-851 (2005).
160. "MNI Average Brain (305 MRI) Stereotaxic Registration Model", retrieved http://www.bic.mni.mcgill.ca/ServicesAtlases/MNI305.
161. "Linear ICBM Average Brain (ICBM152) Stereotaxic Registration Model", retrieved http://www.bic.mni.mcgill.ca/ServicesAtlases/ICBM152Lin.
162. J. L. Lancaster, D. Tordesillas-Gutierrez, M. Martinez, F. Salinas, A. Evans, K. ZilleS, J. C. Mazziotta, and P. T. Fox, "Bias between MNI and talairach coordinates analyzed using the ICBM-152 brain template," *Human brain mapping* **28**, 1194-1205 (2007).
163. "NIHPD Objective atlases ", retrieved http://www.bic.mni.mcgill.ca/ServicesAtlases/NIHPD-obj2.
164. S. Brigadoi, P. Aljabar, M. Kuklisova-Murgasova, S. R. Arridge, and R. J. Cooper, "A 4D neonatal head model for diffuse optical imaging of pre-term to term infants," *Neuroimage* **100**, 385-394 (2014).
165. D. L. Collins, A. P. Zijdenbos, W. F. C. Baare, and A. C. Evans, "ANIMAL+INSECT: Improved cortical structure segmentation," *Information Processing in Medical Imaging, Proceedings* **1613**, 210-223 (1999).
166. V. Ntziachristos, X. Ma, Yodh, A. G., and B. Chance, "Multichannel photon counting instrument for spatially resolved near infrared spectroscopy," *Review of Scientific Instruments* **70**, 193-201 (1999).
167. K. Uludag, J. Steinbrink, A. Villringer, and H. Obrig, "Separability and cross talk: optimizing dual wavelength combinations for near-infrared spectroscopy of the adult head," *Neuroimage* **22**, 583-589 (2004).
168. C. E. Cooper, S. J. Matcher, J. S. Wyatt, M. Cope, G. C. Brown, E. M. Nemoto, and D. T. Delpy, "Near-infrared spectroscopy of the brain: relevance to cytochrome oxidase bioenergetics," *Biochem Soc Trans* **22**, 974-980 (1994).

169. K. Isobe, T. Kusaka, Y. Fujikawa, M. Kondo, K. Kawada, S. Yasuda, K. Hirao, and S. Onishi, "Changes in cerebral hemoglobin concentration and oxygen saturation immediately after birth in the human neonate using full-spectrum near infrared spectroscopy," *J Biomed Opt* **5**, 283-286 (2000).
170. P. J. Kirkpatrick, "Use of near–infrared spectroscopy in the adult.," *Philosophical Transactions of the Royal Society of London B: Biological Sciences* **352**, 701-705 (1997).
171. D. Comelli, A. Bassi, A. Pifferi, P. Taroni, A. Torricelli, R. Cubeddu, F. Martelli, and G. Zaccanti, "In vivo time-resolved reflectance spectroscopy of the human forehead," *Appl Opt* **46**, 1717-1725 (2007).
172. E. Okada, M. Firbank, M. Schweiger, S. R. Arridge, M. Cope, and D. T. Delpy, "Theoretical and experimental investigation of near-infrared light propagation in a model of the adult head," *Appl Opt* **36**, 21-31 (1997).
173. E. Okada, M. Firbank, and D. T. Delpy, "The effect of overlying tissue on the spatial sensitivity profile of near-infrared spectroscopy," *Phys Med Biol* **40**, 2093-2108 (1995).
174. H. Dehghani and D. T. Delpy, "Near-infrared spectroscopy of the adult head: effect of scattering and absorbing obstructions in the cerebrospinal fluid layer on light distribution in the tissue," *Appl Opt* **39**, 4721-4729 (2000).
175. O. Pucci, V. Toronov, and K. St Lawrence, "Measurement of the optical properties of a two-layer model of the human head using broadband near-infrared spectroscopy," *Applied optics* **49**, 6324-6332 (2010).
176. R. J. Hunter, M. S. Patterson, T. J. Farrell, and J. E. Hayward, "Haemoglobin oxygenation of a two-layer tissue-simulating phantom from time-resolved reflectance: effect of top layer thickness," *Phys Med Biol* **47**, 193-208 (2002).
177. D. A. Boas and A. M. Dale, "Simulation study of magnetic resonance imaging-guided cortically constrained diffuse optical tomography of human brain function," *Appl Opt* **44**, 1957-1968 (2005).
178. W. M. Wells III, W. E. L. Grimson, R. Kikinis, and F. A. Jolesz, " Adaptive segmentation of MRI data," *IEEE transactions on medical imaging* **15**, 429-442. (1996).
179. D. L. Pham, C. Xu, and J. L. Prince, "Current methods in medical image segmentation," *Annu Rev Biomed Eng* **2**, 315-337 (2000).
180. D. L. Collins, C. J. Holmes, T. M. Peters, and A. C. Evans, "Automatic 3-D model-based neuroanatomical segmentation," *Human brain mapping* **3**, 190-208 (1995).
181. D. L. Collins, T. M. Peters, W. Q. Dai, and A. C. Evans, "Model Based Segmentation of Individual Brain Structures from Mri Data," *P Soc Photo-Opt Ins* **1808**, 10-23 (1992).
182. Y. Zhou and J. Bai, "Atlas-based fuzzy connectedness segmentation and intensity nonuniformity correction applied to brain MRI," *IEEE Trans Biomed Eng* **54**, 122-129 (2007).
183. B. Fischl, D. H. Salat, E. Busa, M. Albert, M. Dieterich, C. Haselgrove, A. van der Kouwe, R. Killiany, D. Kennedy, S. Klaveness, A. Montillo, N. Makris, B. Rosen, and A. M. Dale, "Whole brain segmentation: automated labeling of neuroanatomical structures in the human brain," *Neuron* **33**, 341-355 (2002).
184. H. K. Hahn and H. O. Peitgen, "The skull stripping problem in MRI solved by a single 3D watershed transform," *Lect Notes Comput Sc* **1935**, 134-143 (2000).
185. H. Hricak, C. Alpers, L. E. Crooks, and P. E. Sheldon, "Magnetic resonance imaging of the female pelvis: initial experience," *AJR. American journal of roentgenology* **141**, 1119-1128 (1983).
186. L. Lemieux, G. Hagemann, K. Krakow, and F. G. Woermann, "Fast, accurate, and reproducible automatic segmentation of the brain in T1-weighted volume MRI data," *Magnetic resonance in medicine : official journal of the Society of Magnetic Resonance in Medicine / Society of Magnetic Resonance in Medicine* **42**, 127-135 (1999).
187. B. R. Sajja, S. Datta, R. He, M. Mehta, R. K. Gupta, J. S. Wolinsky, and P. A. Narayana, "Unified approach for multiple sclerosis lesion segmentation on brain MRI," *Ann Biomed Eng* **34**, 142-151 (2006).

188. R. A. Heckemann, J. V. Hajnal, P. Aljabar, D. Rueckert, and A. Hammers, "Automatic anatomical brain MRI segmentation combining label propagation and decision fusion," *Neuroimage* **33**, 115-126 (2006).
189. H. Tang, E. X. Wu, Q. Y. Ma, D. Gallagher, G. M. Perera, and T. Zhuang, "MRI brain image segmentation by multi-resolution edge detection and region selection," *Computerized medical imaging and graphics : the official journal of the Computerized Medical Imaging Society* **24**, 349-357 (2000).
190. R. Stokking, K. L. Vincken, and M. A. Viergever, "Automatic morphology-based brain segmentation (MBRASE) from MRI-T1 data," *Neuroimage* **12**, 726-738 (2000).
191. J. Suckling, T. Sigmundsson, K. Greenwood, and E. T. Bullmore, "A modified fuzzy clustering algorithm for operator independent brain tissue classification of dual echo MR images," *Magn Reson Imaging* **17**, 1065-1076 (1999).
192. M. S. Atkins and B. T. Mackiewich, "Fully automatic segmentation of the brain in MRI," *IEEE Trans Med Imaging* **17**, 98-107 (1998).
193. C. A. Cocosco, A. P. Zijdenbos, and A. C. Evans, "A fully automatic and robust brain MRI tissue classification method," *Med Image Anal* **7**, 513-527 (2003).
194. R. C. Gur, F. Gunning-Dixon, W. B. Bilker, and R. E. Gur, "Sex differences in temporo-limbic and frontal brain volumes of healthy adults," *Cereb Cortex* **12**, 998-1003 (2002).
195. J. Ashburner and K. J. Friston, "Unified segmentation," *Neuroimage* **26**, 839-851 (2005).
196. S. M. Smith, "Fast robust automated brain extraction," *Hum Brain Mapp* **17**, 143-155 (2002).
197. J. Z. Wang, J. Kong, Y. H. Lu, M. Qi, and B. X. Zhang, "A modified FCM algorithm for MRI brain image segmentation using both local and non-local spatial constraints," *Computerized Medical Imaging and Graphics* **32**, 685-698 (2008).
198. M. A. Balafar, A. R. Ramli, M. I. Saripan, and S. Mashohor, "Review of brain MRI image segmentation methods," *Artificial Intelligence Review* **33**, 261-274 (2010).
199. P. M. Thompson, R. P. Woods, M. S. Mega, and A. W. Toga, "Mathematical/computational challenges in creating deformable and probabilistic atlases of the human brain," *Hum Brain Mapp* **9**, 81-92 (2000).
200. R. Kikinis, M. E. Shenton, D. V. Iosifescu, R. W. McCarley, P. Saiviroonporn, H. H. Hokama, A. Robatino, D. Metcalf, C. G. Wible, C. M. Portas, R. M. Donnino, and F. A. Jolesz, "A digital brain atlas for surgical planning, model-driven segmentation, and teaching," *Ieee T Vis Comput Gr* **2**, 232-241 (1996).
201. A. Klein, B. Mensh, S. Ghosh, J. Tourville, and J. Hirsch, "Mindboggle: automated brain labeling with multiple atlases," *BMC medical imaging* **5**, 7 (2005).
202. M. Murgasova, L. Dyet, D. Edwards, M. Rutherford, J. Hajnal, and D. Rueckert, "Segmentation of brain MRI in young children," *Acad Radiol* **14**, 1350-1366 (2007).
203. B. Fischl, A. van der Kouwe, C. Destrieux, E. Halgren, F. Segonne, D. H. Salat, E. Busa, L. J. Seidman, J. Goldstein, D. Kennedy, V. Caviness, N. Makris, B. Rosen, and A. M. Dale, "Automatically parcellating the human cerebral cortex," *Cereb Cortex* **14**, 11-22 (2004).
204. C. f. M. A. a. M. G. Hospital, "IBSR, Internet brain segmentation repository", retrieved www.cma.mgh.harvard.edu/ibsr/.
205. D. W. Shattuck, M. Mirza, V. Adisetiyo, C. Hojatkashani, G. Salamon, K. L. Narr, R. A. Poldrack, R. M. Bilder, and A. W. Toga, "Construction of a 3D probabilistic atlas of human cortical structures," *Neuroimage* **39**, 1064-1080 (2008).
206. J. M. Lotjonen, R. Wolz, J. R. Koikkalainen, L. Thurfjell, G. Waldemar, H. Soininen, and D. Rueckert, "Fast and robust multi-atlas segmentation of brain magnetic resonance images," *Neuroimage* **49**, 2352-2365 (2010).
207. C. D. Good, I. S. Johnsrude, J. Ashburner, R. N. Henson, K. J. Friston, and R. S. Frackowiak, "A voxel-based morphometric study of ageing in 465 normal adult human brains," *Neuroimage* **14**, 21-36 (2001).
208. J. Ashburner and K. J. Friston, "Image segmentation," in *Human Brain Function,* 2nd ed., R. S. J. Frackowiak, K. J. Friston, C. Frith, R. Dolan, C. J. Price, S. Zeki, J. Ashburner, and W. D. Penny, eds. (Academic Press, 2003).

209. J. Ashburner and K. Friston, "Multimodal image coregistration and partitioning - A unified framework," *Neuroimage* **6**, 209-217 (1997).
210. U. Herwig, P. Satrapi, and C. Schonfeldt-Lecuona, "Using the International 10-20 EEG system for positioning of transcranial magnetic stimulation," *Brain Topography* **16**, 95-99 (2003).
211. B. A. Ardekani, S. Guckemus, A. Bachman, M. J. Hoptman, M. Wojtaszek, and J. Nierenberg, "Quantitative comparison of algorithms for inter-subject registration of 3D volumetric brain MRI scans," *J Neurosci Methods* **142**, 67-76 (2005).
212. B. rn Hamre, "Three-dimensional image registration of magnetic resonance MRI head volumes," (university of bergen Norway, 1998).
213. M. L. Lipton, E. Gulko, M. E. Zimmerman, B. W. Friedman, M. Kim, E. Gellella, and C. A. Branch, "Diffusion-Tensor Imaging Implicates Prefrontal Axonal Injury in Executive Function Impairment Following Very Mild Traumatic Brain Injury 1," *Radiology* **252**, 816-824 (2009).
214. W. R. Crum, T. Hartkens, and D. L. Hill, "Non-rigid image registration: theory and practice," *Br J Radiol* **77 Spec No 2**, S140-153 (2004).
215. M. M. Coselmon, J. M. Balter, D. L. McShan, and M. L. Kessler, "Mutual information based CT registration of the lung at exhale and inhale breathing states using thin-plate splines," *Medical physics* **31**, 2942-2948 (2004).
216. S. Shimizu, H. Shirato, S. Ogura, H. Akita-Dosaka, K. Kitamura, T. Nishioka, K. Kagei, M. Nishimura, and K. Miyasaka, "Detection of lung tumor movement in real-time tumor-tracking radiotherapy," *International journal of radiation oncology, biology, physics* **51**, 304-310 (2001).
217. B. F. Hutton and M. Braun, "Software for image registration: algorithms, accuracy, efficacy," *Seminars in nuclear medicine* **33**, 180-192 (2003).
218. J. B. Maintz, P. A. van den Elsen, and M. A. Viergever, "Comparison of edge-based and ridge-based registration of CT and MR brain images," *Med Image Anal* **1**, 151-161 (1996).
219. D. L. G. Hill, D. J. Hawkes, J. E. Crossman, M. J. Gleeson, T. C. S. Cox, E. E. C. M. L. Bracey, A. J. Strong, and P. Graves, "Registration of Mr and Ct Images for Skull Base Surgery Using Point-Like Anatomical Features," *Brit J Radiol* **64**, 1030-1035 (1991).
220. J. A. Schnabel, D. Rueckert, M. Quist, J. M. Blackall, A. D. Castellano-Smith, T. Hartkens, and D. J. Hawkes, "A generic framework for non-rigid registration based on non-uniform multi-level free-form deformations," *Medical Image Computing and Computer-Assisted Intervention–MICCAI*, 573-581 (2001).
221. P. Kellman, C. Chefd'hotel, C. H. Lorenz, C. Mancini, A. E. Arai, and E. R. McVeigh, "Fully automatic, retrospective enhancement of real-time acquired cardiac cine MR images using image-based navigators and respiratory motion-corrected averaging," *Magnetic resonance in medicine* **59**, 771-778 (2008).
222. A. Goto, H. Moritomo, T. Murase, K. Oka, K. Sugamoto, T. Arimura, J. Masumoto, S. Tamura, H. Yoshikawa, and T. Ochi, "In vivo three-dimensional wrist motion analysis using magnetic resonance imaging and volume-based registration," *Journal of Orthopaedic Research* **23**, 750-756 (2005).
223. Y. Seppenwoolde, H. Shirato, K. Kitamura, S. Shimizu, M. van Herk, J. V. Lebesque, and K. Miyasaka, "Precise and real-time measurement of 3D tumor motion in lung due to breathing and heartbeat, measured during radiotherapy," *Int J Radiat Oncol* **53**, 822-834 (2002).
224. B. M. Dawant, "Non-rigid registration of medical images: Purpose and methods, a short survey," *2002 Ieee International Symposium on Biomedical Imaging, Proceedings*, 465-468 (2002).
225. A. Gholipour, N. Kehtarnavaz, R. Briggs, M. Devous, and K. Gopinath, "Brain functional localization: a survey of image registration techniques," *IEEE Trans Med Imaging* **26**, 427-451 (2007).
226. S. M. Smith, M. Jenkinson, M. W. Woolrich, C. F. Beckmann, T. E. J. Behrens, H. Johansen-Berg, P. R. Bannister, M. De Luca, I. Drobnjak, D. E. Flitney, R. K. Niazy, J. Saunders, J. Vickers, Y. Y. Zhang, N. De Stefano, J. M. Brady, and P. M. Matthews, "Advances in

functional and structural MR image analysis and implementation as FSL," *Neuroimage* **23**, S208-S219 (2004).
227. R. A. McLaughlin, J. Hipwell, D. J. Hawkes, J. A. Noble, J. V. Byrne, and T. Cox, "A comparison of 2D-3D intensity-based registration and feature-based registration for neurointerventions," *Medical Image Computing and Computer-Assisted Intervention—MICCAI 2002*, 517-524 (2002).
228. O. Clatz, H. Delingette, I. F. Talos, A. J. Golby, R. Kikinis, F. A. Jolesz, N. Ayache, and S. K. Warfield, "Robust nonrigid registration to capture brain shift from intraoperative MRI," *IEEE Trans Med Imaging* **24**, 1417-1427 (2005).
229. M. Prümmer, J. Hornegger, M. Pfister, and A. Dörfler, "Multi-modal 2D-3D non-rigid registration," *Progress in biomedical optics and imaging* **7**(2006).
230. G. K. Rohde, S. Pajevic, and C. Pierpaoli, "Multi-channel registration of diffusion tensor images using directional information," *2004 2nd Ieee International Symposium on Biomedical Imaging: Macro to Nano, Vols 1 and 2*, 712-715 (2004).
231. Q. X. Huang, B. Adams, M. Wicke, and L. J. Guibas, "Non-rigid registration under isometric deformations," *Computer Graphics Forum* **27**, 1449-1457 (2008).
232. A. Azar, C. Xu, X. Pennec, and N. Ayache, "An interactive hybrid non-rigid registration framework for 3D medical images," *I S Biomed Imaging*, 824-827 (2006).
233. D. Tsuzuki and I. Dan, "Spatial registration for functional near-infrared spectroscopy: from channel position on the scalp to cortical location in individual and group analyses," *Neuroimage* **85 Pt 1**, 92-103 (2014).
234. Q. Zheng, A. Sharf, A. Tagliasacchi, B. Chen, H. Zhang, A. Sheffer, and D. Cohen-Or, "Consensus Skeleton for Non-rigid Space-time Registration," *Computer Graphics Forum* **29**, 635-644 (2010).
235. J. Elseberg, D. Borrmann, K. Lingemann, and A. Nuchter, "Non-Rigid Registration and Rectification of 3D Laser Scans," *Ieee Int C Int Robot*, 1546-1552 (2010).
236. M. Ferrant, A. Nabavi, B. Macq, F. A. Jolesz, R. Kikinis, and S. K. Warfield, "Registration of 3-D intraoperative MR images of the brain using a finite-element biomechanical model," *IEEE transactions on medical imaging* **20**, 1384-1397 (2001).
237. T. Hartkens, D. L. Hill, A. D. Castellano-Smith, D. J. Hawkes, C. R. Maurer, Jr., A. J. Martin, W. A. Hall, H. Liu, and C. L. Truwit, "Measurement and analysis of brain deformation during neurosurgery," *IEEE Trans Med Imaging* **22**, 82-92 (2003).
238. D. Lee, W. H. Nam, J. Y. Lee, and J. B. Ra, "Non-rigid registration between 3D ultrasound and CT images of the liver based on intensity and gradient information," *Phys Med Biol* **56**, 117-137 (2011).
239. T. Ur Rehman, E. Haber, G. Pryor, J. Melonakos, and A. Tannenbaum, "3D nonrigid registration via optimal mass transport on the GPU," *Med Image Anal* **13**, 931-940 (2009).
240. G. K. Matsopoulos, K. K. Delibasis, N. A. Mouravliansky, P. A. Asvestas, K. S. Nikita, V. E. Kouloulias, and N. K. Uzunoglu, "CT-MRI automatic surface-based registration schemes combining global and local optimization techniques," *Technology and health care : official journal of the European Society for Engineering and Medicine* **11**, 219-232 (2003).
241. P. Cachier, J. F. Mangin, X. Pennec, D. Rivière, D. Papadopoulos-Orfanos, J. Régis, and N. Ayache, "Multisubject non-rigid registration of brain MRI using intensity and geometric features," *Medical Image Computing and Computer-Assisted Intervention–MICCAI 2001*, 734-742 (2001).
242. K. Rohr, H. S. Stiehl, R. Sprengel, T. M. Buzug, J. Weese, and M. H. Kuhn, "Landmark-based elastic registration using approximating thin-plate splines," *IEEE transactions on medical imaging* **20**, 526-534 (2001).
243. R. Szeliski and J. Coughlan, "Spline-based image registration," *International Journal of Computer Vision* **22**, 199-218 (1997).
244. Y. Wang and L. H. Staib, "Physical model-based non-rigid registration incorporating statistical shape information," *Med Image Anal* **4**, 7-20 (2000).

245. Y. M. Wang and L. H. Staib, "Elastic model based non-rigid registration incorporating statistical shape information," *Medical Image Computing and Computer-Assisted Intervention - Miccai'98* **1496**, 1162-1173 (1998).
246. G. E. Christensen, S. C. Joshi, and M. I. Miller, "Volumetric transformation of brain anatomy," *IEEE Trans Med Imaging* **16**, 864-877 (1997).
247. A. Hagemann, K. Rohr, and H. S. Stiehl, "Coupling of fluid and elastic models for biomechanical simulations of brain deformations using FEM," *Medical image analysis* **6**, 375-388 (2002).
248. S. Marsland, C. J. Twining, and C. J. Taylor, "Groupwise non-rigid registration using polyharmonic clamped-plate splines," *Medical Image Computing and Computer-Assisted Intervention - Miccai 2003, Pt 2* **2879**, 771-779 (2003).
249. T. Rhee, J. P. Lewis, K. Nayak, and U. Neumann, "Adaptive non-rigid registration of 3D knee MRI in different pose spaces," *Biomedical Imaging: From Nano to Macro, 2008*, 1111-1114 (2008).
250. D. Rueckert, L. I. Sonoda, C. Hayes, D. L. G. Hill, M. O. Leach, and D. J. Hawkes, "Nonrigid registration using free-form deformations: Application to breast MR images," *IEEE transactions on medical imaging* **18**, 712-721 (1999).
251. J. Ashburner and K. J. Friston, "Rigid body registration," in *Statistical Parametric Mapping: The Analysis of Functional Brain Images* (Academic Press, London, 2004).
252. J. P. W. Pluim, J. B. A. Maintz, and M. A. Viergever, "Mutual information matching and interpolation artefacts," *Proc Spie* **3661**, 56-65 (1999).
253. J. V. Hajnal, N. Saeed, E. J. Soar, A. Oatridge, I. R. Young, and G. M. Bydder, "A registration and interpolation procedure for subvoxel matching of serially acquired MR images," *J Comput Assist Tomogr* **19**, 289-296 (1995).
254. T. F. Cootes, S. Marsland, C. J. Twining, K. Smith, and C. J. Taylor, "Groupwise diffeomorphic non-rigid registration for automatic model building," *Computer Vision - Eccv 2004, Pt 4* **2034**, 316-327 (2004).
255. I. H. Habboush, K. D. Mitchell, R. V. Mulkern, P. D. Barnes, and S. T. Treves, "Registration and alignment of three-dimensional images: an interactive visual approach," *Radiology* **199**, 573-578 (1996).
256. H. J. Huppertz, M. Otte, C. Grimm, R. Kristeva-Feige, T. Mergner, and C. H. Lucking, "Estimation of the accuracy of a surface matching technique for registration of EEG and MRI data," *Electroencephalography and clinical neurophysiology* **106**, 409-415 (1998).
257. P. J. Besl and N. D. McKay, "A Method for registration of 3-D shapes," *IEEE transaction on pattern analysis and machine intelligence* **14**, 239-256 (1992).
258. R. J. Koshel, "Enhancement of the downhill simplex method of optimization," *International Optical Design Conference 2002* **4832**, 270-282 (2002).
259. K. Deb, "An efficient constraint handling method for genetic algorithms," *Computer methods in applied mechanics and engineering* **186**, 311-338 (2000).
260. P. R. Andresen and M. Nielsen, "Non-rigid registration by geometry-constrained diffusion," *Med Image Anal* **5**, 81-88 (2001).
261. C. Wu, P. E. Murtha, and B. Jaramaz, "Femur statistical atlas construction based on two-level 3D non-rigid registration," *Computer aided surgery : official journal of the International Society for Computer Aided Surgery* **14**, 83-99 (2009).
262. J. Kim and J. A. Fessler, "Intensity-based image registration using robust correlation coefficients," *IEEE Trans Med Imaging* **23**, 1430-1444 (2004).
263. W. M. Wells, 3rd, P. Viola, H. Atsumi, S. Nakajima, and R. Kikinis, "Multi-modal volume registration by maximization of mutual information," *Med Image Anal* **1**, 35-51 (1996).
264. J. Salvi, C. Matabosch, D. Fofi, and J. Forest, "A review of recent range image registration methods with accuracy evaluation," *Image and Vision computing* **25**, 578-596 (2007).
265. P. Hellier, C. Barillot, I. Corouge, B. Gibaud, G. Le Goualher, D. L. Collins, A. Evans, G. Malandain, N. Ayache, G. E. Christensen, and H. J. Johnson, "Retrospective evaluation of intersubject brain registration," *IEEE Trans Med Imaging* **22**, 1120-1130 (2003).

266. G. C. Sharp, S. W. Lee, and D. K. Wehe, "ICP registration using invariant features," *Ieee T Pattern Anal* **24**, 90-102 (2002).
267. M. P. Dubuisson and A. K. Jain, "A modified Hausdorff distance for object matching. In Pattern Recognition," *1-Conference A: Computer Vision & Image Processing., Proceedings of the 12th IAPR International Conference* **1**, 566-568 (1994).
268. D. P. Huttenlocher, G. Klanderman, and W. J. Rucklidge, "Comparing images using the Hausdorff distance," *Pattern Analysis and Machine Intelligence, IEEE Transactions on* **15**, 850 – 863 (1993).
269. T. O. McBride, B. W. Pogue, S. Poplack, S. Soho, W. A. Wells, S. Jiang, U. L. Osterberg, and K. D. Paulsen, "Multispectral near-infrared tomography: a case study in compensating for water and lipid content in hemoglobin imaging of the breast," *J Biomed Opt* **7**, 72-79 (2002).
270. J. B. West, J. M. Fitzpatrick, S. A. Toms, C. R. Maurer, and R. J. Maciunas, "Fiducial point placement and the accuracy of point-based, rigid body registration," *Neurosurgery* **48**, 810-816 (2001).
271. W. R. Crum, T. Hartkens, and D. L. G. Hill, "Non-rigid image registration: theory and practice," *Brit J Radiol* **77**, 140-153 (2004).
272. K. J. Friston, "Introduction: experimental design and statistical parametric mapping," in *Human brain function,* 2nd ed., R. S. J. Frackowiak, K. J. Friston, C. Frith, R. Dolan, C. J. Price, S. Zeki, J. Ashburner, and W. D. Penny, eds. (Academic Press, 2003).
273. F. Bevilacqua, D. Piguet, P. Marquet, J. D. Gross, B. J. Tromberg, and C. Depeursinge, "In vivo local determination of tissue optical properties: applications to human brain," *Applied optics* **38**, 4939-4950 (1999).
274. D. A. Boas, T. Gaudette, G. Strangman, X. Cheng, J. J. Marota, and J. B. Mandeville, "The accuracy of near infrared spectroscopy and imaging during focal changes in cerebral hemodynamics," *Neuroimage* **13**, 76-90 (2001).
275. D. Chetverikov, D. Svirko, D. Stepanov, and P. Krsek, "The trimmed iterative closest point algorithm," *Int C Patt Recog* **3**, 545-548 (2002).
276. P. Giacometti, K. L. Perdue, and S. G. Diamond, "Algorithm to find high density EEG scalp coordinates and analysis of their correspondence to structural and functional regions of the brain," *Journal of neuroscience methods* **229**, 84-96 (2014).
277. V. Jurcak, D. Tsuzuki, and I. Dan, "10/20, 10/10, and 10/5 systems revisited: their validity as relative head-surface-based positioning systems," *Neuroimage* **34**, 1600-1611 (2007).
278. Y. Zhan, A. T. Eggebrecht, J. P. Culver, and H. Dehghani, "Image quality analysis of high-density diffuse optical tomography incorporating a subject-specific head model," *Front Neuroenergetics* **4**, 6 (2012).
279. H. Dehghani, B. R. White, B. W. Zeff, A. Tizzard, and J. P. Culver, "Depth sensitivity and image reconstruction analysis of dense imaging arrays for mapping brain function with diffuse optical tomography," *Applied optics* **48**, D137-143 (2009).
280. Y. Pei, H. L. Graber, and R. L. Barbour, "Influence of Systematic Errors in Reference States on Image Quality and on Stability of Derived Information for dc Optical Imaging," *Appl Opt* **40**, 5755-5769 (2001).
281. G. Strangman, M. A. Franceschini, and D. A. Boas, "Factors affecting the accuracy of near-infrared spectroscopy concentration calculations for focal changes in oxygenation parameters," *Neuroimage* **18**, 865-879 (2003).
282. P. T. Fox, M. A. Mintun, M. E. Raichle, F. M. Miezin, J. M. Allman, and D. C. Van Essen, "Mapping human visual cortex with positron emission tomography," *Nature* **323**, 806-809 (1986).
283. K. K. Kwong, J. W. Belliveau, D. A. Chesler, I. E. Goldberg, R. M. Weisskoff, B. P. Poncelet, D. N. Kennedy, B. E. Hoppel, M. S. Cohen, R. Turner, and et al., "Dynamic magnetic resonance imaging of human brain activity during primary sensory stimulation," *Proc Natl Acad Sci U S A* **89**, 5675-5679 (1992).
284. M. E. Raichle, "Behind the scenes of functional brain imaging: a historical and physiological perspective," *Proc Natl Acad Sci U S A* **95**, 765-772 (1998).

285. S. Arridge and M. Schweiger, "Gradient-based optimisation scheme for optical tomography," *IEEE Trans Med Imaging* **18**, 262-271 (1999).
286. A. H. Hielscher, A. D. Klose, and K. M. Hanson, "Gradient-based iterative image reconstruction scheme for time-resolved optical tomography," *IEEE Trans Med Imaging* **18**, 262-271 (1999).
287. B. Biswal, F. Zerrin Yetkin, V. M. Haughton, and J. S. Hyde, "Functional connectivity in the motor cortex of resting human brain using echo-planar mri," *Magnetic resonance in medicine* **34**, 537-541 (1995).
288. A. C. Nobre, G. N. Sebestyen, D. R. Gitelman, M. M. Mesulam, R. S. Frackowiak, and C. D. Frith, "Functional localization of the system for visuospatial attention using positron emission tomography," *Brain : a journal of neurology* **120**, 515-533 (1997).
289. E. Courchesne, K. Pierce, C. M. Schumann, E. Redcay, J. A. Buckwalter, D. P. Kennedy, and J. Morgan, "Mapping early brain development in autism," *Neuron* **56**, 399-413 (2007).
290. M. Mesulam, "Defining neurocognitive networks in the BOLD new world of computed connectivity," *Neuron* **62**, 1-3 (2009).
291. V. Menon, "Large-scale brain networks and psychopathology: a unifying triple network model," *Trends in cognitive sciences* **15**, 483-506 (2011).
292. K. A. Pelphrey, S. Shultz, C. M. Hudac, and B. C. Vander Wyk, "Research review: Constraining heterogeneity: the social brain and its development in autism spectrum disorder," *Journal of child psychology and psychiatry, and allied disciplines* **52**, 631-644 (2011).
293. M. E. Phelps and J. C. Mazziotta, "Positron emission tomography: human brain function and biochemistry," *Science* **228**, 799-809 (1985).
294. J. Sergent, S. Ohta, and B. MacDonald, "Functional neuroanatomy of face and object processing. A positron emission tomography study," *Brain : a journal of neurology* **115 Pt 1**, 15-36 (1992).
295. S. A. Engel, G. H. Glover, and B. A. Wandell, "Retinotopic Organization in Human Visual Cortex and the Spatial Precision of Functional MRI," *Cerebral cortex* **7**, 181-192 (1997).
296. M. Wolf, M. Ferrari, and V. Quaresima, "Progress of near-infrared spectroscopy and topography for brain and muscle clinical applications," *J Biomed Opt* **12**, 062104 (2007).
297. F. Irani, S. M. Platek, S. Bunce, A. C. Ruocco, and D. Chute, "Functional near infrared spectroscopy (fNIRS): an emerging neuroimaging technology with important applications for the study of brain disorders," *The Clinical neuropsychologist* **21**, 9-37 (2007).
298. F. Scholkmann, S. Kleiser, A. J. Metz, R. Zimmermann, J. M. Pavia, U. Wolf, and M. Wolf, "A review on continuous wave functional near-infrared spectroscopy and imaging instrumentation and methodology," *Neuroimage* **85**, 6-27 (2014).
299. A. Torricelli, D. Contini, A. Pifferi, M. Caffini, R. Re, L. Zucchelli, and L. Spinelli, "Time domain functional NIRS imaging for human brain mapping," *Neuroimage* **85 Pt 1**, 28-50 (2014).
300. X. Wu, A. T. Eggebrecht, S. L. Ferradal, J. P. Culver, and H. Dehghani, "Quantitative evaluation of atlas-based high-density diffuse optical tomography for imaging of the human visual cortex," *Biomedical Optics Express,* **5**, 3882-3900 (2014).
301. V. L. Towle, J. Bolanos, D. Suarez, K. Tan, R. Grzeszczuk, D. N. Levin, R. Cakmur, S. A. Frank, and J. P. Spire, "The spatial location of EEG electrodes: locating the best-fitting sphere relative to cortical anatomy," *Electroencephalogr Clin Neurophysiol* **86**, 1-6 (1993).
302. T. D. Lagerlund, F. W. Sharbrough, C. R. Jack, B. J. Erickson, D. C. Strelow, K. M. Cicora, and N. E. Busacker, "Determination of 10-20 System Electrode Locations Using Magnetic-Resonance Image Scanning with Markers," *Electroencephalography and clinical neurophysiology* **86**, 7-14 (1993).
303. D. Tsuzuki, D. Cai, H. Dan, Y. Kyutoku, A. Fujita, E. Watanabe, and I. Dan, "Stable and convenient spatial registration of stand-alone NIRS data through anchor-based probabilistic registration," *Neurosci Res* **72**, 163-171 (2012).

304. M. E. Eames, B. W. Pogue, P. K. Yalavarthy, and H. Dehghani, "An efficient Jacobian reduction method for diffuse optical image reconstruction," *Opt Express* **15**, 15908-15919 (2007).
305. N. Tzourio-Mazoyer, B. Landeau, D. Papathanassiou, F. Crivello, O. Etard, N. Delcroix, B. Mazoyer, and M. Joliot, "Automated anatomical labeling of activations in SPM using a macroscopic anatomical parcellation of the MNI MRI single-subject brain," *Neuroimage* **15**, 273-289 (2002).
306. D. Pantazis, A. Joshi, J. Jiang, D. W. Shattuck, L. E. Bernstein, H. Damasio, and R. M. Leahy, "Comparison of landmark-based and automatic methods for cortical surface registration," *Neuroimage* **49**, 2479-2493 (2010).
307. M. Okamoto, H. Dan, K. Sakamoto, K. Takeo, K. Shimizu, S. Kohno, I. Oda, S. Isobe, T. Suzuki, K. Kohyama, and I. Dan, "Three-dimensional probabilistic anatomical cranio-cerebral correlation via the international 10-20 system oriented for transcranial functional brain mapping," *Neuroimage* **21**, 99-111 (2004).
308. A. G. Sanfey, J. K. Rilling, J. A. Aronson, L. E. Nystrom, and J. D. Cohen, "The neural basis of economic decision-making in the ultimatum game," *Science* **300**, 1755-1758 (2003).
309. H. Walter, B. Abler, A. Ciaramidaro, and S. Erk, "Motivating forces of human actions - Neuroimaging reward and social interaction," *Brain Research Bulletin* **67**, 368-381 (2005).
310. T. Singer, "The neuronal basis of empathy and fairness," *Novartis Found Symp* **278**(2007).
311. K. R. Müller, M. Tangermann, G. Dornhege, M. Krauledat, G. Curio, and B. Blankertz, "Machine learning for real-time single-trial EEG-analysis: from brain–computer interfacing to mental state monitoring," *Journal of neuroscience methods* **167**, 82-90 (2008).
312. R. Christopher deCharms, K. Christoff, G. H. Glover, J. M. Pauly, S. Whitfield, and J. D. Gabrieli, "Learned regulation of spatially localized brain activation using real-time fMRI," *Neuroimage* **21**, 436-443 (2004).
313. S. Johnston, D. E. J. Linden, D. Healy, R. Goebel, I. Habes, and S. G. Boehm, "Upregulation of emotion areas through neurofeedback with a focus on positive mood," *Cogn Affect Behav Ne* **11**, 44-51 (2011).
314. R. Sitaram, S. Lee, S. Ruiz, M. Rana, R. Veit, and N. Birbaumer, "Real-time support vector classification and feedback of multiple emotional brain states," *Neuroimage* **56**, 753-765 (2011).
315. R. Sitaram, R. Veit, B. Stevens, A. Caria, C. Gerloff, N. Birbaumer, and F. Hummel, "Acquired Control of Ventral Premotor Cortex Activity by Feedback Training: An Exploratory Real-Time fMRI and TMS Study," *Neurorehabilitation and neural repair* **26**, 256-265 (2012).
316. A. D. Craig, ""How do you feel? Interoception: the sense of the physiological condition of the body," *Nature Reviews Neuroscience* **3**, 655-666 (2002).
317. S. M. Coyle, T. E. Ward, and C. M. Markham, "Brain–computer interface using a simplified functional near-infrared spectroscopy system," *Journal of neural engineering* **4**, 219 (2007).
318. S. G. Mason, R. Bohringer, J. F. Borisoff, and G. E. Birch, "Real-time control of a video game with a direct brain--computer interface," *J Clin Neurophysiol* **21**, 404-408 (2004).
319. N. Weiskopf, K. Mathiak, S. W. Bock, F. Scharnowski, R. Veit, W. Grodd, R. Goebel, and N. Birbaumer, "Principles of a brain-computer interface (BCI) based on real-time functional magnetic resonance imaging (fMRI)," *IEEE Trans Biomed Eng* **51**, 966-970 (2004).
320. S. M. LaConte, S. J. Peltier, and X. P. P. Hu, "Real-time fMRI using brain-state classification," *Human brain mapping* **28**, 1033-1044 (2007).
321. S. Thesen, O. Heid, E. Mueller, and L. R. Schad, "Prospective acquisition correction for head motion with image-based tracking for real-time fMRI," *Magnetic resonance in medicine : official journal of the Society of Magnetic Resonance in Medicine / Society of Magnetic Resonance in Medicine* **44**, 457-465 (2000).
322. N. Weiskopf, R. Veit, M. Erb, K. Mathiak, W. Grodd, R. Goebel, and N. Birbaumer, "Physiological self-regulation of regional brain activity using real-time functional magnetic

resonance imaging (fMRI): methodology and exemplary data," *Neuroimage* **19**, 577-586 (2003).
323. M. Beauregard and J. Levesque, "Functional magnetic resonance imaging investigation of the effects of neurofeedback training on the neural bases of selective attention and response inhibition in children with attention-deficit/hyperactivity disorder," *Appl Psychophysiol Biofeedback* **31**, 3-20 (2006).
324. A. Joshi, W. Bangerth, and E. M. Sevick-Muraca, "Adaptive finite element based tomography for fluorescence optical imaging in tissue," *Optics express* **12**, 5402-5417 (2004).
325. K. D. Paulsen and H. Jiang, "Enhanced frequency-domain optical image reconstruction in tissues through total-variation minimization," *Applied optics* **35**, 3447-3458 (1996).
326. M. Guven, B. Yazici, K. Kwon, E. Giladi, and X. Intes, "Effect of discretization error and adaptive mesh generation in diffuse optical absorption imaging,," *Inverse Probl* **23**, 1135 (2007).
327. K. D. Paulsen and H. B. Jiang, "Spatially Varying Optical Property Reconstruction Using a Finite-Element Diffusion Equation Approximation," *Medical physics* **22**, 691-701 (1995).
328. S. Gupta, P. K. Yalavarthy, D. Roy, D. Piao, and R. M. Vasu, "Singular value decomposition based computationally efficient algorithm for rapid dynamic near-infrared diffuse optical tomography," *Med Phys* **36**, 5559-5567 (2009).
329. M. Schweiger, "GPU-accelerated finite element method for modeling light transport in diffuse optical tomography," *Journal of Biomedical Imaging* **10**(2011).
330. Y. Lu and A. F. Chatziioannou, "A Parallel Adaptive Finite Element Method for the Simulation of Photon Migration with the Radiative-Transfer-Based Model," *Commun Numer Methods Eng* **25**, 751-770 (2009).
331. S. R. Arridge and M. Schweiger, "Photon-measurement density functions. Part2: Finite-element-method calculations," *Applied optics* **34**, 8026-8037 (1995).
332. S. R. Arridge and J. C. Schotland, "Optical tomography: forward and inverse problems," *Inverse Problems* **25**(2009).
333. S. R. Arridge, J. P. Kaipio, V. Kolehmainen, M. Schweiger, E. Somersalo, T. Tarvainen, and M. Vauhkonen, "Approximation errors and model reduction with an application in optical diffusion tomography," *Inverse Problems* **22**, 175-195 (2006).